

Time-resolved characterisation of pulsed magnetron discharges for the deposition of thin films with plasma diagnostic methods

Habilitationsschrift

zur Erlangung des akademischen Grades

doctor rerum naturalium habilitus

(Dr. rer. nat. habil.)

vorgelegt

der Fakultät für Naturwissenschaften der Technischen Universität Chemnitz

von

Dr. Thomas Welzel

geboren am 14. Oktober 1970 in Glauchau

Preface

Research on the characterisation and understanding of pulsed magnetron discharges used for the deposition of thin, especially dielectric, films has been carried out between 2003 and 2008 at Chemnitz University of Technology. This thesis is a collection and summary of the original research during this period.

In the main part of the thesis, work published in peer-reviewed scientific papers is summarised and yet unpublished results are given in more detail. Different aspects highlighted in the publications are described in a general context of the characterisation of the pulsed discharges for the principal understanding. The cross-linking of the published results is addressed and where necessary extensions to the publications are given. The main part is organised in three sections. In the first one, basics of pulsed magnetron discharges, their application, and important questions are summarised. The second section describes general results and physics of the discharges that have been obtained during the research work. It also emphasises the successful development or modifications of experimental techniques for the time-resolved characterisation. The third section addresses the possibilities to modify and control the process by external parameters that are typically accessible during the application or required by it. An appendix to the thesis comprises selected published research work which is made available as reprints of the original publications. Other publications which are not included as reprints are referenced to in the main part.

The work has been carried out in the group of Prof. Frank Richter at Chemnitz University of Technology. He offered the opportunity to investigate the discharges of the many magnetron sputter deposition processes used in the group and to acquire research projects aiming at the understanding of the basic physics behind those deposition processes. The author of the thesis is also indebted to many very fruitful and sometimes controversial discussions which have taken place over the years. The thesis would not have been possible without the work of several diploma and

PhD students who have carried out laborious experiments and analyses. Particularly, Thoralf Dunger should be thanked at this point. Many other colleagues and friends, especially the whole team at Prof. Richter's group, supported the work presented here. International Cooperation with groups at Liverpool University and Manchester Metropolitan University as well as close contacts to colleagues from Ghent University, Sheffield Hallam University, and the University of Plzen lead to many beneficial discussions and ideas, which helped to improve the thesis. Finally yet importantly, financial support through several projects is greatly acknowledged. Funding of the work has been partly obtained from the German Research Council, the German Academic Exchange Service, the Saxon Ministry for Labour and Economic Affairs, and the European Union within the frame of the EFRE programme.

Contents

| | |
|---|-----------|
| Preface | 1 |
| 1. Introduction | 5 |
| 1.1. Deposition of insulating thin films with magnetron sputtering | 6 |
| 1.2. Energy of species involved in film formation | 7 |
| 1.3. Pulsed magnetron sputtering processes | 8 |
| 1.4. Objective of the work | 9 |
| 2. Basics of pulsed magnetron sputtering | 11 |
| 2.1. Sputtering of solids | 11 |
| 2.2. Low pressure gas discharges | 17 |
| 2.3. Magnetron sputtering | 23 |
| 2.4. Pulsed Magnetrons | 28 |
| 3. Fundamental properties of pulsed magnetron discharges and qualified investigation methods | 33 |
| 3.1. Introduction | 33 |
| 3.2. Densities and energies of charged particle within the discharge | 35 |
| 3.2.1. The time-resolved (Langmuir) double probe | 36 |
| 3.2.2. Development of the charge carrier density within one pulse | 40 |
| 3.2.3. Model description of the ignition during the 'on' phase | 43 |
| 3.2.4. Spatial distribution of the charge carrier density | 48 |
| 3.2.5. Optical emission | 51 |
| 3.2.6. Excitation mechanisms and temporal behaviour of emission lines | 56 |
| 3.3. Potential in the discharge volume | 59 |
| 3.3.1. Measurement technique – the emissive probe | 60 |
| 3.3.2. General temporal development | 63 |
| 3.3.3. Spatio-temporal distribution of the plasma potential | 65 |
| 3.4. Ion energies at the substrate | 68 |
| 3.4.1. Measurement – the plasma monitor | 69 |
| 3.4.2. Energies in d.c. discharges | 72 |
| 3.4.3. Pulsed magnetron discharges | 79 |
| 3.5. Summary of fundamental properties | 86 |

| | | |
|-----------|--|------------|
| 4. | Dependence on operation parameters and magnetron configuration | 91 |
| 4.1. | Introduction | 91 |
| 4.2. | Target material and reactive gas | 91 |
| 4.3. | Discharge pressure | 101 |
| 4.4. | Discharge geometry and wall potentials | 108 |
| 4.5. | Cylindrical rotatable magnetrons | 115 |
| 4.6. | Summary of external influences and process control | 119 |
| 5. | Conclusions | 123 |
| | References | 125 |
| | References available as reprints | 134 |
| | List of frequently used symbols | 135 |
| | List of publications | 137 |
| | Declarations | 141 |
| | Appendix | 143 |
| A1 | T. Welzel, T. Dunger, H. Kupfer, F. Richter, A Time-Resolved Langmuir Double Probe Method for the Investigation of Pulsed Magnetron Discharges, J. Appl. Phys. 96, 12 (2004) 6994-7001 | |
| A2 | T. Welzel, T. Dunger, F. Richter, <i>Reactive Gas Effects in Pulsed Magnetron Sputtering: Time-Resolved Investigation</i> , Surf. Coat. Technol. 201, 7 (2006) 3959-3963. | |
| A3 | T. Welzel, T. Dunger, B. Liebig, F. Richter, <i>Spatial and temporal development of the plasma potential in differently configured pulsed magnetron discharges</i> , New J. Phys. 10 (2008) 123008. | |
| A4 | T. Welzel, R. Kleinhempel, T. Dunger, F. Richter, <i>Ion Energy Distributions in Magnetron Sputtering of Zinc Aluminium Oxide</i> , Plasma Processes and Polymers, in press, DOI: 10.1002/ppap200930805. | |

1. Introduction

Magnetron sputtering with pulsed discharges in different forms has become one of the most popular techniques to deposit thin, especially dielectric, films. It has been established technologically and is nowadays commonly applied in a variety of production processes. The major advantage of the technique is the suppression of process instabilities due to the pulsing while keeping the benefits of conventional magnetron sputtering which are large-area and high-rate deposition with moderate particle energies. While processes for e.g. specific film materials or substrate geometries have been established it is still a challenge to modify or optimise them for an adjustment to altered circumstances, e.g. when the chamber geometry has to be adapted to different substrates. This failure which is often bypassed by time-consuming trial-and-error methods is a result of up to date insufficient understanding of the basics of pulsed magnetron discharges, especially of the dependence of particle currents and energies onto the substrates on the pulse parameters. This is particularly the case because in pulsed magnetrons these quantities are supposedly strongly modulated during a single pulse and their average value is not adequate to describe the deposition process or compare it to d.c. processes. It is therefore necessary to investigate particle densities and currents and their energy on a time-scale shorter than one pulse of typically one microsecond. To achieve this objective, appropriate measurement techniques have to be developed or improved in order to obtain a time-resolution better than 1 μ s.

It is the objective of the present work to make a considerable contribution to the basic physical understanding of the temporal behaviour of essential parameters of pulsed magnetron discharges. The main focus is laid on discharge parameters which are most important for the film deposition: the density of ions and electrons, the energies of the electrons and the potential distribution, the latter two prevalingly governing the energy of the ions.

In section 2, the basics and history of magnetron sputtering which are needed for a better understanding of the time-resolved investigations and interpretations are summarised. Also, the key ideas of pulsed magnetron sputtering are presented. Section 3 outlines the results which are common to pulsed magnetron discharges and the models derived from them. Within this section, the development of the time-resolved techniques and their peculiarities are also given in detail. In Section 4, the influence of external parameters or magnetron design which may be used to control particular discharge properties in the future is described and discussed. The results are finally summarised and conclusions are drawn in section 5.

Prior to the detailed description in sections 2-4, the motivation of the work shall be extended in the following paragraphs.

1.1. Deposition of insulating thin films with magnetron sputtering

Plasma-assisted methods – with magnetron sputtering being a specialised form of them - are frequently utilised both in physical (PVD) and chemical vapour deposition (CVD). One advantage is common to these methods: it is possible to optimise the growing films by energetic particles that are generated in the plasma discharge or created by the extraction from it. Whereas e.g. for a classical condensation film forming particles exhibit only the thermal energy of less than 1 eV when they arrive at the substrate, the energy of at least some species in plasma-assisted PVD may reach up to several 100 eV. Another important advantage of the plasma is that it may form reactive species such as oxygen from a proper admixture of reactive gas. Thus compound materials can be deposited even with properties far from equilibrium.

One of the most popular plasma-assisted processes which is nowadays widely used in industrial fabrication of coated products is magnetron sputtering where by a sophisticated magnetic field configuration at the sputtering target the discharge is confined close to it. As a result, magnetron sputter sources can be operated with moderate voltages and low pressure compared to other PVD processes. The high plasma density at the target leads to high deposition rates and the process is in

principle scaleable to large-area coating through an increase of the target size. Both facts are highly demanded by most industrial applications.

1.2. Energy of species involved in film formation

Despite of the common application, the basic mechanisms affecting the film quality are up to date still not well enough understood to optimise the deposition process in modified environments. This may be the adjustment to a different process chamber or production line or the change of the film material. The reason is the variety of species produced directly (e.g. ions) or indirectly (e.g. sputtered atoms) by the plasma which all can have their own contribution to the film formation via their current density and energy. The substrate or film is subject to fluxes of neutral species that either originate from the working gas and have a thermal energy of 0.03 eV or are sputtered from the target. The latter have typical energies of up to several 10 eV but may be significantly cooled down on their way to the substrate. It is further speculated that ions bombarding the target could be reflected and reach the substrate as very high energetic neutrals. Obviously, the substrate is also subject to currents of charged particle due to its contact with the plasma. Electrons have typical energies of several eV. In many cases, it is desired to take advantage of positive ions, e.g. from the working gas in which the discharge is operated, which are extracted with a defined energy by a negative voltage at the substrate. Ion energies then range between several eV up to several 100 eV. To add to the complexity, in reactive sputtering for the formation of compound materials negative ions, supposedly with high energies (~ 100 eV), are assumed to play a role and dissociation products are added either in the form of neutrals or ions. The plasma further delivers radiation (~ 10 eV) to the substrate. In consequence, up to date, magnetron deposition processes are still optimised with trial-and-error experiments. To take the faster way to adjust single physical quantities to tailor the process, there is still need of knowledge which species are the important ones and how they can be controlled by technological parameters.

1.3. Pulsed magnetron sputtering processes

Since the end of the last century, pulsed magnetron sputtering with frequencies of about 100 kHz in different modifications has been rapidly introduced in industrial production processes of thin films. The reason is that during the conventional deposition of dielectric thin films with d.c. discharges, insulating layers that form on the target accumulate charges on their surface which leads to arcing and process instabilities that drastically impair the film quality. By pulsing the discharge with an appropriate frequency the charges can be neutralised and the process is stabilised. Shown by many examples, the quality of the dielectric films is thus greatly enhanced.

Apart from this quite well understood motivation for the application of pulsed discharges, only little has been known about the consequences on the properties of the plasma and how this may influence the film growth further. This lack of knowledge has been the motivation for the research work presented in this thesis. Through pulsing the discharge, the target voltage and discharge power will be highly modulated. Because the discharge is driven by these parameters and it has to be expected that the potentials associated with the plasma, i.e. the plasma and floating potential, will be modulated as well. Therefore, changes in the energy of the charged particles can be supposed when they travel through the sheaths in front of the electrodes. This will be important for the discharge when energetic particles, e.g. electrons, are injected into it as well as for the substrate or films through electrons or ions extracted out of the plasma. The latter is especially important because elevated energies of the arriving particles may e.g. enhance the mobility on the surface or lead to the densification of the film. On the other hand and depending on the film material, high energetic bombardment may cause damage in the film. It is hence important to know the energies of the arriving species and how they can be controlled. Of interest in this respect is not only the average energy but also the energy at any moment because even short "pulses" of energetic bombardment could be damaging. The film growth will, however, also be determined by the total energy influx, i.e. by the product of the energies of the particles and their current which is given by their density. The latter is supposed to be modulated as well following the modulated power applied to the discharge. To optimise the deposition process, the development of the density therefore has to be known as well. These additional dynamics make a detailed

understanding of the deposition process even more difficult than described above for d.c. magnetron sputtering. They may also take effect on the time-averaged quantities that are important for the mechanisms of the film growth.

1.4. Objective of the work

In fact, prior to this work, very first results from Langmuir and thermal probe investigations were published that the average charge carrier density or electron temperature was altered by pulsing the discharge compared to the d.c. case. First investigations of the ion energies at the substrates further indicated that higher ion energies appear in pulsed discharges. The results were, however, hard to compare because of very different operating conditions. They were therefore not suited for a generalisation with respect to mechanisms dominating the pulsed magnetron discharge and make up differences to d.c. operation.

Moreover, to recognise the mechanisms behind a change of the time-averaged values, the physics at each moment of one pulse have to be investigated. Hence time-resolved measurements of physical quantities such as density and energy or potential on the sub-pulse time-scale are imperative to understand the discharge behaviour even on the time-averaged scale. Considering typical frequencies for such discharges of 100 kHz, plasma diagnostics were required with a time-resolution of 1 μs or better. One objective of the thesis was to develop such diagnostic methods based on the time-averaged techniques which were approved within the group. As a further challenge, the diagnostics had to be optimised for conditions where contamination due to the deposition process is unavoidable. Double probes and emissive probes as well as optical emission spectroscopy are primarily dealt with in this thesis. Time-averaged investigations with an energy-dispersive mass spectrometer assist the time-resolved measurements. From the combined results of these methods, common properties and qualitative models of pulsed magnetron discharges shall be derived which are transferable to similar systems. These properties are investigated in dependence on externally accessible parameters – such as pressure or environment geometry – to introduce the possibility to control or optimise pulsed magnetron discharges by technologically easily accessible variables.

2. Basics of magnetron sputtering

2.1. Sputtering of solids

The process of liberating atoms or molecules from a solid (target) surface into the gas phase by heavy particle bombardment with high energies of at least several 10 eV is called sputtering. Practically, it is frequently performed with ions from either an ion beam source or an adjacent plasma because ions can be easily accelerated to the required energy. Sputtering occurs mainly in two main regimes. At high incident energies (and high ion masses), the energy in the target is distributed in a thermal spike, where the atoms in the volume around the atom which is hit by the incident ion are set in motion by the collision. In many practical cases such as magnetron sputtering, the energy of the incident ion is much lower than 1 keV and sputtering is dominated by a collision cascade which develops below the target surface. In this case, the primary ion or a recoil target atom produced by it collides with another single target atom which is at rest before. The cascade develops until the initial energy is distributed within the cascade so that the primary ion and every recoil do not have sufficient energy above the displacement energy to set another recoil atom in motion. Within the collision cascade, the initial direction of the movement is altered so that finally, some recoils at the target surface have a velocity component away from the target and can leave it if the corresponding energy exceeds the surface binding energy.

Particularly important for magnetron sputtering are two quantities in. One is the sputtering yield Y which is the number of ejected atoms per incident ion. The second is the energy with which the atoms leave the target characterised by the energy distribution function $\Phi(E)$. Based on Sigmund's early theory of sputtering in the isotropic cascade regime under normal ion incidence on a polycrystalline monoatomic target leading to [1]

$$Y(E_i) = \frac{0.042}{U_s} \kappa S_n(E_i) \quad (1)$$

(E_i – energy of the incident ion, U_s – surface binding energy, S_n – nuclear stopping cross section, κ - energy independent function of the ratio of M_1 , the mass of the incident ion, and M_2 , the mass of the target atom; the numerical factor being in \AA^{-2}), Yamamura and Tawara [2] have extended it to lower incident energy and to high energy sputtering of light ions. From comparison to many experimental data they have derived a semi-empirical formula for the sputtering yield

$$Y(E_i) = 0.042 \frac{W_2(Z_2) \kappa^*}{U_s} \cdot \frac{S_n(E_i)}{1 + \frac{(M_1/7)^3}{W_1(Z_2) \cdot k_e \hat{\epsilon}^{0.3}}} \left(1 - \sqrt{\frac{E_{th}}{E_i}}\right)^\rho \quad (2)$$

Within this, $W_1(Z_2)$, $W_2(Z_2)$, and δ are dimensionless best-fit values, the threshold sputtering energy, E_{th} , has also been obtained as a fitting parameter to be

$$E_{th} = \begin{cases} \frac{6.7}{\Gamma} U_s & M_1 \geq M_2 \\ \frac{1 + 5.7(M_1/M_2)}{\Gamma} & M_1 \leq M_2 \end{cases} \quad (3)$$

with the energy transfer factor for elastic collisions

$$\Gamma = 4 \frac{M_1 M_2}{(M_1 + M_2)^2} \quad (4)$$

The terms k_e and κ^* are also only dependent on the atomic number and mass of the incident projectile and the target atom:

$$k_e = 0.079 \frac{(M_1 + M_2)^{3/2}}{M_1^{3/2} M_2^{1/2}} \frac{Z_1^{2/3} Z_2^{1/2}}{(Z_1^{2/3} + Z_2^{2/3})^{3/4}} \quad (5)$$

$$\kappa^* = \begin{cases} 0.249(M_2/M_1)^{0.56} + 0.0035(M_2/M_1)^{1.5} & M_1 \leq M_2 \\ 0.0875(M_2/M_1)^{-0.15} + 0.165(M_2/M_1) & M_1 \geq M_2 \end{cases} \quad (6)$$

S_n is the nuclear stopping cross section¹

$$S_n(E_i) = 84.78 \frac{Z_1 Z_2}{(Z_1^{2/3} + Z_2^{2/3})^{1/2}} \frac{M_1}{M_1 + M_2} s_n^{TF}(\hat{\epsilon}) \quad (7)$$

which is expressed in terms of the reduced stopping power

¹ Note, that the numerical value has been corrected by a factor of 10 compared to the original publication.

$$s_n^{TF}(\hat{\epsilon}) = \frac{3.441\sqrt{\hat{\epsilon}} \ln(\hat{\epsilon} + 2.718)}{1 + 6.355\sqrt{\hat{\epsilon}} + \epsilon(6.882\sqrt{\hat{\epsilon}} - 1.708)} \quad (8)$$

and the reduced energy

$$\hat{\epsilon} = \frac{0.03255}{Z_1 Z_2 (Z_1^{2/3} + Z_2^{2/3})^{1/2}} \frac{M_2}{M_1 + M_2} E_i. \quad (9)$$

The values of M are in atomic mass units, the energies E_i , E_{th} , and U_S in electron volts, the stopping cross section is in $eV \cdot \text{\AA}/\text{atom}$. Equations (2) to (9) demonstrate that the sputtering yield is primarily dependent on the mass of target atoms and incident ions and of the energy of the ions, typical calculated energy dependences are shown in Figure 1 for materials which are used within this thesis. The formalism does not account for different incident angles of the ions which typically result in maximum sputtering yield for about 70° incidence. Such angles are, however, not relevant for magnetron sputtering because the ions are accelerated from the plasma through a very thin sheath of about 1 mm in front of the target.

Although equations (2) to (9) have been derived for mono-elemental solids, they are also frequently applied to approximate the sputtering yield of alloys and compounds. For alloys, the surface composition is modified by preferential sputtering of different components. Once the surface has reached its stationary new composition, the sputtering yields correspond to the bulk composition of the material and the yield for each component is calculated as if it formed a monoatomic target [3]. Compound materials such as oxides investigated in this work, in most cases have a higher heat of sublimation so that U_S is increased and as a rule of thumb according to equation (2) the sputtering yield of oxides (or nitrides) is much lower than for the pure metal (cf. Figure 1). If U_S for the compound is known, the sputtering yield can be estimated taking $W_1(Z_2) = 0.35 \cdot U_S$, $W_2(Z_2) = 1$, and $\rho = 2.5$ as Yamamura and Tawara [2] suggest for untabulated mono-atomic solids. Experimental data of the surface binding energy of the compounds materials are scarce. Malherbe et. al. emphasise they can be estimated from the pure metal properties taking the different bonding strengths of metal-metal, metal-oxygen, and the oxygen-oxygen bonds into account and that the resulting U_S is different for the metal and oxygen atoms of the compound material [4]. They calculated U_S for many common metal oxides including those that have been used in this work according to the equations

$$U_{s,O} = \frac{x}{x+y}D(M-O) + \frac{y}{x+y}D(O-O) + \frac{1}{2}(\chi_M - \chi_O)^2 \quad (10)$$

for the oxygen atoms and

$$U_{s,M} = H_S + \frac{1}{2}(\chi_M - \chi_O)^2 \quad (11)$$

for the metal atoms, where H_S is the heat of sublimation of the pure metal, $D(M-O)$ and $D(O-O)$ are the strength of the metal oxygen and oxygen-oxygen bond, respectively, and χ_M and χ_O are the electronegativities of the metal and oxygen, respectively, for a M_xO_y material. Data of materials related to this work and taken to calculate the yield values of Figure 1 are summarised in Table 1.

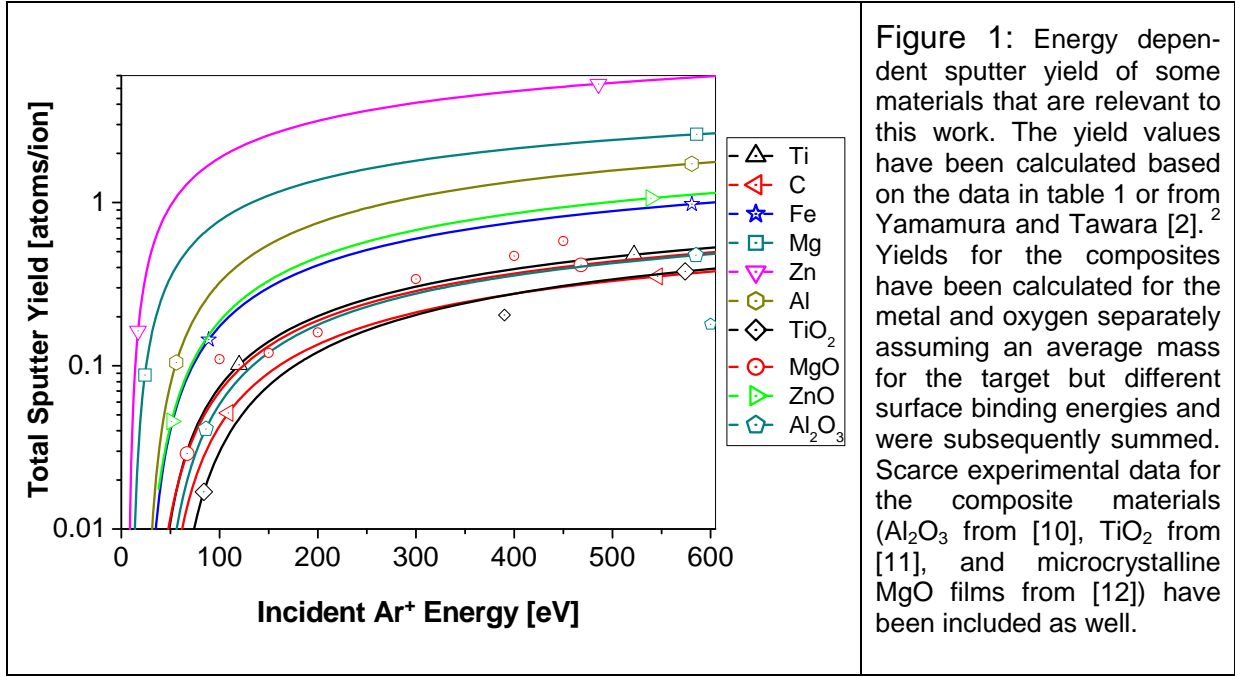
| Material | U_s [eV] | W_2 | W_1 [eV] | ρ | Y(300 eV) [atoms/ion] | γ_{iSEE} [electr./ion] |
|--------------------------------|----------------------------|----------|--------------------|---------|--------------------------|----------------------------------|
| C | 7.42 [5] | 1.7 [2] | 1.84 [2] | 2.5 [2] | 0.21 | 0.187 [6]* |
| Mg | 1.52 [5] | 1 | 0.532 | 2.5 | 1.8 | 0.136 [7] |
| MgO | M: 4.11 [4] O: 7.24 [4] | 1 | M: 1.44 O: 2.53 | 2.5 | M: 0.21 O: 0.08 | 0.409 [8] |
| Ti | 4.90 [5] | 0.54 [2] | 2.57 [2] | 2.5 [2] | 0.3 | 0.114 [7] |
| TiO ₂ | M: 7.27 [4] O: 6.68 [4] | 1 | M: 2.54 O: 2.38 | 2.5 | M: 0.06 O: 0.14 | 0.078 [8] |
| Zn | 1.35 [5] | 1 | 0.473 | 2.5 | 4.1 | n.a. |
| ZnO | M: 3.04 [4] O: 5.70 [4] | 1 | M: 1.06 O: 2.00 | 2.5 | M: 0.3 O: 0.19 | 0.051 ... 0.076 [9]** |
| Al | 3.42 [5] | 1 [2] | 1.84 [2] | 2.5 [2] | 1.1 | 0.091 [7] |
| Al ₂ O ₃ | M: 5.45 [4] O: 7.01 [4] | 1 | M: 1.91 O: 2.45 | 2.5 | M: 0.14 O: 0.14 | 0.198 [8] |
| Fe | 4.28 [2] | 0.75 [2] | 1.20 [2] | 2.5 [2] | 0.6 | n.a. |

Table 1: Values of the surface binding energy U_s , the Yamamura parameters W_1 , W_2 , and ρ used to calculate the sputter yield at 300 eV Ar^+ ion incidence, and the ion induced secondary electron emission coefficient (γ_{iSEE}) of some materials related to this work. The Yamamura parameters which are given without reference have been selected according to the suggestion in [2]. γ_{iSEE} taken from Depla et al. [7, 8] were measured in the ion energy range 260 - 392 eV except for MgO (156 eV).

* The high γ_{iSEE} for carbon is rather questionable because in the same reference a value for 300 eV of 0.502 for copper is given, which is much higher than 0.082 as obtained by Depla et al. [7].

** γ_{iSEE} for ZnO:Al were measured with 200 eV Ar^+ onto films of different thickness of 180 - 600 nm.

Further complications may arise from the roughness of the target or channelling in single crystal targets which will not be discussed here because roughness effects will probably dominated by the overall inhomogeneity of the sputter rate in magnetron sputtering due to the inhomogeneous ion bombardment and mono-crystalline targets are hardly used.



Thompson has calculated the energy distribution of the atoms ejected from the target for the cascade regime under normal ion incidence. He obtained for the flux of sputtered atoms Φ in dependence on their energy E and their ejection angle φ [13]

$$\Phi(E, \varphi) \cdot dE \cdot d\Omega = C \cdot \cos \varphi \cdot \frac{1 - \sqrt{(U_s - E)/\Gamma E_i}}{E^2 (1 + U_s/E)^3} \cdot dE \cdot d\Omega \quad (12)$$

It shows that the angular distribution of the sputtered flux is cosine-like. Depending on the surface morphology and the deviation from the linear cascade, it may deviate from the cosine distribution, which is often described by a rational power law of the cosine function. The constant C depends on the combination of incident ions and the target material, mainly on its atomic density, mass, and the interatomic potential, and the ion influx [13]. Integrating (12) over the emission angle and energy, the total sputter flux is obtained and can be compared to (2) once the ion flux is known. For the investigation of the sputter energy distribution it is therefore often sufficient to consider only normal ejection in (12)

$$\Phi(E) = C \cdot \frac{1 - \sqrt{(U_s - E)/\Gamma E_i}}{E^2 (1 + U_s/E)^3} \quad (13)$$

² Note that all figures within this work – except Figure 1, 2, and 17 which have been calculated according to the given formulae or reference – contain own experimental results and reference to published papers from the author is given where applicable.

and normalise it in an appropriate way, e.g. the energy integral to be one. This is shown in Figure 2 for a surface binding energy of 7.4 eV (carbon) and for different argon ion energies of 300, 500, and 900 eV.

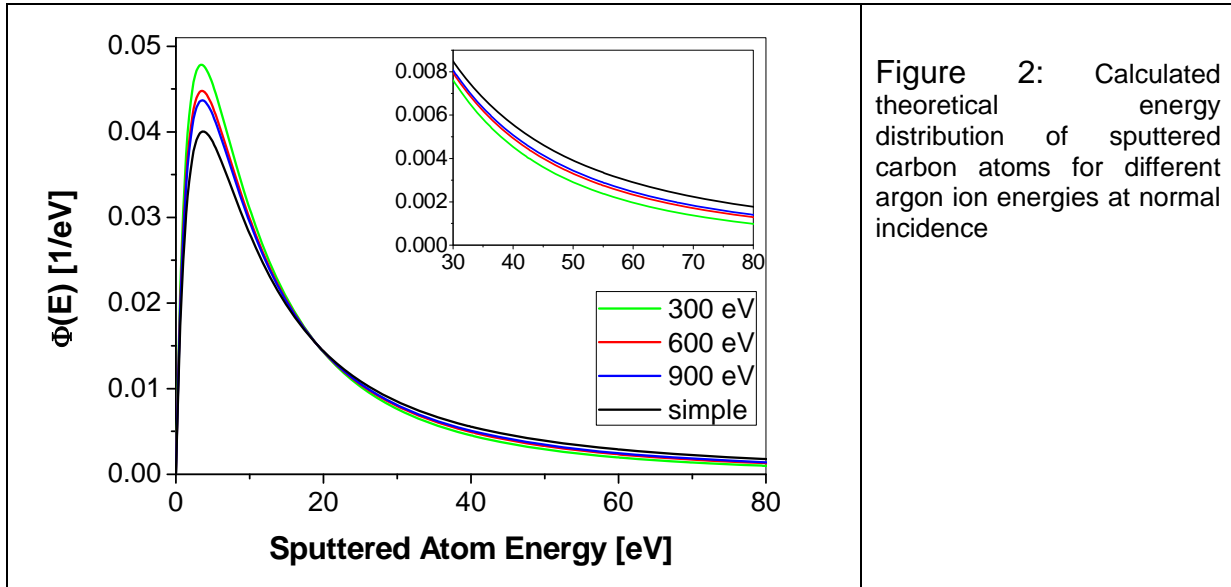


Figure 2: Calculated theoretical energy distribution of sputtered carbon atoms for different argon ion energies at normal incidence

The distributions all have the same form and are only very weakly dependent on the energy of the incident ion energy through the root in Equation (13). All exhibit a maximum at an energy of $U_s/2$ which is slightly decreasing in intensity with increasing ion energy. At the same time, shown in the inset in Figure 2, the high-energy tail slightly increases with increasing ion energy. Consequently, the average sputtered atom energy will slightly increase with the ion energy. The weak dependence on the ion energies has lead to the use of a more simplified formula which is completely independent of the ion energy and can be found in many textbooks

$$\Phi(E) = C' \cdot \frac{E}{(E + U_s)^3}, \quad (14)$$

with $C' = 2U_s$ for a normalisation of the distribution to one. It is given in Figure 2 as the black curve. Clearly, it slightly deviates from the more exact description but reproduces the maximum at $U_s/2$ and the overall shape well. It best approximates the high ion energy limit above 1 keV which is, however, barely applied in magnetron sputtering.

2.2. Low pressure gas discharges

When a sufficiently high voltage is applied between two electrodes in a gas under low pressure, a gas discharge is ignited and the gas is transformed into the state of a plasma. Within the plasma, only a weak electric field is present resulting in a constant drift of electrons to the anode and positive ions to the cathode. From outside, although consisting of free charges, the plasma as a macroscopic object is neutral. This phenomenon is commonly called quasi-neutrality

$$n_e + \sum_z z_- n_{z-} = \sum_z z_+ n_{z+} \quad (15)$$

(n_e – electron density, n_{z-} and n_{z+} – density of the negative and positive ions, respectively, z – charge number). Macroscopic deviations from equation (15) by space charges otherwise were generating high electric fields which would prevent charges of opposite sign to leave the plasma volume. In technological discharges such as magnetron sputtering, equation (15) is often simplified for practical reasons assuming that the majority of the ions is singly positive charged (e.g. Ar^+) so that quasi-neutrality means

$$n_e = n_i = n . \quad (16)$$

Because of their low mass electrons are able to gain more energy per time from the electric field between two collisions with the background gas than the heavy ions. On the other hand, the energy exchange of the electrons in elastic collision with the background gas is very weak due to the mass difference and low Γ (Equation (4)) between the colliding particles. As the result, in low-pressure plasmas the mean electron energy is typically orders of magnitude higher than that of the ions and of the neutral atoms or molecules. Assuming that collisions between the electrons are very frequent and they form – at least roughly – a Maxwellian velocity distribution, this fact is often expressed in terms of temperatures

$$T_e \sim 50000 \text{ K} \gg T_i > T_n \sim 500 \text{ K} . \quad (17)$$

The important consequence from this different heating by the applied electric field is that most processes within the discharge are governed by the high energetic electrons.

Deviations from the prerequisite of quasi-neutrality are possible on the microscopic scale, both on short distances and for short times. The times for which a deviation

can occur can be calculated by an electron cloud oscillating around a positive ion. The frequency of the oscillation is obtained to be

$$\omega_{pl,e} = \sqrt{\frac{e^2 n_{(e)}}{\epsilon_0 m_e}}, \quad (18)$$

the so-called (electron) plasma frequency. It determines the time scale $1/f_{pl,e} = 2\pi/\omega_{pl,e}$ on which electrons are able to react on an external change. In some cases such as the formation of a stable sheath, it is also important how fast ions may compensate a sudden change, e.g. the electrode potential. This is determined by the lower ion plasma frequency which is obtained by substituting the electron quantities in equation (26) by their ionic counterpart:

$$\omega_{pl,i} = 2\pi f_{pl,i} = \sqrt{\frac{e^2 n_{(i)}}{\epsilon_0 M_i}} \quad (19)$$

Given equation (16) $\omega_{pl,i}$ is - due to a factor of 73000 higher mass (argon) - by a factor of 270 lower than $\omega_{pl,e}$. Ions therefore respond more than 2 orders of magnitude slower than electrons.

There may also be a spatial violation of the quasi-neutrality because of the finite density of the charge carriers and their ability to electrically shield a perturbation due to their thermal motion. A negative object brought into the plasma will repel electrons from its vicinity thereby leaving a positive space charge around it, which shields its negative charge against the plasma. This can be solved for a negatively charged infinite sheet with the one-dimensional Poisson's equation

$$\frac{d^2 V(x)}{dx^2} = -\frac{e}{\epsilon_0} (n_i - n_e) \quad (20)$$

and yields for the potential distribution in front of it

$$V(x) = V(0) \cdot \exp\left[-\frac{x}{\lambda_D}\right], \quad (21)$$

where x is the distance from the sheet, $V(0)$ its potential, and the potential at infinity is set to zero. In (21)

$$\lambda_D = \sqrt{\frac{\epsilon_0 k_B T_e}{e^2 n_{(e)}}} \quad (22)$$

has been introduced which is the (electronic) Debye shielding length. For a point source rather than a sheet is gives the distance at which its potential is decreased by

$1/e$ against the unshielded Coulomb potential. At $k_B T_e = 5 \text{ eV}$ and $n = 10^{10} \text{ cm}^{-3}$, $\lambda_D = 170 \text{ }\mu\text{m}$ is obtained.

Any electrode in contact with the plasma which is fixed in its potential implies a perturbation to the plasma similar to the sheet considered above because of the potential difference. Most important in this respect are strongly negative electrodes in front of which a sheath is formed. The potential drops from that of the plasma, V_{pl} , to that of the electrode within this thin layer where quasi-neutrality is strongly violated.

The simplest model of such a high-voltage sheath is the matrix sheath. Within it, the (positive) ion density is uniform and the electron density drops exponentially to the electrode according to Boltzmann's law. The sheath thickness s_M is then calculated to

$$s_M = \lambda_D \sqrt{\frac{2eU_M}{k_B T_e}}, \quad (23)$$

where U_M is the voltage drop between the sheath edge and the electrode. Because the ion attraction to the electrode is not considered for the matrix sheath setting their density constant, this sheath model is suited for very rapid changes of the electrode potential to negative values.

In the stationary state, the movement of the ions to the electrode and their density decrease has to be considered as well. The electrons are assumed to contribute no current through the sheath and the ions from the plasma enter the sheath edge with negligible energy compared the voltage drop U_{CL} . The stationary sheath which develops is then the space-charge limited Child-Langmuir sheath, the thickness s_{CL} of which is given by

$$s_{CL} = \frac{\sqrt{2}}{3} \lambda_D \left(\frac{2eU_{CL}}{k_B T_e} \right)^{3/4}. \quad (24)$$

The assumption of ions starting from the sheath edge with zero velocity leads to the problem that for the Child-Langmuir law an infinite ion density at the sheath edge is obtained. Further, currents measured at the cathode are higher than the Child-Langmuir law predicts. Bohm found that sheath is preceded by a typically much wider region of a small potential drop [14]. This pre-sheath can be described as being quasi-neutral but exhibiting a potential drop of $k_B T_e / 2e$. The ions then enter the actual sheath with an initial Bohm velocity v_B

$$v_B = \sqrt{\frac{k_B T_e}{M_i}}, \quad (25)$$

known as the Bohm sheath criterion that determines the current through the sheath.

To ignite a self-sustained discharge, the losses of charge carriers to the electrodes must be compensated by the generation of new charges. The balance is made for electrons which are generated by secondary electron emission from the cathode and volume ionisation by electron impact. The result is the breakdown condition

$$\gamma(\exp[\alpha d]-1)=1, \quad (26)$$

where α is the gas, pressure, and electric field dependent 1st Townsend coefficient (volume ionisation coefficient) and γ is the 2nd Townsend coefficient (secondary electron emission coefficient). For the conditions of breakdown, α can be set constant in space because there is no change in the field along d and hence equation (26) has a very simple form. The pressure, p , and electric field, E , dependence of α can be expressed as [15]

$$\alpha = \tilde{A}p \cdot \exp\left[-\frac{\tilde{B}p}{E}\right], \quad (27)$$

where \tilde{A} and \tilde{B} are constants for a given gas in a wide range of p and E , with \tilde{B} being proportional to the ionisation limit, and E may be expressed as U/d . Combining equations (26) and (27) leads to the "Paschen curve"

$$U_b = \frac{\tilde{B}pd}{\ln(\tilde{A}pd) - \ln[\ln(1 + 1/\gamma)]} \quad (28)$$

for the breakdown voltage U_b at a certain $p \cdot d$. A minimum U_b is required for optimum breakdown conditions, e.g. 265 V for argon at $p \cdot d = 200$ Pa·cm with a Fe cathode [16]. A deviation in $p \cdot d$ necessitates higher voltages.

A stationary discharge is based on the same processes and similar dependences. The difference is that in a stationary discharge the charge balance is governed only by the cathode region because in the cathode sheath the γ electrons gain their full energy which they stepwise transfer to ionisations in the region adjacent to the sheath. The rest of the stationary discharge volume is a positive column – strictly speaking the plasma – or an extended negative glow region as for most sputtering discharges. The calculation for the sheath is more complicated than for the

breakdown because α is not constant due to a variation of the E field in the sheath. However, a similar result as the Paschen curve is obtained when the sheath voltage is plotted vs. the current density j : a voltage minimum that separates the normal glow (at low j) from the abnormal glow (to high j) in which magnetrons are operated [15]. The quantity determining the volume ionisation in a stationary discharge, is the ionising collision frequency of the electron f_{iz} which is similar to α [15]

$$f_{iz} = C \cdot p \cdot \exp\left[-\frac{E_{iz}}{k_B T_e}\right] \quad (29)$$

in its dependence but the arguments of the exponential function have changed: the nominator is the actual ionisation energy and the electron temperature has to be used in the denominator because the majority of the ionisation occurs in the region outside the sheath with a weak field.

2.3. Magnetron Sputtering

Besides ion beams, a versatile method to sputter a target is to bring it in contact with a gas discharge and use it as its cathode as long as the target material itself is conducting enough to carry the discharge current. The sputtering process in this case is rather inefficient and necessitates high voltages in the kilovolt range and high pressure above 4 Pa to achieve acceptable deposition rates. The latter leads to thermalisation and scattering of the sputtered flux that is often not beneficial for the desired film growth. The high voltage further tends to arcing events making the process unstable and causing impurities in the films. These disadvantages are overcome by magnetron sputtering sources through a special magnetic field configuration which confines the plasma close to the target thus increasing the ion current to it and the sputter and deposition rate.

The first such configuration was introduced by Penning [17] back in 1939 when he reported about the disintegration of a rod-like cathode in a glow discharge and the strong enhancement of this sputtering by the application of a magnetic field that confines the discharge close to the cathode. To obtain a significant enhancement Penning noticed that the electric and magnetic field should be tilted against each other with an optimum for an angle of 90° , i.e. perpendicular fields. This basic

geometry was occasionally used with different modifications for thin film deposition during the middle of the last century in the form of cylindrical or post magnetrons [18]. In principle, a cylindrical cathode is sputtered and a magnetic field is applied parallel to its axis forcing electrons on a gyration motion parallel to the surface and the axis. Through the $E \times B$ drift a further circular electron current is obtained. Plates at both ends of the cathode on which the magnetic field lines terminate prevent the electrons from escaping to ensure the high plasma density along the cathode. Such post magnetrons are specially suited to deposit in cylindrical geometries like the inner walls of tubes why they are eventually still in use.

It took almost 40 years until Penning's concept was broadly introduced into deposition technology. The breakthrough was the invention of the planar magnetron by Chapin in 1973 [19, 20]. Its basic idea is the placement of permanent magnets with different poles behind the planar sputtering target which create an arch-shaped magnetic field in front of the cathode. Field lines to which the electron movement is bound thus terminate on the negative electrode on both ends just like at the end plates of the post magnetron. Therefore, an effective confinement of the electrons above the cathode between the magnetic poles is obtained. The curved nature of the magnetic field at least partially provides a component perpendicular to the electric field which itself is perpendicular to the planar cathode. Thus, an $E \times B$ drift current is obtained which further promotes the ionisation in the region where this current flows. It is most intense at positions on top of the arch shape where the magnetic field is parallel to the target surface, i.e. roughly between the poles of the permanent magnets.

The requirement of a performing magnetron is that this drift current forms a closed loop to prevent electron loss. Magnetrons therefore generally exhibit a torus of high electron density which is visible through radiation emission following electron-impact. The electron confinement in a magnetron if there were no collisions is consequently given by a complex overlap of the gyration along the arch-shaped magnetic field with reflection at the negatively target and the drift parallel to it. It should be noted that the $E \times B$ drift is the most illustrative drift but is typically assisted by other drifts such as gradient and curvature drift. Given the requirement of a closed loop, planar target shapes may be manifold, the most prominent and technologically appropriate are

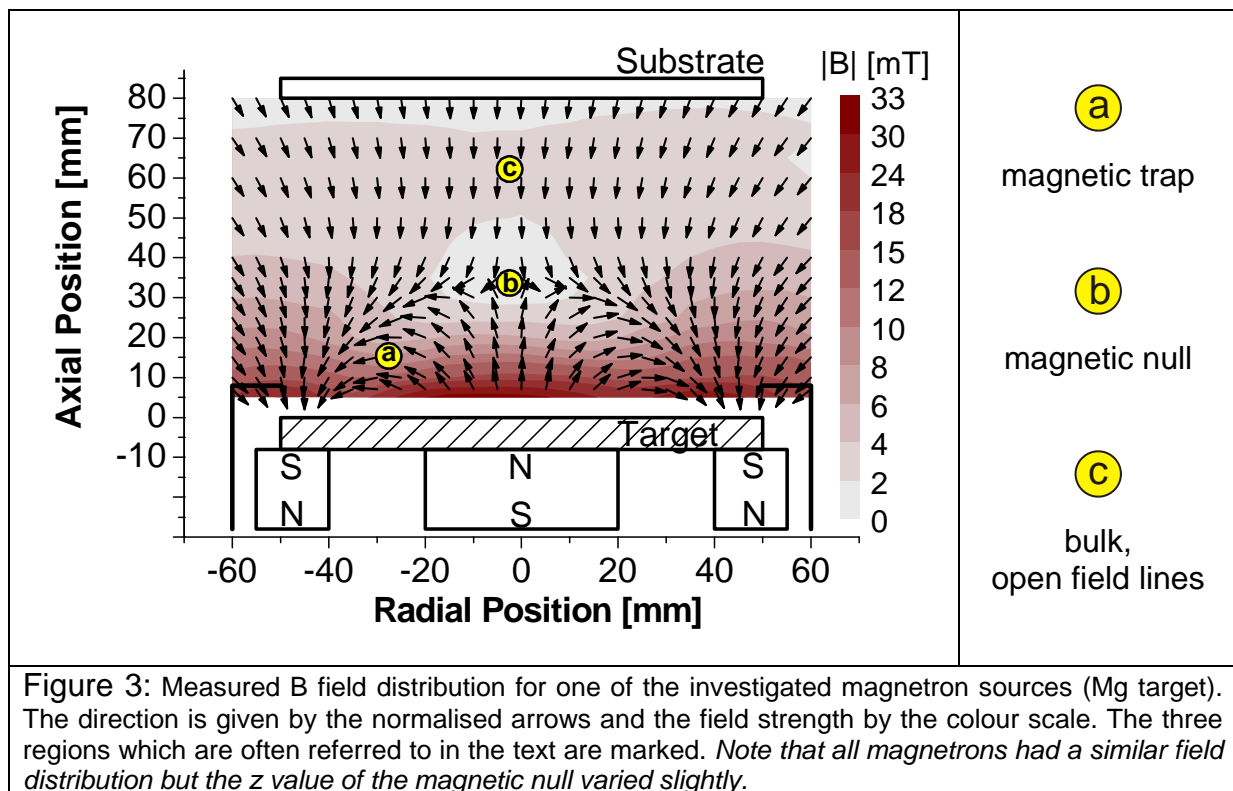
circular or rectangular targets [20]. Modern magnetrons consist of a central magnet and – separated through a gap – an outer magnet of opposite polarity surrounding it. In this work, mostly circular planar magnetrons of such a configuration were used.

Through the high ionisation in front of the cathode magnetrons are able to provide a high erosion/deposition rate and a rather low operating voltage. Especially the rectangular configuration further enables a principal scalability and large-area deposition when the aspect ratio of the rectangle side is chosen large (in industrial use, target lengths of almost 4 m are applied [21]).

Typically, the magnetic flux directly at the target surface of a magnetron is up to few 100 mT, up to about 50 mT in the torus region where the field lines are parallel to the surface, and decreases to few mT in the substrate region away from the target. In this work, different magnetrons with 30 ... 100 mT at the target and 10 ... 20 mT in the torus were investigated. An example of a cross section for one of the circular planar magnetrons (diameter 100 mm) is given in Figure 3. Taking a representative value of 10 mT and an electron with an energy of 5 eV, a gyration radius r_c around the magnetic field lines of 0.85 mm is obtained. For the same magnetic field, an argon ion with a typical energy of 0.05 eV has $r_c = 4$ cm. Given the dimensions of the torus which is 1-3 cm above the target, the electrons are thus strongly magnetised while the ions can be considered as being unmagnetised. Consequently, the ion flux at the target is approximately a summed projection of the plasma density distribution onto the target; most ions impinge on the target at radial positions where the magnetic field above is parallel to the surface, i.e. between the plasma torus. Thereby the target is predominantly sputtered in this small zone often referred to as the "race track". This is also the most significant drawback of any planar magnetron since it dramatically reduces the target utilisation and increases production costs.

Much work has been done to improve this target utilisation, e.g. by moving magnet systems or specially shaped targets because target material costs can be a major factor in industrial production (e.g. currently the costs for indium in transparent-conductive tin doped indium oxide production). A recent approach to overcome the problem is to use cylindrical targets with a suited magnet assembly inside the cylinder tube which has been suggested first by McKelvey [22]. The assembly consists of a central magnetic stripe and two outer stripes of opposite polarity

allowing for the required dome-shape magnetic field in front of the cathode surface. To achieve a closed-loop drift current, the outer magnets have to be closed by curved end pieces that surround the inner magnet stripe. The important advantage of the tube-shaped target is that it can be rotated along its longitudinal axis thereby permanently moving different areas of the target surface in the zone of most intense sputtering between the magnetic poles. Thus, a homogeneous erosion of the target is obtained, i.e. almost complete target material utilisation. The tube can be of lengths comparable to the length of rectangular planar magnetrons so that large area deposition is possible with both types. The advantage of the homogeneous erosion is, however, counteracted by a difficult handling of the rotating cathodes and for some materials expensive production of the tubular target.



Since the introduction of planar magnetrons, many modifications have been made to improve their properties or to adjust them to particular requirements of thin film deposition. The most important such is probably the "unbalanced magnetron". Originally, the application of the special magnetic field had – besides the high sputter rate – the advantage of keeping the discharge away from the substrate through the strong concentration at the target. The substrates typically do not act as the discharge anode (as real anode, separate electrodes close to the target were added)

and therefore did not draw a large electron current heating them up. Simultaneously, this prevents a significant film modification through ion bombardment controlled by a negative bias voltage at the substrate. This separation of the substrate from the discharge is obtained with "balanced magnetrons" where the inner and outer magnet deliver the same magnetic field and consequently all magnetic field lines that originate from the target surface also terminate on it. Window and Savvides [23] later found that the plasma distribution and substrate ion current can be significantly altered by strengthening one magnet compared the other and characterised this as "unbalanced magnetron". They classified two types depending on which magnet is the dominating one; their type II with a dominant outer magnet being the important one for ion substrate current enhancement for film deposition. In this case, some magnetic field lines originating from the outer magnet extend to the substrate region and do not terminate on the target but on the backside of the magnetron. This can also be seen in Figure 3. Electrons are thus partly directed to the substrate and ionise the working gas in the substrate region. Window and Savvides report about an enhancement of the substrate ion current density to 10 mA/cm^2 for the type II unbalanced magnetron compared to 0.2 mA/cm^2 for a rather balanced one [23].

For such an unbalanced magnetron, three main regions may be defined which are designated in Figure 3. The first is the magnetic trap which forms the plasma torus due to the electron confinement described above. The second is the region where the field lines from the outer magnet which do not terminate on the target converge to the centre of the discharge – this is referred to as the "plasma bulk". In the centre and close to the target, the magnetic field is oriented as given by the inner magnet. Moving into the region of the plasma bulk, it changes the direction (see Figure 2) into that for the outer magnet. The point of the sign change is designated the "magnetic null" of the magnetron as the field is zero at this position.

Genco Ltd. has established a method to simply quantify the degree of unbalance of a planar magnetron by a single number [24]. They use a factor g defined as

$$g = \frac{z(B_z = 0)}{w_{1/2}} \quad (30)$$

with $z(B_z = 0)$ is the distance of the magnetic null from the target surface and $w_{1/2}$ is half the distance between the centre and the outer magnet (typically half the width of

the target, i.e. the target radius for a circular planar magnetron). Magnetrons are classified into 6 groups ranging from extremely balanced for $g \geq 2$ to extremely unbalanced for $g \leq 1$ in steps of $\Delta g = 0.25$. For the magnetron shown in Figure 3, $z(B_z = 0) = 35$ mm and $r = 50$ mm is obtained yielding $g = 0.7$. It is therefore an extremely unbalanced source. The factor g of the other planar magnetrons used in this work ranged from 0.7 to 1.0. That is to say, all planar magnetrons investigated were of strongly unbalanced nature.

2.4. Pulsed Magnetrons

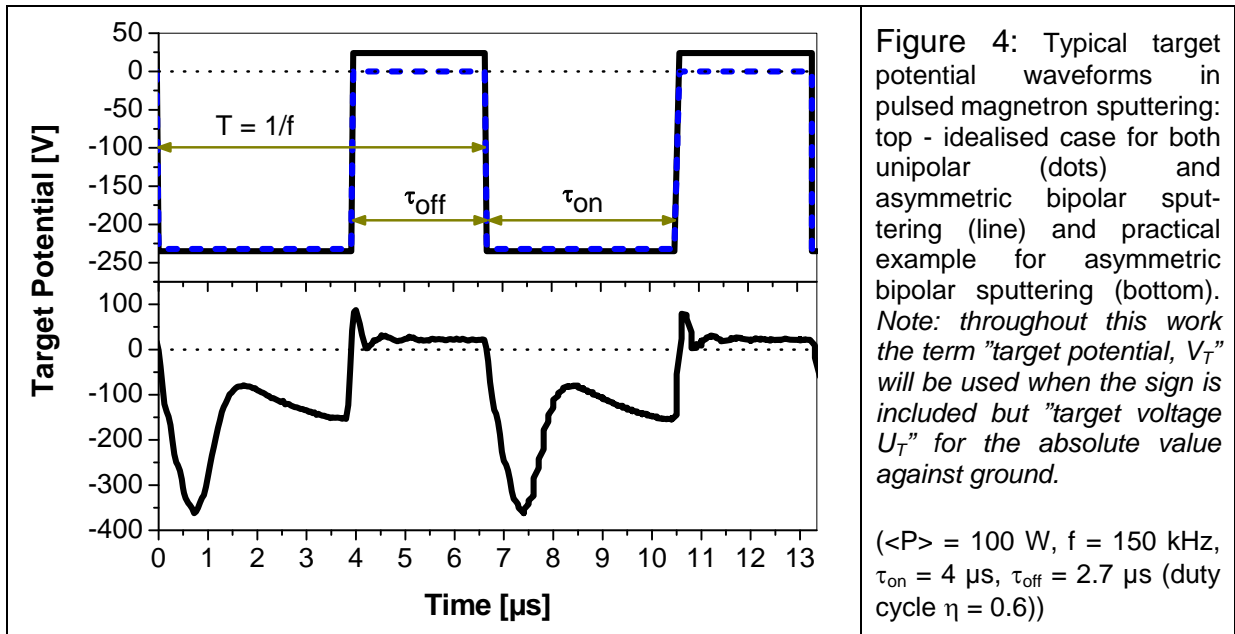
A major principal advantage of magnetron sputtering is the possibility to deposit compound materials without a compound target which is often very expensive or the compound is even not available as bulk material. Rather, a metal target is sputtered and reactive gases (O_2 , N_2 , ...) are added to the (noble) gas carrying the discharge. These are dissociated in the discharge and reactive components are incorporated into the growing film forming oxides, nitrides, etc. The challenge in such reactive sputtering is often that the film material is dielectric (e.g. many transparent oxides) and DC magnetron sputtering tends to get unstable because also the anode and especially the target itself gets covered with an insulating layer. In consequence, due to the negative polarity of the target, positive charges are accumulated on the surface of these layers and produce a high electric field across the layer eventually leading to breakdown. Associated arcs and extreme local heating lead to the emission of particles typically some μm in size (droplets, macro particles) which are incorporated into the film on the substrate impairing its quality.

It is possible to prevent arcing through a periodical interruption of the negative d.c. voltage at the target which is called pulsed (d.c.) magnetron sputtering [25]. During the interruption referred to as the 'off' time and due to the higher thermal current density of the electrons compared that of to the heavy and cold ions, the surface of the insulating layer is then subject to a net negative flux and the accumulated positive charge is by and by neutralised. If the pulse parameters are properly chosen, electrical breakdown and droplet emission are prevented, the deposited films become free of such impurities and have a denser structure, are smoother and – in the case

of optical films – much more transparent. This has been shown in several publications (e.g. [25, 26, 27]). Some typical target potential waveforms for pulsed magnetron sputtering are shown in Figure 4, schematically and with the appropriate physical quantities in the upper part and for a practical magnetron used in this work in the lower part.

A pulsed discharge is characterised by its pulse parameters that are given in the schematic rectangular waveform in Figure 4. During the ‘on’ time, τ_{on} , the negative sputter potential is applied. The duration of the interrupt is given by the ‘off’ time, τ_{off} . Both together define the pulse duration (T) or its inverse, the pulse frequency (f). It is convenient to either simply switch ‘off’ and keep the target at ground potential (unipolar mode), or to apply a small positive potential (asymmetric bipolar mode) to the target during the ‘off’ time. In the latter case, this phase is also equivalently termed “reverse” time, τ_{rev} . The ratio of τ_{on} and T is defined as the duty cycle η of the discharge:

$$\eta = \frac{\tau_{on}}{\tau_{on} + \tau_{off}} = \frac{\tau_{on}}{T} = f \cdot \tau_{on} = 1 - f \cdot \tau_{off} \quad (31)$$



These times have to fulfil several requirements to stably and efficiently run a pulsed magnetron discharge which depend on the properties of the material deposited and the plasma:

- The 'on' time has to be short enough to prevent arc formation, i.e. the discharge has to be switched 'off' before enough charge for a breakdown is accumulated. This can be roughly estimated by considering the insulating layer on the target as a capacitor with

$$C = \frac{Q}{U} = \epsilon\epsilon_0 \frac{A}{d} \quad (32)$$

(C- capacity, Q – layer surface charge, U – voltage across the layer being approximately the target voltage, ϵ - relative permittivity, d – layer thickness, A – layer surface). Rewriting this becomes for the surface charge density σ becomes

$$j_i \cdot t = \sigma = \frac{Q}{A} = \epsilon\epsilon_0 \frac{U}{d} = \epsilon\epsilon_0 E \quad (33)$$

(E – (constant) electrical field within the layer, j_i – (ion) current density onto the surface). If the strong inhomogeneity of the plasma in the target region is neglected, the average current density is estimated from the stationary target current I and the target area A. For the circular planar magnetrons used in this work, the diameter is 100 mm and the target current is of the order of 1 A which yields an ion current density j of about 13 mA/cm². Taking this, the critical time for the electrical breakdown is obtained from

$$t = \epsilon\epsilon_0 E / j \quad (34)$$

to be ~ 0.3 ms using the breakdown field E_{br} for E (e.g. ~ 5 MV/cm and $\epsilon \sim 10$ for MgO [28]). Thus, to be safe, the 'on' time should be < 100 μ s.

- In contrast to that, the 'on' time has also to be long enough for the ions to cross the sheath and gain their full energy. Otherwise, the sputter yield would significantly drop making the deposition process less efficient. A simple estimation of the time an argon ion needs to cross the sheath in the stationary state of the 'on' time may be derived from the current density given above for a typical voltage of 500 V and neglecting any secondary electron emission. The Child-Langmuir sheath law (24) then gives a sheath thickness of about 1 mm. Taking a simplified linear potential drop within the sheath, an ion starting from rest at the sheath boundary needs 40 ns to reach the surface. A similar value is obtained using the fact that the reaction time of an ion is about the inverse ion frequency $1/f_{pl,i}$; inserting j into the Bohm speed equation (25) and taking a representative $k_B T_e$

for the stationary 'on' time of 5 eV, an ion density of $2 \cdot 10^{11} \text{ cm}^{-3}$ at the sheath boundary is obtained. With equation (19) this yields $1/f_{pl,i} \approx 100 \text{ ns}$. However, at the beginning of the 'on' time, the density (and also the electron temperature) will be much lower after their decay in the 'off' time. Allowing for about two orders of magnitude in density decay, the time to cross the sheath as well as $1/f_{pl,i}$ increases by one order of magnitude. The minimum 'on' time should therefore be chosen to keep above $1 \text{ } \mu\text{s}$. A similar result of 2-3 μs has been published by Schiller et al. [25] for a sinusoidal voltage where the effect of a finite rise time of the voltage itself during the 'on' phase is also included.

- Finally, the 'off' time has to be long enough to allow a complete neutralisation of the accumulated charge on the insulator surface by the electron thermal current density. This duration is hard to estimate as it depends on many factors, not at least the decay rate of the plasma. Taking this into account and assuming that the maximum charge density at the layer surface has been reached at the end of the 'on' time, with the random thermal electron current density $j_{th,e} = n_e v_{th,e}/4$ and neglecting the T_e decay it's possible to write

$$\varepsilon\varepsilon_0 E_{br} = \sigma_{br} = \int_0^{t_{min}} j(t') dt' = \frac{v_{th,e}}{4} e \int_0^{t_{min}} n_{e,0} \cdot \exp\left[-\frac{t'}{\tau}\right] dt'. \quad (35)$$

Integration of equation (35) then gives

$$t_{min} = -\tau \cdot \ln\left(1 - \frac{4\varepsilon\varepsilon_0 E_{br}}{\tau e v_{th,e} n_{e,0}}\right). \quad (36)$$

This can be estimated using the initial electron density of $2 \cdot 10^{11} \text{ cm}^{-3}$, the material parameters given above, and a typical initial decay of the plasma with $\tau_{dec} \sim 1 \text{ } \mu\text{s}$ [29]. If for the electron temperature in $v_{th,e}$ a reduced value of 3 eV is inserted to account for the T_e decay, too³, t_{min} is equated to 1.2 μs . Thus, the 'off' time should be chosen to be at least few μs for practical purposes. As shown in Figure 4 the target potential is often set to slightly positive values to support the neutralisation process.

Summarising these estimates ($1 \text{ } \mu\text{s} < \tau_{on} < 100 \text{ } \mu\text{s}$, $1 \text{ } \mu\text{s} < \tau_{off}$), practical pulsed magnetron discharges are operated in the frequency range between several kHz and

³ The result is almost the same when an initial $k_B T_e$ of 5 eV and the same decay constant as for the density is used.

several 100 kHz with duty cycles between 0.1 and 0.9. As shown above, ions can follow these frequencies and consequently do the electrons with their higher plasma frequency. Such pulsed magnetron discharges thus work by switching the whole discharge 'on' and 'off', at least in the simplest view.

3. Fundamental properties of pulsed magnetron discharges and qualified investigation methods

3.1. Introduction

The improvement of the properties of dielectric films by the process stabilisation due to surface charge neutralisation at the target has early been shown for several examples [25, 30, 31, 32]. However, it has emerged quickly, that pulsing the discharge also affects the plasma in a way that alters the film properties even without the necessity of arc prevention. A good example is given in [33] for titanium deposition in argon. The conducting films show improved adhesion and surface roughness when a pulsed magnetron is used instead of a d.c. magnetron for the same average input power. The properties of the films also changed with the frequency applied, especially by a different argon concentration in the films [33] and the surface roughness [34], both increasing with the pulse frequency. The pulsing of the magnetron discharge therefore has a profound – and as observed beneficial in most cases – effect on the plasma properties adjacent to the substrate itself. The reasons for this behaviour based on physical quantities have been only vague.

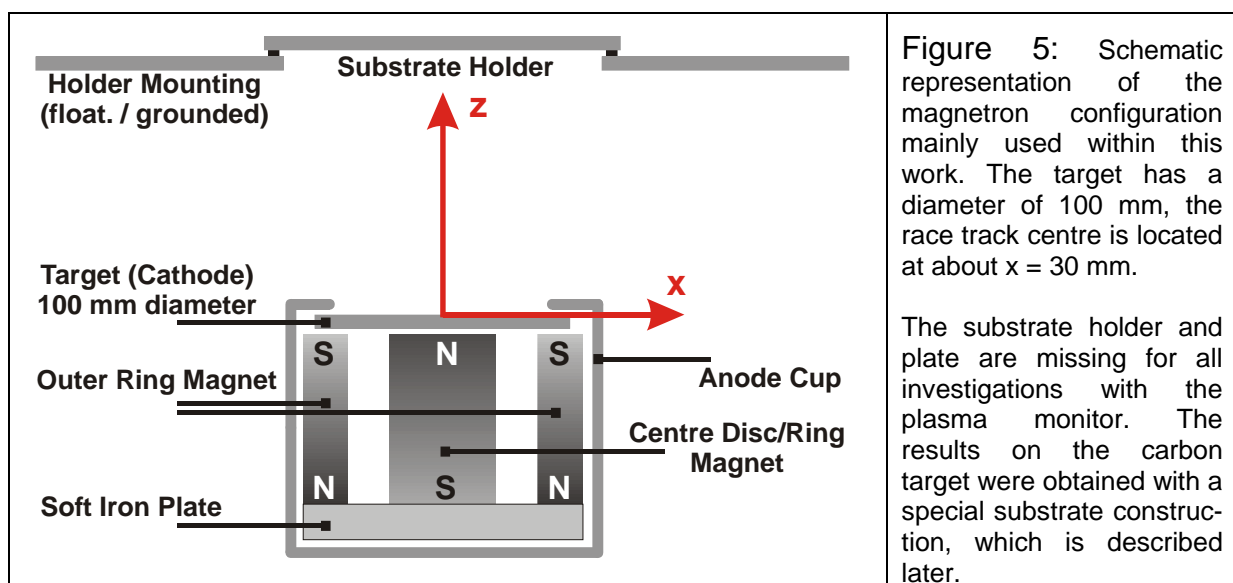
Only a few publications dealt with the phenomena at the beginning of this work. Those were however not consistent to each other: Glocker [35] used a thermal probe and recognised an increase in the energy flux at the substrate by more than 50 % when using a pulsed discharge instead of d.c. with simultaneously lower deposition rate. He correlated this with an increase in the average plasma density by a factor of 4 and of the electron temperature by 30 % for a pulsed discharge compared to d.c. Similarly, Bradley et al. [36] found an increase in both quantities by up to 30 % while both depended on the pulse frequency. A similar frequency dependence was reported by Lee et al. [37] with only slight changes in the average density. Mahoney et al. [38] found an increase in the average electron temperature with increased frequency but no change in the average density. Bartzsch et al. [39] observed no

significant change in either ion current density or thermal substrate load for unipolar pulsing but a significant increase for the symmetric-bipolar mode of a dual magnetron. The results are hard to compare with each other as different power supplies and geometries were used. Another problem is that they were obtained with the power supply either delivering a constant power for all plasma parameters [35, 36, 38, 39] or - different to that - a constant current [37] of the discharge sometimes even for different pulse modes, which made them hardly comparable. Additionally, most investigations were done on a time-averaged scale and do not give insight into the physical mechanisms within each pulse. However, as shown in section 2, electrons as well as ions in pulsed magnetron discharges may follow voltage changes within one pulse and therefore the investigation of the plasma parameters has to be performed on the same time-scale.

The very first such time-resolved measurements were reported by Mahoney et al. [38] who used a planar Langmuir probe during pulsed aluminium sputtering. The electron density and temperature were found to significantly vary during one pulse by a factor of up to 3. Their average values increased with pulse frequency. Thermal probes showing an increase in the thermal flux with pulse frequency backed the results. Later, Bradley et al. [36, 40] used a commercial Hiden Langmuir probe system and measured the plasma parameters temporally resolved. They found a peak in the effective electron temperature at the beginning of the 'on' phase, under some conditions even two peaks while the value was constant over the rest of the cycle. The peaks were correlated to changes in the floating potential and the authors attributed them to groups of electrons with different origin. The electron density in their study rose slowly during the 'on' time within 4 μ s and fell slowly during the 'off' time.

Both studies show that the plasma parameters during a pulse exhibit dynamics which strongly depend on the pulse parameters and the target voltage waveform. These phenomena may have significant influence on technological deposition processes that use pulsed magnetron as the thermal load measured by Glocker [35] shows. They have been investigated in the frame of the present work with special emphasis on charged particle densities and energies, potentials in the discharge, and ion energies at the substrate for the case of an asymmetric-bipolar pulsed discharge

unless otherwise stated. The magnetron system mostly used is schematically shown in Figure 5, special configurations or other magnetrons will be mentioned in the text. In this section, general features of such discharges shall be demonstrated and methods to characterise them – particularly those variations that were developed within the work – introduced. The international research over the last years has led to the emergence of a more common picture of the phenomena in pulsed magnetron discharges to which the work presented in this thesis contributed. This is documented in review articles, partly with the author of this thesis being co-author [41, 42, 43] to which the reader is referred to for an even broader overview.



3.2. Densities and energies of charged particles within the plasma

The state of the discharge is predominantly characterised by the density of the charged particles and their energy in the region between the sheaths. Ions are generally rather cold (~ 500 K) and obtain their energy relevant for film deposition in the sheath. They may be comprised of positive and negative ions. If present in a significant amount, negative ions can violate the simple quasi-neutrality in that the density of positive ions equals the density of electrons and negative ions instead of electrons alone. In reactive sputtering for dielectrics, especially oxygen or oxygen containing species may form negative ions. The measurement of their density is rather difficult. Publications addressing their measurement in Ar/O₂ gas mixtures with less O₂ than Ar indicate that it stays below 10% of the electron density during the 'on'

phase [44, 45]. They will therefore be neglected in this section and the simple quasi-neutrality is used allowing to set the electron and positive ions density equal (“charge carrier density”) for the investigations. A further quantity of importance is the electron energy within the plasma as it is high compared to that of the ions.

3.2.1. The time-resolved (Langmuir) double probe

Electrical probes are still the most frequent method to determine electron or ion densities and the electron energies in discharges. Although their first description by Langmuir [46] dates back to 1923, their rather simple experimental setup and the local information they provide are still a major advantage. The classical single probe – simply expressed consisting of an electrode (wire) inserted into the plasma and measuring the current for a ramp of voltages – under ideal conditions enables the determination of electron and positive ion density, plasma and floating potential, and the electron energy distribution function (EEDF). A double probe of two (identical) small electrodes which was suggested by Johnson and Malter [47] has some advantages when the conditions severely deviate from the ideal case. However, this is obtained at the expense of the number of detectable quantities: with it the charge carrier density (assuming $n_e = n_{i+}$) and to certain extend the electron temperature (assuming at least nearly a Maxwellian distribution) can be accessed.

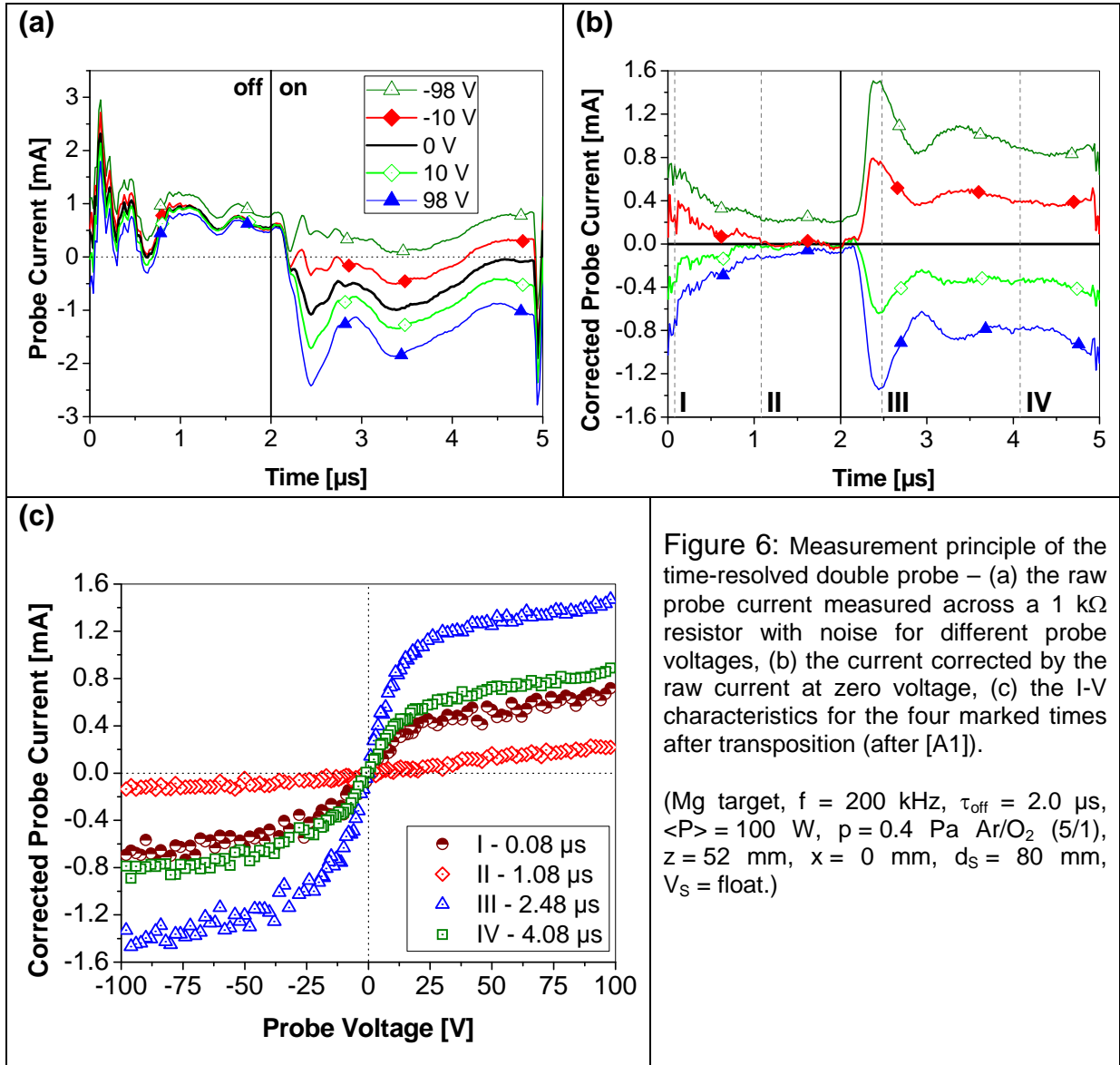
The advantages are based on the fact that the scanning probe voltage is applied between the two probe electrodes and not to a reference potential that is needed by the single probe. The complete probe system is isolated against ground. It is therefore possible to measure even under conditions where the surrounding potential that determines the current is itself fluctuating to certain extent as given in pulsed magnetron discharges. A double probe can thus be used for time-averaged measurements whereas this is questionable for single probes as ground (or any fixed) potential is no suitable reference for the probe currents because of which the results of [35], [37] and [39] have to be critically viewed. A double probe has further advantages in magnetron deposition discharges that all relate to the fact that due to the floating nature the negative electron current to one electrode has to be compensated by the positive ion current to the other. The probe does not drain a net current from the discharge and the maximum current is determined by the low ion

saturation current. The measurement is therefore possible for higher density and less susceptible to magnetic fields as the ions are less affected. The symmetrical shape of the characteristics further enables detection of a falsification by deposited layers on the probe.

Such a double probe system had been developed in the group where the work was done and used to good effect in several conventional magnetron discharges [48, 49, 50, 51, 52], facing-target magnetrons [53], PECVD discharges [54], and plasma jets [55]. To obtain the required time-resolution for the pulsed discharges, it was taken as the basis and was modified as described in detail in [A1] and is sketched here only briefly. Instead of acquiring the probe current through an internal resistor in the adapting electronics that generate the voltage ramp, it was taken across a 1 k Ω resistor inserted in each probe line. The probe voltage is varied stepwise and the probe current I_{raw} is measured versus time with a fast digitising oscilloscope (Tektronix, TDS 620B). The measurement is repeated and averaged over typically 20 cycles to smooth the signal enough for processing [A1].

Thus a set of data $I_{\text{raw}}(t)|_U$ is obtained for each probe voltage U_d which is shown in Figure 6a for 5 selected probe voltages. As it turned out, the raw current exhibits a significant interference background signal seen by the fact that in Figure 6a almost no distinction between the 'on' and 'off' time is possible and the current in the 'off' time is partially higher than during 'on'. A sufficient reduction of the background signal proved to be impossible and therefore it was taken advantage of the floating nature of the probe. This implies that the real current is zero when no voltage is applied between the electrodes and both are at floating potential. Looking at the 'on' time in Figure 6a, the current spread is symmetrical to the signal measured at $U_d = 0$ V indicating that the background is independent of the probe voltage. The signal $I_{\text{raw}}(t)|_{U=0}$ has therefore been taken as the background and been subtracted from all other current signals. The result from the data of Figure 6a is shown in Figure 6b proving a symmetrical behaviour (against U_d) and an expected decrease of the corrected current $I_{\text{cor}}(t)|_U$ during the 'off' phase. The data matrix $I_{\text{cor}}(t)|_U$ is then transposed into $I_{\text{cor}}(U)|_t$ and delivers a set of double probe characteristics, each for a certain time within the pulse as shown in Figure 6c. The shape of the characteristics is reliable within the 'on' time and the beginning of the 'off' time. As shown for trace II

in Figure 6c, at the end of the ‘off’ time the characteristics become distorted and are not symmetrical due to the subtraction of same order noisy current values.



For each time step, the characteristics can be analysed using standard procedures for the double probe [48] based on the theory of Johnson and Malter [47], and Yamamoto and Okuda [56]. Klagge and Tichy [57] derived a formula for the calculation of the electron temperature in the collisionless case

$$\frac{k_B T_e}{e} = \frac{I_{i,fl}}{2 \left(\frac{dI_d}{dU_d} \right)_{fl} + \left(\frac{dI_d}{dU_d} \right)_{sat}} \quad (37)$$

from the slopes of the characteristics in the centre $(dI_d/dU_d)_{fl}$, the slopes in the saturation regions $(dI_d/dU_d)_{sat}$, and the junction of the latter slopes with the current

axis $i_{i,fl}$ representing the ion current at the floating potential. This simplification assumes essentially a Maxwellian distribution of the electrons which is obtained from the region of the centre of the double probe characteristics, i.e. the floating potential which probes electrons with about 10-30 eV. Thus, an extrapolation of this energy region to a complete Maxwellian EEDF has to be assumed which makes the double probe less susceptible to changes in the correct EEDF, especially in the low-energy range. To obtain the density of the charge carriers, the evaluation has been adapted to the experimental investigations of Sonin who provided a parametrised graph for

$$\left(\frac{r_p}{\lambda_D}\right)^2 i_i = \beta = \frac{r_p^2}{\varepsilon_0} \sqrt{\frac{2\pi M_i}{e}} \left(\frac{e}{k_B T_e}\right)^{3/2} j_i \quad (38)$$

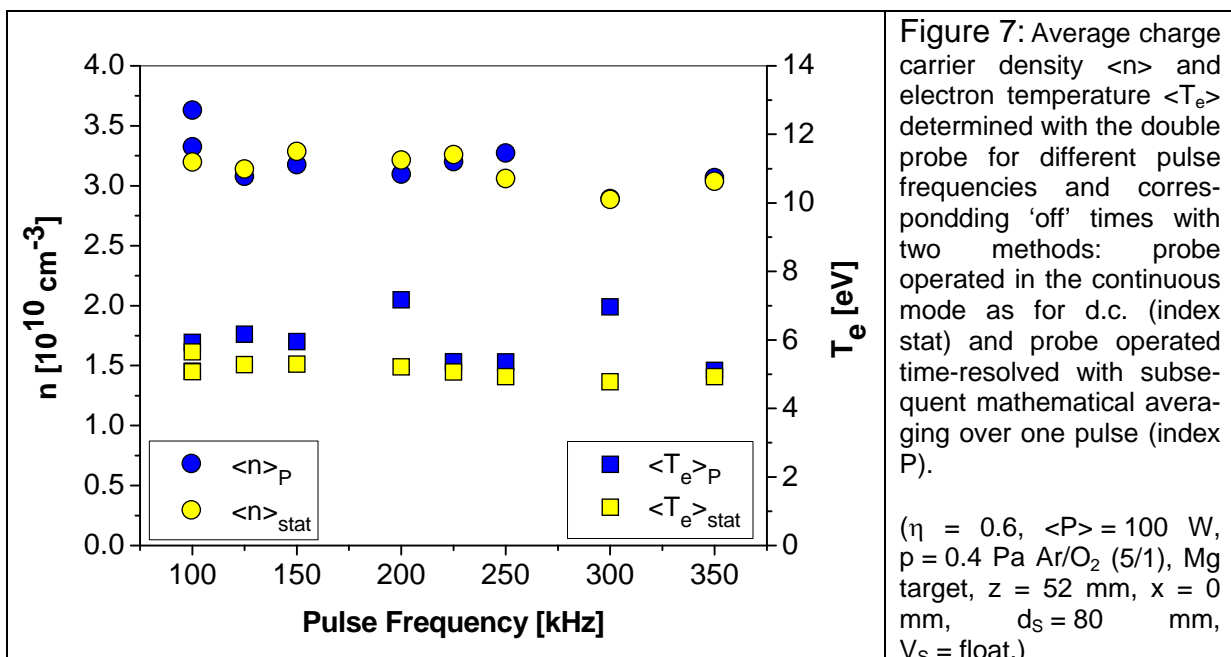
(r_p – probe radius, λ_D – Debye length, M_i – ion mass, i_i – dimensionless ion current) for the (ion) current density to the probe j_i at a selected probe potential of $V_{fl} - 10 \cdot k_B T_e / e$ (i.e. for the double probe at $U_d = \pm 10 k_B T_e / e$) for a variety of plasma conditions [58]. It should be noted that with a double probe the electron density is obtained after equation (38) from the ion current to the probe. Hence, the quasi-neutrality in the simple form of equation (16) is assumed. To account for this, the term "charge carrier density", n , will be used in the following.

The time resolution of the the double probe is determined by the response time of the circuitry to the changes in the plasma and the sheath around the probe. The response of the circuitry has been checked with a 100 MHz sine generator with the measurement electronics connected or disconnected and the probe end being short-circuited instead. The result for the current measured with the oscilloscope were identical [A1] proving that the circuitry can follow fluctuations faster than 10 ns or at least 100 ns which is enough for taking 100 data points in a 100 kHz pulse. The limitation of the time resolution by the sheath around the probe is given by the fact that changes in the discharge will alter the sheath. To obtain a stable probe current that can be related to the new plasma parameters, the sheath has to be re-adjusted. This happens on a time scale $\tau \sim 1/f_i$ because the transport of both fast electrons and slow positive ions has to stabilise. Unfortunately, the ion plasma frequency itself is dependent on n , the quantity to be determined. Hence a fixed time resolution cannot be given. For typical charge carrier densities that have been measured in the stable 'on' time of $n \sim 5 \cdot 10^{10} \text{ cm}^{-3}$ the plasma frequency in argon according to equation (19) is $\omega_{pl,i} \sim 47 \text{ MHz}$ so that $\tau \sim 130 \text{ ns}$ [A1]. The time τ scales with $n^{-1/2}$, hence the

time resolution will worsen at lower density. For $n \sim 5 \cdot 10^9 \text{ cm}^{-3}$ it is $\tau \sim 420 \text{ ns}$ which would still be acceptable because such densities are expected in the 'off' time when no fast fluctuations should occur (cf. section 3.2.2). Additionally, the estimated τ should provide an upper limit because the sheath is not newly formed but only altered.

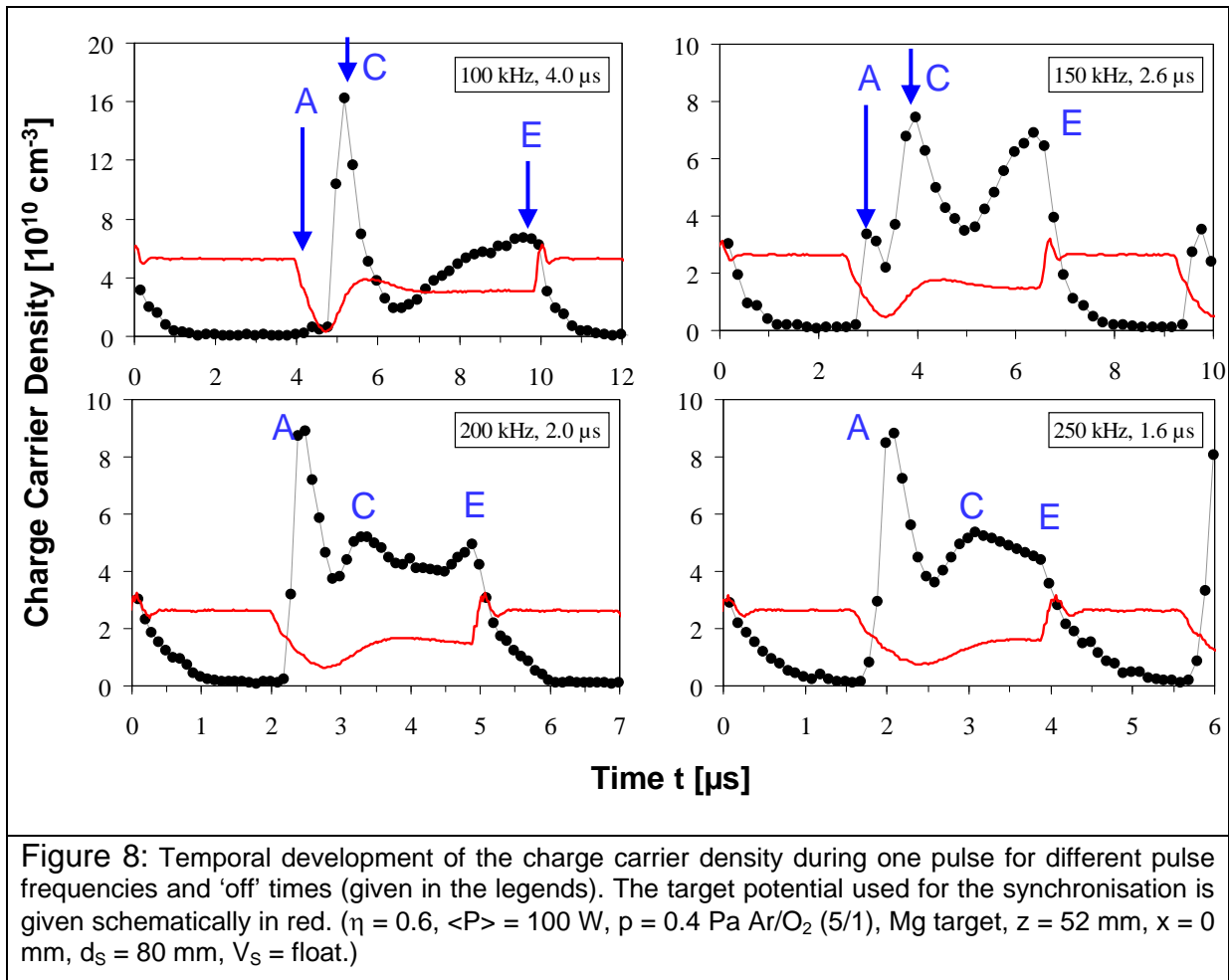
3.2.2 Development of the charge carrier density during a pulse

A typical result of the time-averaged (i.e. measured as a classical double probe in a d.c. discharge) charge carrier density $\langle n \rangle_{\text{stat}}$ and electron temperature $\langle T_e \rangle_{\text{stat}}$ obtained for the bulk plasma of a pulsed magnetron discharge for different pulse frequencies is shown in Figure 7. Both quantities do not change significantly when the frequency is changed. This is for one thing not surprising because all discharges were run with the same averaged power of 100 W in power-controlled mode. A similar energy input and distribution into the discharge can thus be expected since all other conditions were also unaltered. Consequently, the behaviour shown in Figure 7 has also been observed when other pulse parameters were changed [A1]. Also included in Figure 7 are the values $\langle n \rangle_P$ and $\langle T_e \rangle_P$, which were obtained by the newly developed time-resolved technique and a subsequent mathematical averaging. The results of both methods agree quite well and do not exhibit any systematic deviation proving that the time-resolved measurements are reliable.

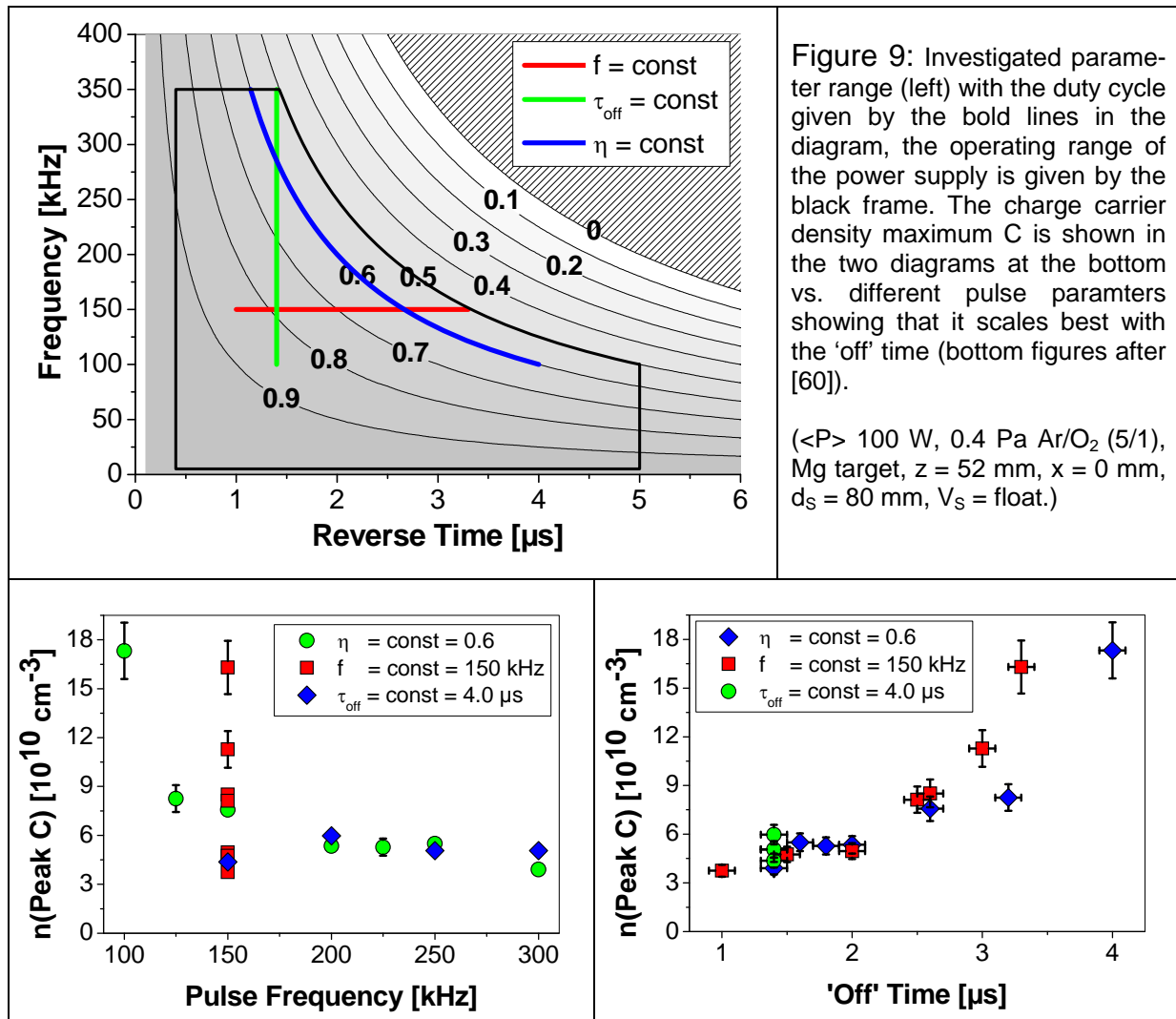


Despite the rather constant average plasma parameters, their temporal development during one pulse is strongly dependent on the choice of the pulse parameters. This is shown exemplarily in Figure 8 for four different pulse frequencies at constant duty cycle with otherwise same conditions as for Figure 7 for the charge carrier density $n(t)$. Expectedly, n decreases during the 'off' time and is increased in the 'on' time. However, there are marked peaks during the 'on' time that do not simply follow the waveform of the target potential that is also given schematically. This is most visible in the example for 150 kHz: one peak in n appears before the voltage reaches its negative peak value and is followed by a second one after the voltage peak. Subsequently, after going through a minimum, n increases slowly to another maximum that is, however, only developed because the increase is interrupted by the end of the 'on' phase. To better address the minima and maxima they have been labelled as in Figure 8 from A to E. Clearly, the relation of the first two maxima (A, C) is dependent on the pulse frequency in the example: for low frequency, A is hardly visible and C dominates the pulse while for high frequency, A is strongly increased and C decreased. The apparent maximum E (i.e. n at the end of the 'off' time) is only weakly dependent on the pulse frequency. The behaviour described above is general feature of such pulsed discharges for the particular power supply as it has been observed for other target materials (Ti, C) in different environments as well [29, 59].

To explore the origin of the peaks and the connection with one of the different pulse parameters, time-resolved measurements with the Mg target have been carried out in the available pulse parameter space. According to Figure 4, two pulse parameters can be chosen independently, e.g. the 'on' time and the duty cycle, which determine the others, e.g. the 'off' time and the frequency. The power supply takes account for this by providing two independent control parameters, the pulse frequency and the 'off' time. Time-resolved studies have been carried out by keeping one parameter fixed (being not necessarily one given by power supply) and varying one other. As shown in Figure 9, a certain range of the parameter space was such covered. The analysis of the results has been done with respect to the temporal appearance and the intensity of the peaks, with the intensity of the maximum C being the most expressive quantity. The at first surprising result was that it is not correlated to 'on' phase related parameters as the 'on' time, the frequency (shown in Figure 9 (left)) or the duty cycle.



The important parameter for the control of the peak is, however, the duration of the 'off' time as shown in Figure 9 (right) – the intensity of the peak C exhibits the same trend for the different parameter variations. Consequently, the physics behind the development of the peaks at the beginning of the 'on' phase have to be related to processes in the 'off' phase. As these will be predominantly the decay rates of the plasma, the determining value for the ignition in the 'on' phase is obviously the amount of charge carriers which are still left over from the previous pulse. Based on this finding, a simple model for the re-ignition and the peak formation has been developed [60] which is described in the following section.



3.2.3 Model description of the ignition during the 'on' phase

The model consists of three subsequent steps that, however, in practice cannot be strictly separated but overlap each other. Remnant charge carries from the previous pulse are considered to be homogeneously distributed for simplicity and the magnetic field is neglected at first.

- Acceleration of remnant electrons

In the first step, as soon as the target potential goes to negative values, electrons that are mobile are immediately accelerated away from the target by the negative potential leaving behind a matrix sheath of the heavy ions. On their way to the substrate, they ionise gas atoms so that an increase in the charge carrier density is observed. The process is stopped when all remnant electrons have left the volume

which occurs quickly, so forming peak A. The peak is increased with the density of residual electrons at the beginning of the 'on' time, i.e. with decreasing duration of the 'off' time (see Figure 8). Simply assuming a linear potential drop between the target and the substrate, the electrons would reach the substrate and the probe close to it after less than 100 ns, i.e. much earlier than the target voltage has reached its peak value [A2]. During this time and bearing in mind that the target voltage itself is still low, the electrons can only gain an energy of about 20 eV. This explains, why peak A is often observed rather weakly or not at all if the energy is even below the ionisation limit. A more realistic case with the formation of a matrix sheath where most of the voltage drop occurs will lead to even quicker loss (~1 ns) of the electrons initially located at the target but slower movement of electrons originating from the bulk which still may gain enough energy to reach the ionisation limit. Together with the magnetic field that lengthens their way, an ionisation in the probe region close to the substrate ~500 ns after switching 'on' as detected by the probe is reasonable. Irrespective of the target material, working gas and its pressure, input power, and geometry the appearance of peak A has always been observed ~500 ns after the start of the 'on' phase proving that the fast movement of residual electrons is the reason for its presence. The temporal appearance of the peak is not correlated to the peak in the target voltage but only the movement of the remnant electrons out of the discharge volume. It is important to note that even in cases of a strong peak A in the volume no simultaneous peak in the discharge current can be observed [A1] proving that it is not related to charges arriving at the target and not to secondary electron emission.

- Acceleration of remnant ions and secondary electrons

The ions that were left in the matrix sheath are accelerated onto the target but due to their higher mass on a much longer time scale. With a matrix sheath width of $s_M = (2\epsilon_0 U_T / en)^{1/2} = 6 \text{ mm}$ for an average voltage of $U_T = -300 \text{ V}$ and a residual density of $n_0 = 10^9 \text{ cm}^{-3}$, the transit time through the sheath from its edge can be calculated to $0.3 \text{ } \mu\text{s}$ [60]. Once the ions hit the target, they release secondary electrons which are accelerated into the volume by the full sheath potential at that time. The ionisation that they cause in the discharge volume is measured as the second peak C with the probe. This is significantly quicker than the appearance of peak C in the results. However, the gradual increase of the target voltage with an

increase of the sheath width has to be considered, with the voltage peaking about $0.8 \mu\text{s}$ after the start of the 'on' phase. Adding up increase and transit time, C is expected at about $1 \mu\text{s}$ where it has been observed. Ions arriving at the target at the end of the voltage increase will have highest energies and liberate more secondary electrons. These will experience a particularly strong acceleration and hence obtain high energies and cause more ionisation events. The final stage of the target potential overshoot is therefore most important for the formation of peak C.

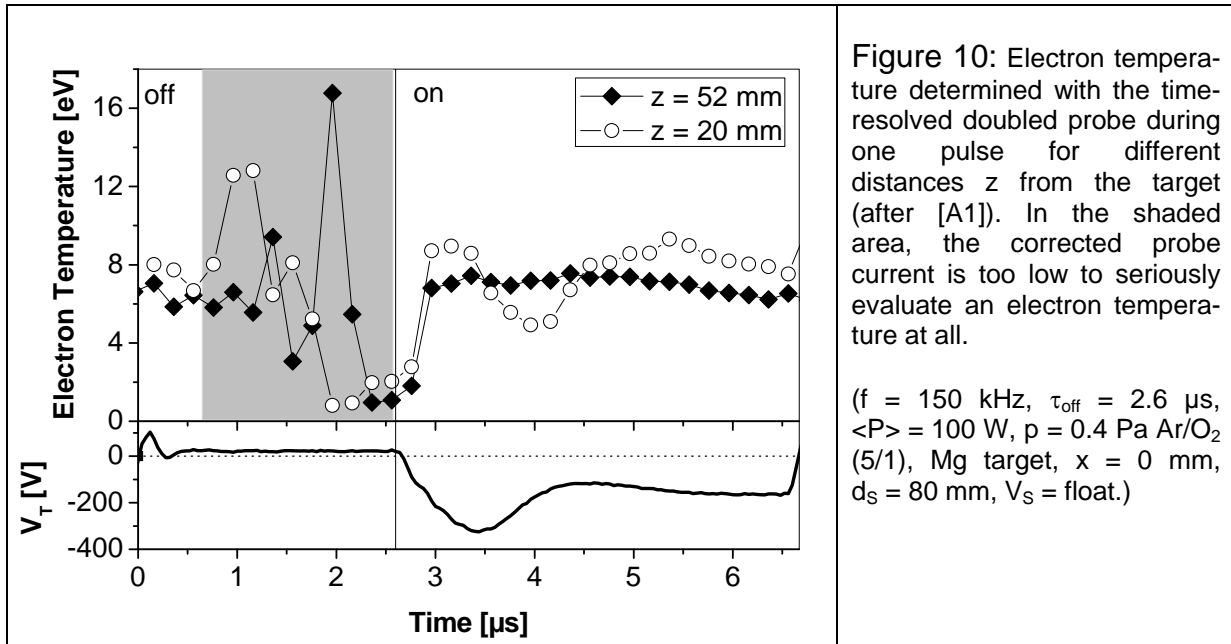
- Transition into the stationary state

This second ionisation peak is followed by a transition into the stationary state where the charge carrier density more or less follows the target voltage waveform. For very long 'on' times it would finally reach the state of a d.c. discharge characterised by an equilibrium of electron drain to the substrate(s), ion current to the target and current of secondary electrons into the plasma as well as a stable sheath in front of the target. An indication of this can be seen for the lowest frequency (100 kHz) in Figure 8 where at the end of the 'on' time only weak changes are still observed. The transition will start as soon as new charge carriers are generated that dominate after the two peaks attributed to the residual charges.

With this model, the charge carrier density development during the ignition of the 'on' phase (Figure 8) and the pulse parameter dependences (Figure 9) are explained. For low pulse frequency (at constant duty cycle), the 'off' time is long and, due to the decay of the plasma, only few charge carriers are left from the previous pulse. Consequently, peak A is rather weakly developed because only few electrons are available to cause ionisation. The higher the frequency and thus the shorter the 'off' time is the stronger peak A is developed. At first surprisingly, peak C shows an opposite dependence although it is caused by the remnant ions that are also increased. However, the reaction of the power supply has to be taken into account. It is optimised to drive to necessary current within the 'on' time to deliver the adjusted average power. As more charge carriers are available for shorter 'off' times allowing higher current at ignition, the voltage peak is significantly reduced, from 373 V for 100 kHz to 279 V for 250 kHz to even 247 V for 350 kHz in the example of the Mg target in Ar/O₂ sputtering atmosphere shown in Figure 8. The released secondary

electrons will therefore gain much less energy to ionise the gas in the discharge volume and the peak C is reduced with increasing frequency.

Other authors for sometimes quite different magnetron systems found similar peaks. The first who have reported about such phenomena were Bradley et al. [36, 40] who found peaks in the effective electron temperature, $T_{e,eff}$, with a single probe within the first 0.5 μs of the 'on' phase and – with a power supply similar to the one used here – a peak in the electron density $\sim 0.7 \mu\text{s}$ after switching 'on'. Later, Swindells et al. [61] found a single peak in the $T_{e,eff}$ as well as in n , both at $\sim 0.5 \mu\text{s}$ and – as here - increasing with shorter 'off' times, for a system comparable to the one described here but with a titanium target. Belkind et al. [62] observed a single peak in T_e but none in n for rather long 'off' times of 10 μs . There are obviously high-energetic electrons at the start of the 'on' phase in all cases and in the cases of short 'off' times these manifest in subsequent ionisation and a density peak after $<1.0 \mu\text{s}$. For longer 'off' times, this density peak is not observed because the number of remnant electrons is not enough to sufficiently ionise. Figure 8 shows the same effect: for the longest 'off' time (4.0 μs at 100 kHz) peak A is hardly detectable. A strong peak in T_e has never been observed in the present work as also shown in Figure 10. The reason is the insensitivity of the double probe method against changes in the EEDF as described above. The electron temperature is obtained from the extrapolation of the small region of the EEDF close to the floating potential. Electrons with different energy, i.e. very low energetic and beam-like electrons which are expected during ignition, are not detected or not properly treated [63], respectively. Figure 10 includes a measurement with the double probe close to the target where highest electron energies are expected [40]. At this distance, an indication of the existence of higher electron energies is observed as a T_e peak of 8 eV is measured within less than 1 μs after switching 'on', followed by a temporal relaxation. The appearance time is consistent with the density peak A and the observation of the other authors. The absolute value, however, is still rather low. For this reason, the obtained time-resolved electron temperatures are further not discussed due to the ineptness of the double probe. The latter is also seen from the 'off' time T_e values in Figure 10 which exhibit a very broad scattering. This is due to the ion saturation limitation and consequently low probe current signal, which is roughly exponentially decreased in the 'off' time making a serious T_e evaluation almost impossible (cf. Figure 6c, time II).



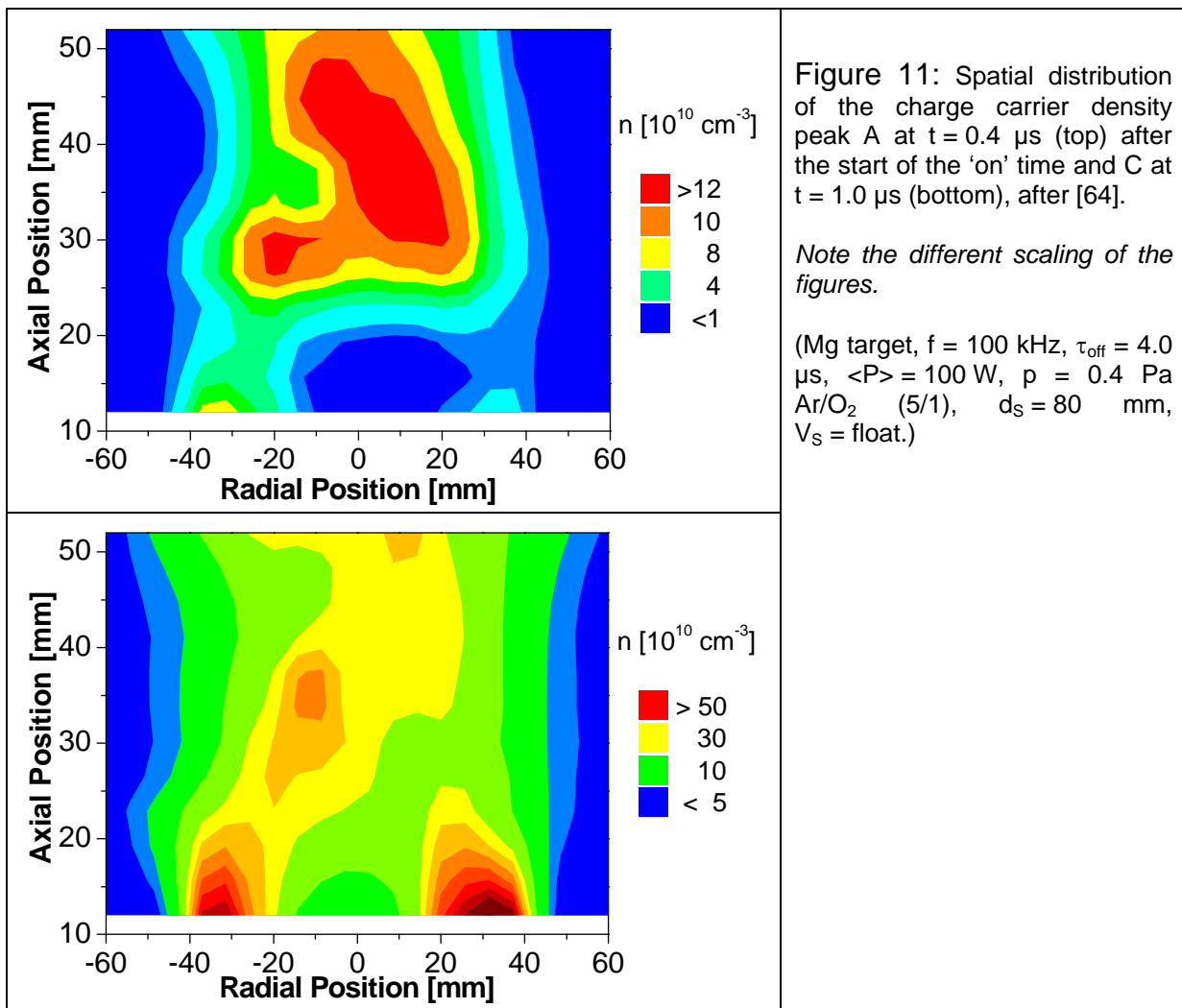
The second peak C is not seen in the density by other groups [36, 61, 62]. Almost all of them used power supplies that are characterised by more rectangular voltage waveforms than the one used here (cf. Figure 4). In contrast to this work, the ion bombardment and secondary electron acceleration is then not as amplified and peak C will be reduced or even diminished and a more continuous transition into the stationary state is observed. Moreover, as most of the other works were carried out with 'off' times much longer than 4 μs , the remnant charges are expected to be much less and their influence on the re-ignition with the peak formation is much reduced. In [40] a similar voltage waveform as here was applied and no second peak (C) was observed. Because an aluminium target was sputtered in pure argon along with a low secondary electron emission coefficient (γ_{ISEE}) of 0.09 compared to that for an MgO surface of 0.41 [7], it seems likely that the γ -electron related peak C is strongly suppressed in the rather peculiar density traces in [40].

3.2.4. Spatial distribution of the charge carrier density

The results described so far were mainly obtained at one particular position in an asymmetric-bipolar pulsed discharge sputtering from an Mg target in an Ar/O₂ gas mixture. Except for the T_e investigation, all studies were done 52 mm from the target on the axis of symmetry, a position that according to Figure 3 is above the magnetic null in the bulk plasma. As shown in section 2, however, a magnetron consists of different regions defined by the magnetic field. To validate and refine the developed

model, the temporal evolution of the charge carrier density within the whole volume of the magnetron discharge must be known. This has been obtained by scanning the cross section of the same discharge with the double probe [64].

The scanning has been restricted to $f = 100$ kHz and $\tau_{\text{off}} = 4.0$ μs and the results essentially confirmed those of Figure 8 in that two peaks at the start of the ‘on’ phase are present and that the discharge develops into a stationary state at the end of the ‘on’ phase. As mentioned above, the temporal positions of the peaks are not altered within the error of measurement throughout the volume because the fast electron movement governs them. This enabled the quantification of the peaks at two fixed times, namely 0.4 μs and 1.0 μs after the start of the ‘on’ phase. The results of the respective charge carrier density are shown in Figure 11. Clearly, peak A and C have a significantly different spatial distribution: A is strong in the bulk of the plasma whereas C exhibits its maximum in the magnetic trap close to the target.

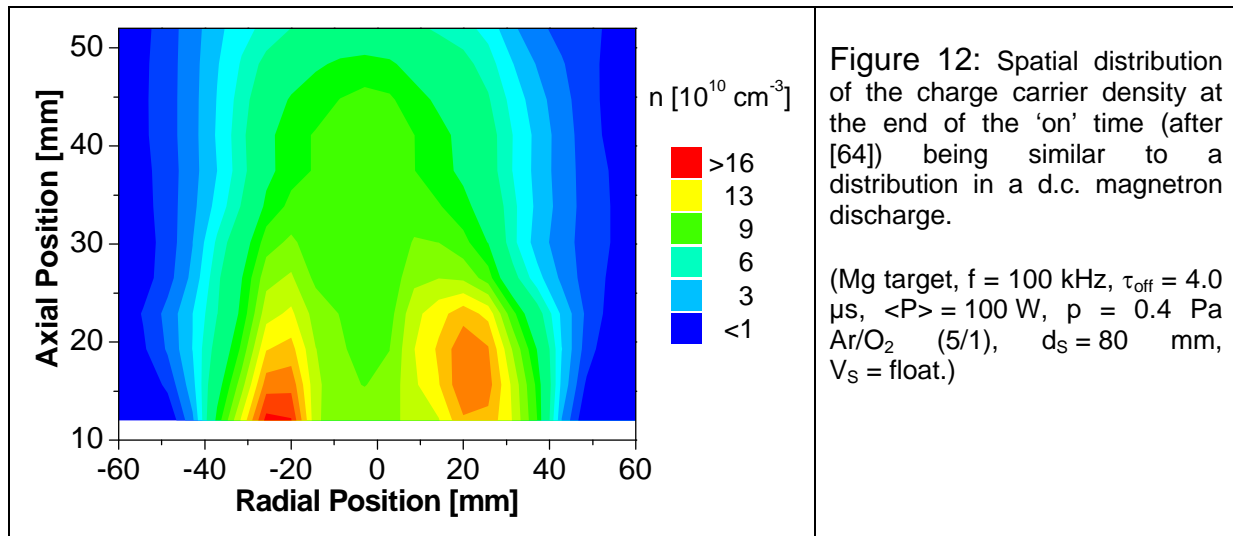


Peak A is – as in Figure 8 for 100 kHz – generally much weaker than peak C. The reason why it is most distinct above the magnetic null is determined by the unbalanced nature of the magnetic field configuration and the initially homogeneous distribution of the remnant electrons. Those of them, which are close to the target, are confined and cannot leave the magnetic trap. Because the potential drop in this early time of the ‘on’ phase is rather extended they can in their majority not acquire enough energy to ionise efficiently. Consequently, the region of the magnetic trap exhibits a rather weak charge carrier density. However, electrons initially located outside the magnetic trap are accelerated towards the substrate region. Due to the unbalanced magnetic field, they are simultaneously driven to the centre of the discharge by the magnetic field lines (cf. Figure 3) being kind of focussed to the region above the magnetic null. The result is a broad region of increased charge carrier density where the magnetic field converges to the line of symmetry of the magnetron.

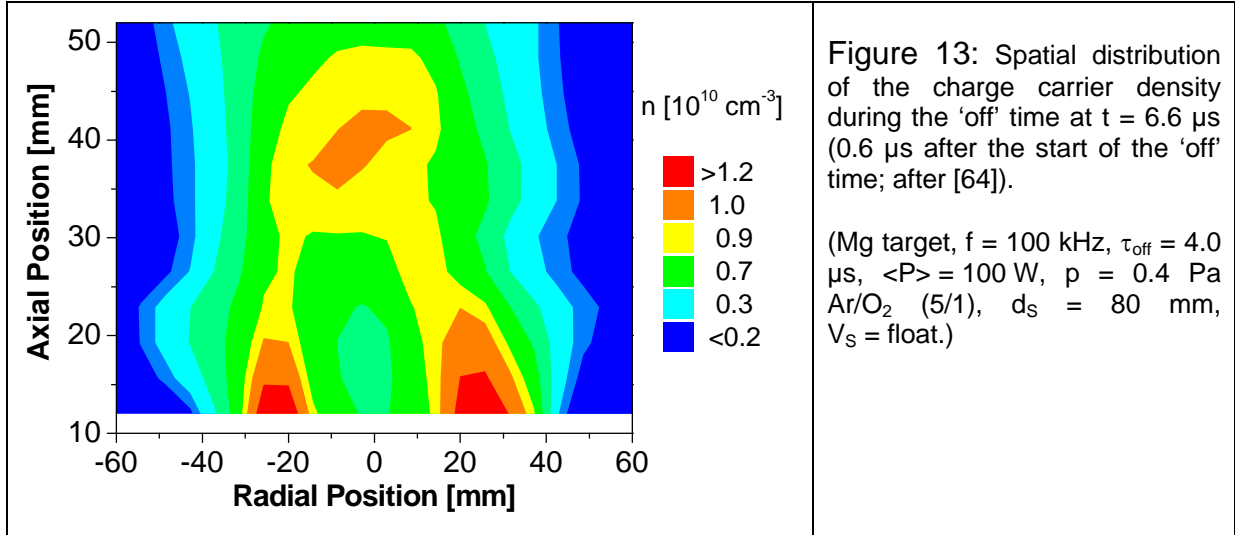
The situation is very different for the electrons causing ionisation peak C. These are initially secondary electrons due to homogeneous ions bombardment at the target. They thus exclusively originate from the target surface and experience the full sheath voltage. The resulting high energy leads to much higher ionisation in the complete discharge volume. However, most of these secondary electrons are trapped within the magnetic field close to the target and ionise in the torus region. The charge carrier density is thus particularly enhanced in the torus region at $x = \pm 30$ mm (cf. Figure 11b). Few secondary electrons are released at the outer target regions with magnetic field lines directing them to the substrate. Additionally, some are scattered from the trap onto these field lines. Given the high energy the electrons during this stage have, the ionisation in the rest of the volume is also increased and the shape of the magnetic field is again reflected.

The final charge carrier density at the end of the ‘on’ phase resembles that of a d.c. discharge with generally lower values throughout the volume (Figure 12). This is because the target voltage is now much weaker (150 V instead of 300 V) so that the secondary electrons gain only half of the energy than at peak C resulting in a lower average ionisation. The distribution of n is a mixture of the situation at peak A and C. This is because the discharge at this moment is – as for peak C – driven by the high-

energetic secondary electrons from the target marking the torus region. At the same time, scattered electrons from earlier stages are distributed in the volume, which follow the ionisation scheme typical for peak A and enhancing the density in the plasma bulk. This is especially seen in the radial gradient of the density in the substrate region which is with a factor of 3 between the centre and $x = 40$ mm (at $z = 45$ mm) intermediate to peak A (factor of 13) and peak C (factor of 2).



In the 'off' phase, the charge carrier density decays quickly within the whole volume of the discharge. Measurements were taken 0.6 μs after switching 'off' at a moment where the probe signal was still high enough to evaluate the probe characteristics. The result is shown in Figure 13. The charge carrier density has dropped down globally by one order of magnitude compared to the end of the 'on' phase. Two regions can be identified where n is increased: the magnetic trap and the magnetic null of the magnetron (at about $z = 35$ mm). The latter is due to electrons that are scattered into this region during the 'on' phase but cannot quickly escape because in any direction the magnetic field is increasing. Hence, they are trapped at the magnetic null during the 'off' phase. In the torus region, one could expect a very fast drain of electrons to the positive target along the magnetic field. However, the remaining positive space charge of the slow ions would exert an attractive force on the electrons preventing a fast escape. Further, the ions themselves are repelled from the positive target. Consequently, the decay in the magnetic trap is driven by slow ambipolar diffusion across the magnetic field.



3.2.5. Optical Emission

The characteristic emission of radiation offers another way to obtain information on particle densities and energies. The spectroscopy of this optical emission is widely used because it is experimentally rather easy to detect the radiation spectrally resolved with an optical spectrometer. One drawback, however, is the integrated detection along the line of sight of the mostly cylindrical detection volume preventing local information. The even greater problem is that the particles and the radiation in technological low pressure plasmas as used here are even in the d.c. case not in equilibrium. The determination of physical quantities is thus very difficult as it necessitates extensive collision-radiation models. From a practical point of view, the simplest of those models, the so-called Corona model, is often used. This reduces the processes leading to the emission from excited states to two considered to be the most important: The excitation of the excited state (k) of a particle is assumed to occur exclusively by direct electron-impact from the ground state (g) of the particle and relaxation is restricted to spontaneous emission of radiation. The density of the excited state (n_k) in the discharge, which is proportional to the emission detected from it, can then be written in the form

$$n_k = \frac{n_g n_e k_{gk}}{\sum_{m < k} A_{km}} = \frac{n_g n_e}{\sum_{m < k} A_{km}} \frac{2}{\sqrt{m_e}} \int_{E_{e,k}}^{\infty} \sigma(E_e) \cdot \Phi(E_e) \cdot \sqrt{E_e} \cdot dE_e \quad (39)$$

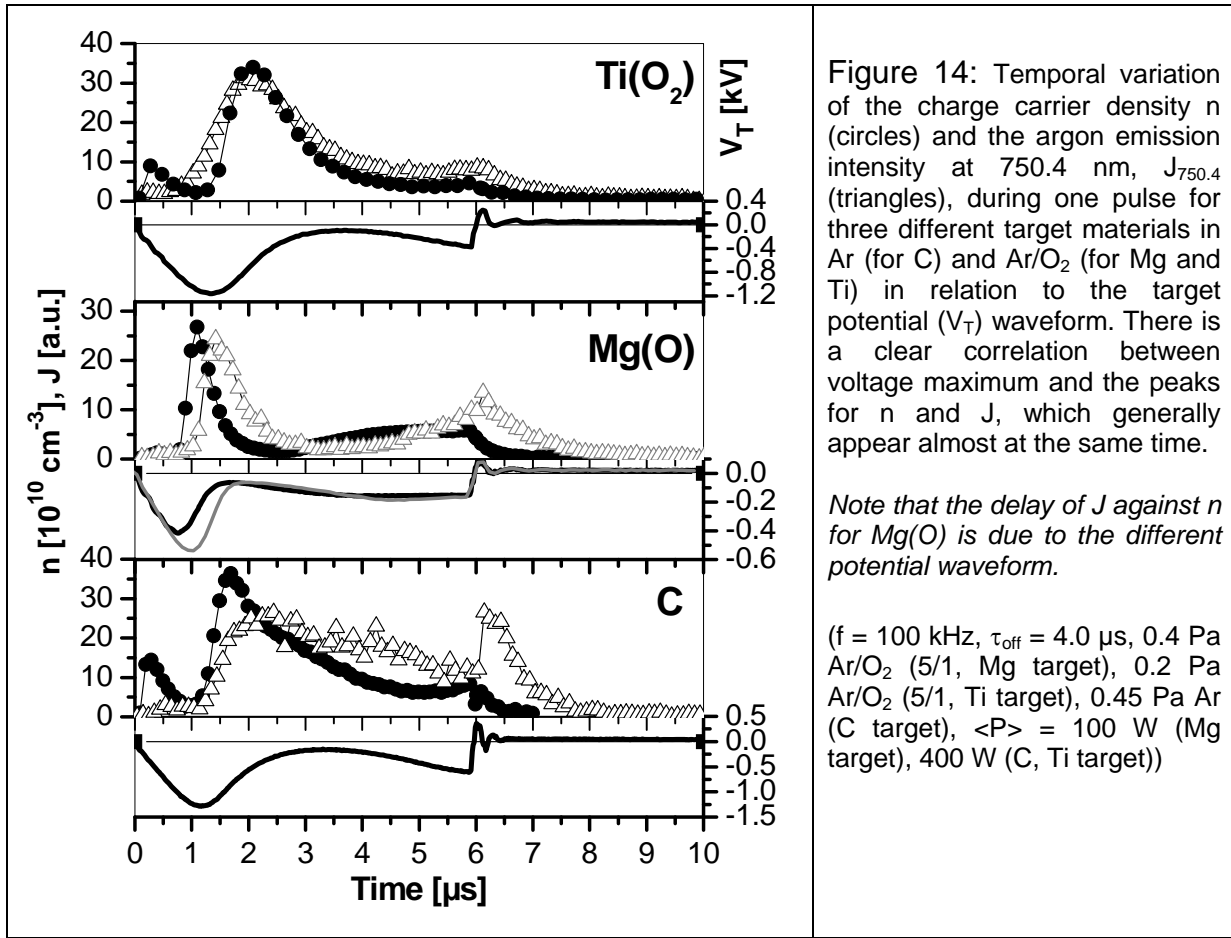
where k_{gk} is the rate coefficient for electron-impact excitation from the ground to the excited state which includes the electron energy dependent cross section σ_{gk} and the

EEDF (Φ) which have to be integrated over the electron energies (E_e). Thus for a given ground state density (e.g. of the working gas), the emission contains information on n_e and the EEDF, or T_e in the case of a Maxwellian distribution.

The measurements have been performed based on an optical emission spectroscopy (OES) setup used for the investigation of stationary discharges [65], with a collimating optics, a quartz fibre and a monochromator. To obtain time-resolution in the sub- μ s range, the original CCD camera has been replaced by a secondary electron multiplier and later an intensified CCD camera (Andor iStar DH720, DH734) that allows fast gating with the amplifier acting as an electronic shutter. A TTL trigger signal generated from the target voltage signal by a self-build electronics initiates the measurement and an internal controller of the iCCD camera moves the gate with respect to the trigger thus scanning the discharge pulse. The temporal resolution given by the gate and step width was 100 ns. More details of the setup can be found in [29, 66]. Spectra for each time step $J_t(\lambda)$ have been processed similar to the probe technique: averaging over many cycles, dark signal subtraction and finally transposition into temporal traces $J_\lambda(t)$ for selected emission lines.

Such temporal variations of the argon emission line at 750.4 nm are shown in Figure 14 for pulsed magnetron discharges in Ar or Ar/O₂ and for different target materials. Irrespective of the different working gas and target material, all traces exhibit the same general trend although the temporal variation of the target voltage is obviously depending on the discharge conditions. The latter effect will be discussed in subsequent sections. However, the emission follows the variation of the voltage in any case with a characteristic modulation in the 'on' time and a rapid decrease in the 'off' time. The modulation in the 'on' time is understood in terms of the Corona model and equation (39) in combination with the development of the charge carrier density which is also given in Figure 14. As discussed above, the density n , which equals n_e , exhibits a very strong peak C shortly after the voltage peak. According to equation (39), the density n_k of the excited argon state $2p_1$ (in Paschen notation [67])⁴ for the 750.4 nm line will be particularly high at this moment followed by subsequent emission. Because the lifetime of $2p_1$ is only 22 ns, almost no delay of $J(t)$ to $n(t)$ is observed, both peaking together shortly (350 ... 600 ns) after the voltage peak.

⁴ This notation will be consistently used in this work unless otherwise stated.

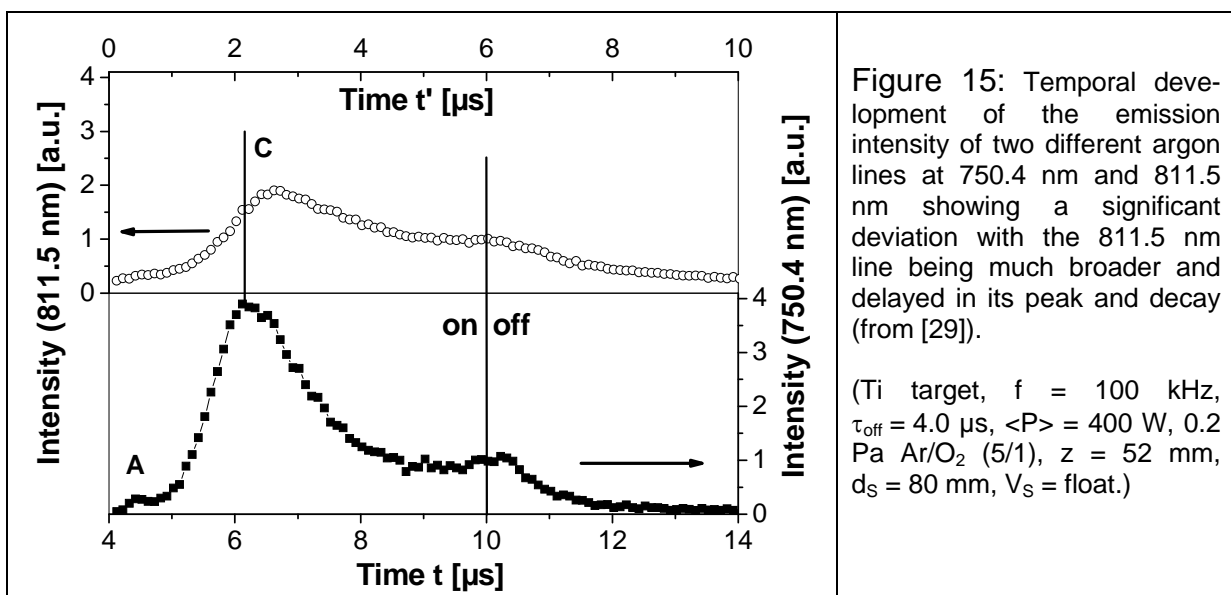


From this reasoning, a similar but smaller peak in the emission intensity is expected at the very early stage of the 'on' phase ($t \sim 0.5$ μs) where a smaller maximum in the charge carrier density is observed and elevated electron energies are supposed. In fact, the emission intensity at this time exhibits a weak maximum because of the elevated density. The peak however is surprisingly weaker than for the density and in the case of the Ti target only seen as a plateau in the rise to peak C. A simultaneous increase in the electron energies, which could not be observed with the double probe, would rather suggest a more distinct peak A in the emission. Up to now, it is not fully understood why the emission peak at this time is such low. The reason may be the different information volume of the probe and the OES. With the double probe, the density peak A is detected locally and particularly strong on the axis of symmetry (cf. section 3.1.4). OES, however, is integrating over the whole discharge cross section including regions with very weak density peak A. Although this is still subject to speculation, the general existence of the two peaks in the optical emission confirms the model of the discharge ignition in the 'on' time developed from the double probe results.

In some cases, just at the transition from the 'on' to the 'off' phase, an additional sharp emission peak is observed (designated 'F' in the scheme used here). In Figure 14, it is present for the carbon target but not for the Ti target and only very weak for the Mg target. Besides the dependence on the target material, it has been found to be strongly dependent on the environment of the discharge and the operating parameters. Under otherwise same conditions, it can be observed in one deposition chamber, but not in another. For the metal targets, it became visible especially at high pressure [68]. Joint investigations at the University of Liverpool which also included the emission from He traces in the working gas indicated that the emission peak is enhanced close to the substrate [69]. Based on that, the colleagues have further studied the substrate influence and found that its presence and potential have a dramatic influence on the markedness of the emission peak F [61]. In contrast to peak C, the existence of the emission peak is not related to an increase in the electron density in the discharge. In [68] this has been particularly reported but has been observed in many other cases. In terms of equation (39) the momentary improved excitation conditions thus have to be correlated to the rate coefficient and the electron energies. A sudden "burst" of few high-energy electrons increases the rate coefficient and thus the emission intensity. Such high-energetic electrons have been observed with single probes by Bradley et al. [40]. They obtain the high energy by rapidly expanding sheaths that result from the rapidly changing target potential that modulates the plasma potential (see next section). In the case of the emission peak F, it is especially the sheath in front of the substrate that accelerates the electrons. This is seen from the enhancement of the peak in the substrate region [69]. Swindells et al. [61] have observed a particularly strong emission peak F when the substrate is grounded instead of floating. In this case, of fixed substrate potential, the sheath is heavily modulated whereas with a substrate at floating potential that follows the plasma potential variations, the modulation is much less. Consequently, electrons are also most strongly accelerated leading to a very high peak. Recently in the own group, Dunger [70] in a comparative study investigated peak F for different target materials and geometries and found, that the steepness of the target voltage transient during the 'on'-'off' transition strongly influences the peak height. This means, the faster the plasma potential (determined by the target potential) changes, the more intense the emission peak is through increased acceleration of the electrons by the sheath. A lower limit of the transient seems to exist which has been

determined to 2.5 kV/ μ s for reactive sputtering of Ti [70]. All the results show that the peak F is determined by fast electrons generated during the transition to the 'off' phase and that in asymmetric-bipolar pulsed sputtering, this transition can not simply considered a passive switching 'off' of the discharge.

Up to now, only the emission of the 750.4 nm line of the argon atom has been discussed. Other argon lines have been investigated in parallel during this work. They have been found to more or less differ from the 750.4 nm line. The most extreme deviation was always observed for another very intense line at 811.5 nm [29, 68, 71]. A comparison of the temporal development of the intensity of the two lines is given in Figure 15. Clearly, the maximum corresponding to the charge carrier density peak C is delayed for the 811.5 nm line against the one at 750.4 nm. The lifetime of the excited level of the 811.5 nm line does with 30 ns not significantly differ from that of the 750.4 nm line. It is further much too short to explain the observed delay of 600 ns – which has been a general observation and not only for this example. The reason, according to equation (39), must lie in the electron energies or the inadequacy of the Corona model because n_g and n_e are of course the same. A different energy dependence of the cross section of the transition could explain a change in the absolute intensity but hardly a delay in the emission. It is thus likely that the simple Corona model does not properly describe the emission of the 811.5 nm line. This is all the more the case as its excited state ($2p_9$) is known to be subject to other excitation mechanisms than direct electron-impact [72, 73].



3.2.6. Excitation mechanisms and temporal behaviour of emission lines

To deeper investigate the possible influence of different excitation processes on the temporal development of various argon emission lines; the decay of the intensity in the 'off' time has been studied. This period is especially suited for such investigations because – except of the very early moments – the target voltage is not changing significantly in time and a feedback of the power supply can be excluded.

13 emission lines of the argon atom, 12 of them with an excited state from the 2p manifold and one with a 3p excited state, were measured for fixed discharge conditions and their decay in the 'off' time was analysed. The decay could well be characterised by a single exponential fit

$$J(t) = J_0 \exp\left[-\frac{(t - t_0)}{\tau_{\text{dec}}}\right], \quad (40)$$

with t_0 and J_0 being the start of the 'off' time and the emission at that time, respectively. At the selected discharge conditions, no peak F appeared leaving J_0 unaffected. The determined decay constants τ_{dec} ranged from 0.7 μs for the 750.4 nm emission line to 1.6 μs for the 811.5 nm line. As mentioned above, the lifetime of the excited states is in all cases much shorter than these values. Consequently, the different decay has to be attributed to diminishing excitation through the decaying plasma. Classifying the emission lines into their excited state proved that within the error of measurement the decay constant is the same for the same state but different for different states. The longest decay constant for the 811.5 nm line belongs to the 2p₉ state. The lowest decay constant is obtained for the 2p₁ state (750.4 nm) and is the same as the similarly determined decay constant of the charge carrier density ($\tau_{\text{dec},n} = 0.7 \mu\text{s}$) under the same conditions.

Chilton et al. [72] and Piech et al. [73] have published electron energy dependent cross sections for the excitation of the 2p levels by electron impact not only for the direct excitation but also for two other processes that are

(1) cascade excitation from any level Ar^* with higher excitation energy



(2) excitation from the two metastable argon states ($1s_3, 1s_5$)



which can also contribute to the emission from the 2p levels. They are shown in Figure 16 in the form of the ratio of the cascade cross section to the cross section for direct electron impact excitation (taken for a sample electron energy of 40 eV) and the absolute value of the cross section from both metastable states (for an electron energy of 10 eV). A comparison of these cross sections with the experimentally determined decay constants reveals that the decay constant is always high when either the cross section from the metastables or the relative cross section for cascading is high. Both indirect processes need two steps to populate the 2p levels. For the cascading, higher levels and the emission from these are involved with lifetimes that are longer than for the 2p levels, which would slow down the emission. Excitation from the metastably excited argon atoms proceeds via two subsequent collisions with electrons which would also slow down the 2p excitation.

Within the error of measurement, a distinction between the contributions of the two indirect processes is difficult. This is all the more the case because no cross section out of metastable is available for $2p_7$ and the decay constant for 772.4 nm comprises two lines corresponding to $2p_2$ and $2p_7$ which were not separable. It is likely that the excitation channel via metastable argon is the dominant mechanism increasing the decay constant. Cascades would necessitate electron energies of at least 13.9 eV. However, the emission from $2p_1$ level (750.4 nm) decays as rapidly as the charge carrier density measured with the double probe. Electrons with energies above 13.5 eV ($2p_1$) which are mainly the secondary electrons accelerated in the target sheath which collapses in the 'off' time thus quickly disappear. The excitation of the 2p levels out of the metastable argon states on the other hand needs only electron energies of at least 1.2 eV. Such electrons should be present in the 'off' phase on a longer timescale. Indeed, Lopez et al. [74] and recently Dunger [70] report that the emission decay may be separated into a fast one with $\tau_{dec,1} < 1 \mu s$ and a slow one

with $\tau_{\text{dec},2} > 2 \mu\text{s}$. The slow decay can be attributed to the loss of cold electrons that additionally further cool down in the 'off' phase.

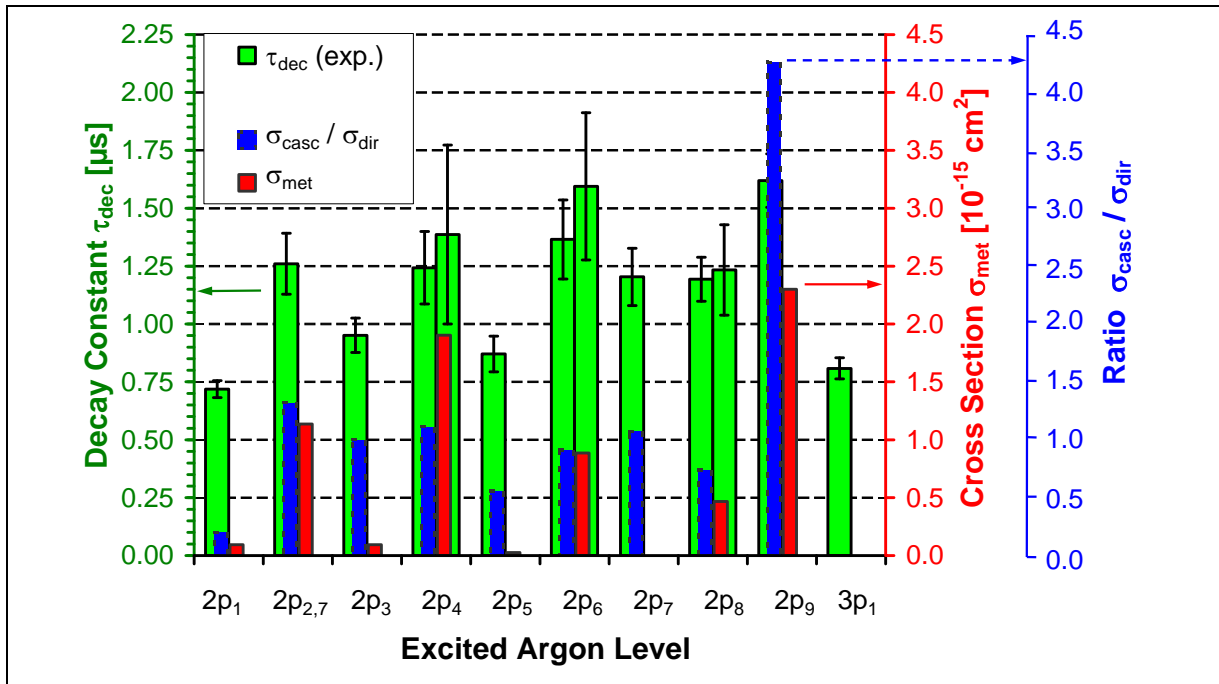


Figure 16: Measured exponential decay time τ_{dec} of emission lines corresponding to different excited states (green), ratio of the cross section for excitation via cascade contributions to direct excitation for an energy of 40 eV (blue – no data available for 3p₁), and cross-sections for the excitation of the excited levels out of the metastable states of argon for an energy of 10 eV (red – no data available for 2p₇), after [29]. (Ti target, $f = 100 \text{ kHz}$, $\tau_{\text{off}} = 4.0 \mu\text{s}$, $\langle P \rangle = 400 \text{ W}$, $p = 0.2 \text{ Pa}$ Ar/O₂ (5/1), $z = 28 \text{ mm}$)

The emission line at 425.9 nm (from the excited 3p₁ level with an energy of 14.74 eV) has a similar low decay constant as the 750.4 nm line. Hence, it is also excited mainly by direct electron-impact. The slightly higher decay constant is a consequence of the longer lifetime (77 ns [75]) of its excited state compared to that for 2p₁ (22 ns). The 3p₁ level is - due to its higher excitation energy - less susceptible to cascade contributions and, according to Boffard et al. [67] the cross section for the excitation out of the metastable states is much lower. This is also seen in table 2, where the different cross-sections have been compared to each other for the lines from the two fast level 2p₁ and 3p₁ and the extremely slow line from 2p₉ where available.

In summary, the simple Corona model is applicable for the investigation of the temporal behaviour of the charge carrier density or electron temperature in pulsed magnetron discharges. However, it has to be restricted to the excited 2p₁ level or the 3p₁ level with, however, is less intense due to its higher excitation energy. Other

states are more or less influenced by other excitation channels, hereby mostly from the two metastable states $1s_3$ and $1s_5$. Whereas direct excitation is sensitive to higher energetic electrons, excitation from the metastables is sensitive to cold electrons. It will be, however, extremely difficult to obtain selective information on the metastable states because in any case, it has to be integrated over the EEDF and complete energy dependent cross-sections are required. The results from the decay in the 'off' time prove that a significant density of metastable argon is present in the discharge to influence the excitation of the argon lines.

| cross-section | | electron energy | $2p_1$ | $2p_9$ | $3p_1$ |
|-------------------------------------|----------------------|-----------------|--------|--------|-------------|
| direct | σ_{dir} | 40 eV | 3.1 | 0.61 | n.a. |
| cascades | σ_{casc} | 40 eV | 0.63 | 2.6 | n.a. |
| apparent | σ_{app} | 40 eV | 3.7 | 3.2 | 0.81 |
| metastable $1s_3$ | $\sigma_{met}(1s_3)$ | 10 eV | < 85 | n.a. | 2.7 |
| metastable $1s_5$ | $\sigma_{met}(1s_5)$ | 10 eV | < 9 | 2300 | 0.63 (9 eV) |

Table 2: Different cross-sections (in 10^{-18} cm^2) for the excitation of the $2p_1$, $2p_9$, and $3p_1$ level of the argon atom. The electron energy at which the cross section has been measured is given in the third column. Although the values for the $3p_1$ level are generally lower, they are exceptionally low for the excitation out of the two metastable states (bottom two lines) indicating that this process does not significantly contribute to the emission from the $3p_1$ state. Data have been compiled from [72, 73, 75, 76].

3.3. Potential in the discharge volume

Very important parameters in any discharge are the two distinct potentials, the floating potential, V_{fl} , and particularly the plasma potential, V_{pl} , at which the plasma particles at any given spatial position are. Whereas the first has its significance for insulating substrates because they adjust to it, the latter is of twofold relevance. It mainly determines the ion energy onto any substrate whether floating or fixedly biased in potential via the sheath in front of it and simultaneously determines the charge carrier movement within the discharge volume through its spatial or – in the case of pulsed discharges – temporal variation. To access V_{pl} , only a few electrical techniques are suited because any probing device may alter the local potential situation.

3.3.1. Measurement technique – the emissive probe

The plasma potential can indirectly be determined from the energy of (positive) ions arriving at a fixedly biased substrate. Devices used are energy-dispersive ion mass spectrometers (see section 3.3) or retarding field analysers. As the ions are accelerated through the substrate sheath, almost only ions from the sheath boundary are probed with such techniques. It is therefore particularly impossible to obtain spatial information on the plasma potential. The most frequent method to investigate V_{pl} also with spatial resolution are still single Langmuir probes. With them, V_{pl} in an ideal case is obtained from the "knee" in the characteristics, i.e. the change of the slope between the electron-retarding region and the electron saturation. This may be either done from a semi-logarithmic plot of the electron current and extrapolating two straight lines for the two regions to their intersection or by the second derivative of the characteristics. Both evaluation methods can suffer from significant uncertainties. If the EEDF is not Maxwellian, a straight line fitting to the retarding region can be problematic which – together with the nearly exponential electron current increase - may shift the determined V_{pl} . Noisy characteristics, as they are typical for time-resolved measurements, hamper the determination of the second derivative. One common problem is that for both methods the complete characteristic, at least around V_{pl} (to be subsequently determined), has to be acquired which requires massive experimental efforts for time-resolved measurements.

An alternative method to determine V_{pl} is the use of a slightly altered probe geometry and another measuring circuit, the emissive probe [77, 78]. Such a probe was developed within this work to measure V_{pl} time-resolved in the volume of the pulsed magnetron discharge [A3, 79]. The basic principle of an emissive probe is to alter the characteristics of a single probe through the emission of thermal electrons by heating the probe wire sufficiently as shown in Figure 17. The thermal electrons leaving the probe are recognised as an apparent additional ion current to the probe. This works as long as the potential of the probe (V_{pr}) is below the plasma potential. When the probe potential is above V_{pl} , the plasma repels the thermal electrons and there is no apparent additional ion current. Because the temperature of the emitted electrons is equal to the wire temperature T_{pr} , they have energies of the order of $k_B T_{pr}/e = 0.2$ eV, much less than typical plasma electrons and are repelled even for V_{pl} being only

slightly above V_{pr} . If the probe wire is sufficiently heated, i.e. the current of the emitted electrons is of the order or more than the plasma electron current to the probe, a sharp kink in the characteristics appears at the plasma potential where the emission current sets in. From this, V_{pl} can be easily determined with a theoretical potential resolution of $k_B T_{pr}/e$. Still, this procedure necessitates the acquisition of characteristics I_{pr} vs. V_{pr} to determine the kink. The electron emission, however, has another effect on the characteristics (see Figure 17). Through the appearance of a virtual ion current, the apparent floating potential, i.e. the probe potential at which no probe current is measured, is shifted to values that are more positive. The more apparent ions (more emitted electrons) are present, the more positive this apparent floating potential becomes. The effect immediately stops at V_{pl} because there is no emission at probe potentials above it. This means, that the apparent V_{fl} approaches V_{pl} for sufficiently high electron emission [80]. The floating-point method makes use of this by the measurement of V_{fl} of the probe with a high-resistance against ground and taking this as V_{pl} . The major advantage of this technique is the possibility to obtain V_{pl} by the reading of just one voltage value. Rather convenient time-resolved measurements thus become possible with the voltage reading done by a fast oscilloscope.

As mentioned, the accuracy of the method in a d.c. discharge is theoretically of the order of $k_B T_{pr}/e$. However, the strong electron emission leads to space charges and a local disturbance of the plasma. The saturation of the apparent V_{pl} is therefore not complete and the real accuracy is only about $k_B T_e/e$ [81]. Further, in pulsed plasmas, the ability of the setup to follow fast transients has to be considered which will be discussed below. Possibilities to heat up the probe reach from self-heating by the discharge at very high plasma densities [78] to laser irradiation [82]. The most common heating mechanism is still the ohmic heating through an external circuit for which the probe tip has to be formed to a closed-loop. In this work, such a system has been set up, the circuitry of which is shown in Figure 18 [A3]. The probe wire is made of thoriated tungsten of 50 μ s diameter formed to a loop of typically 10 mm perimeter that is connected electrically and mechanically to a moveable holder. The loop current is supplied by a battery to minimise the capacity to ground and a variable series resistor to adjust the current. The typical voltage drop across the loop was 3.5 V. To minimise the falsification of the potential reading due to this drop, the

pickup was placed in series between two small resistors to have a situation close to the middle of the loop. The time-resolved voltage against ground was recorded via a 1/10 potential divider and a digitising oscilloscope connected to a computer. The trigger was taken from the rising flank of V_T that was simultaneously recorded.

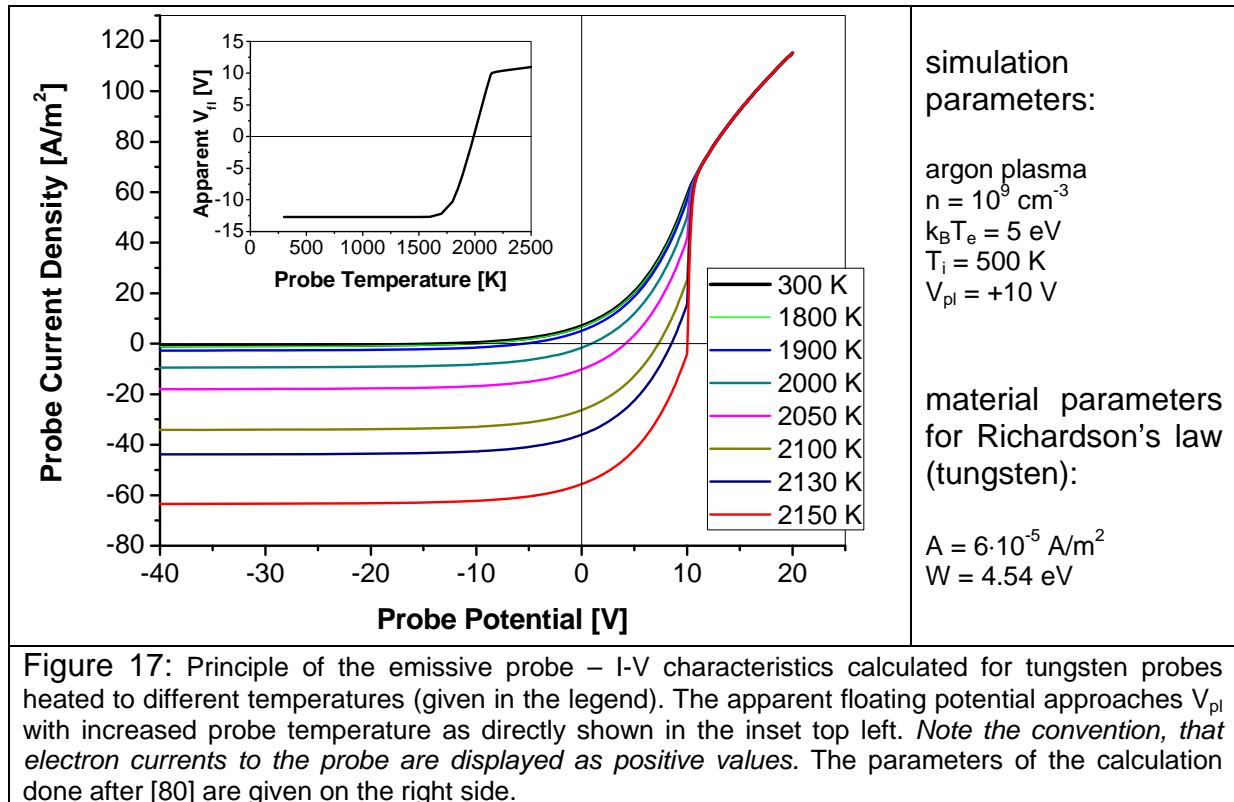


Figure 17: Principle of the emissive probe – I-V characteristics calculated for tungsten probes heated to different temperatures (given in the legend). The apparent floating potential approaches V_{pl} with increased probe temperature as directly shown in the inset top left. *Note the convention, that electron currents to the probe are displayed as positive values.* The parameters of the calculation done after [80] are given on the right side.

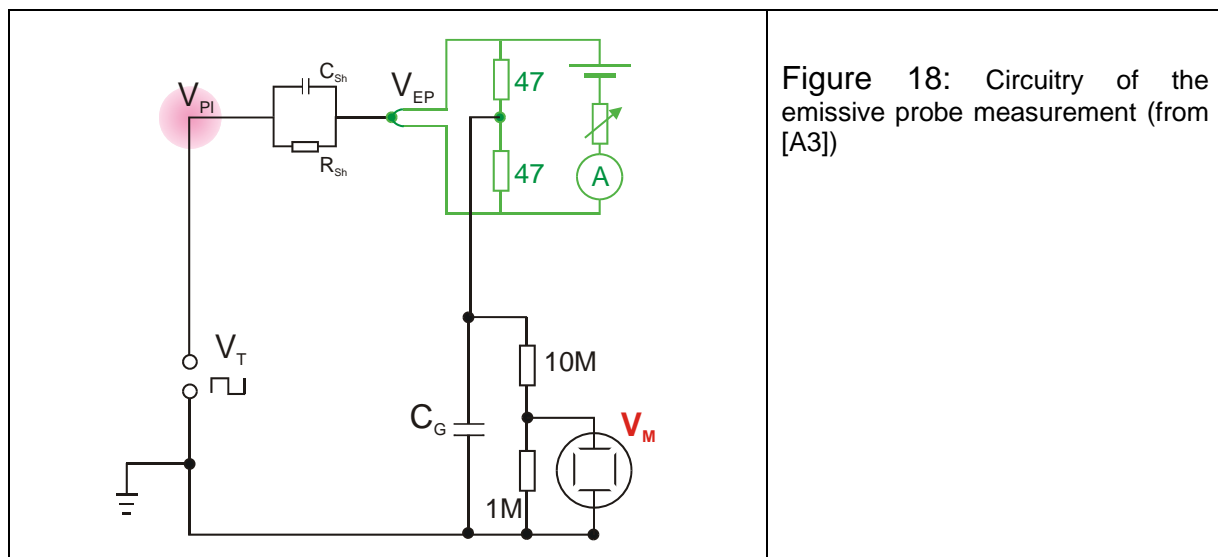
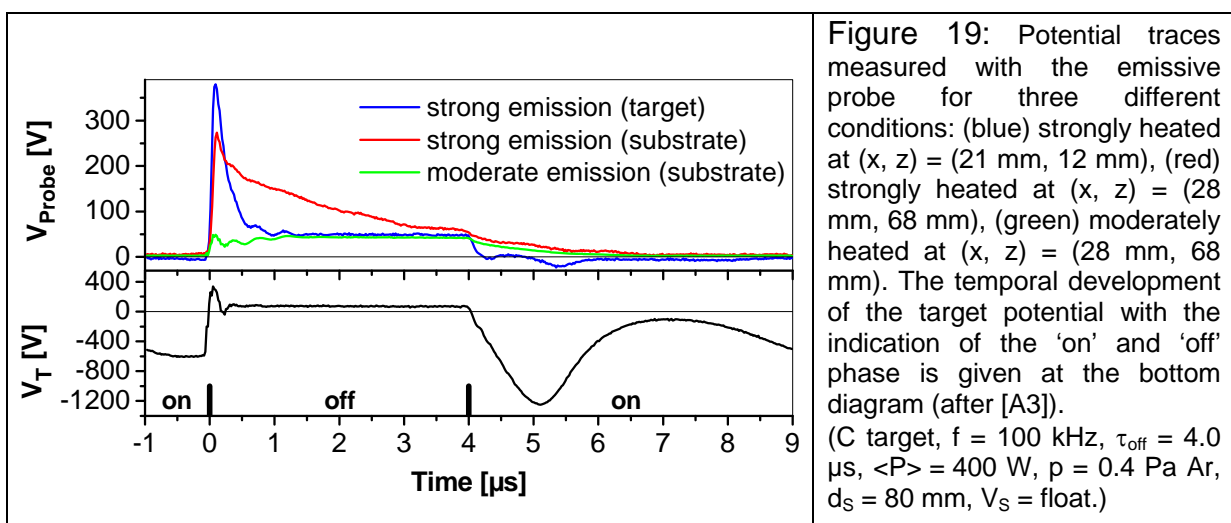


Figure 18: Circuitry of the emissive probe measurement (from [A3])

3.3.2. General temporal development

Typical waveforms for V_{pl} that were obtained with different heating current and at different positions in a pulsed carbon sputtering discharge are given in Figure 19. They clearly show that V_{pl} is very different in the 'on' and 'off' time. In the 'on' time, V_{pl} is generally close to zero and in the 'off' time, it is positive with an overshoot to very positive values at its beginning that is also observed in the asymmetric bipolar target potential. However, significant deviations have been observed for differently hot probes (Figure 19). Rather weak emission is sufficient to saturate the probe signal in the stable 'off' an 'on' phase which can be seen in Figure 19 when comparing the measurement at the target and for the weakly emitting probe at the substrate. An increase of the probe temperature does in most cases not further increase the probe signal at these moments, a behaviour that has also been reported by another group [83, 84, 85]. At the beginning of the 'off' phase and coinciding with an overshoot in the target potential to very high positive values, however, further increase of the probe temperature by the heating current, strongly increases the probe signal until it also saturates for a strongly emitting probe [A3, 79, 83]. The measured potential then decreases rapidly close to the target but does not at the substrate. In the latter case, the slow decrease leads to a seemingly increased plasma potential even at the end of the 'off' time and beyond. To explain this, the response time of the circuit has to be considered.



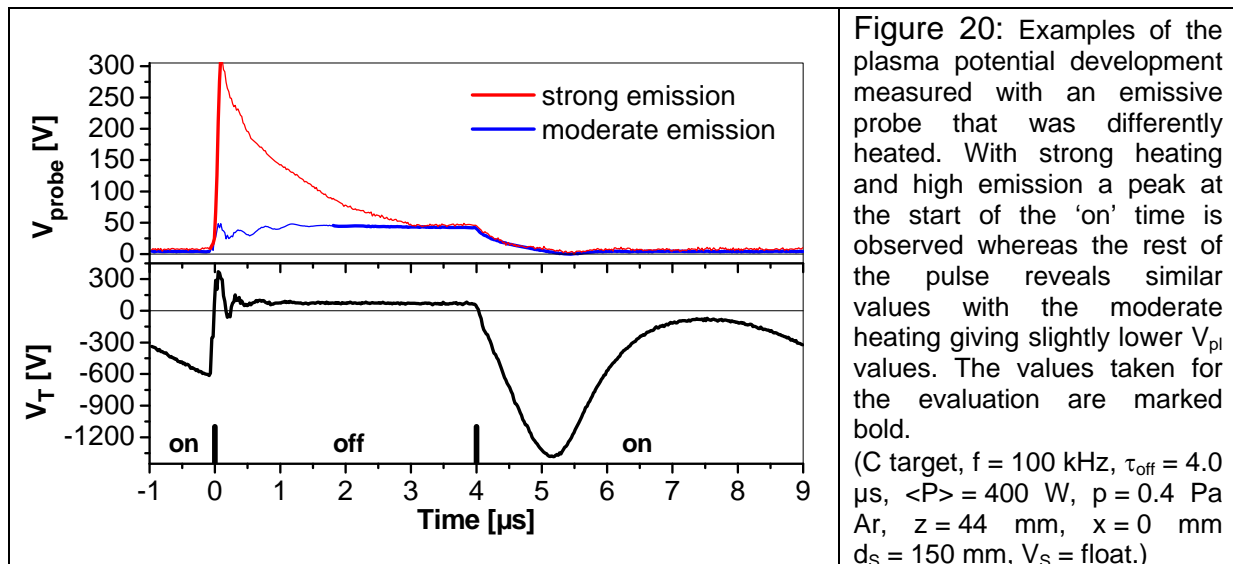
The response time is determined by the combination of the resistance (R_{sh}) and the capacitive impedance (Z_{sh}) of the sheath surrounding the probe, both being

dependent on the plasma conditions, and the fixed capacity of the setup against ground (C_g). The latter has been determined experimentally to ~ 130 pF. With this value, response times τ of ~ 10 ns (for $n = 5 \cdot 10^{11}$ cm $^{-3}$ and $T_e = 5$ eV, typical for the target region) up to ~ 500 ns (for $n = 5 \cdot 10^9$ cm $^{-3}$ and $T_e = 2$ eV, typical for the substrate region) have been estimated with $\tau \sim R_{sh}Z_{sh}C_g/(R_{sh}+Z_{sh})$ [A3]. These values are sufficient to investigate potential changes within one pulse but with the emissive probe reacting slower at the weakly ionised substrate region to rapid potential changes (seen in Figure 19 for the weakly heated probe at the beginning of the ‘on’ phase). The response will further be strongly slowed down at times with falling plasma potential when the probe is strongly emitting. The suddenly more negative plasma then repels the emitted electrons and the resulting space charge around the probe effectively increases the sheath resistance [84]. Thus, the probe reading can be significantly falsified for very hot probes and weakly ionised plasmas at falling V_{pl} what is seen in Figure 19 for the strong emission at the substrate region. On the other hand, the strong emission is required to correctly measure the potential overshoot at the beginning of the ‘off’ phase. For this reason, the investigations should always be divided into two runs as done in [A3]:

- (a) The peak value of the overshoot, for which the response time during the falling flank is insufficient, is measured with a very hot probe.
- (b) The stable phases are measured with a moderately heated probe with improved response time during the falling flanks so that V_{pl} in longer intervals of these phases is sensibly detected and additionally the probe’s lifetime is increased.

An example of the results obtained that way is shown in Figure 20 for the two heating cases with the taken regions marked bold and the target potential V_T as reference. During the ‘on’ time, V_{pl} adjusts close to zero. The adjustment starts as soon as the target potential begins to decrease to negative values. The slower decrease is thereby probably due to the response time of the probe. Shortly after the strong negative overshoot of the target potential, especially close to the target, a small dip in V_{pl} is also observed (this can be even more clearly seen in the waveform of V_{pl} from the target region in Figure 19). For the rest of the ‘on’ time V_{pl} stays constant. As soon as the target potential starts to rise to positive values, V_{pl} follows this increase and adjusts itself close to the positive potential value of the target in all cases

investigated. During the positive overshoot of V_T at the start of the 'off' phase of several 100 V, V_{pl} is simultaneously raised to very high values close to V_T . It can thus be stated that V_{pl} throughout the whole pulse is always close to the most positive surface surrounding the discharge, either the grounded wall or substrate in the 'on' time or the positive target in the 'off' phase. This is consistent with the findings of the group of Bradley in similar pulsed magnetron systems [83-86]. However, there has been a discrepancy in the relation of the absolute values of V_{pl} to V_T in the 'off' time which remained at first peculiar: whereas in this work, V_{pl} was mostly below V_T , the investigations of the Bradley group found V_{pl} always above the most positive electrode potential, i.e. the target at the 'off' phase. The reasons for these seemingly contradicting results will be addressed in sections 3.3.3 and 4.4.



The very positive high plasma potential has been observed in any configuration investigated within this work [A3, 79]. It appears exactly at the time the target potential peaks in the 'off' time as shown in Figure 20. Moreover, using a technique suggested by Karkari et al. [84] to provide an additional path to ground for the electrons and thus improving the temporal response, it has turned out that V_{pl} qualitatively even follows the subsequent oscillations in V_T . The necessary modification of the circuitry, however, falsifies the measured absolute value of V_{pl} and could thus not be used for quantitative measurements.

The suddenly elevated V_{pl} at the start of the 'off' time has a twofold consequence. On the one hand, electrons in front of any surface at fixed potential (e.g. especially a

grounded substrate) will be strongly accelerated into the plasma bulk. The resulting temporary excitation in the discharge volume was observed with OES and is discussed in section 3.1.5. The sudden high potential difference between the (positive) plasma and surfaces surrounding it will on the other hand lead to positive ions of high energy impinging on the surface. This is important for the film deposition especially for grounded substrates because such high-energetic ions may cause damage and deteriorate optical or electronic properties. The situation is less problematic for floating substrates with their potential following the V_{pl} changes and ions will still arrive at the substrate with energies of $e(V_{pl}-V_{fl}) \sim 20$ eV. However, even in this case the film growth may be affected because all surrounding walls or mountings are typically grounded and may be sputtered by the high-energetic ions. The peak in V_{pl} can thus pose a source of impurities for the films.

The general behaviour of V_{pl} over one pulse has been described by a simple macroscopic model which was adapted from d.c. diode discharges. It basically applies the demand of quasi-neutrality of the plasma for a stationary state of the discharge on time scales longer than the inverse plasma frequency [A3]. To maintain quasi-neutrality, the electron current to any positive electrode (anode)

$$I_e = \frac{1}{4} \cdot e \cdot n_e \cdot \sqrt{\frac{8k_B T_e}{\pi m_e}} \cdot A_e \cdot \exp\left[-\frac{e(V_{pl} - V^{(A)})}{k_B T_e}\right] \quad (43)$$

has to be compensated by the Bohm ion current to any negative electrode (cathode)

$$I_i = 0.61 \cdot e \cdot n_i \cdot \sqrt{\frac{k_B T_e}{m_i}} \cdot A_i \quad (44)$$

at any time during the pulse for which an electron retarding potential difference at the anode (with potential $V^{(A)}$) of

$$V_{pl} - V^{(A)} = \frac{k_B T_e^{(A)}}{e} \ln \left[\frac{n_e^{(A)} A^{(A)}}{0.61 \cdot n_i^{(C)} A^{(C)}} \left(\frac{m_i T_e^{(A)}}{2\pi m_e T_e^{(C)}} \right)^{1/2} \right] \quad (45)$$

is necessary when secondary electron emission (typically only ~ 10 % of the ion current) is neglected. In equation (45), the electron temperature T_e , and the charge carrier density ($n_i = n_e = n$) have been superscripted (A) or (C) accounting for differences of the plasma parameters at the cathode (area $A^{(C)}$) and anode (area $A^{(A)}$) in the inhomogeneous discharge. Taking typical values for the 'on' time of $n^{(C)} = 5 \cdot 10^{11} \text{ cm}^{-3}$, $k_B T_e^{(C)} = 5$ eV at the target, $n^{(A)} = 5 \cdot 10^9 \text{ cm}^{-3}$, $k_B T_e^{(A)} = 2$ eV, and typical dimensions of the magnetron (10 cm diameter) and the substrate holder

(similar size), a potential difference of 2.5 V is obtained from equation (45) for argon when a grounded substrate acts as the anode ($V^{(A)} = 0$ V) [A3]. This is a value of V_{pl} that has been observed in the 'on' time (cf. Figure 20).

In the 'off' time, the potential situation is reversed and the target acts as the anode whereas a grounded substrate acts as the cathode. To prevent a significant deviation from quasi-neutrality by an excess electron current to the target, V_{pl} has to be elevated to be generally close to the target potential. However, a quantitative estimation in the 'off' time is rather impossible because the electron current to the target is impaired by the magnetic field shielding the target magnetically against most of the electrons from the plasma bulk [A3]. Furthermore, it has been found that the value of V_{pl} in both the 'on' and 'off' time is subject to the substrate potential and chamber and magnetron geometry. This effect will be discussed in section 4.4.

3.3.3. Spatio-temporal distribution of the plasma potential

The macroscopic model is capable to explain the general temporal variation of V_{pl} . However, the very inhomogeneous magnetic field of the magnetron associated with electron trapping in the 'on' time and shielding effects in the 'off' time will not result in a homogeneous distribution of V_{pl} or a very weak and constant electric field as in the positive column of a classical glow discharge. The distribution of a strongly inhomogeneous V_{pl} is essential for the movement of the charge carriers and its knowledge is necessary to understand the energy of ions that impinge on the substrate.

With the development of the moveable emissive probe, it became possible to measure the plasma potential distribution spatially resolved within the whole discharge volume [79]. The approach to the interesting region close to the target was limited to a distance of 12 mm – and with a purpose-build probe construction to 4 mm [A3]. However, a too close approach also led to a perturbation of the discharge. To obtain a complete mapping, the discharge of cylindrical geometry has been scanned with the probe in its cross-section. This has been realised with radial scans of $\Delta x = 7$ mm ($x = -49$ mm ... +49 mm) for different distances from the target

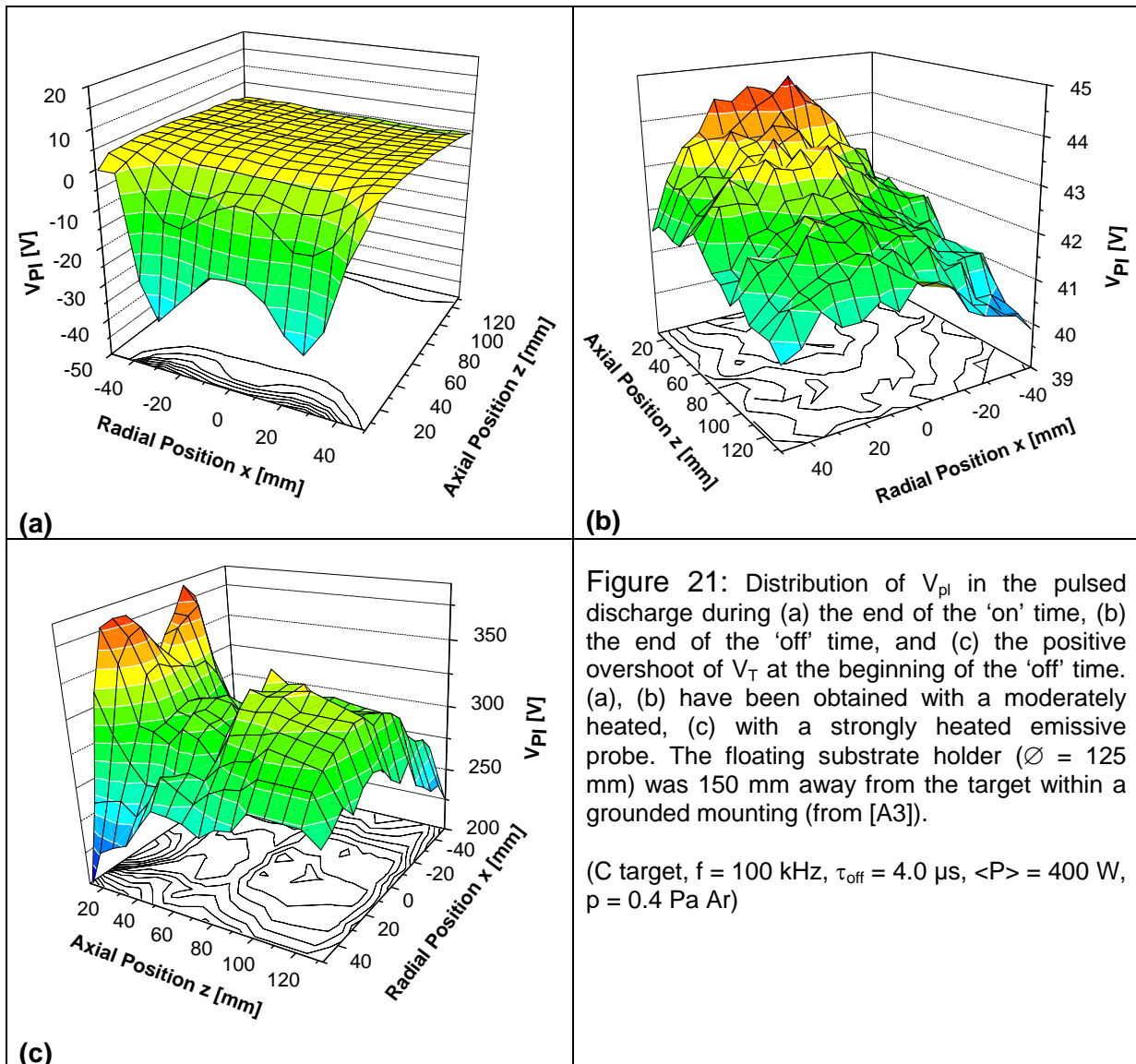
($z = (4), 12 \dots 132$ mm) in steps of $\Delta z = 8$ mm. The result for the pulsed discharge in argon with a carbon target is shown in Figure 21.

At the end of the 'on' time (Figure 21a) while V_T is ~ -600 V, the distribution of V_{pl} resembles that of a d.c. discharge as has been observed for the charge carrier density (section 3.3.4). At greater distances z of 40 mm, V_{pl} is almost constant and due to a grounded mounting plate around the floating substrate holder slightly above zero. In fact, V_{pl} decreases very weakly towards the substrate leaving a very weak potential maximum at the magnetic null of the magnetron. Towards the target, V_{pl} is rapidly decreasing to values of -25 V in the centre and -40 V in the racetrack 4 mm in front of the target. Thus, an extended pre-sheath of up to 40 mm exists in the stable 'on' phase with an average axial electric field of ~ 800 V/m and significant radial field components (~ 2000 V/m) in the region of the magnetic trap. Ions, which are anyway mostly concentrated above the race track and are weakly influenced by the magnetic field, are due to these radial electric field components further focussed into the centre of the race track. During the negative overshoot of the target potential down to $V_T \sim -1250$ V the plasma potential close to the target is also decreased and at 4 mm distance reaches values of -80 V above the race track. The electric field in the pre-sheath is more than doubled at this moment. For the very negative target potentials, also a weak decrease of V_{pl} in the plasma bulk along the magnetic field lines is observed with a resulting V_{pl} slightly below zero.

As soon as the discharge is switched to the 'off' phase, V_T reaches a positive value of $+340$ V [A3]. Electrons are affected from this potential change within nanoseconds and move to the positive target. V_{pl} is such also elevated throughout the whole volume to prevent further electron loss (Figure 21c). The effect is most significant in the magnetic trap where the magnetic field lines along which the electrons may drift are terminating on the positive target. The plasma potential in the trap region is therefore raised to values of up to $+400$ V, even above the target potential. In the rest of the discharge, spatial changes in V_{pl} are rather weak, resulting in an average axial field pointing towards the substrate of ~ 150 V/m. The dip in V_{pl} at about $z = 40$ mm is not real but a consequence of fluctuations of V_T to which V_{pl} is strongly connected [A3]. Close to the substrate (at $z = 132$ mm, i.e. 18 mm from the substrate), V_{pl} is still $+290$ V. Positive ions in this region will thus be strongly accelerated through a thin

sheath to a substrate at ground potential and may cause sputtering as supposed above.

When the target potential settles at about +70 V during the stable 'off' time, V_{pl} is also decreased again and reaches about +42 V (Figure 21b). As mentioned above, the relation between V_T and V_{pl} differs from those of other authors with V_{pl} being below V_T even close to the target. The spatial distribution of V_{pl} , however, is in agreement with the literature. There is a very weak axial electric field of ~ 25 V/m towards the substrate causing the $E \times B$ drift adjacent to the target to collapse. The magnetic trap is hence not represented in the distribution of V_{pl} .



Similar investigations have been performed in a slightly deviating geometry with a magnesium target and in reactive Ar/O₂ atmosphere that correspond to the measurements of the charge carrier density with the double probe (cf. section 3.1.2). The results confirm those given here for the carbon target [79]: in the ‘on’ phase, V_{pl} is close to zero with an extended presheath in front of the target and in the stable ‘off’ phase it is close to the positive V_T . However, in that system in the ‘off’ time $V_{pl} > V_T$ as in [83-86]. The distribution in the stable phase is comparable to the results presented here. Those studies further proved that the method of the emissive probe is even applicable in reactive ambient containing O₂ where a more rapid disintegration of the hot probe is expected. Indeed, the faster consumption of the probe has been observed which resulted in no possibility of a mapping of the potential distribution during the positive overshoot. Single quick measurements with a very hot probe confirmed a very positive V_{pl} during this moment of the pulse, too, with $V_{pl} > V_T$ in this case [79].

3.4. Ion energies at the substrate

Any substrate immersed into the plasma will be subject to ion bombardment with a certain energy or energy spectrum. In contrast to the light electrons, the energetic ions due to their momentum are suited to modify the film properties. In some cases, such a bombardment is even desired and realised by a fixed bias potential that is applied to the substrate holder.

In the simplest case of a d.c. discharge at low pressure with a collisionless sheath, the energy E_i of the ions arriving at the substrate is determined by the sheath voltage between the plasma potential V_{pl} taken as homogeneous for simplicity and the substrate potential V_s

$$E_i = q(V_{pl} - V_s) + E_0 \quad (46)$$

where E_0 denotes a possible directed intrinsic energy of the ion towards the substrate in the plasma. Thus, for a positive ion formed in the plasma bulk from a neutral at rest (e.g. Ar at room temperature) and a grounded substrate, its energy is proportional to the plasma potential. Equation (46) further shows that negative ions which may be

formed in electronegative gases will never reach the substrate as long as they don't have a sufficient E_0 to overcome the potential barrier to the substrate.

The situation is slightly different when the substrate is insulated at floating potential. Its potential then adjusts itself relative to V_{pl} according to the plasma conditions in front of it. Inserting V_{fl} and the current equilibrium into equation (46) yields

$$E_i = q(V_{pl} - V_{fl}) + E_0 = zk_B T_e \left(\frac{1}{2} + \ln \left(\frac{M_{eff}}{2\pi m_e} \right) \right) + E_0, \quad (47)$$

where M_{eff} is the effective ions mass. Again, negative ions without a starting energy E_0 will never reach the substrate because generally $V_{fl} < V_{pl}$. The difference here is for the positive ions: V_{fl} is always coupled to V_{pl} according to equation (47) by the parenthesis on its right hand side. For argon $V_{pl} - V_{fl}$ equals about $5k_B T_e/e$ so the positive ions in the collisionless case will always have an energy of $5k_B T_e$ independent of the absolute value of V_{pl} .

The realistic situation, however, cannot be described with the simple assumptions made above. Even for d.c. discharges the ion energy distributions (IEDF) at the substrate may not be as monoenergetic as given by equations (46) and (47) because of e.g. different intrinsic energies of different origin, collisions, and a not homogeneous plasma potential as discussed in section 3.3.3. This will be dealt with in section 3.4.2. Section 3.4.3 will then focus on additional modifications caused by the pulsed discharge and its strongly varying target and plasma potential. These may result in different energies within the IEDF, run-time effects and a non-constant E_0 in the mentioned equations.

3.4.1. Measurement – the plasma monitor

A simple method to determine the ion energies are retarding field analysers (RFA) where the IEDF is measured by scanning the potential of a retarding grid. The disadvantage of the purely electrical method is that positive ions are only detected in their entirety, i.e. there is no distinction between different ions. Negative ions cannot be separated from electrons at all. More sophisticated is the application of energy-dispersive mass spectrometers – so called plasma monitors - that measure the IEDF at certain mass-to-charge number (m/z) ratios for both positive and negative ions.

The problem with the typically dominating electron current in the negative range is thus simultaneously solved.

In this work, a commercial plasma (process) monitor PPM 422 (Inficon) has been used with slight modifications to the standard model to optimise it for different magnetron sputtering systems. So, an additional magnetic shield surrounds the barrel of the instrument. Further, the typical 90 degree deflection of the detector had been given up in favour of an in-line version with more flexibility in terms of the distance from the magnetron. This model of the PPM can detect ions with m/z in the range from 1 to 512 and allows energy scans from 0 to 500 eV for both positive and negative ions. Calibration of the energy has been performed by the ionisation of neutral gas at a given potential inside the instrument. The barrel was generally mounted opposite the target with the entrance orifice of 100 μs facing the target to allow the detection of ions from the gas with $E_0 \approx 0$ as well as ions moving away from the target with $E_0 > 0$. The separation of the entrance orifice from the target was fixed to 10 cm in most cases.

The PPM offers the possibility to bias the entrance orifice with respect to ground instead of grounding it directly. Several preliminary investigations in d.c. discharges where the entrance orifice was varied in potential showed that the IEDFs were altered as soon as the entrance potential was close to zero or above it. The barrel front end hence acted as an effective electrode for the discharge and elevated the plasma potential as described in section 3.3.2. Negative potentials, especially below V_{fi} had no significant influence on the IEDFs. It was therefore chosen to float the entrance for all experiments. Besides the practical simplicity, the intention was to provide a rather constant sheath for the ion collection throughout the whole pulse as V_{fi} varies with V_{pl} . At fixed potential, the entrance orifice otherwise may act as blocking potential in certain pulse phases. For the negative ions, the floating entrance has the consequence, that they must have at least an E_0 which corresponds to $e(V_{pl} - V_{fi})$ to enter the instrument at all.

Inside the barrel, after passing the ion optics, the ions are first selected according to their energy by a cylindrical mirror analyser (CMA) before the selection of m/z by a quadrupole mass analyser. The construction prohibits an experimental integration

over the ion energies because the CMA can only be passed for a certain energy. To obtain a transmission independent of the pass energy for the IEDFs, the pass energy itself is not varied but the ions are accelerated or decelerated by a scanning potential to a fixed pass energy that was typically 40 eV in this work. This scanning potential is varied during the measurement of an IEDF. The ions are finally amplified by a secondary electron multiplier (SEM) and detected by an ion counter. For the detection of positive and negative ions, the first dynode of the SEM is at very high (~ 3 kV) negative or positive potential. Ion energies are always displayed with respect to ground. A time-resolution to directly probe different phases of the discharge pulse was not possible with the PPM, because the transit time of the ions inside the instrument is much longer than the pulse duration, and it is dependent on the mass of the ion and its particular trajectory. An argon ion of the pass energy of 40 eV would e.g. take 35 μs in case of a direct path from the entrance to the detector. A recalculation into the pulse phases is thus not possible. The only chance of obtaining time-resolution in the μs range is a front gating of the measurement with a fast gating electronics inside the entrance hood of the barrel as shown by Voronin et al. [87] which has, however, not been attempted in the work.

An inherent property of the PPM is that it detects only ions which enter the orifice from directions which are only slightly inclined to the axis of symmetry. The reason is that only such ions can be successfully focussed by the ion optics onto the PPM axis and into the CMA. The supplier cannot give a particular angle of acceptance because it depends on the ion optical potentials, which have to be optimised for each application, and on the sheath that forms in front of the orifice, which is plasma dependent. It is generally assumed that the full acceptance angle is very small with about 3 degrees [88]. The restriction to almost perpendicular entrance has on the other hand the advantage that small regions of the plasma bulk and eventually the target are probed. Given the distance from the target of 10 cm, an area of it from which ions may be detected that directly move to the PPM is a circle of 2.6 mm radius. This has been used in the presented investigations by shifting the PPM axis relative to the target axis thus probing different regions. In particular, the PPM was directed to the target centre and to the racetrack region by moving the magnetron, which is experimentally easier than moving the PPM.

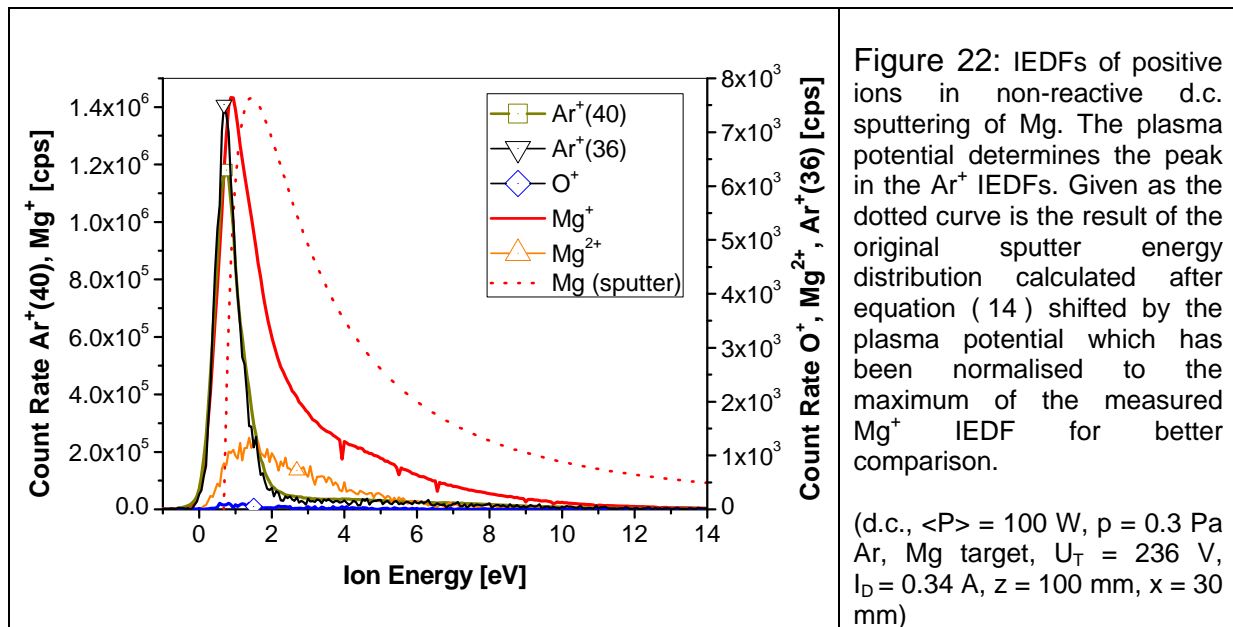
3.4.2. Energies in d.c. discharges

The IEDFs in d.c. magnetron discharges are comparably simple because the plasma potential is not modulated in time so that the average ion energy spectra measured by the PPM are determined by a single plasma potential value and no run-time effects complicates them. D.c. discharges are therefore useful to understand basic physical phenomena that have influence on the IEDFs. Examples for the IEDFs of positive ions for sputtering of a magnesium target in inert gas (argon) are shown in Figure 22. The argon ions, which result from ionisation of the cold gas with $E_0 \approx 0$, exhibit a single sharp peak at about 0.7 eV, thus after equation (46) V_{pl} is slightly positive with +0.7 V. It should be noted that Ar^+ may be detected with a very high count rate at $m/z = 40$ of its prevalent isotope (abundance 99.6 %) but with a significant count rate for its isotope (0.337 %) at $m/z = 36$ as well. Both isotopes will be used throughout this work when appropriate because, as shown in Figure 22 their IEDFs are expectedly identical except for their absolute intensity.

Figure 22 shows that besides a low signal of impurities (O^+), other positive ions detected are that of the target material, either singly or (very weakly) doubly ionised. The IEDFs of these ions are generally much broader than that for Ar^+ , particularly to high energies. The reason is that material from the target which is ionised at the plasma potential, carries an energy E_0 resulting from the sputter process additional to the energy from the difference between V_{pl} and ground. According to Equations (12)-(14) E_0 in this case has its own overlapping distribution enhancing the high-energy tail of the IEDFs. However, the contribution is much less than it would be expected for the original Thompson distribution (cf. Section 2.1) as given in Figure 22 by the dotted curve. This is due to collisions between the sputtered atoms with the cold working gas and the beginning of thermalisation of the sputtered flux. Taking the hard sphere model, the mean free path of an Mg atom in argon under the conditions of Figure 22 is 5 cm, so that in average an Mg atom has undergone two collisions between the target and the substrate.

Consequently, the Mg atoms that are ionised on their way the substrate lose energy which enhances the low-energy part of the energy distribution and reduces the high-energy tail. Thus, the maximum of the IEDF is shifted down to eV_{pl} instead of

$eV_{pl} + U_S/2$ as seen in Figure 22. The resulting average ion energy obtained from the data in Figure 22 is 1.7 eV for Ar^+ and 2.6 eV for Mg^+ . Without collisional cooling of $Mg^{(+)}$ an average energy calculated with $U_S = 1.53$ eV from equation (14) of 7.9 eV⁵ for E_0 plus the shift by eV_{pl} (0.7 eV obtained from the peak position of Ar^+) . The average energy of Ar^+ is also slightly higher than the peak energy. This is due to a small hump in the IEDF up to 10 eV. It is assumed that this weak increase is due to the heating of the gas by the collisions with the sputtered flux. Such gas heating has been reported to cause a gas rarefaction [89] and to be relevant at pressures above several 0.1 Pa [90] in d.c. magnetrons. The suggestion is supported by the fact the hump is intensified when the discharge power is increased. The effect is only weak because the mass of Mg is low.



For an aluminium doped zinc oxide (AZO) target sputtered at 0.4 Pa, the IEDFs of different target material ions could be studied, namely Zn^+ , Al^+ , O^+ , and AlO^+ . The investigations showed that the high-energy tail resulting from the sputter energy distribution deviates from ion to ion. It was most reduced for ions of intermediate masses [A4]. This has been explained by the different energy loss during elastic collisions. The energy exchange during an elastic collision is determined by the energy transfer function given in equation (4) and is maximum for equal masses. If it is assumed that for the compound material all constituents experience the same surface binding energy, atoms with a mass close to 40 amu will have the most

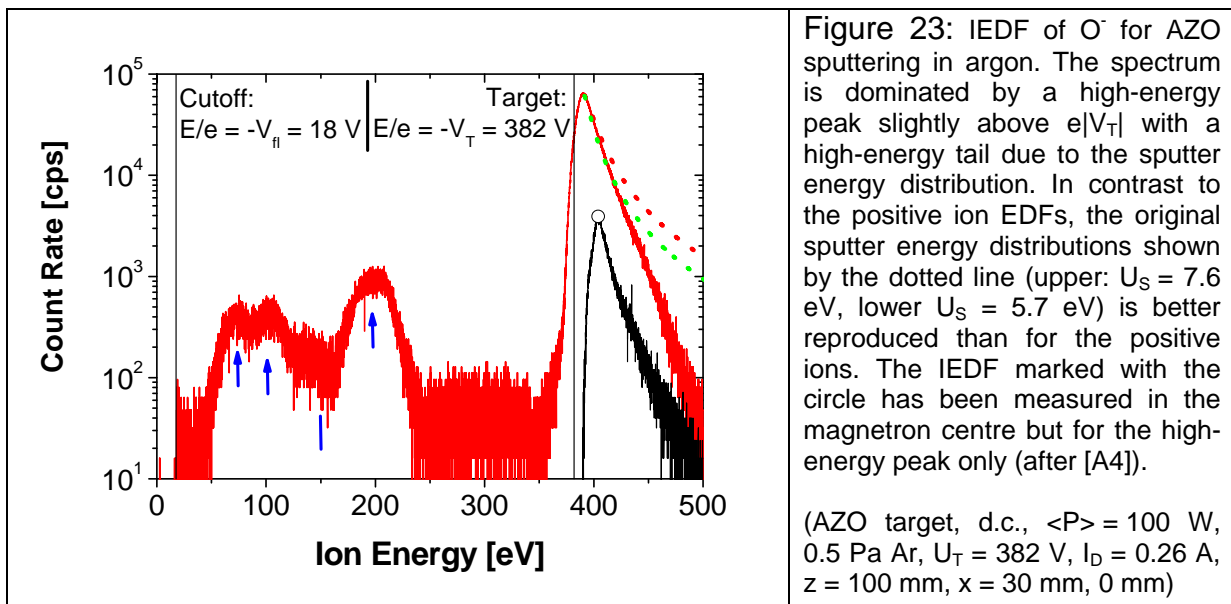
⁵ integrated up to 60 eV only to compare with the measured range

reduced energy [A4]. In fact, this has been found in the IEDFs with O^+ having an average energy 5.1 eV, Al^+ 3.0 eV, and Zn^+ 2.0 eV. Additional to the average energy the shape of the IEDF indicates a more effective thermalisation for a mass close to that of the working gas: Al^+ and Zn^+ showed a distinct low-energy peak and a weak high-energy shoulder whereas for O^+ the peak was much less developed [A4]. The lowest average energy was found for AlO^+ with 1.8 eV but here a comparison is difficult because the bonding energy of the molecule may change the original sputter energy.

While the IEDF of positive ions is mainly determined by V_{pl} and hence is comprised of low energetic structures below 100 eV, the IEDF of negative ions is very different. This is shown in Figure 23 for the IEDF of O^- obtained during non-reactive AZO sputtering in Figure 23 [A4]. The most significant feature is the main peak at very high energy of 390 eV. To obtain such a high energy, the O^- has to be formed at very negative potential. The energy corresponds to the negative potential of the target which was -382 V. The sharp flank to low energies implies that O^- is formed directly at the target and not somewhere in the target sheath where the potential is higher and its energy would be less. This formation is reasonable because in contrast to the very low electron density in the sheath the supply of electrons at the negative target is large so that an atom leaving the target can easily capture an electron given a positive electron affinity ($E_{aff} = 1.46$ eV for O). The effect will be enhanced by an easy release of electrons, i.e. a high γ_{iSEE} coefficient. This connection between negative ion formation and γ_{iSEE} has recently also been proven experimentally by Mahieu et al. [91]. Electrons are further captured by the oxygen in the dense bulk plasma and magnetic trap. The plasma potential in these regions is, however, not negative enough to extract those negative ions to a substrate or the PPM.

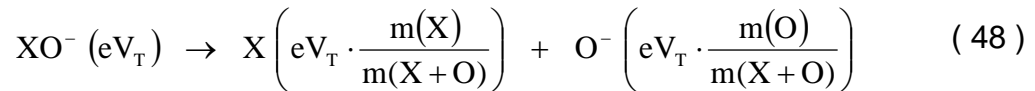
The high-energy peak exhibits an extended tail to higher energies. This is similar to the positive ions from the target material and indicates that O^- in its majority are no gas atoms that capture an electron at the target but that the O^- originates from O sputtered from the surface and therefore exhibits the typical sputter energy distribution. The difference to the positive ions is that the extension of the distribution for O^- to energies above the peak value resembles much more the original one (given as the upper dotted lines in Figure 23 for $U_S = 7.6$ eV published by Ellmer et al. [92] and for $U_S = 5.7$ eV after Malherbe et al. [4]). The reason is that positive ions

undergoing collisions will re-appear in their distribution at low energies thus enhancing the maximum that is already at the low energies. Negative ions losing a comparable percentage of the original energy (e.g. 400 eV) will - if at all - re-appear in the IEDF at much lower energies than the peak. It is, however, more likely, that the electron is stripped off upon collision or the ion is scattered off the detection direction.⁶ As the result, negative ions that collided are completely removed from the IEDF above the peak so that the remaining tail still represents the original sputter energy distribution. The deviation between the two simulated curves shows that for composite materials, where the surface binding energy is often not exactly known, the sputter distribution itself provides a significant uncertainty.



At the low-energy end of the IEDF, a sharp cut-off is observed. As mentioned above, this is caused by the floating entrance orifice which negative ions having E_0 less than the difference between V_{pl} and V_{fi} can not pass. The floating potential, in this case -18 V, can therefore be directly taken from the IEDF of negative ions. At moderate energies between 50 and 250 eV, the O^- IEDF exhibits weak but distinct peaks. The peak formation has no reason in the potential because there are no such localised potential minima in the discharge as shown in section 3.3.3. Instead, the peaks appear at energies that correspond to suspected larger negative molecules formed also at the target that are dissociated during their transit to the substrate [A4] into:

⁶ The scattering will also occur for positive ions. The result on the IEDF is, however, not as significant because due to their low energy they will be focussed into the PPM by the sheath, which the fast negative ions will be not.

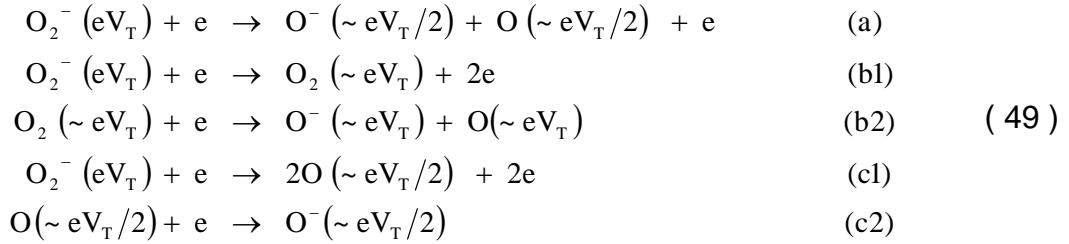


with X representing any combination of atoms and the kinetic energy of the particles given in parentheses. This suggestion of a fragmentation has been confirmed by a more detailed investigation of different negative ions in AZO sputtering (Figure 24). A similar argumentation has also been published by other authors [93, 94, 95]. Figure 24 clearly shows that the suggested fragmentation peaks are observed for many negative ions but their energetic position depends on the masses involved as indicated by the assignment to the parent molecules XO^- in the figure. Figure 24 reveals two other interesting results: there are very small amounts of Al^- because Al has a positive electron affinity of 0.441 eV but no Zn^- that is unstable [96]. Further, even rather complex molecules are present as Al_2O_4^- (measured directly and from a fragment) and Zn_2O_4^- (measured as a fragment only). As they either show up directly at the full energy corresponding to the target voltage or at fragmentation energies which require the full energy, they are all formed at the target, i.e. sputtering of such big molecules occurs and it is most likely that they are also formed in neutral states. Similar fragmentation pattern have been observed while sputtering a titanium target in oxygen atmosphere: signals of TiO_2^- and (very weak) TiO^- where measured directly while TiO_3^- and TiO_2^- could be deduced from fragment peak energies in the IEDFs of the smaller molecules [97].

Given the small acceptance angle of the PPM, the detection of such fragments require that they move almost perpendicular to the target surface as the accelerated parent molecules do. A fragmentation due to collisions with heavy particles (e.g. the working gas) can therefore be ruled out because the momentum transfer would alter the flight direction of the fragments, moreover, probably detaching the electron upon collision. The formation of the fragments without significantly changing their direction may proceed via autodissociation according to equation (48) when the molecule (XO) has a positive electron affinity but the negatively charged molecule (XO^-) which is formed at leaving the target is in a repulsive state. Lieberman reports that this is particularly likely for complex molecules and that the lifetime of XO^- may exceed 1 μs (e.g. for SF_6^-) [98]. This is in the order of the transit time of the fast negative ions in the magnetron discharge: an O_2^- ion with 400 eV needs 2 μs to cross the space to the substrate or PPM. Because the dissociation or attachment energies are much

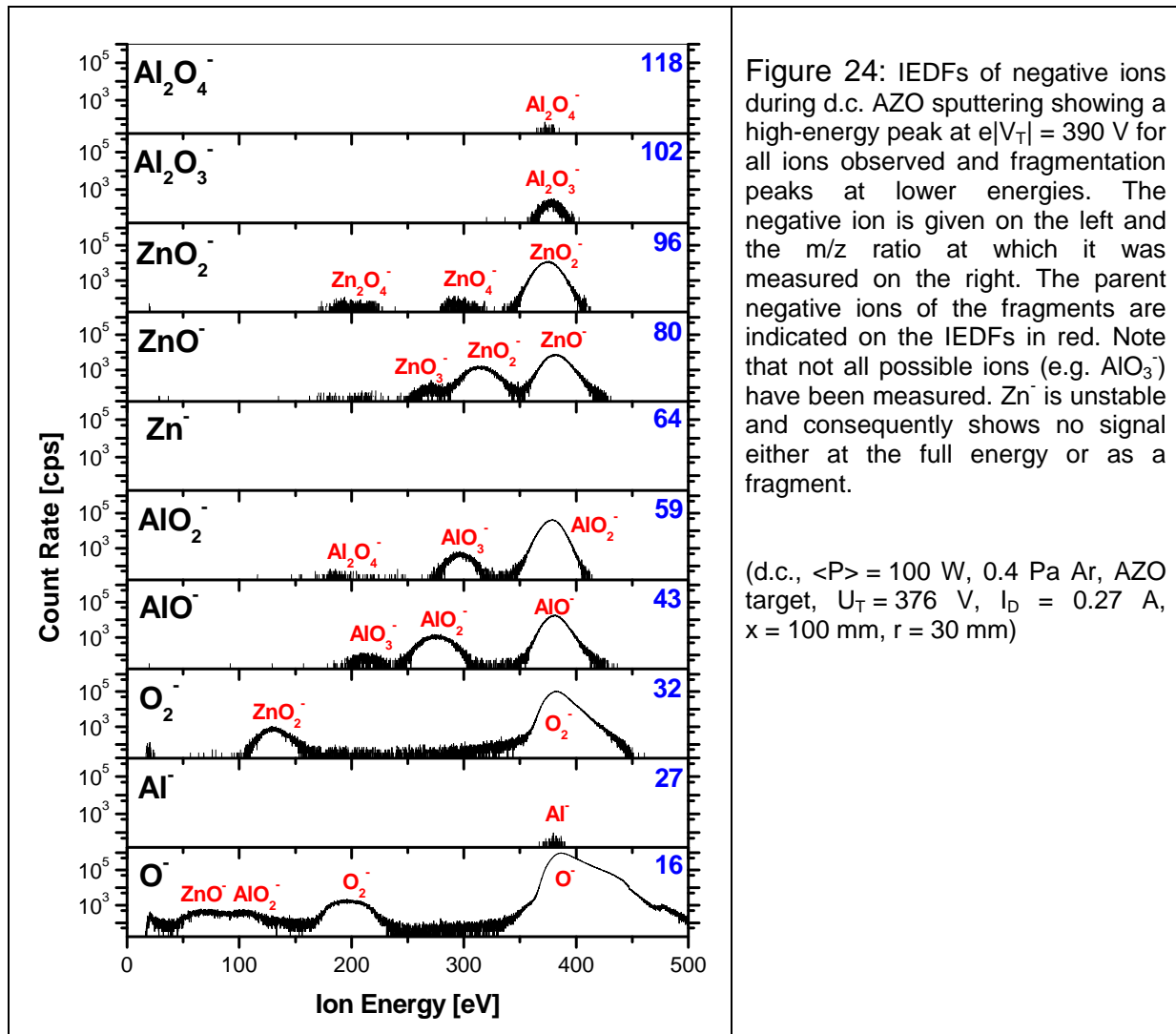
smaller than the kinetic energy of the molecule, the direction of the fragments is almost the same as for the autodissociated parent molecule.

The autodissociation scheme does not fit for the O_2^- molecule because it has no repulsive state [98]. The formation of negative fragments having the same direction that have been observed (Figure 24) then has to proceed via electron-impact processes:



Because the density of O_2^- is low compared to O^- [99] as observed here, almost no reaction data on O_2^- are available. Gudmundsson et al. [100] for $k_B T_e = 5$ eV give a rate coefficient for reaction (b2) of $3 \cdot 10^{-17}$ m³/s and for the reaction (b1), however for O^- and not O_2^- , of $2 \cdot 10^{-13}$ m³/s stating that this reaction is one of the main loss channels for O^- in oxygen discharges. As the energies involved in all the processes, are similar with $E_{\text{aff}}(O_2) = 0.4$ eV, $E_{\text{aff}}(O) = 1.5$ eV and $E_{\text{diss}}(O_2) = 5.1$ eV, $E_{\text{diss}}(O_2^-) = 4.1$ eV [98], it is likely that a mixture of them is responsible for the fragmentation of O_2^- and will also add to the fragmentation of the other molecules that have been observed.

It should be noted that traces of high-energetic ions reaching up to the equivalent to the full target voltage have even been occasionally found in the IEDFs of O^+ ions in oxygen discharges in this work. Because in d.c. discharges a plasma potential of several 100 V does nowhere exist, the origin of those positive ions has to be negative ions which are accelerated in the target sheath. Subsequent charge exchange in the plasma transforms them into positive ions. Because they are detected by the PPM with the small acceptance angle only electron collisions similar to those of equation (49) can be involved.



As shown in Figure 24, the integral count rate of O^- is much higher than for O_2^- by one order of magnitude [A4]. This relation has been observed consistently as soon as oxygen was present in the magnetron system. For instance, sputtering of Mg, in Ar/ O_2 or pure O_2 , however in pulsed mode, yields a factor of about 20 more O^- ion signal than for O_2^- . Figure 24 reproduces the situation with a target saturated in its oxygen concentration (AZO) sputtered in argon. Given sputtering mainly of atoms, a dominance of O^- against O_2^- could be expected. The situation, however, was not changed when the working gas was O_2 . Contrary, both O^- and O_2^- were reduced in intensity. This can be explained by a lower sputter yield of the reactive gas. The more important fact is that this behaviour shows that the negative ions originate from target and not from the gas perhaps reflected at the target surface. Otherwise, the intensity had to be increased in O_2 compared to Ar. Moreover, the extended tail of the high-energy peak in the O^- IEDF indicates that O^- is sputtered from the target and not only desorbed as speculated by Mraz [94] because for desorbed atoms the sputter energy

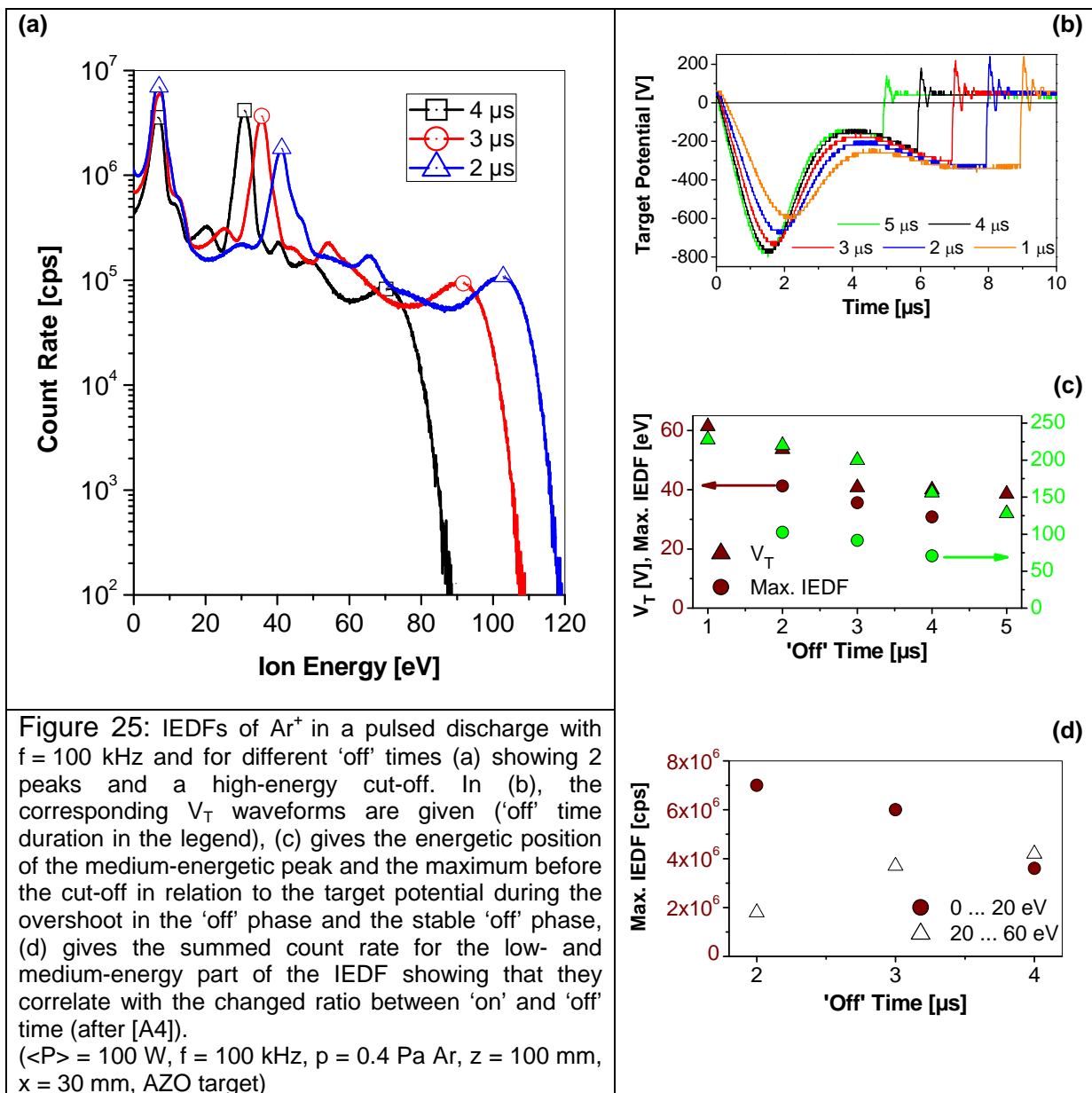
distribution which makes up the tail (see above) would be missing. For the Mg target, both O^- and O_2^- were increased when the gas composition was changed from $Ar/O_2 = 100/20$ to $0/100$ by a factor of two. This is supposed to be due to a more saturated target surface in its oxygen concentration.

Another important finding is the lateral inhomogeneity of negative ions impinging perpendicularly on the substrate. This has been investigated with different positions of the PPM relative to the magnetron axis making use of its small acceptance angle. Taking a value of 3° for this [88], only a circle of 5.2 mm diameter on the target is probed. The PPM has been placed such that it once probed the racetrack area and once the centre of the circular target, both for an AZO target sputtered in O_2 . The result was a 35 times increased flux of O^- ions opposite the racetrack compared to the centre that is shown in Figure 23. Given the acceleration of the negative ions perpendicular to the target due to the very thin sheath in front of it, a significant lateral inhomogeneity of the ion bombardment by high-energetic negative ions is expected at the substrate with a maximum along a circle opposite the racetrack. It can, however, not be excluded that other areas of the substrate are subject to bombardment with energetic ions or neutrals that are scattered out of the original "beam" and were not detected with the PPM [A4].

3.4.3. Pulsed magnetron discharges

V_{pl} and V_T mainly determine the ion energies at the substrate for the positive and negative ions, respectively, as shown in the previous sections. In pulsed magnetron sputtering, both quantities vary in time (section 3.2) so that the IEDFs are significantly changed. The result is shown in Figure 25a for Ar^+ during AZO sputtering [A4]. As in the d.c. discharge, there is a low-energy peak close to 0 eV which is dependent on the pulse parameters (here the 'off' time) in its intensity. In addition, another peak which is not observed in d.c. discharges appears at several 10 eV. For this one, the intensity and also its energetic position depend on the pulse parameters. As a third component, there is an extension of the IEDF to high energies even above 100 eV, which is dependent on the pulse parameters in its energy. To simplify the further discussion, the low-energy peak shall be addressed with (i), the medium-energy peak with (ii), and the high-energetic maximum with (iii).

The peak (i) can be attributed to ions born in the ‘on’ phase in which V_T is very negative and V_{pl} adjusts close to ground as described in section 3.3. V_{pl} does not significantly depend on the particular waveform of V_T in this phase (shown in Figure 25b) and so (i) is not shifted in its energy with the pulse parameters. Its intensity is, however, dependent on the duration of the ‘on’ phase – being inverse to the ‘off’ time length for the constant duty cycle of 0.6 - from which those ions originate. This is seen from Figure 25d.



Peak (ii) corresponds to ions from the stable ‘off’ phase where V_{pl} is elevated to positive potentials of several 10 V. Consequently, its intensity is proportional to the length of the ‘off’ phase (Figure 25d). The shift in its energy with the ‘off’ time is

explained by the changes of V_T in the 'off' time shown in Figure 25c: the longer the 'off' time is, the lower is V_T . As shown in section 3.3, V_{pl} follows V_T and so, according to equation (46), the ion energy is reduced. E_i is consistently lower than eV_T which is in agreement to the findings with the emissive probe that V_{pl} stays typically a few volts below V_T in the stable 'off' time.

Maximum (iii) has even higher energies than eV_{pl} in the stable 'off' phase. Its origin is therefore attributed to the V_T overshoot at the beginning of the 'off' phase that is connected to a very high positive V_{pl} (Figure 21). As seen from Figure 25c, the energy of (iii) and V_T (and consequently V_{pl}) have the same dependence on the 'off' time. However, E_i is much lower than eV_T would suggest. The reason is the short time, V_T and V_{pl} attain such high positive values – the heavy ions cannot receive the high energy before the sheath collapses again. A simple estimation shows this: assuming after section 3.3.3 that V_{pl} close to the substrate is only somewhat below to the positive value of V_T and that the electrons are almost immediately pushed away from a grounded surface, a matrix sheath with a linear potential drop of about 200 V (Figure 25b) remains. The width of the sheath for $n = 10^{10} \text{ cm}^{-3}$ and $k_B T_e = 5 \text{ eV}$ is 1.5 mm for simplicity assumed to be constant. Taking into account that V_T needs about 100 ns to develop (linear increase rate taken) its maximum value and so do V_{pl} and the sheath voltage, than an Ar^+ ion starting from the sheath edge would need 140 ns to reach the substrate or has only crossed 0.5 mm when the sheath starts to collapse again. Within this range, it will only acquire 70 eV instead of 200 eV, which is in agreement with Figure 25. The calculated energy may be slightly underestimated because of the neglected sheath expansion and the collapse time (again 100 ns) of the sheath. Nevertheless, ions cannot obtain the maximum sheath voltage energy but (see Figure 25c) the maximum energy increases with increasing overshoot potential.

The IEDFs described above exemplarily for the sputtering of a planar AZO target in argon are a general feature of the asymmetric-bipolar pulsed magnetron discharges and have been observed for all other planar systems investigated as well [101, 102]. The three maxima have additionally been observed by other authors in similar magnetron systems [103, 104, 105]. Misina and Karkari with co-workers [104, 106] and later Voronin et al. [87] were further able with a front-gating measurement

technique to "pin" the peaks observed to certain moments within the pulse. The shape of the IEDF is, however, not a feature of planar magnetron but has been observed similarly within this work also for asymmetric-bipolar pulsed rotatable cylindrical magnetrons [102, 107]. It should be noted that the IEDFs of Ar^+ are representative for all positive ions. To the IEDFs of ions formed from species sputtered from the target E_0 from the remnant sputter energy distribution is added as shown for the single peak in the d.c. case (cf. section 3.3.2) according to equation (46).

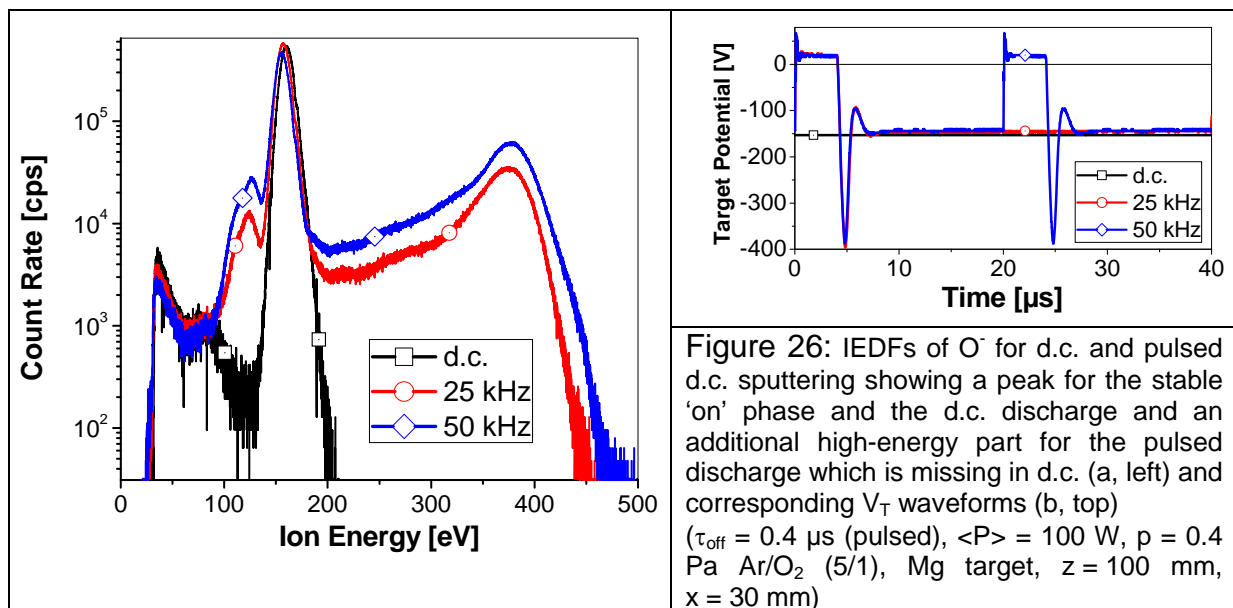
The high-energy parts on the IEDFs of the positive ions that are generated through the pulsing will increase the energy transferred to substrates at fixed bias potential (e.g. ground). They will have, on the other hand, no effect on the ion energies at floating substrates. These are given by equation (47). Because the floating potential follows temporal variations of V_{pl} in the order of the ion plasma frequency, the potential difference accelerating positive ions to the substrates will be at any time only given by the electron temperature, also in the 'off' time.

The IEDFs of the negative ions are also modified against those from the d.c. discharges. This has been recently published for AZO sputtering [101, 107, 108]. While in the d.c. discharges, a single peak corresponding to the target voltage with the high-energy sputter tail rapidly decreasing to zero is observed, in the pulsed discharges, the count rate of the ions again increases towards higher energy above the peak. It has been speculated that the d.c. like peak in the IEDF originates from ions from the stable 'on' phase while the higher energy ions are generated during the 'on' phase overshoot of V_T . A histogram of V_T supports this interpretation [107] which, however, suffers from the fact that the maximum detectable energy of the PPM is with 500 eV lower than $e|V_T|$ for the V_T minimum for AZO and many other materials.

The investigations have therefore been more thoroughly repeated with a magnesium target and Ar/O_2 atmosphere in fully reactive mode. This setup allows very small target voltages with even the peak V_T keeping above -500 V [A2] because of the high γ_{ISEE} coefficient of the oxide formed at the target surface [8, 11]. The resulting IEDFs of O^- for two different pulse frequencies and the comparison to the d.c. discharge are shown in Figure 26a. In the d.c. discharge a single high-energy peak is measured at

160 eV slightly above $e|V_T|$ of 153 eV due to the sputter energy distribution. The result thus confirms those of the AZO target (Figure 23). As soon as the discharge is pulsed, a higher energy extension additionally appears in the IEDF having its maximum at 380 eV almost exactly at $e|V_T| = 390 \dots 400$ eV (see Figure 26b) which is completely missing in the d.c. discharge. The slightly reduced energy is again due to the effect that the ions will not completely cross the sheath before it starts to collapse. The assumption is thus confirmed that in pulsed d.c. sputtering much higher energies of the negative ions occur because of the target potential overshoot in the 'on' phase and that those ions impinge on the substrate with about the energy corresponding to the full cathode fall voltage at the moment of the overshoot. The amount of these high-energy ions increases with the frequency as shown in Figure 26a because – as seen in Figure 26b – the very negative V_T is attained more often at higher frequency. The intensity of the middle energy peak at 150 eV is on the other hand almost unaltered at least for the low frequencies shown. A tiny shift to lower energy with increasing frequency corresponds to a change in the stable 'on' time V_T .

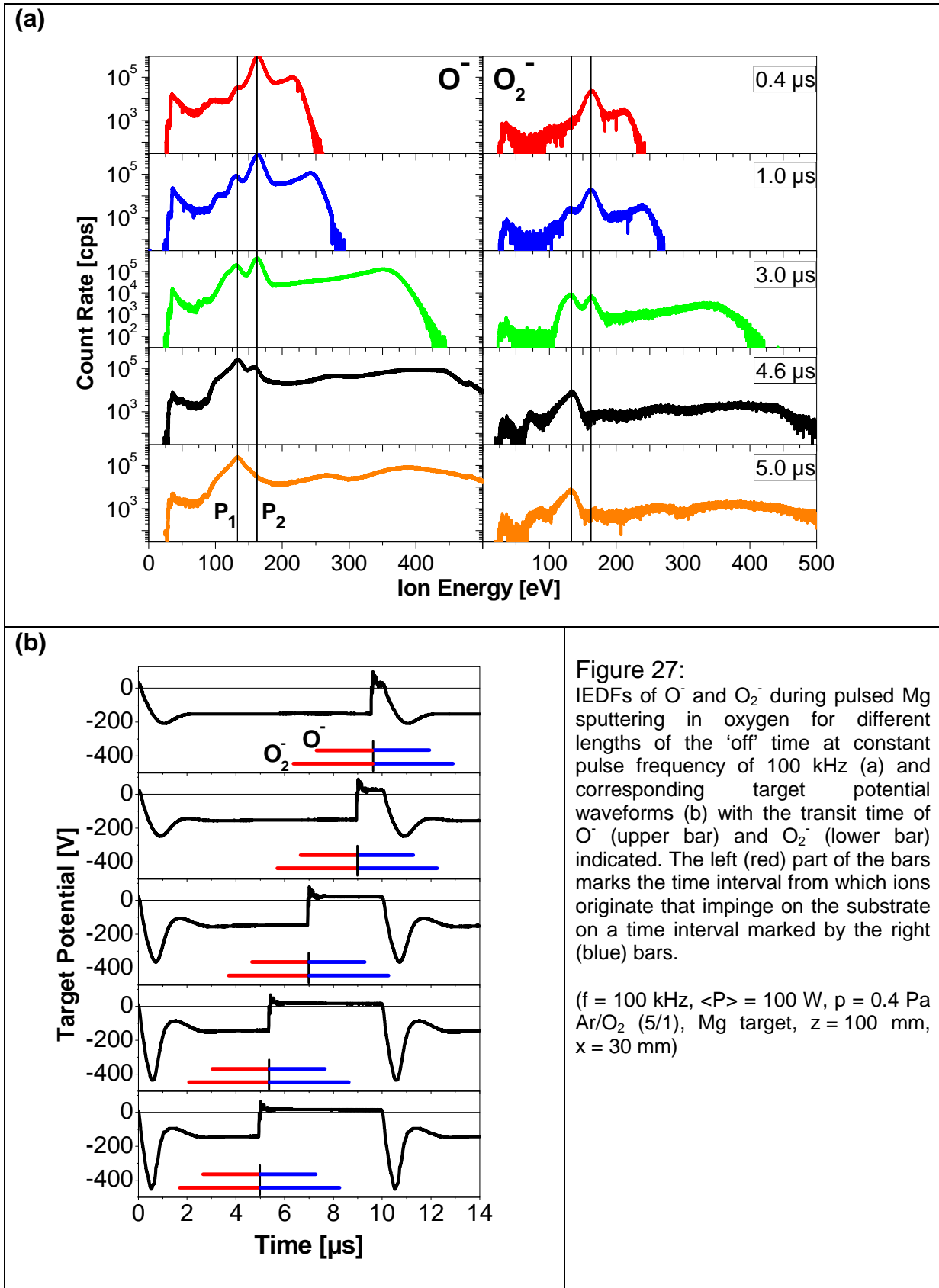
A striking new feature in the IEDF in pulsed mode is an additional peak below the main peak at 120 ... 130 eV which has no counterpart in the V_T waveform. This has been investigated in a separate set of experiments to identify its origin.



The low voltage magnesium sputtering in oxygen was used for these experiments, too. The frequency was fixed at its standard value of 100 kHz and the 'off' time was

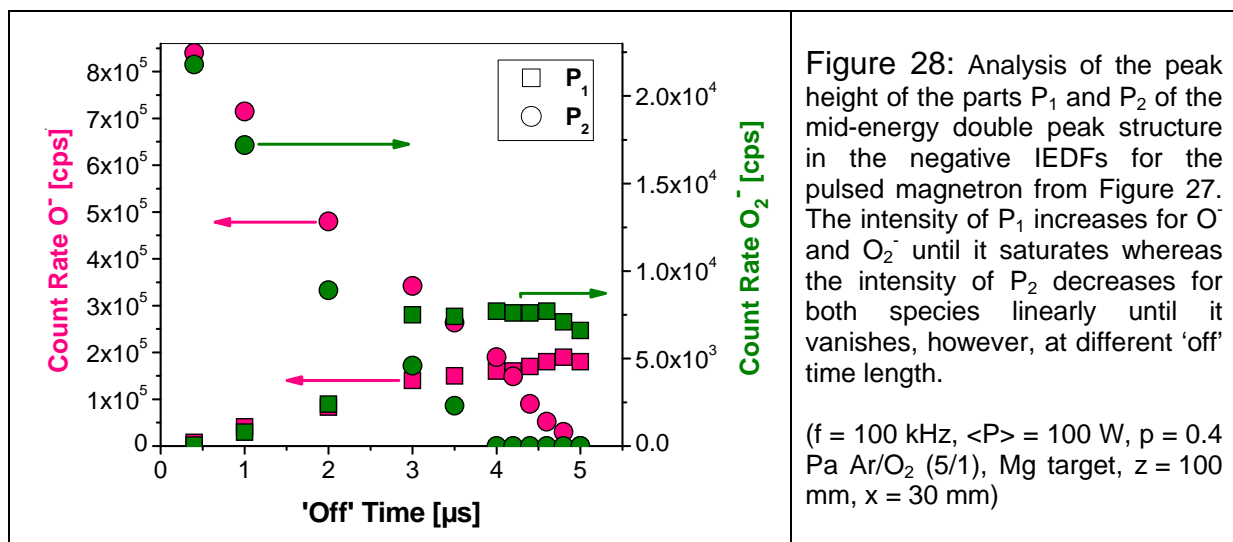
varied. IEDFs of O^- and O_2^- were taken for each pulse parameter set. Only selected examples which were all taken with the same settings at the PPM are shown in Figure 27a for a better visibility. For every 'off' time, the count rate of O_2^- is generally much lower than that of O^- confirming the results described above. In its form, the IEDFs of both species are similar: the high-energy end moves to higher energy with increasing 'off' time and there is a double peak structure at medium energy of about 130 eV and 160 eV with the first peak increasing but the second one decreasing with increasing 'off' time. Nevertheless, there is an important difference between O^- and O_2^- : the second peak vanishes for O_2^- for an 'off' time of 4.6 μs whereas it does for O^- at 5.0 μs .

To find an answer to the question why the energy of negative ions generated at the target surface during the stable 'on' phase - to which the medium-energy range belongs - splits up into two peaks, the target potential waveforms have to be analysed and the transit time of the ions through the discharge has to be taken into account. Taking an O^- ion that is accelerated to 160 eV in the very thin target sheath at the stable 'on' time, it will need 2.3 μs to cross the discharge and reach the substrate or the PPM. This means that O^- generated in the interval marked by the upper red bar in Figure 27b will not reach the substrate during the 'on' time but rather in the 'off' time - during an interval marked by the upper blue bar in Figure 27b. However, while moving through the discharge the potential of the target and simultaneously the plasma potential around the moving ion changes from ~ 0 V (stable 'on') to ~ 25 V (stable 'off') in this case. To reach a grounded surface during the 'off' time, the O^- then has to overcome an additional potential barrier and will be slowed down consequently impinging on the grounded surface with 25 eV less energy. This is almost exactly what is observed in the IEDFs in Figure 27a as an additional energy peak P_1 30 eV below the "main peak" P_2 . The peaks P_1 and P_2 change their relative intensity with the pulse parameters. The longer the 'off' time and consequently the shorter the 'on' time, the less becomes the P_2 intensity. This is better seen in Figure 28 and results from the fact that for decreasing 'on' time less ions generated during stable 'on' reach the substrate still in the 'on' time. For an 'off' time of 5.0 μs , all O^- ions generated in the stable 'on' time arrive at the substrate during the 'off' time (cf. Figure 27b) and consequently P_2 completely vanishes.



The trend is different for the low-energy peak P_1 (Figure 28). From long 'off' times down to $2.3 \mu\text{s}$ all O^- generated during the last $2.3 \mu\text{s}$ of the 'on' time arrives at the substrate during the 'off' time and thus P_1 exhibits a rather constant intensity. When the 'off' time is chosen even shorter, some of the ions (starting from those generated at the very end of the 'on' time) experience a second plasma potential change down to $\sim 0 \text{ V}$. That means they arrive at the substrate within the subsequent 'on' time and are not decelerated and thus do not add to P_1 . P_1 is therefore reduced to very short 'off' times more and more.

The only difference for the measurements of O_2^- is the ion mass being twice that of O^- . The consequently increased transit time of $3.2 \mu\text{s}$ is represented by the lower bars in Figure 27b. As shown in Figure 27a and Figure 28, the behaviour is almost identical to O^- with the exception: peak P_2 vanishes not at $5.0 \mu\text{s}$ 'off' time but at $4.0 \mu\text{s}$ instead because the time interval from which the ions are transferred to the 'off' time is longer for O_2^- . Consistently, the range of saturated P_1 should begin at longer 'off' times for O_2^- that is, however, not seen in Figure 28 because 'off' times between $3.0 \mu\text{s}$ and $2.0 \mu\text{s}$ have not been measured.



The investigations have shown that the IEDFs are much more structured in pulsed magnetron discharges than in d.c. ones. This holds for both, positive and negative ions. However, one has to distinguish between an effect on floating or fixed bias substrates. For fixed bias substrates such as grounded ones, all modulations leading to high-energy extensions will be important because V_{pl} determines the ion energy onto the substrate only. When the substrate is insulated, its V_{fl} will follow changes in

V_{pl} and the modulations of the IEDF against ground due to V_{pl} will have no significant effect. This is the case for the high-energetic positive ions and the observed peak splitting for the negative ions. High-energetic ions with energies corresponding to the full cathode fall voltage and its overshoot will affect both floating and fixed substrates.

3.5. Summary of fundamental properties

Pulsed magnetron discharges were introduced in coating technology to avoid arc formation during the deposition of dielectrics by the neutralisation of surface charges due to the modulation of the target voltage. The results presented in this thesis demonstrate that the potential modulation of the target as the most important electrode for the magnetron discharge significantly changes its properties as well so that pulsed discharges significantly differ from their d.c. equivalent. The density of the charged particles and hence their current to the substrate as well as the potentials and ion energies to the substrate are altered and modulated according to the temporal variation of the target voltage.

The most intuitive reaction is the modulation of the potential of the discharge. It follows changes of the target potential rapidly on the time scale of the electron plasma frequency at any moment. In phases of negative target potential, the plasma stays close to ground potential due to the surrounding walls. For positive target potentials, the plasma adjusts close to that positive value. As known for d.c. discharges, the plasma hence couples to the electrode with the most positive potential. This has the important consequence for bipolar pulsing that high positive values of the plasma potential are temporarily obtained. Due the overshoots of the power supply during the switching to the 'off' phase this can not be prevented. It has been shown that the plasma is lifted to such high values within the whole volume extending to the substrate.

The temporarily very high positive plasma potential has two consequences. First, the discharge is subject to high energetic electrons from the substrate and wall sheaths in the early 'off' phase. Second and important for film deposition, positive ions are accelerated to substrates at ground potential and may cause radiation damage with

energies exceeding 100 eV. Even for deposition on insulating substrates, the high potential has to be taken serious because the grounded walls can be sputtered resulting in impurities.

Generally, the rapid potential changes during the switching between the pulse phases give rise to transient phenomena caused by the acceleration of the charge carriers – especially the electrons. This is particularly the case for the charge carrier density development in the ‘on’ phase. Here, two sharp peaks are formed at its beginning before the discharge begins to transform into a stationary state. For the peaks, a simple general model of the discharge build-up has been developed which relies on homogeneously distributed charges at the end of the ‘off’ time of the last pulse. At first, the remaining electrons are accelerated through the discharge. The resulting high energies could not be observed with the double probe in this work but have been frequently reported in the literature. However, the high energetic electrons cause an ionisation maximum that is observed as a density peak. Subsequently, the second peak is caused by high energetic secondary electrons from the cathode which are released by the slower ions. The second effect is enhanced by a simultaneous target voltage peak.

The generation of fast electrons in the early ‘on’ time which precedes the density peaks, however, gives rise to an increased heat flux to substrates even at floating potential with increased pulse frequency.

The combination of these two fundamental processes together with the amount of residual charges that depends on the length of the ‘off’ time complicates the comparison of different magnetrons, i.e. the results of different groups. A general finding, which is consistent to the literature, is that for very long ‘off’ times, the re-establishment of the discharge in the ‘on’ phase occurs on a considerably long time scale. Because the required duration of the ‘off’ time is determined by the surface charge neutralisation, the only possible method to speed up the discharge development is to provide an independent d.c. source of charge carriers.

Optical emission confirms the results of the charge carrier density peaks during the ‘on’ time. Additionally, information on the electron energies have been obtained with

it. Most importantly, the origin of a peak at the start of the 'off' phase could be ascribed to momentary high-energy electrons accelerated in the substrate sheath enhancing the excitation in the substrate region. A temporal delay of the emission against the charge carrier density indicated a significant density of metastable argon atoms in the discharge. These affect the emission of most argon lines because they are subject to indirect excitation. As a result, the line at 750.4 nm has been found the only intense signal to correctly reproduce the density development of the pulsed discharge.

The global potential modulation leads to additional high ion energies not present in d.c. discharges. Generally, for the ion energies which are practically of most interest at the substrate, it has to be differentiated between positive and negative ions because their origin is physically very different. Positive ions that impinge on the substrate are formed in the plasma and their energy is determined by the plasma potential. Negative ions originate in their majority from the target and their energy is hence determined by the target potential. However, because both potentials are significantly modulated in pulsed discharges the energy distributions of both ion types exhibit more complex shapes than for d.c. discharges.

Positive ions shown an additional energy peak compared to d.c. at several 10 eV which is due to the stable 'off' phase plasma potential. The energy distribution further extends to about 100 eV because of the potential spike at the beginning of the 'off' phase. For the positive ions which are formed from sputtered atoms, all structures in the energy distribution are always broadened to higher energy due to the initial energy of the sputter energy distribution. An important fact is that the additional energy peak in pulsed discharges will have different influence on grounded or floating substrates. They will contribute significant additional energy to grounded substrates. However, this is not the case for floating substrates as the substrate potential follows change in the plasma potential.

This is different for the negative ions. Those are generated in the 'on' time at the target gaining high energy in the target sheath of several 100 eV. Because the floating potential is not connected to the target potential, the ions impinge on grounded and floating substrates as well with their high energy. This has the

consequence that in pulsed sputtering with overshooting target voltage extremely high ion energies occur of up to the full overshoot voltage equivalent. These can even exceed 1 keV. The direct flux of negative ions has further been demonstrated to be very inhomogeneously distributed at the substrate being most intense opposite the magnetron race track which may lead to local change in the film properties and local damage.

The transit time of the negative ions from the target to the substrate results in a further diversification of their energy spectra. This is due to the similarity of the time-of-flight and the pulse period. Sudden changes of the local plasma potential along the ion path lead to deceleration or acceleration of the ions in the substrate sheath. The effect which was first observed within the frame of this thesis by a peak splitting may be particularly important for deposition onto fixedly biased substrates by shifting the ion energy.

4. Dependence on operation parameters and magnetron configuration

4.1. Introduction

The fundamental properties discussed in the previous section are subject to many parameters that can be adjusted on a pulsed magnetron deposition process. One set of those, the pulse parameters like pulse frequency and 'off' time have been dealt with in the previous section. This section will concentrate on the influence of parameters which are of technological relevance. These are partly determined by the desired film material itself like target material or working gas atmosphere or by the deposition chamber setup like the position of the substrate holder. They may also be rather easily accessible in process engineering like the gas mixture, gas pressure, or the electrical potential, especially of the substrate holder. All these parameters are known to influence d.c. magnetron discharges and should have an effect on the physical properties of pulsed discharges as well.

4.2. Target material and reactive gas

The two mechanisms that sustain a discharge are the volume ionisation by fast electrons (α -process) and the ejection of secondary electrons from the cathode (γ -process) by ion bombardment (cf. section 2.2). The target materials – or more exactly the surface of the targets - which may have very different ion induced secondary electron emission coefficients (γ_{iSEE}) therefore play an important role in the characteristics of d.c. and pulsed discharges. In table 3, the operating voltages and currents for d.c. and pulsed discharges displayed by the power supplied are summarised for different target materials used in this work both in inert (Ar) and reactive (Ar/O₂ or O₂) ambient. The compilation shows three important facts, which will be discussed in the following.

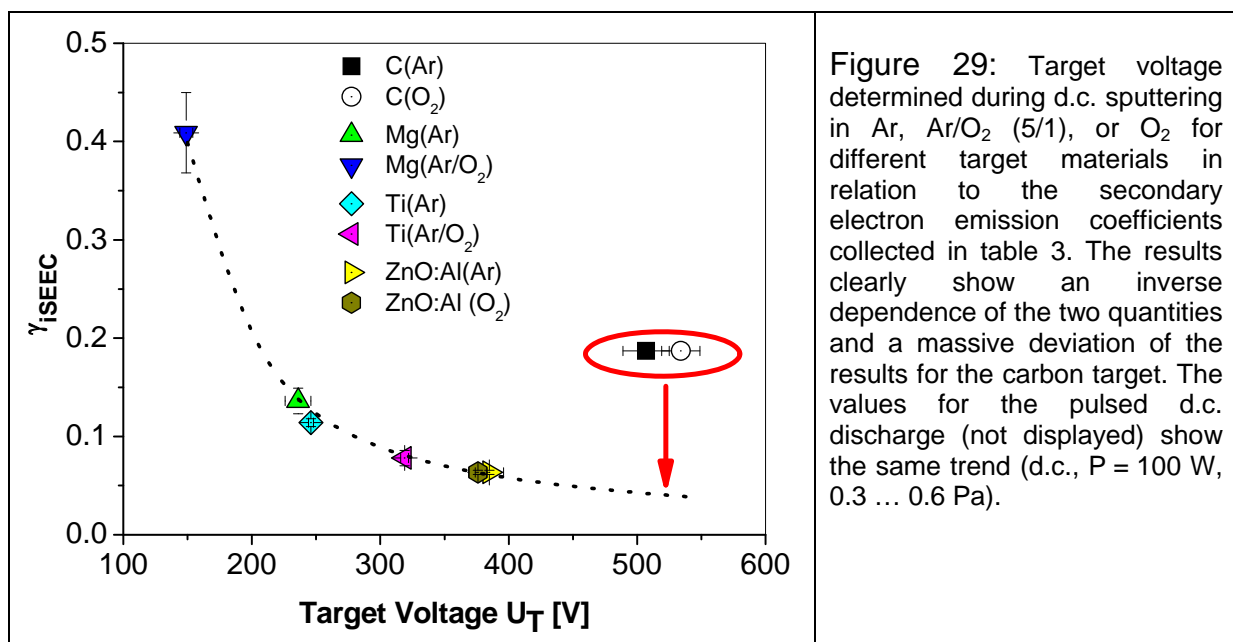
| | | DC power supply Advanced Energy MDX 1.5k | | Pulse power supply AE Pinnacle Plus 5k | |
|-----------------------|---------------------------|---|---|---|---|
| | | Ar | Ar/O ₂ or O ₂ (*) | Ar | Ar/O ₂ or O ₂ (*) |
| C | U_T [V] | 507 ± 18 | 534 ± 15 | 244 ± 22 | 234 ± 6 |
| | I_D [mA] | 197 ± 5 | 187 ± 5 | 410 ± 34 | 427 ± 11 |
| Mg | U_T [V] | 236 ± 10 | 149 ± 5 * | 152 ± 2 | 98 ± 8 * |
| | I_D [mA] | 424 ± 17 | 671 ± 22 * | 658 ± 9 | 1020 ± 77 * |
| Ti | U_T [V] | 246 ± 2 | 319 ± 3 * | 145 ± 2 | 153 ± 6 * |
| | I_D [mA] | 407 ± 3 | 256 ± 2 * | 690 ± 9 | 654 ± 25 * |
| ZnO:Al (2 wt%) | U_T [V] | 383 ± 11 | 378 ± 7 | 186 ± 1 | 188 ± 2 |
| | I_D [mA] | 263 ± 7 | 265 ± 5 | 538 ± 3 | 532 ± 6 |

Table 3: Target voltages U_T and discharge currents I_D displayed by the power supplies for four target materials in d.c. and pulsed magnetron discharges sputtered with inert and reactive working gas. The values were obtained in the pressure range between 0.3 Pa and 0.6 Pa with very similar magnetron sources. All discharges were operated in power-controlled mode with a nominal discharge power of 100 W. The pulsed discharges were run with a frequency of 100 kHz and 4.0 μ s 'off' time.

(1) For argon sputtering in the d.c. mode, different target voltages are obtained for the target materials. Because all discharges were operated under otherwise similar conditions, the influence of the volume ionisation (α) is negligible and the various target voltages are a consequence of different electron ejection into the discharge from the target (γ). In fact, when comparing U_T from table 3 with the γ_{iSEE} coefficients from table 1, Mg and Ti with the highest γ_{iSEE} produce the lowest U_T while it is higher for ZnO with a much lower γ_{iSEE} . This corresponds to a relation proposed by Thornton that $U_T \propto 1/\gamma_{iSEE}$ as shown by Depla et al. [7, 109]. The relation is shown in Figure 29, which also includes the data from the reactive ambient. The carbon target exhibits the highest U_T indicating a very low γ_{iSEE} , which is not in agreement with the literature data (table 1). As Figure 29 shows, the U_T values are way off the $1/\gamma_{iSEE}$ dependence of all the other discharges. The data taken from [6] are therefore doubtful. The own results suggest a γ_{iSEE} for carbon in the range of 0.04 instead of 0.187.

(2) When the discharge is operated in reactive gas, the target voltage in the case of Mg and Ti is altered due to the formation of an oxide layer on the target surface and a corresponding change in γ_{iSEE} . MgO has very high γ_{iSEE} causing U_T to drop dramatically with a simultaneous increase in I_D to achieve the set nominal power. The behaviour of the Ti target is reversed because γ_{iSEE} of the oxide is lower than that of the metal. Both reactive discharges were operated with 20 % of the total gas flow being oxygen that was enough to be in fully reactive mode of the target so that the target should be close to stoichiometric oxide and the γ_{iSEE} is reasonable. The relation of U_T to γ_{iSEE} is also given for the reactive processes in Figure 29. Clearly, U_T

for ZnO:Al and C does not change significantly when reactive gas is inserted because there is no oxide formation for the carbon and ZnO:Al was stoichiometric oxide even when sputtering with argon. Consequently, γ_{iSEE} does not change. It is important, however, to note the constancy of the target voltage although operating in 100 % O_2 in these cases. This means that the volume ionisation (α -process) is not significantly different between both Ar and O_2 . This offers the possibility to independently study the influence of γ_{iSEE} on the plasma parameters within a pulse by selecting a proper target material as Mg with a big difference between γ_{iSEE} for the metal and the oxide, which will be demonstrated later.



(3) The U_T and I_D values displayed for the pulsed mode show the same trends for (1) and (2) but consistently lower U_T and higher I_D are observed resulting in the set power of 100 W. This is at first surprising because α and γ are expected to be the same for the same combination of magnetron, target, and gas mixture. To understand the difference, the operation of the pulsed power supply and the dynamic response of the plasma have to be considered. The values displayed on the Pinnacle Plus power supply are those of the output of the integrated d.c., U_{dc} and I_{dc} . The subsequent pulse unit transforms these values into those delivered to the plasma between cathode and anode, U_{plas} and I_{plas} [110]. For a rectangular output waveform, the relations between the quantities are connected with the duty cycle

$$U_{\text{plas}} = \frac{U_{\text{dc}}}{\eta} \quad (50)$$

$$I_{\text{plas}} = \eta I_{\text{dc}}$$

During the 'off' time the circuit of the Pinnacle Plus is optimised to produce a small voltage of 10% of that in the 'on' time with different polarity. Furthermore, the current in the 'off' time is close to zero so that

$$I_{\text{plas}} = \eta I_{\text{on}} + (1 - \eta) I_{\text{off}} \sim \eta I_{\text{on}} \quad (51)$$

Given the requirement that the output power (neglecting losses) has to be that of the d.c. power supply

$$P_{\text{dc}} = U_{\text{dc}} I_{\text{dc}} = U_{\text{plas}} I_{\text{plas}} = P_{\text{plas}} = \eta P_{\text{on}} + (1 - \eta) P_{\text{off}} \approx \eta P_{\text{on}} \quad (52)$$

and combining (50), (51), and (52) one obtains

$$U_{\text{on}} \sim \frac{U_{\text{dc}}}{\eta} \quad (53)$$

$$I_{\text{on}} \sim I_{\text{dc}}$$

Taking the voltage display value (U_{dc}) of the pulsed discharges from table 1 and applying equation (53) for the duty cycle of 0.6 used there one comes up with nearly the value which is obtained for the corresponding d.c. discharge in any case. The effect of the duty cycle is more clearly seen in Figure 30a for the Mg target in the reactive gas mixture, when the pulse frequency was varied at constant 'off' time, i.e. the duty cycle was changed from 0.5 to 0.96 and compared to the d.c. discharge. While U_{ps} is decreasing with the frequency, the voltage delivered during the 'on' phase, U_{on} , stays constant at the value for the d.c. discharge (Figure 30a). Simultaneously the current I_{on} increases thus increasing the power P_{on} delivered in the 'on' phase. The fact that during the 'on' time U_{on} is almost constant while I_{on} changes with frequency contradicts the usual conception developed by Thornton that for a particular magnetron the current I_{D} is related to the target voltage U_{T} by [18]

$$I_{\text{D}} = c U_{\text{T}}^n \quad (54)$$

with c and n being fixed parameters at constant operating conditions except of the electrical parameters. To look at this more closely, the waveforms of V_{T} , I_{D} , and P_{D} for a very low frequency, i.e. closest to the d.c. magnetron, are shown in Figure 30b. After the overshoot at the beginning of the 'on' time, which has settled 3 μs after its start, U_{on} maintains a constant value while $|I_{\text{on}}|$ is continuously decreasing from 0.84 A above the d.c. values I_{DC} (0.67 A) but finally dropping below (0.6 A) that.

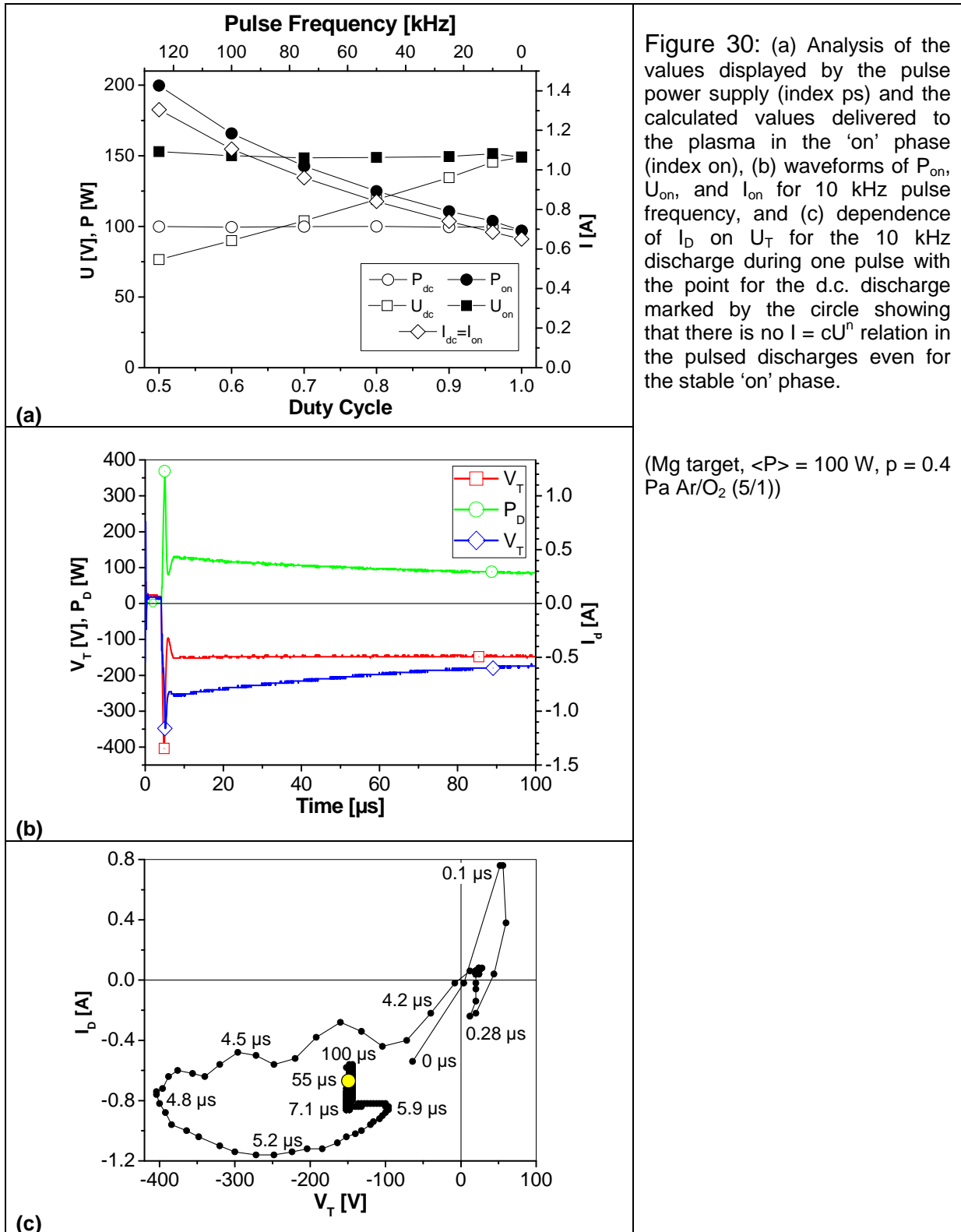


Figure 30: (a) Analysis of the values displayed by the pulse power supply (index ps) and the calculated values delivered to the plasma in the 'on' phase (index on), (b) waveforms of P_{on} , U_{on} , and I_{on} for 10 kHz pulse frequency, and (c) dependence of I_D on U_T for the 10 kHz discharge during one pulse with the point for the d.c. discharge marked by the circle showing that there is no $I = cU^n$ relation in the pulsed discharges even for the stable 'on' phase.

(Mg target, $\langle P \rangle = 100$ W, $p = 0.4$ Pa Ar/O₂ (5/1))

The complex relationship between U and I is best seen from Figure 30c where I_D is plotted against V_T for every time within the pulse. During the first part of the 'on' time (4 μ s to 7 μ s) where the remnant charges are accelerated and the sheaths form, the discharge is far from a stationary state and the I-V plot shows a hysteresis-like shape. Nevertheless, even when V_T has settled indicating a stationary state, this is

not reached with I_D still drifting. The important consequence from these investigations is that the I-V characteristics of magnetrons with pulsed power supplies even with long 'on' times cannot be described with Thornton's relation for d.c. magnetrons.

As mentioned in (2), γ_{iSEE} is changed between metals and their oxides that form on the target surface. Simultaneously (cf. table 1), the sputter yield of metals and their oxide is different. This leads to the effect that the discharge is switched between the metal mode and reactive mode very rapidly as shown in Figure 31a,b for the target voltage and discharge current when the oxygen flow is varied. The reason for the rapid change is the decreasing gettering of oxygen when the target becomes oxidised and – due to the decreased sputter yield of the oxide – much less metal atoms are released. The consequence for reactive sputtering is that in uncontrolled operation with a fixed flow of O_2 (Figure 31) a hysteresis occurs and stable sputtering is only possible in the range left to the hysteresis (metal mode) or right to it (reactive mode). The modes are different in their electrical discharge parameters U_T and I_D , an effect that has been discussed for table 1. It is reproduced in the I-U characteristics in Figure 31 for 400 W nominal power: the transition to the reactive mode is accompanied by an increase of the discharge impedance for Ti but a strong decrease for the Mg target, corresponding to the different γ_{iSEE} . The sudden change in the plasma impedance is observed for the argon lines in OES, too (Figure 31c,d). According to equation (39), the emission line intensity is proportional to $n_g n_e$. While n_g for Ar is barely changing within the hysteresis flow range, n_e that is roughly proportional to I_D changes: following γ_{iSEE} the Ar intensity is increased in the reactive mode for Mg but decreased for Ti. Further changes in the reactive mode result from the altered Ar density because Ar is replaced by O_2 . Simultaneously (only measured for Mg), the O signal rises.

Important is the signal change of the metal emission line because for its intensity both n_g and n_e change upon mode switch. The sputter yield is in most cases lower for the oxide than for the metal [111]. The change in n_e follows γ_{iSEE} . Figure 31 reveals that in the case of Ti and Mg the metal intensity is always much lower in the reactive mode, because for Ti both Y (by a factor of 5) and γ_{iSEE} (1.5) decrease. In the case of Mg the decrease in Y (factor of 9) and n_g overcompensates the parallel increase in γ_{iSEE} (3) and n_e . The effect of the strongly decreasing metal emission intensity has

been used for many years for the active control of the reactive sputtering process with plasma emission monitors; PEM [112, 113]. This provides the possibility to operate the discharge within the range of the hysteresis curve with the profit that high yields and high deposition rates (the metal mode characteristic) and the deposition of stoichiometric oxides at the substrate (the reactive mode characteristic) can be combined. The strong gradient of the metal emission is typically used with this technique to adjust its value to a certain setpoint. Deviations from this setpoint are immediately compensated by an adjustment of the reactive gas flow. Doing so, a working point along a line within the hysteresis can be stabilised.

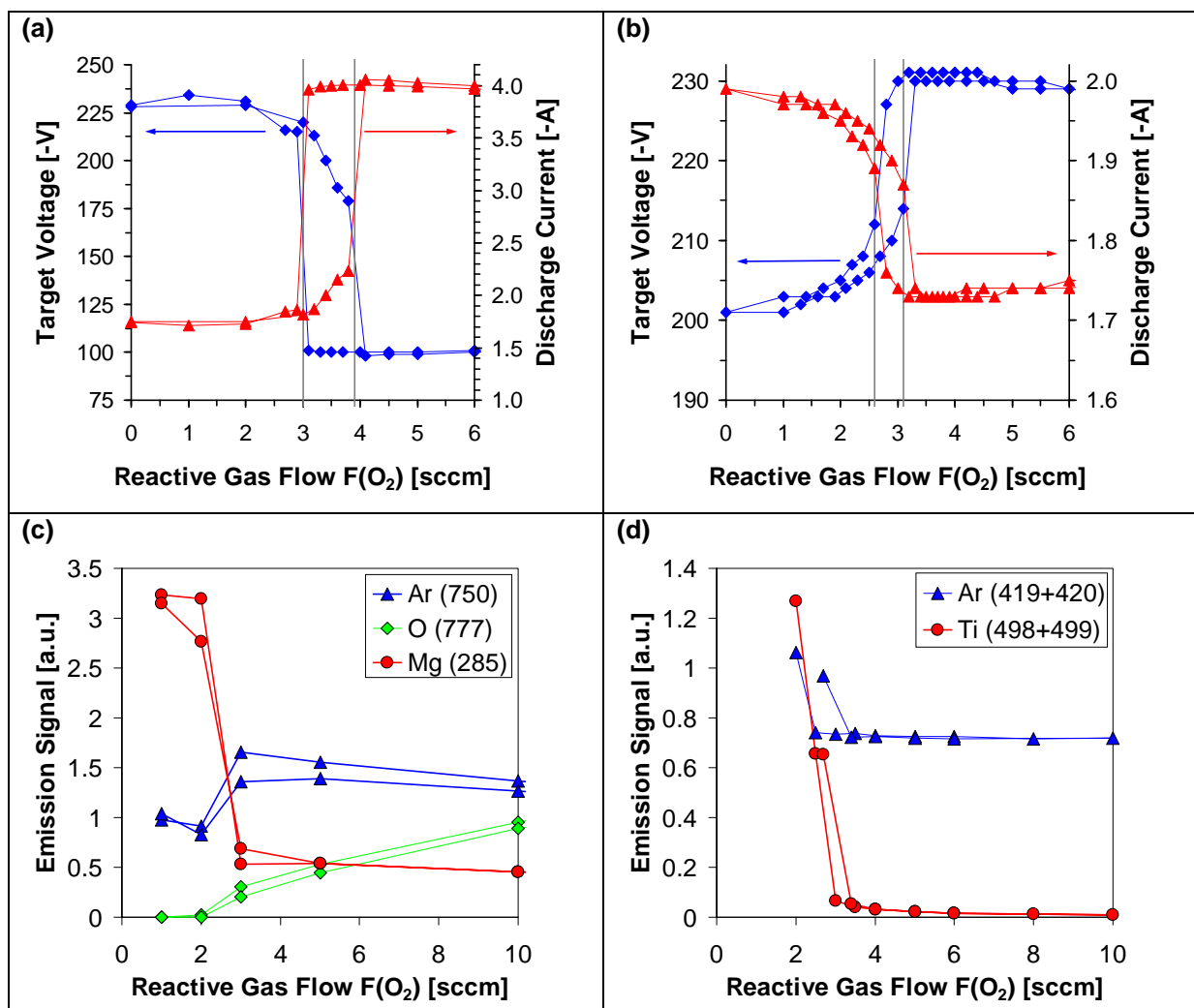


Figure 31: Hysteresis behaviour of U_T and I_D during reactive sputtering of Mg (a) and Ti (b) following the changes in γ_{iSEE} between the metal and the oxide and changes in optical emission intensities for the transition additionally representing the changes in Y . Note that the hysteresis itself is not resolved in the OES results due to poor flow resolution during the measurements. Wavelengths of the emission lines are given in parentheses in the legend.

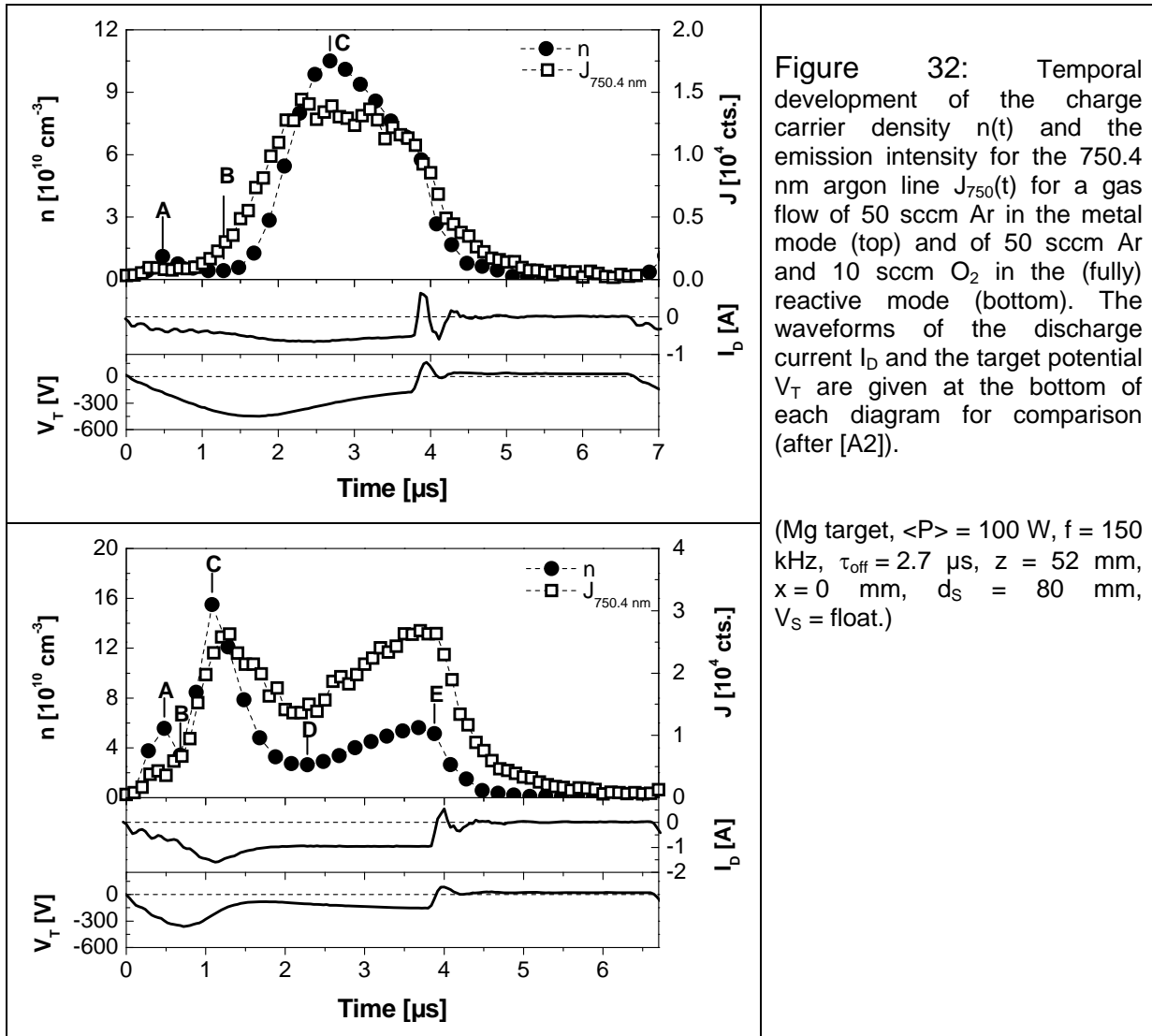
($\langle P \rangle = 400$ W, $f = 100$ kHz, $\tau_{off} = 4.0$ μ s, $F_{total} = 100$ sccm, $p = 0.4$ Pa, $z = 52$ mm)

Although the method is widely used nowadays, it is not suited for every material, which is explained by the two concurring processes depending on Y and γ_{iSEE} . The procedure works as long as the metal emission intensity is a monotonic function of the sputtering yield for reactive gas flow changes, at best with a very steep gradient. If, however, the yield change is not dominating over a γ_{iSEE} change in the opposite direction, the PEMs will fail. Such failure has been reported for SnO_x [114]. Zinc, in fact has a very low metal sputter yield difference between 0.8 (metal) and 0.5 (oxide) according to Yamamura's formalism (cf. sect. 2). Own works on MgO with counteracting Y and γ_{iSEE} dependence proved a difficult control that had to be optimised for a dual magnetron [115]. TiO_2 processes with the γ_{iSEE} dependence supporting that of Y on the other hand are easily controlled with a PEM [116].

The global change of the U-I characteristics of the discharge (2) due to changes in γ_{iSEE} affects the temporal development of U_T , I_D , and the plasma parameters as the charge carrier density as well. This has been investigated in this work and was published for the system Mg/MgO that has the most different γ_{iSEE} between the metal and the oxide [A2]. The temporal development of $n(t)$ together with that of the Ar emission intensity of the 750.4 nm line $J_{750.4}(t)$ is presented in Figure 32 for the metal mode and in one example for the reactive mode. In the reactive mode, similar courses as given in Figure 9 are observed: a strong maximum C both in $n(t)$ and $J(t)$ slightly more than 1 μs after the initiation of the 'on' time and a weaker maximum A about 0.5 μs after the initiation which is hardly seen in the OES. The second maximum coincides with the peak in the discharge current which is somewhat delayed to the target voltage peak. For the metal mode, A is not significantly altered. The maximum C, however, appears much later than in the reactive mode and is broader which has the consequence that during the duration of the 'on' time of 4.0 μs the subsequent minimum D and the increase to E at the end of the 'on' phase are not seen in the metal mode. Simultaneously, U_T and I_D are delayed and especially their peaks shift to later times. A closer inspection of these appearance times for a wider range of gas mixtures (Figure 33) reveals that there is a sharp transition at the change from metal to reactive mode rather than a continuous one. The reason is the enhanced production of secondary electrons in the reactive mode. Due to their higher current, the power supply (operated in power controlled mode) is able to drive the discharge current necessary to establish the required power with less voltage at the

target. Given a similar increase rate of the target voltage, the necessary voltage to obtain the current is hence earlier reached and the voltage subsequently reduced. It thus forms its peak responsible for the maxima C earlier so they also appear quicker. Figure 33 shows exactly this behaviour as all maxima belonging to C are dramatically quickened in the reactive mode. It is important to note that the fundamental reason for the faster development of the discharge within the pulse leading to almost reaching a quasi-stationary state at the end of the 'on' phase is the increase of γ_{iSEE} in the reactive mode but that the faster development itself is a consequence of the reaction of the power supply and its output characteristic. There is even a slightly higher increase rate of the target voltage to its maximum in reactive mode reflecting the feedback of the plasma to the power supply [A2]. The average charge carrier density in the reactive mode is only up to 20% higher than in the metal mode accounting for the power control of the power supply: instead of a dramatically increased n through γ_{iSEE} , the driving voltage is simultaneously reduced (cf. table 1). This has the additional effect that the ion energies at the substrate are reduced for high γ_{iSEE} – which has been used in section 3.4.3.

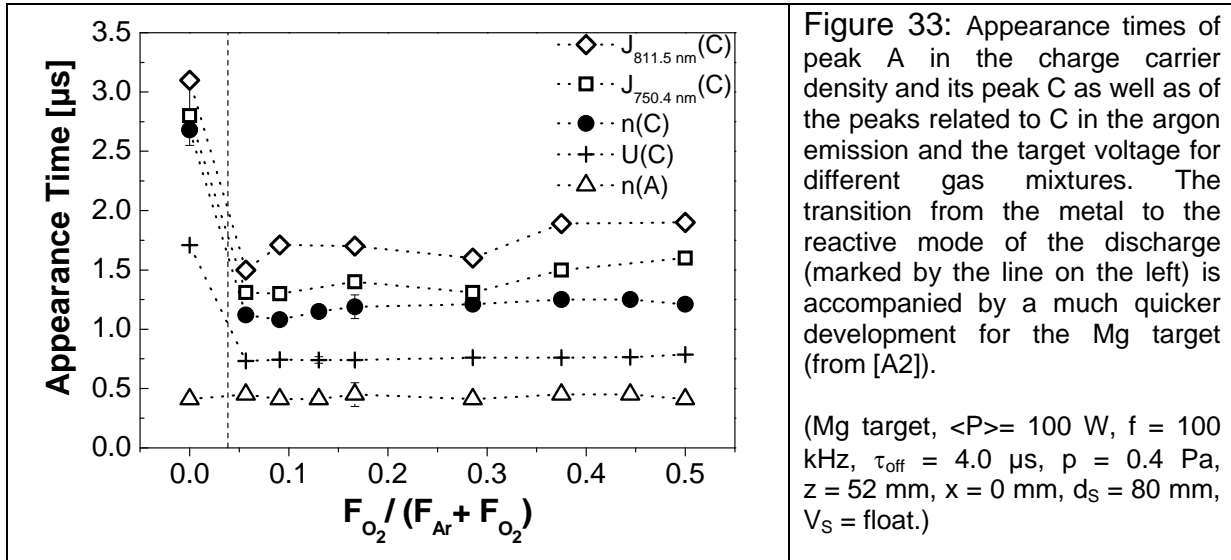
Whereas the maxima related to the ion bombardment and the secondary electron emission are hindered in their development in the metal mode and shift, the first maximum A does not (cf. Figure 33). This constancy proves that its formation is independent of the target material and γ_{iSEE} but has its origin in the gas and the residual electrons as supposed in the model introduced in section 3.2.3. The remnant electrons in the gas phase are accelerated as soon as the target potential goes to negative values. They cause ionisation once the accelerating voltage has reached the ionisation potential of the gas, most efficiently, however, at energies of about 100 eV. The target potential reaches a value of -100 V at 0.15 μ s to 0.3 μ s after the initiation of the 'on' phase [A2] almost independent of the surface state – the small deviation in the rise of the voltage can be neglected here. Within the time resolution of the probe, the ionisation these electrons cause is detected as a small density peak at 0.4 μ s in the metal and in the oxide mode (Figure 33). The maximum formation will be reliant on the magnetic field preventing electrons from escaping too fast out of the discharge volume. For a free flow of electrons to the substrate they would leave within several 10 ns before the target voltage could reach the value necessary for sufficient ionisation.



It should be noted that the observed decay of the plasma in the ‘off’ phase does also not depend on the surface state of the target. This is to be expected because in the ‘off’ phase, any secondary electrons escape quickly and no new high energetic electrons from the target are generated. Consequently, n decays with a rate of $\sim 500 \text{ ns}$ and J_{750} only slightly slower with $\sim 700 \text{ ns}$ in both modes [A2].

For the Ti target, no such temporal effect was clearly observed between reactive and metal mode, which is not surprising because γ_{iSEE} does not change as much between metal and oxide. Generally, appearance times of the maximum C of 2.0 – 3.2 μs were observed at 0.2 Pa [29], which were found to decrease with the discharge power up to 600 W [66]. At 100 W, 3.2 μs were measured for the reactive mode. This is in line with the results for Mg with a higher γ_{iSEE} and an appearance of C at 2.7 μs . Investigations with a carbon target, however at 400 W, revealed appearance times of

maximum C in the range 1.7 – 2.3 μs [59] which indicate a low γ_{ISEE} similar to that of TiO_2 but not as extremely low as the nominal target voltage (Figure 4) suggests.

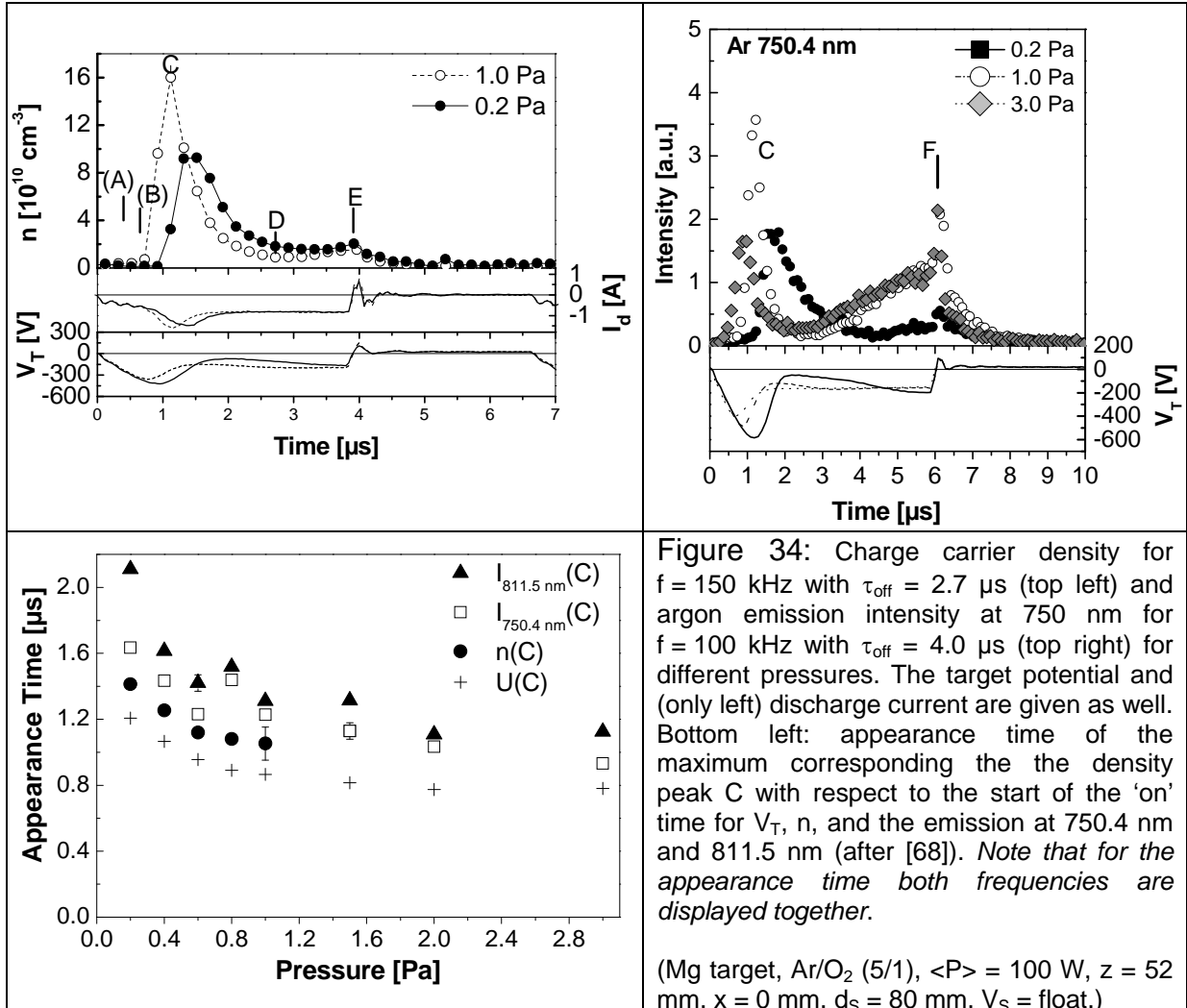


4.3. Discharge Pressure

A parameter that determines the ionisation in the plasma volume, which is at the same time easy to change in deposition technology, is the pressure of the working gas of discharges. It is therefore of interest how the pressure influences the temporal development of the pulsed discharge. At the same time, a change in the pressure alters the flux and especially the energy of the particles impinging on the substrate, sputtered neutral as well as the ions.

Figure 34a shows $n(t)$ for the Mg deposition discharge at a pulse frequency of 150 kHz and Figure 34b the argon emission intensity $J_{750}(t)$ for a frequency of 100 kHz both at a duty cycle of 0.6 for different pressure. The results are the same in one important respect: the maximum C as well as the subsequent depletion in $n(t)$ and $J(t)$ (minimum D) appear consistently earlier when the pressure is increased. The same holds for the maximum of the target voltage that also settles earlier at a stationary value. This is evaluated for the maxima in Figure 34c for the complete set of pressures investigated. The relation between the different quantities found earlier (section 4.2) is reproduced: the target voltage U_T peaks first, followed by n , which is delayed due to the ion transit time through the matrix sheath. Peak C for J_{750} and J_{811}

appears subsequent, the latter being slowed by the two-step excitation via metastable argon. However, the appearance time of the maximum of all quantities decreases significantly to higher pressure.



At first astonishing in Figure 34a,b is the height of the maximum for pressures of up to 1.0 Pa: whereas the driving voltage is decreased with pressure, both $n(C)$ and $J(C)$ increase. The expectation would be a decrease because the secondary electrons acquire less energy in the sheath. However, the pressure increase has the additional effect that the collision frequency of the secondary electrons in the magnetic trap is increased. The ionisation in front of the target is thus enhanced lowering the impedance of the discharge and increasing the current to the target. Hence, the current necessary to achieve the set power is reached faster. The consequence is that for higher pressure less voltage is needed to drive the current and the maximum in U_T is weaker. Because the voltage increase rate of the power supply is constant

this lower voltage is furthermore achieved earlier. The combination of the better ionisation and the feedback from the power supply leads to an increase in n and a faster peak formation. Due to the higher collision frequency the discharge in the rest of the pulse also develops faster so that the stationary state is reached in shorter times (cf. Figure 34a,b). This is in agreement with Ehasarian et al. [117] who found the same trend for the ion current to the substrate in a high power impulse magnetron (HIPIMS) and Musil et al. [118] who observed a faster discharge current development with increasing pressure in a low-frequency pulsed magnetron.

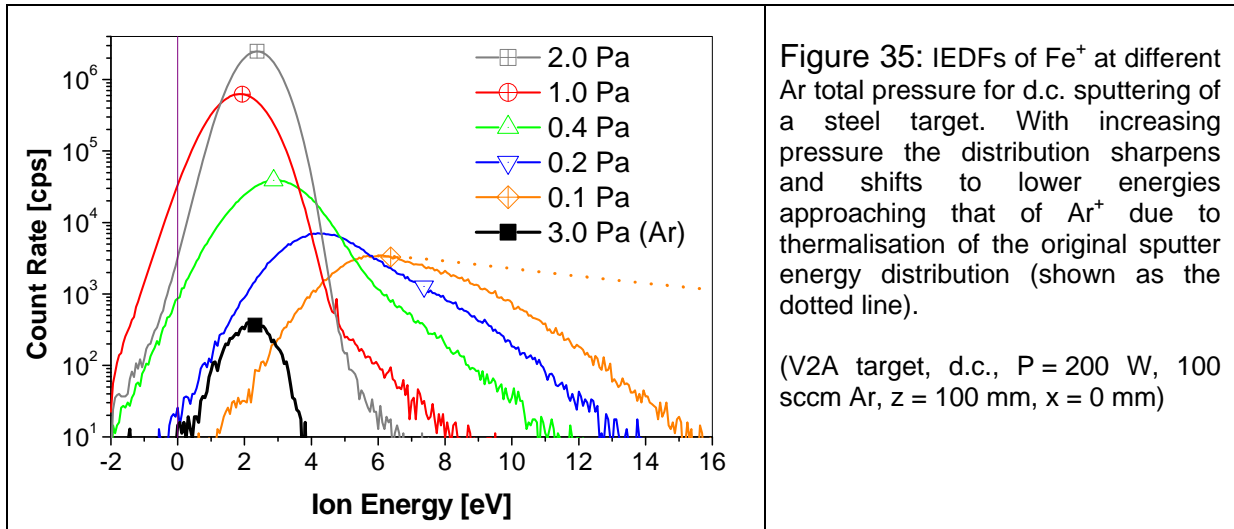
When the pressure exceeds 1.0 Pa, the height of the maximum of J starts to decrease again. The reason is probably a then too efficient cooling of the secondary electrons by inelastic collisions that together with the further decreased peak voltage may lead to less excitation in the measurement region close to the substrate. This should be accompanied by less ionisation which necessitates even more energy (15.7 eV onset compared to 13.5 eV for the excitation of the 750.4 nm argon line), however, it couldn't be confirmed because the probe measurements were performed only up to 1.0 Pa [68].

At pressures below 1.0 Pa, the emission intensity maximum at the start of the 'off' phase that has been introduced in section 3.2.5 is not observed. The reason is that the collision frequency of the electrons accelerated through the substrate sheath during the positive overshoot in V_{pl} with the background gas is too low to cause significant excitation enhancement adjacent to the substrate. With increasing pressure and collision frequency, the electrons can excite enough neutral. This excitation is then concentrated more locally close to the substrate where the measurement was done. At low pressure the excitation region, it will be more extended resulting in a too weak local excitation to be observed.

In the 'off' time, both n and J decrease rapidly, accounting for the missing sustainment of the discharge by secondary electron emission. The decay for all pressures can be approximated by an exponential fit with a single decay rate as described above. The decay rate of the charge carrier density measured with the double probe is such found to be independent of pressure and has a value of (600 ± 300) ns. Hence, within the whole pressure range, volume recombination is negligible

and the loss of charges is by ambipolar diffusion to the walls dominate. The decay rate of the emission lines, however, decreases with pressure [68]. This is consistent with a simultaneous decrease in the electron temperature which further impairs the excitation.

The IEDFs of the positive ions have been studied for d.c. sputtering of a V2A steel target in argon for the $^{56}\text{Fe}^+$ ions. The result is shown in Figure 35 for the pressure range between 0.1 Pa and 2.0 Pa. At high pressure, the IEDFs exhibit a sharp peak just like $^{36}\text{Ar}^+$ which corresponds to V_{pl} . The sputtered atoms that are post-ionised in the discharge hence behave like the cold working gas because they are almost completely thermalised by collisions. At decreased pressure, a high-energy shoulder appears, which is the remainder of the Thompson distribution with which the atoms leave the target. Up to now, a straightforward quantitative description of transport and cooling of sputtered atoms through the working gas is difficult and even elaborate Monte Carlo simulations have the problem of finding the correct interaction potential [119].



To estimate the collisional energy loss for practical purposes and to compare it to published results, the mean free path λ_{mfp} giving the average distance of travel before a collision can be taken together with the ideal gas law and hard sphere interactions of fast particles in an ambient at rest

$$\lambda_{\text{mfp}} = \frac{1}{n_n \sigma} = \frac{k_B T_g}{p \cdot \pi (r_s + r_g)^2}, \quad (55)$$

where T_g is the neutral gas temperature, n_n its density, p the gas pressure and r_s and r_g the atomic radii of the sputtered atoms and gas atoms respectively. Restructuring (55) yields

$$\lambda_{\text{mfp}} p = \frac{k_B T_g}{\pi(r_s + r_g)^2} = \text{const} \quad (56)$$

a constant value for a given set of sputtered atoms in a gas for a fixed gas temperature. So, different systems can be roughly compared to each other in that the average number of collisions is constant for a given product of distance and gas pressure.

Meyer et al. [120] used a hard sphere model to calculate the thermalisation of Nb and Cu and found a reduction of the average energy by more than one order of magnitude at 1.5 Pa (Ar) at a distance of 10 cm. For a velocity proportional stopping, Gras-Marti et al. [121] defined a projected range

$$R(U_s) \sim \frac{0.012}{M_g} \sqrt{1 + \frac{1}{\mu}} (1 + \mu^{3/2})^{3/4} \frac{T[\text{K}]}{p[\text{Pa}]} \cdot U_s^{1/2} \quad (57)$$

for which half of the sputtered atoms is thermalised, with μ being the ratio between the mass of the sputtered atoms M_s and that of the gas atoms M_g . For the case of Fe, an assumed gas temperature of 400 K and $p = 1.0$ Pa, $R(U_s)$ is calculated to 4 cm which is equivalent to a thermalised portion [121]

$$\frac{N_{\text{therm}}}{N} = \frac{z^2}{(R(U_s) + z^2)}, \quad (58)$$

of almost 90 % at 10 cm distance showing that most of the atoms have be thermalised. This is in agreement with Figure 35 showing only a very small shoulder to higher energies. However, the measured still directional portion (above 5 eV) is with 1 % even much smaller than estimated. The reason is that the formalism of Gras-Marti et al. treat only completely thermalised atoms (having a Maxwellian distribution) as such whereas in the measured IEDFs a significant part of cooled but not thermalised atoms contribute to the peak which can not be separated. Down to 0.1 Pa, the thermalised part decreases more and more and becomes almost invisible as a separate peak for 0.2 Pa. As shown in Figure 36, the average kinetic energy is still much below the original average energy at the target, even for the lowest pressure of 0.1 Pa. This is reasonable because sputtered atoms/ions that undergo a collision will be transferred to the lower energy part of the energy distribution

reducing the high-energy tail. For being completely thermalised, many collisions are necessary. Still, for 0.1 Pa, the strong reduction is astonishing because the mean free path for hard core interaction (equation (55)) is twice the distance of the PPM from the target so that in average only half of the atoms should have collided and lost energy. Ellmer et al. [122] have published a much shallower decrease of the high-energy tail for similar condition during Fe sputtering. It cannot be excluded that at very low-pressure parts of the high energetic ions have been missed due to the low acceptance angle of the PPM that was in this case positioned on-axis. Further research at different positions is thus necessary to understand the measured strong energy reduction.

Nevertheless, a strong reduction of the energy of the sputtered atoms measured for their post-ionised ions is found leading to almost complete transfer to the low-energy peak above 1 Pa. Given the measurement distance of 10 cm, as a rule of thumb, an effective cooling above the product $p \cdot d = 1 \text{ Pa} \cdot \text{cm}$ may be generally proposed deviating to slightly higher values for very light or very heavy ions. Counteracting on the energy decrease, the number of the ions is increasing with pressure (Figure 34) due to better ionisation [68].

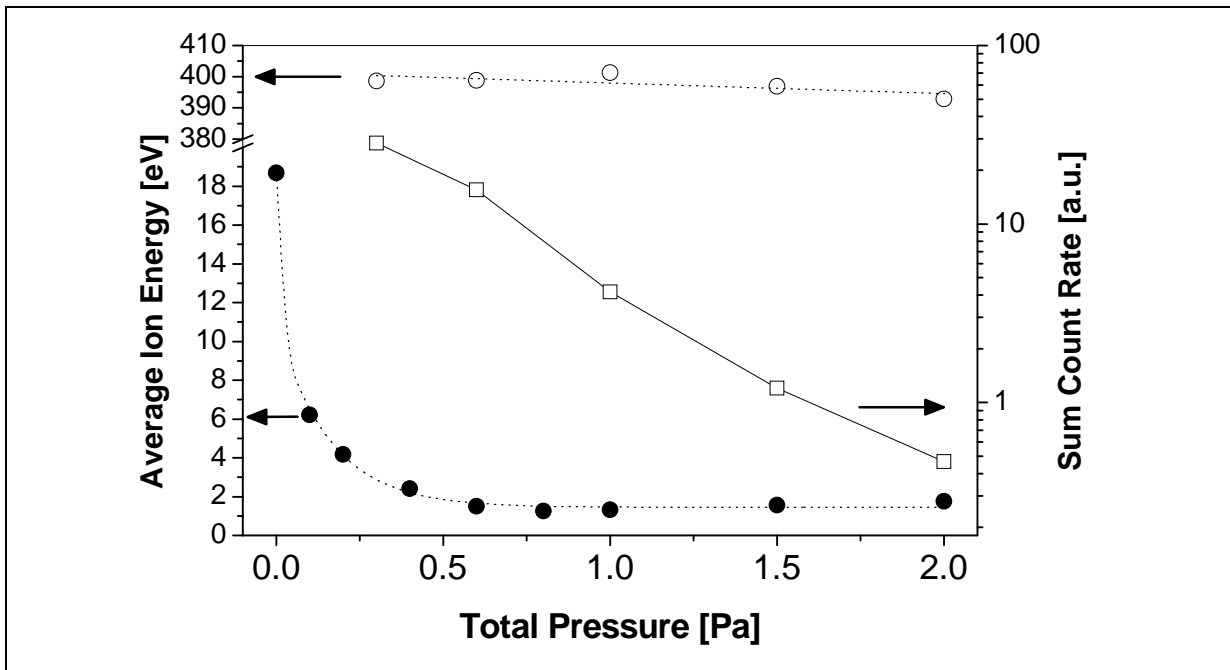
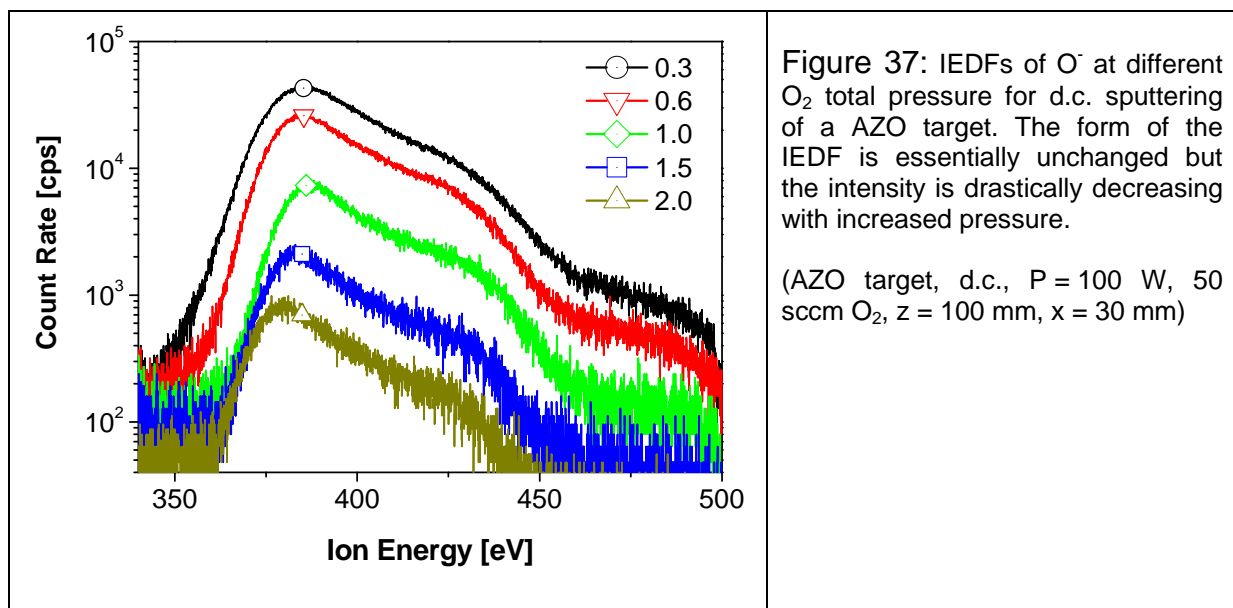


Figure 36: Average energy of Fe^+ ions and O^- ions in dependence on the total gas pressure. Data have been evaluated from the results shown in Figure 35 and Figure 37. The average energy of the positive ions is composed of the plasma potential contribution (about 2 eV) and the remaining sputter energy. The point at 0 Pa represents the calculated situation that no gas phase collision would have occurred. Also displayed is the integrated (over energy) count rate of the negative ions.

While the IEDFs of the positive target material ions reveal a significant decrease in the average ion energy due to thermalisation with increased pressure, those of the measured negative ions do not. This is shown for the O^- IEDFs during d.c. sputtering of AZO in Figure 37 for O_2 as working gas. Only the high-energy part was measured because no notable intensities were observed below. All IEDFs have exactly the same shape irrespective of the working gas pressure and exhibit a maximum at 380 eV with a sharp low-energy edge and an extended high-energy tail. As explained in section 3.4.2, the high-energy tail represents the Thompson distribution of the O atoms, which take up an electron at the target, and thus the IEDF is shifted by $e|V_T|$.



The constant form of the IEDF confirms the finding that the high-energetic O^- colliding with gas atoms are completely removed from the IEDF above 350 eV and there is no "redistribution" as for the positive ions. Hence, the average energy of the O^- ions is independent of the pressure (cf. Figure 36). Instead, the complete IEDF is reduced in its count rate. The decrease is exponential (Figure 36) because it obeys the scattering law. From this exponential decay the scattering cross section can be calculated according to $d(\ln(\text{count rate}))/dp = -\sigma k_B T/z$ to $\sigma = 1 \cdot 10^{-15} \text{ cm}^2$ (for $T = 300$ K, $z = 100$ mm) which is of the same order of magnitude as for the scattering of neutral oxygen ($\sigma = 3 \cdot 10^{-15} \text{ cm}^2$ assuming $r_O = 100$ pm, $r_{O_2} = 290$ pm) showing that the scattering of negative ions can be approximated by neutral scattering. The difference results from the high energy of the negative oxygen ions which reduces the cross section. Any collision of O^- therefore leads to a removal from the

forward "beam" into another direction or even to a neutralisation. Ions, which are detected with the PPM, are only those that have moved collisionless from the racetrack to the substrate.

The result of the pressure dependence of the ion energies at the substrates shows that with this parameter the energetic bombardment of the substrate can be strongly influenced. With increasing pressure, the energy of the target material arriving at the substrate can be drastically reduced and above about 1 Pa an almost thermalised flux arrives. At the same time, the integrated (over energy) flux of the positive ions increases due to enhanced ionisation. Most importantly, while the energy of the very high-energetic negative ions stays constant (as long as the target voltage does not change), their flux will be exponentially reduced. Therefore, particularly in terms of the prevention of radiation damage, a high pressure seems advantageous. The drawback is that the deposition rate will simultaneously decrease due to increased scattering of the sputter flux. Moreover, no statement can be given at this moment as to what influence products of collided high energetic negative ions may have. They may hit the substrate as undetectable neutrals with still high energies or O^- impinging inclined thus being not recognised by the PPM. To investigate these effects, an extensive combination of angle resolved measurements and simulations would be necessary in the future. The formation of the high energetic O^- in oxide deposition itself may not be prevented because as shown they originate from atomic oxygen leaving the target, which is an inherent property of the oxide deposition process. This even holds for reactive sputtering of metal targets where a compound layer is always formed at the target.

4.4. Discharge geometry and wall potentials

The periphery of a magnetron discharge such as the walls or electrodes surrounding it and their potential – either typically insulated (floating) or grounded – have a distinct effect on the discharge properties. This is particularly the case for the substrate holder that is inherently in contact with the plasma in deposition systems. The influence is often hard to characterise because the geometry of the chamber is fixed. This sometimes makes results of different groups difficult to compare. For this

reason, probe measurements were carried out in a purpose-built cylindrical chamber with a simple setup where the 10 cm diameter planar magnetron with a carbon target was placed in the centre and the opposite substrate holder could be moved to two different distances of 80 mm and 150 mm [A3, 59, 79]. The substrate holder ($\varnothing = 125$ mm) was mounted in grounded plate 150 mm opposite the target.

The spatio-temporal development of the plasma potential was investigated in this system for the two substrate holder distances with the substrate holder either grounded or insulated [A3]. For the floating holder at the large distance, the results have been shown in section 3.3.3. When it is moved closer to the target (80 mm), V_{pl} in the 'on' time is decreased in the discharge centre close to the substrate (bulk) which is shown in Figure 38a. The decrease is explained by the effective currents of electrons and ions to the walls and the conservation of quasi-neutrality in [A3]: For the floating holder at 80 mm distance, it intersects almost all magnetic field lines along which the electrons move away from the target. It hence effectively prevents an electron drain to grounded components downstream the discharge. A further obstruction of the electron current by a potential barrier is not necessary to keep the balance to the target ion current because electron loss to the system is only by those few that get past the substrate holder or cross-drift to the anode cup surrounding the magnetron. The situation is different for the substrate holder at 150 mm distance (Figure 21a) where the magnetic field lines are not intersected and many electrons reach the grounded plate around the substrate holder [A3]. Similarly, with the substrate holder at the small distance but grounded, V_{pl} must be raised to prevent a net electron drain out of the discharge because the majority of the magnetic field lines terminate on the grounded holder (Figure 38b). In this case, most of the magnetic field lines of the unbalanced field extending to the substrate region terminate on the grounded holder (Figure 3) which would result in a large electron current if a potential barrier was missing. V_{pl} hence is raised above ground potential.

In the 'off' time, V_{pl} is raised to positive values following the positive V_T which has been shown in Figure 21. This general behaviour is independent of the potential and position of the substrate holder. This is shown in Figure 39 for 150 mm distance of the grounded substrate holder during the stable 'off' phase and the peak at its beginning. Both distributions are similar to those presented in Figure 21 in its form

but also with respect to the absolute values. However, they exhibit slightly lower V_{pl} throughout the whole volume, an effect that has also been observed for the distance of 80 mm. This is explained by the net ion current to the substrate when it is at ground potential, which it does not draw at floating potential. The plasma potential is decreased to allow an electron current to the target that can compensate this [A3]. The investigations thus show that the potential distribution is strongly dependent on any surface and its potential that surrounds the discharge. It is therefore not surprising that the results of the group of Bradley [83-86] differ from those presented here because the magnetron itself is slightly different.

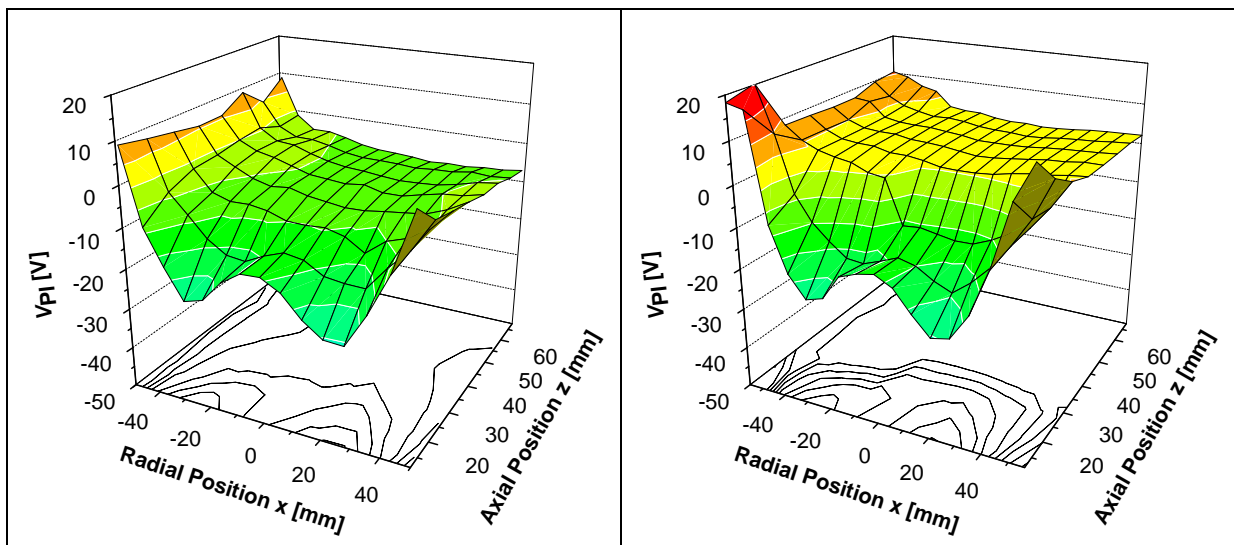


Figure 38: Distribution of V_{pl} for a substrate holder distance of 80 mm from the target when the substrate holder is (a) floating and (b) grounded (from: [A3]).
(C target, $\langle P \rangle = 400$ W, $f = 100$ kHz, $\tau_{off} = 4.0$ μ s, $p = 0.45$ Pa Ar, $d_S = 80$ mm)

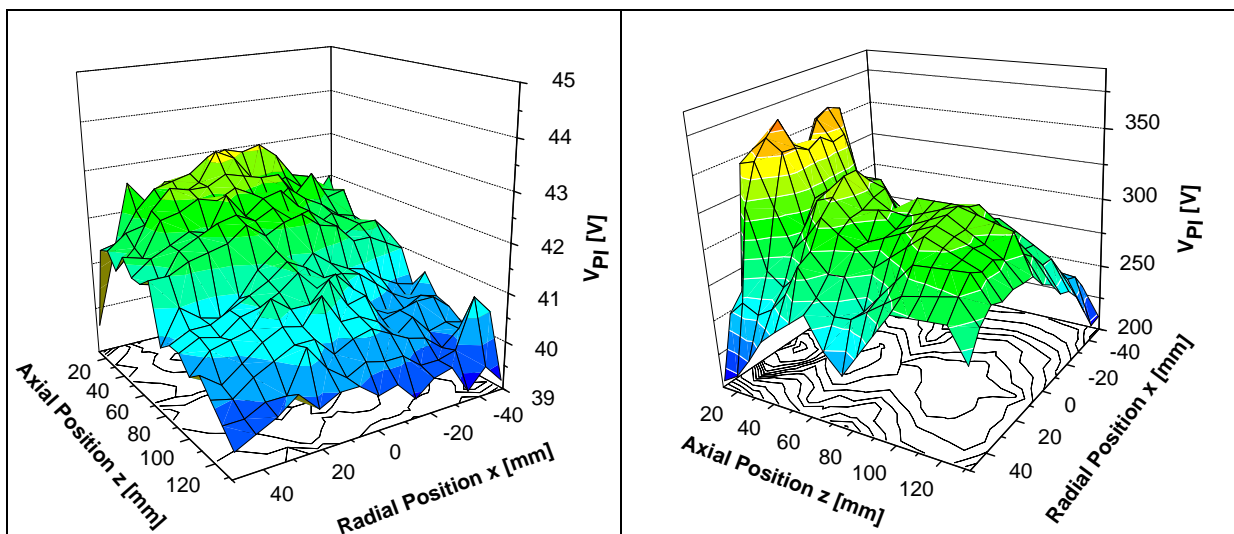


Figure 39: Distribution of V_{pl} during the 'off' phase with the floating substrate holder at 150 mm distance from the target and grounded. (a) represents the stable 'off' phase and (b) the target voltage overshoot at the beginning of the 'off' phase (from [A3]).
(C target, $\langle P \rangle = 400$ W, $f = 100$ kHz, $\tau_{off} = 4.0$ μ s, $p = 0.45$ Pa Ar, $d_S = 150$ mm, $V_S = \text{float.}$)

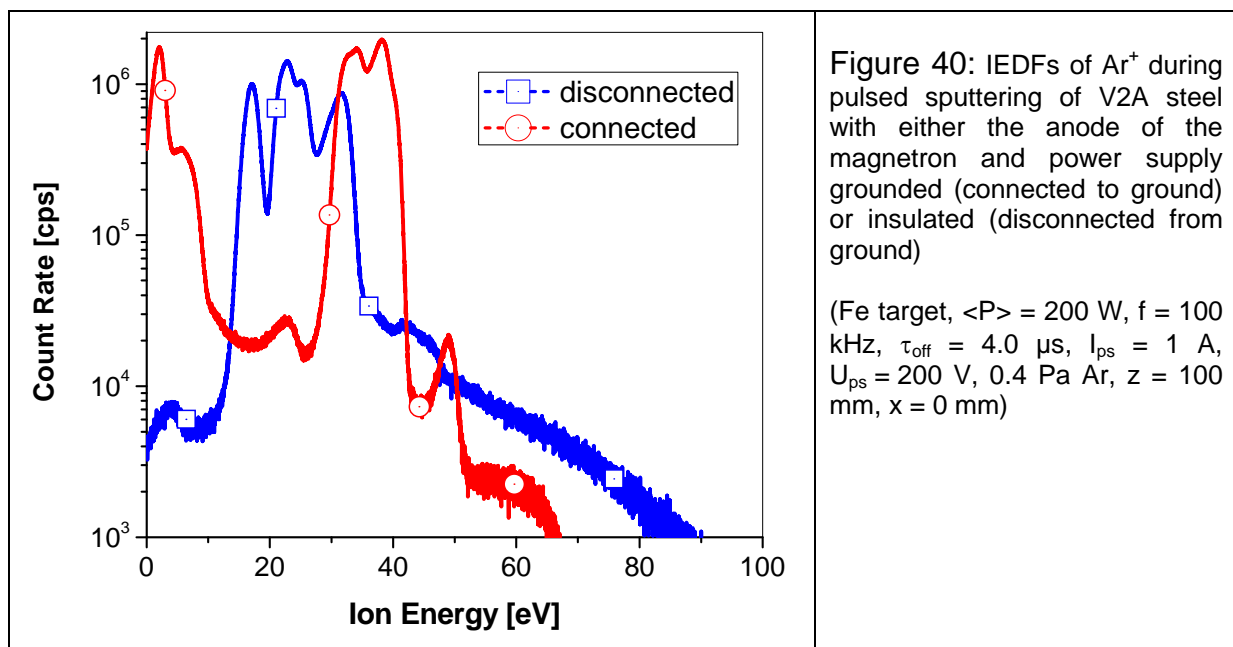
In the present work, the magnetron has been constructed with an anode cup that screens the outer edge of the targets thereby partly intersecting magnetic field lines terminating on the outer magnet. It hence prevents electrons from reaching the target along these field lines in the 'off' time. In the magnetron of the Bradley group, such a blocking electrode is not present and an efficient path for the electrons to the target is provided in the 'off' time. To prevent an excess electron current out of the plasma, their V_{pl} has to be raised above V_T , which is not the case for the magnetron used here. Consequently, the group of Bradley has measured $V_{pl} > V_T$ in the 'off' time while in this work mostly $V_{pl} < V_T$ is observed.

The connection of the anode of the power supply has been identified as a crucial parameter. The output of the power supply is generally applied between the target and the anode surrounding the target or being close to it. There are, however, two possibilities for the grounding of the system. One is to disconnect target and anode as well from ground. The other, common, method is to clamp to anode to ground. All the results presented so far have been obtained with the latter configuration. Few measurements with the PPM were done with the scarcer configuration of disconnected ground. The result is given in Figure 40 for Ar^+ that represents the plasma potential. Instead of the typical peaks at low energy (~ 0 eV) for the 'on' time and at medium energy (~ 35 eV) for the stable 'off' time plus the high-energy part extending to 60 eV for the overshoot at the start of the 'off' time, a single broad but structured maximum occurs at about 20 ... 30 eV.

The change in the IEDF becomes understandable if the functionality of the wall or any grounded surface in the case of the disconnected anode is considered. The discharge current flows exclusively from the target to the anode cup through a drift across the magnetic field. Any grounded surface adjacent to the plasma may not draw discharge current. In other words, the net current to the grounded surface such as the chamber wall is zero and the surface hence has to behave like a floating electrode [123]. Because the potential of the grounded surface is by definition zero but the floating condition has to be achieved likewise, V_{pl} will adjust according to equation (47) for $V_{fl} = 0$ V. For an argon plasma, V_{pl} is then merely dependent on the electron temperature and will have a value for argon of $V_{pl} \sim 5.2 \cdot k_B T_e$. The absolute potential of both cathode and anode will adjust themselves according to the

discharge conditions in their vicinity with the restriction that their potential difference must match U_T delivered by the power supply. The most important fact for the temporal development of the plasma potential is that all these relations are the same for the 'on' and 'off' time. Grounded surfaces will be "inactive", i.e. have to float, in both phases and the system of cathode and anode will be "riding" with the plasma at any moment with just U_T between them fixed.

In the case of the anode being disconnected from ground, V_{pl} will be at $+5.2 \cdot k_B T_e$ (for argon) for the whole pulse period. Figure 40 has been measured in argon, so that the three peaks in the broad structure of the IEDFs may be attributed to different electron temperatures. It can be speculated that the high-energy peak at $E_i = 32$ eV ($k_B T_e = 6.2$ eV) belongs to ions generated during peaks A and C in the 'on' time, or F in the 'off' time, where high electron temperatures are expected, the mid-energy peak around $E_i = 25$ eV ($k_B T_e = 4.8$ eV) to ions from the stable 'on' time and the low-energy peak at $E_i = 17$ eV ($k_B T_e = 3.3$ eV) to ions from the decaying plasma in the 'off' time. Up to now it is, however, open to question how the few measured high energetic ions up to 90 eV are generated.



In contrast to the situation discussed above, when the anode is connected to ground, V_{pl} will be determined by the fixed potential of the grounded surfaces ('on' time) or the positive V_T ('off' time) which itself is fixed against ground (anode) by U_T . The

peaks in the IEDF are hence not determined by T_e but the U_T waveform and ground (cf. Figure 40) as discussed in section 3.4.3.

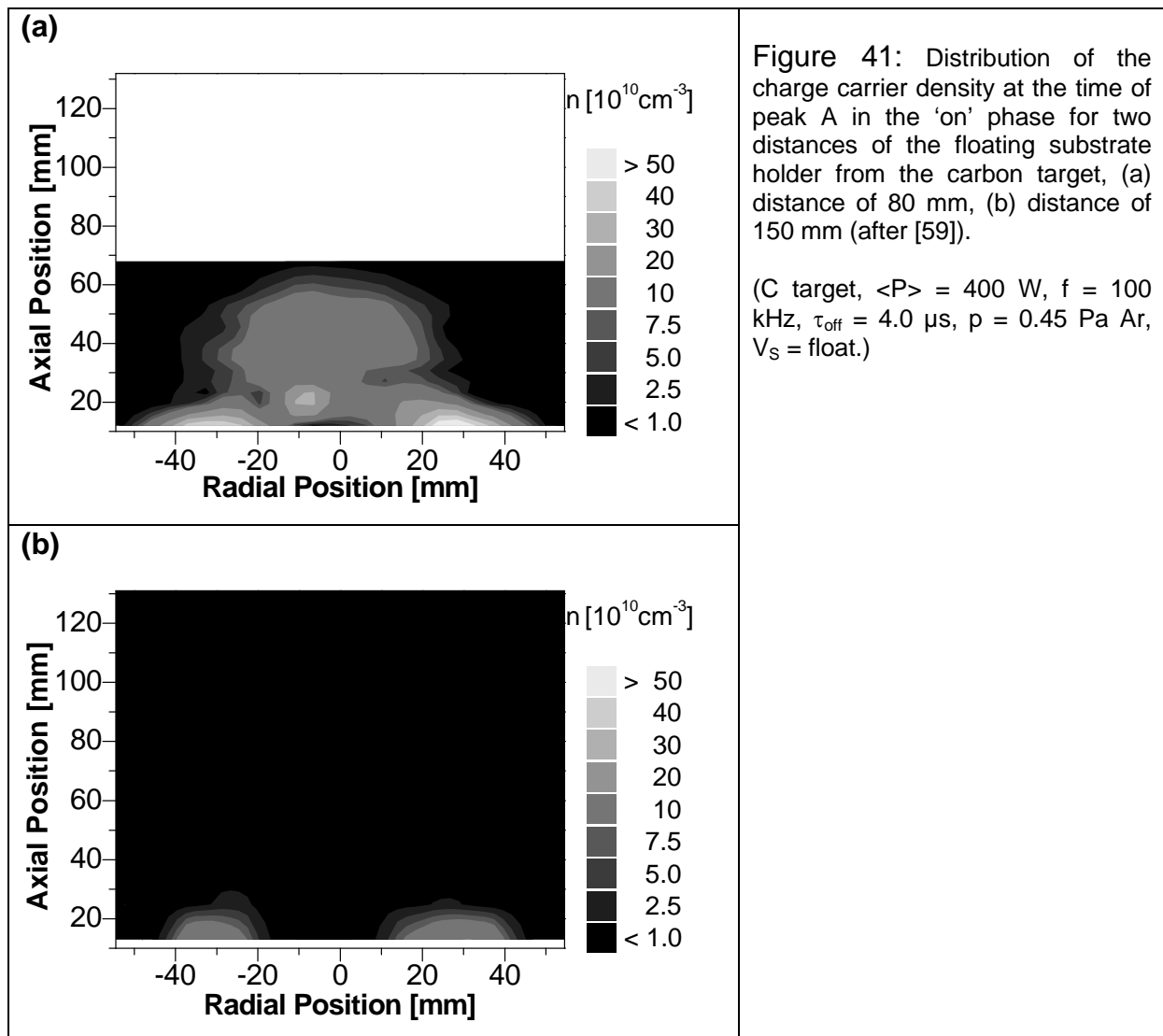
The spatio-temporal evolution of the charge carrier density is extremely dependent on the concrete environment of the discharge, too. This has been investigated for the same magnetron setup with the moveable substrate holder as for the V_{pl} measurements [59]. The results confirmed those described in section 3.2.4 for reactive sputtering of Mg but also showed some remarkable differences.

Once again, two peaks were observed with peak A at $t \sim 0.4 \mu\text{s}$ but with peak C at $t \sim 2 \mu\text{s}$ in this case which is a consequence of the later peaking target voltage due to the lower γ_{iSEE} . More interestingly, peak A was strongly observed for a short substrate holder distance (80 mm) but very weakly for a long distance (150 mm) in the bulk (see Figure 41). The first compares to the situation with the Mg target and shows that a close floating substrate which effectively reflects the electrons responsible for peak A back and such forming a trap in the plasma bulk strongly enhances the ionisation in the very early stage of the 'on' phase. When the substrate is at 150 mm distance, the ionisation is lowered by two effects. First, the power is dissipated in twice the volume so the density will be only half. Second and more important is the fact observed in the potential measurements that electrons might escape to the grounded substrate holder plate instead of being reflected into the bulk.

With the carbon target, peak A was also observed within the magnetic trap, contrary to the magnesium target. It is assumed that this is due to the much higher target voltage (peak value of 1300 V instead of 300 V) with a doubled increase rate that allows the electrons to gain enough energy before they are trapped.

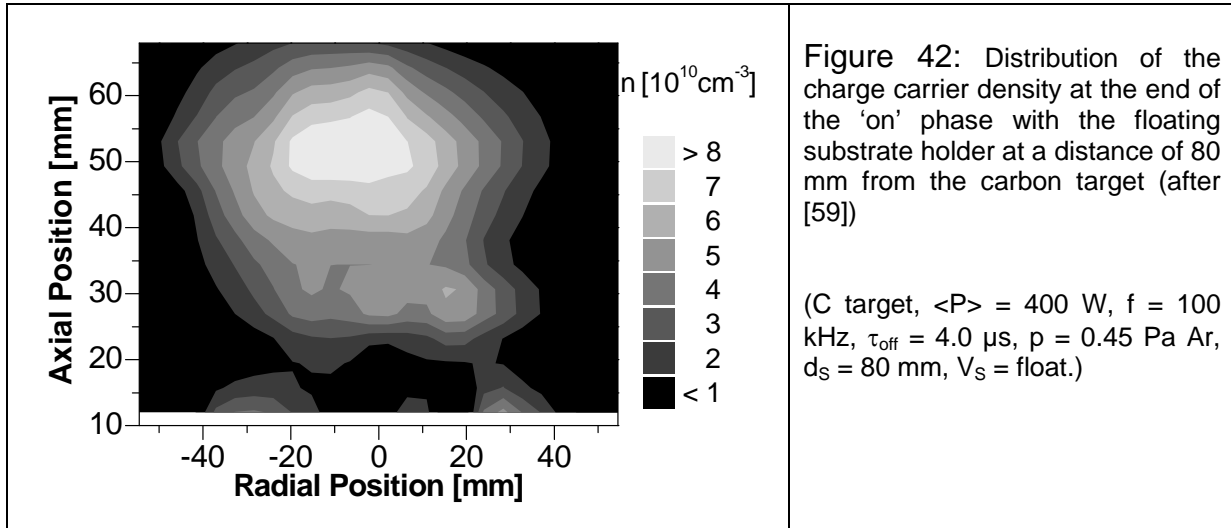
Another important finding is the almost vanished plasma torus at the end of the 'on' phase (Figure 42) which is again in contrast to the Mg target (cf. Figure 12). This has its reason in the slow development of the target voltage due to the low γ_{iSEE} and a recapture of electrons at the rising flank of the target potential waveform [59]. Electrons that are released from the target at very high negative potential move back to the target along the magnetic field lines of the trap and eventually arrive at it when the target potential has developed to much less negative values. If the electrons have

not experienced several collisions they may overcome the now smaller potential barrier and be re-absorbed by the target. The effect has been suggested to be important even for d.c. magnetrons because of the small initial energy of the γ electrons [124] but becomes more significant in pulsed discharges. The recapture of electrons out of the trap has been recognised here because of an almost vanished charge carrier density in the magnetron torus at the end of the 'on' phase [59]. Strong re-capture will be a general effect for pulsed discharges with waveform parts $dV_T/dt > 0$ in the 'on' time but has been particularly observed with the carbon target at the end of the 'on' phase as the target voltage waveform is much slower and the target voltage minimum is reached only shortly before end-'on' [59].



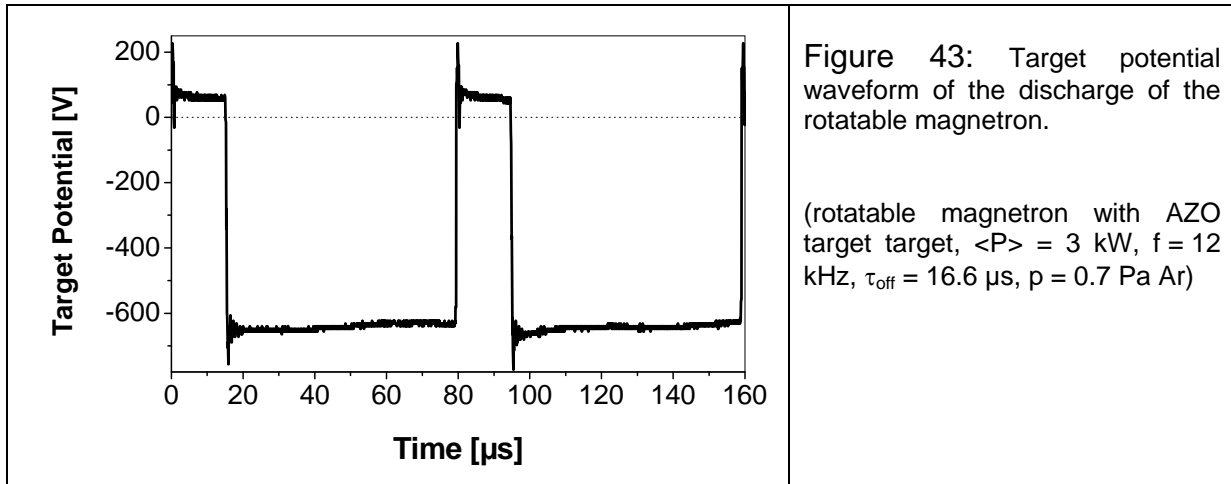
The missing supply of high energetic electrons during this phase has the second effect that the discharge in almost the complete volume extinguishes (Figure 42).

Consequently, a spatial distribution of n similar to the early 'off' time is observed with a density maximum at the magnetic null (at $z = 55$ mm for this magnetron). New ionisation is negligible and the existing charges are drifting to the substrate. As in the 'off' phase, those charge carriers around the magnetic null are unable to drift along the magnetic field and are preserved for a rather long time forming the density maximum in this region.



4.5. Cylindrical Rotatable Magnetrons

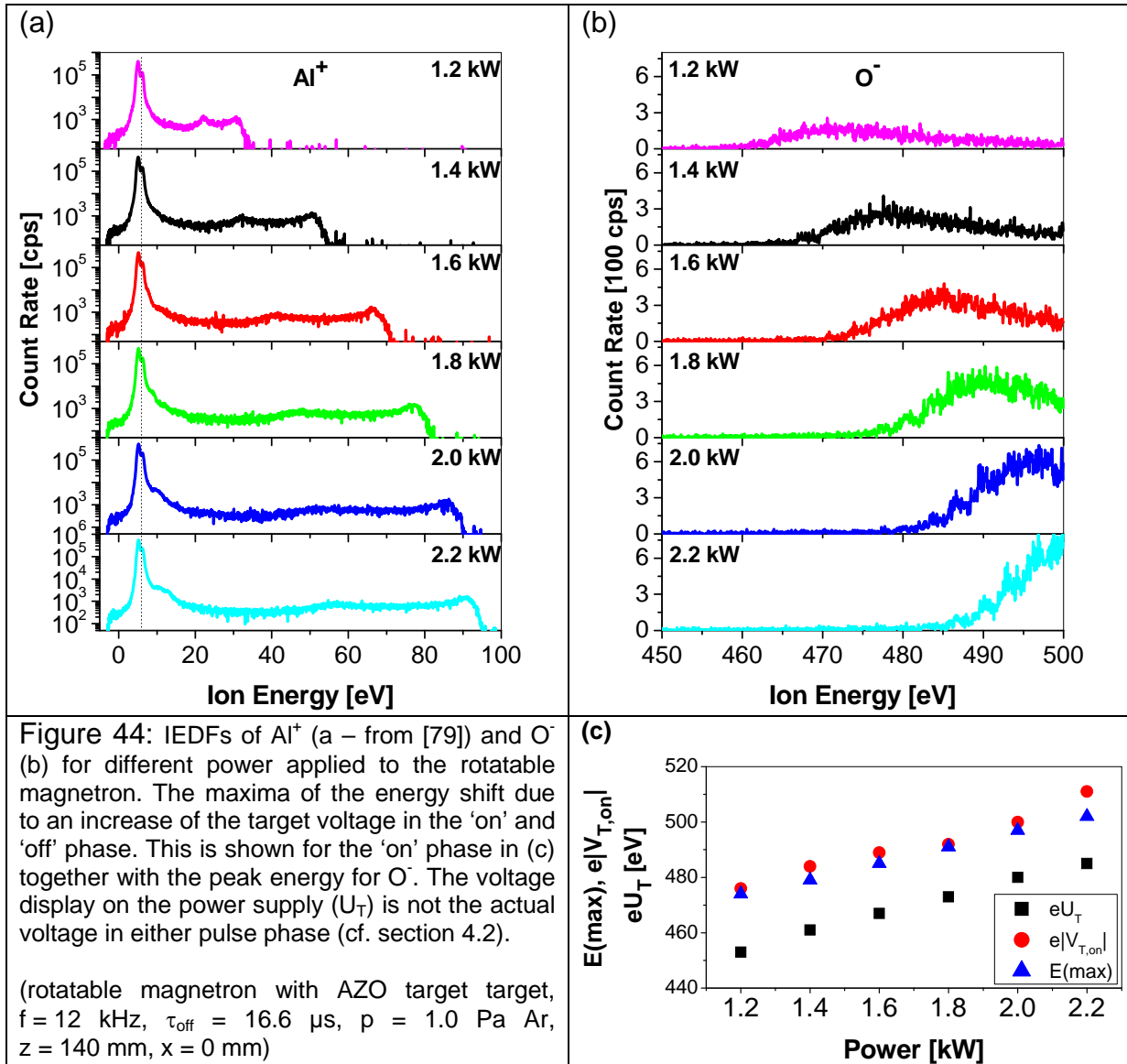
The investigations described so far were all done on circular planar magnetrons on a laboratory scale (target diameter of 100 mm). With the plasma monitor, additional measurements were performed on a very different magnetron, a cylindrical rotatable dual magnetron on an industrial scale (i.e. a cylinder diameter of 160 mm and a cylinder length of 950 mm) within an industry cooperation. The target material was aluminium-doped zinc oxide (AZO) and the discharge was operated in asymmetric-bipolar mode with only one of the two targets being active. The waveform of the target voltage delivered by a Hüttinger TIC 30 DC power supply connected to that particular magnetron is shown in Figure 43. It seems to have a more rectangular shape than that used for the planar magnetrons. Especially in the 'on' time with the negative potential, this is in fact the case with the overshoot being only about 20% above the stable potential. However, for the 'off' phase it is more a consequence of the longer period. Again, the stable 'off' voltage is about 10% that of the 'on' voltage.



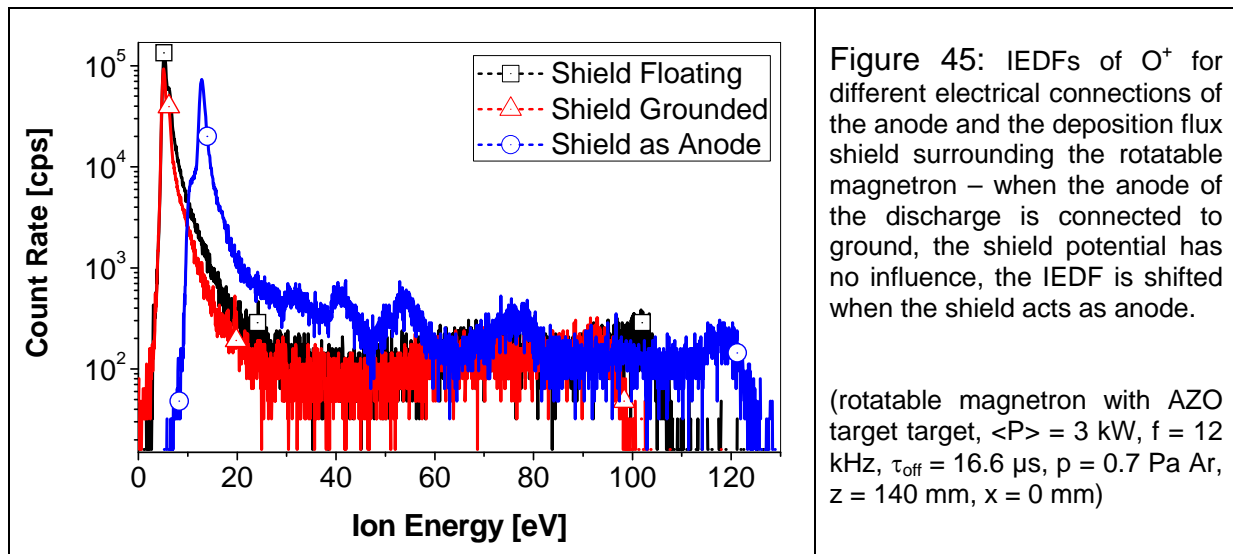
The IEDFs of the positive ions have been found to be all of similar shape, as an example for that the Al^+ IEDF is given in Figure 44a for an average power between 1.2 kW and 2.2 kW. As in the case of the planar magnetrons, the IEDFs show a very distinct peak at low energy of 6 eV which corresponds to the plasma potential in the 'on' phase. The peak has a weak tail to higher energies due to the initial energy of the Al atoms sputtered from the target. However, it is even weaker than for the planar magnetron. This is no consequence of the different magnetron type but a result of the high pressure (1.0 Pa) and the increased measurement distance (140 mm). The IEDF extends to high energies with the edge energy increasing with the applied power. The peak before the edge corresponds in all cases almost exactly to the target voltage in the 'off' phase that is increasing with power because the positive target potential increases and so does V_{pl} in the 'off' time. No signal has been measured at high energies that correspond to the positive overshoot in the 'off' phase because it is extremely short compared to the stable 'off' time. Although the energetic position of the high-energy edge of the IEDF follows V_{T} , it is not yet clear why such a broad distribution is observed. The very rectangular waveform of V_{T} would rather suggest a sharp peak. The low-energy peak is dominant in comparison to the planar magnetron reflecting the high duty cycle of 80%.

The IEDFs of O^- exhibit only one peak at high energy between 470 eV and 500 eV which is shifting to higher energy with increased power (Figure 44b). The energetic position is at $e|V_{\text{T,on}}|$ which is also shown in Figure 44c. Although the peak is close to the detection limit of 500 eV of the system (shifting parts of it out of range for higher power) it is not expected that a significant amount of ions with higher energy are present because of the rectangular target potential waveform. There is, however, a

slight decrease in the target voltage to later moments in the 'on' time by 10 to 20 V which broadens the peak. The absolute count rates of O^- are extremely low in the case of the rotatable magnetron. The reason lies in the configuration in which the measurements were done. The entrance of the PPM was facing the cross-sectional centre of the cylinder at about the middle of its length. It was hence pointing directly between the two straight racetracks. As in the situation for the planar magnetron, few negative ions originate from this region. The cylindrical shape of the rotatable magnetron target further decreases the detectable O^- flux because the majority of O^- emitted from the racetracks is directed sideways away from the PPM. The physical basis of the results is thus in very good agreement with the planar magnetrons.



A further result, which confirms the similarity between the planar and the rotatable magnetron is shown in Figure 45. Here, the connection of the anode was changed comparable to the measurement in section 4.4. For the rotatable magnetron, there are three possible configurations which include the cylindrical target, a shield to reduce deposition out of the substrate area, and the wall or ground: the target can either be operated against (a) wall at ground potential but the shield floating, (b) shield and wall at ground potential, (c) the shield only, with the wall being a passive electrode. In situation (a) and (b), the target potential is always related to ground and hence the IEDFs are the same, consisting of the low-energy peak corresponding to V_{pl} slightly above ground during the ‘on’ phase and some high energetic ions from the ‘off’ phase. In situation (c) the discharge voltage is applied between the target and the shield which has no relation to ground – similar to the disconnected anode cup in the planar magnetron. The peak of the IEDF hence moves to a value which is related to the electron temperature (cf. section 4.4) instead of being related to ground



The selected results that have been presented here have been partially published in [107] and are documented and discussed more extensively in [102] have one in common. They show that the operation of planar and rotatable magnetrons leads to similar IEDFs and that the underlying physics is the same and will lead to other comparable quantities. The basics results from one type of magnetron may therefore be transferred to the other. Of course, differences exist due to deviating environment or other operating parameters but these have been shown to be relevant to one of these magnetron systems alone.

4.6. Summary of external influences and process control

Besides the knowledge of fundamental processes which determine the properties of pulsed discharges it is important to know how these can be controlled by externally accessible parameters. This has been investigated in this chapter from which – also technologically - important conclusions can be drawn.

The plasma potential distribution and its exact relation to the positive target potential in the 'off' phase are very sensitive to the environment of the discharge. With a simple model of the current equality of positive and negative charges the dependence on the substrate potential has been explained. It shows that the plasma potential at any moment adjusts to (re)-establish the quasineutrality of the plasma. From this, differences to other works in terms of the absolute potential could be explained showing that a comparison of absolute results is only possible for very similar geometries and magnetron environment. It has been particularly shown that the magnetic confinement and the location of the magnetron anode in this work effectively shield the target from an electron current in the 'off' time leading to a plasma potential decrease.

The plasma potential and hence the IEDFs at the substrate have been shown to be strongly dependent on the connection of the asymmetric-bipolar pulsed power supply to the magnetron anode. When the anode of the power supply and the magnetron are connected to ground, the plasma potential is strongly modulated during one pulse and the IEDFs show up to three separated peaks. If, however, magnetron and power supply anode are insulated against ground, target and plasma potential float with respect to ground and the IEDFs consist of a broad maximum related to the electron temperature. The trend is identical for planar and cylindrical rotatable magnetrons showing that the investigation of fundamental properties allows a generalisation of pulsed magnetron discharges.

The peak formation in the charge carrier density at the beginning of the 'on' time has been shown to be a combination of the release of secondary electrons and electron impact ionisation in the discharge volume. These two fundamental processes can be influenced externally by control parameters of the discharge. If they are enhanced,

the discharge in the 'on' time develops quicker, reaching the stationary state earlier, and hence the effect of fluctuations will be reduced. This has been shown in this work by

- an increase of the γ_{iSEE} of the target bulk material sputtered,
- an increase of the γ_{iSEE} of a surface compound layer formed during reactive sputtering,
- an increase of the volume ionisation due to increased pressure.

All three variations are accompanied by a reduction of the discharge impedance. They are also connected to a faster reaction of the power supply proving that the feedback of the particular power supply to changes in the discharge plays an important role.

The relation of the density maxima is further – and of course besides the pulse parameters which determine the residual charge carrier density – significantly influenced by the location and the potential of close electrodes or walls as the substrate holder. This is due to a different electron trapping and volume ionisation. Thus, the temporal and spatial distribution of the charge carrier density may be extremely different although the average charge carrier density is insensitive to a wide range of parameters. A prominent example for this is the variation of the pulse parameters for constant discharge power.

The IEDFs of the ions at the substrate significantly depend on the discharge pressure, however differently for positive and negative ions. Increased pressure leads to reduced average energy for many positive ions by a direct energy reduction but for the negative ions by a reduction of the current of high-energetic ions. The energy reduction in the case of positive ions is due to a thermalisation of the sputtered atoms which are post-ionised in the discharge. Negative ions, however, which arrive at the substrate with energies equivalent to the full target sheath voltage, are increasingly scattered at higher pressure so that their current at the substrate is exponentially decreased. To prevent the direct high energetic bombardment by negative ions, the pressure may be hence increased. However, up to date it is not clear what consequences scattered high energetic species will result in. Moreover, a pressure increase is often undesirable because of simultaneous scattering of the sputter flux reducing its energy and decreasing the deposition rate.

To reduce the high energetic bombardment of the films by positive as well as negative ions, the results suggest an optimisation of the pulsed power supplies or a proper selection of the most suited for a certain process. Where applicable, unipolar pulsing should be used to eliminate the positive overshoot at the start of the 'off' phase. This will be dependent on the sufficient neutralisation of the surface charges. For bipolar pulsing, the design of the power supplies should generally aim at reducing the voltage spike. A similar argument holds for the negative target potential in the 'on' time. Negative ions with high energy equivalent to the target voltage can never be completely avoided when electronegative species are involved. To minimise the potential damage caused by them, the voltage overshoot should be kept as low as possible. Consequently, power supplies with a rectangular target voltage waveform will be the best choice. They will simultaneously reduce the density fluctuations at the beginning of the 'on' phase as well as high-energetic electrons.

5. Conclusions

The present thesis has been focussed on a certain type of pulsed single magnetron – an asymmetric bipolar pulsed discharge. The findings will, in their majority, nevertheless be characteristic for unipolar pulsing of single magnetron and for the understanding of dual magnetron operation. The results show that due to the modulation of the target potential the discharge behaves in part completely different from a d.c. discharge for the same magnetron configuration. This is the case for all relevant discharge parameters such as densities, potentials, and energies. Additional peaks in these quantities are often not compensated by minima so that also their average values are different from d.c. discharges.

The charge carrier density in the pulsed discharge has been shown to exhibit a modulation not only between the ‘on’ and the ‘off’ phase but also in the ‘on’ phase itself. These results could be achieved with the development of a time-resolved Langmuir double probe which has been applied for the first time. The technique has the advantage to float with temporally changing potentials present in pulsed discharges making it independent of their determination. Peaks of high density have been found at the beginning of the ‘on’ phase which are not a simple image of the target voltage waveform. With the introduction of a qualitative model based on remnant electrons from the previous pulse and secondary electrons emitted from the target by the bombardment with remnant ions, the formation of the density peaks could be explained by bursts of high-energetic electrons. With this model, the dependence of the discharge development during the ‘on’ phase on the pulse parameters, the pressure, target material, and discharge geometry can be understood. Spatio-temporal studies have further revealed that the formation of the maxima depends on the region within the discharge.

A similar phenomenon is a peak at the beginning of the ‘off’ phase which has been observed with optical emission spectroscopy. In this case, however, the reason are

fast electrons from the substrate and not from the target which are detected by enhanced emission. These findings clearly show that pulsed magnetron discharges may not be considered as a simple switching 'on' and 'off'. Instead, dynamics on a time scale of several inverse ion plasma frequencies play an important role making the transient phases dominant for the used pulse periods of several μs . It has further been shown for the first time that the target voltage waveform driving the discharge is itself dependent on the discharge formation by a feedback of the power supply.

With the successful development of a time-resolved emissive probe, the potential distribution within the discharge could be investigated at different moments within the pulse. It has been shown that the plasma potential immediately reacts to target potential changes and at any time adjusts itself close to the most positive potential surrounding the discharge. In asymmetric bipolar discharges the plasma potential hence is lifted to high positive values in the 'off' phase. With a simple model its absolute value has been related to the discharge geometry by the fluxes of the charge carriers. Thus, discrepancies between the literature and the present work have been solved. However, it has been shown that it is generally subtle to compare discharges with differing environment.

The modulation of the target and plasma potential significantly affects the ion energies at the substrates. The energy distributions of positive ions exhibit additional high-energy parts compared to d.c. operation. These have been shown to originate from the 'off' phase with high positive potential. Negative ions partly exhibit extremely high energies which considerably exceed those in d.c. discharges. Their origin is the modulation of the target potential in the 'on' phase down to extremely low negative potential which may exceed 1 kV producing ions which strike the substrate with more than 1 keV. For the first time, a further diversification of the ion energy distributions has been found which could be correlated to potential changes during the transit of the ions between the target and the substrate. Generally, an increase of the pressure reduces the average energy the positive and even more the negative ions. Additionally, a different connection of the magnetron to ground has been found to not only shift but completely change the ion energy distribution.

References

- [1] P. Sigmund, Phys. Rev. 184 (2) (1969) 383.
- [2] Y. Yamamura, H. Tawara, Atomic Data Nucl. Data Tables 62 (2) (1996) 149.
- [3] R. Behrisch, *Festkörperzerstäubung durch Ionenbeschuss* (Sputtering of Solids by Ion Irradiation), in: S. Flügge, F. Trendelenburg, Ergebnisse der exakten Naturwissenschaften (Results of the exact sciences), Bd. 35, Springer-Verlag, Berlin, 1964, Kap. 295.
- [4] J. B. Malherbe, S. Hoffmann, J. M. Sanz, Appl. Surf. Sci. 27 (1986) 355.
- [5] J. A. Kerr, *Strengths of Chemical Bonds*, in: D. R. Lide, H. P. R. Frederikse (eds.), CRC Handbook of Chemistry and Physics, CRC Press, Inc., Boca Raton, Ann Harbor, London, Tokyo, 1994, ch. 9.
- [6] A. Anders, Surf. Coat. Technol. 183 (2004) 301
- [7] D. Depla, S. Heirwegh, S. Mahieu, J. Haemers, R. De Gryse, J. Appl. Physics 101 (2007) 013301.
- [8] D. Depla, X. Y. Li, S. Mahieu, R. De Gryse, J. Phys. D: Appl. Phys. 41 (2008) 202003.
- [9] T. W. Kim, D. C. Choo, Y. S. No, W. K. Choi, E. H. Choi, Appl. Surf. Sci. 253 (2006) 1917.
- [10] M. Konuma, *Film Deposition by Plasma Techniques*, Springer Series on Atoms and Plasmas, Springer Verlag, Berlin, Heidelberg, 1992.
- [11] D. Depla, S. Mahieu, R. De Gryse, Thin Solid Films 517 (2009) 2825.
- [12] K. Hine, S. Yoshimura, K. Ikuse, M. Kiuchi, J. Hashimoto, M. Terauchi, M. Nishitani, S. Hamaguchi, Jpn. J. Appl. Phys. 46(46) (2007) L1132.
- [13] M. W. Thompson, Phil. Mag. 18 (1952) 377.

-
- [14] D. Bohm, *Minimum Ionic Kinetic Energy for a Stable Sheath*, in: A. Guthrie, R. K. Wakerling, *The Characteristics of Electrical Discharges in Magnetic Fields*, McGraw-Hill Book Company, Inc., New York, Toronto, London, 1949, Ch. 3
- [15] M. A. Lieberman, A. J. Lichtenberg, *Principles of Plasma Discharges and Materials Processing*, John Wiley & Sons, Inc., New York, Chichester, Brisbane, Toronto, Singapore, 1994, ch. 3 & 14.
- [16] A. v Engel, *Ionized Gases*, AIP Press, Woodbury 1994, ch. 7.
- [17] F. M. Penning, US Patent 2146025, 1939.
- [18] J. A. Thornton, *J. Vac. Sci. Technol.* A15(2) (1978) 171.
- [19] J. S. Chapin, *Magnetron Sputtering Apparatus*, US Patent 4166018, 1979.
- [20] R. K. Waits, *J. Vac. Sci. Technol.* A15(2) (1978) 179.
- [21] H. J. Gläser, *Vakuumbeschichtung von Architekturglas – ein historischer Abriss (Vacuum Coating of Architectural Glass – A Historic Review)*, *Vakuum in Forschung und Praxis* 20(3) (2008) 12.
- [22] H. E McKelvey, *Magnetron Cathode Apparatus*, US Patent 4356073, 1982, US Patent 4422916, 1983.
- [23] B. Window, N. Savvides, *J. Vac. Sci. Technol.* A4, 2 (1986) 196.
- [24] Gencoa Ltd, Liverpool, UK, URL=<http://www.gencoa.com/1,96-Balance-unbalance.htm>; V. Bellido-Gonzalez, S. Powell, D. Monaghan, *A review on Magnetron Sputtering Sources and its Applications. Past, present and Future*, Presentation at the Conference on Frontiers of Surface Engineering (FSE 2001), Nagoya, Japan, Oct 30, 2001.
- [25] S. Schiller, K. Goedicke, J. Reschke, V. Kirchhoff, S. Schneider, F. Milde, *Surf. Coat. Technol.* 61 (1993) 331.
- [26] P. J. Kelly, R. D. Arnell, *Vacuum* 56 (2000) 159.
- [27] P. J. Kelly, C. F. Beevers, P. S. Henderson, R. D. Arnell, J. W. Bradley, H. Bäcker, *Surf. Coat. Technol.* 174-175 (2003) 795.
- [28] C. Bondoux, P. Prene, P. Belleville, F. Guillet, S. Lambert, B. Minot, R. Jerisian, *J. Europ. Ceramic. Soc.* 25 (2005) 2795.

-
- [29] T. Welzel, S. Welzel, F. Richter, *Time-resolved investigation of the optical emission in a pulsed magnetron deposition discharge*, in: E. M. van Veldhuizen (ed.), *Proceedings of the 27th International Conference on Phenomena in Ionised Gases*, Eindhoven, the Netherlands, July 17-22, 2005, #8-082.
- [30] A. Belkind, A. Freilich, R. Scholl, *Surf. Coat. Technol.* 108-109 (1998) 558.
- [31] A. Belkind, A. Freilich, R. Scholl, *J. Vac. Sci. Technol. A* 17(4) (1999) 1934.
- [32] P. J. Kelly, P. S. Hendersson, R. D. Arnell, G. A. Roche, D. Carter, *J. Vac. Sci. Technol. A* 18(6) (2000) 2890.
- [33] P. S. Henderson, P. J. Kelly, R. D. Arnell, H. Bäcker, J. W. Bradley, *Surf. Coat. Technol.* 174-175 (2003) 779.
- [34] R. D. Arnell, P. J. Kelly, J. W. Bradley, *Surf. Coat. Technol.* 188-189 (2004) 158.
- [35] D. A. Glocker, *J. Vac. Sci. Technol A* 11, 6 (1993) 2989.
- [36] J. W. Bradley, H. Bäcker, P. J. Kelly, R. D. Arnell, *Surf. Coat. Technol.* 135 (2001) 221.
- [37] J. W. Lee, J. J. Cuomo, M. Bourham, *J. Vac. Sci. Technol. A* 22, 2 (2004) 260.
- [38] L. Mahoney, G. McDonough, D. Carter, G. Roche, H. Walde, *Substrate and Plasma Heating within High Frequency Pulsed-DC Magnetron Sputtering Applications*, 46th AVS Int. Symp., Seattle, Washington, USA, October 25-29, 1999.
- [39] H. Bartzsch, P. Frach, K. Goedicke, *Surf. Coat. Technol.* 132 (2000) 244.
- [40] J. W. Bradley, H. Bäcker, P. J. Kelly, R. D. Arnell, *Surf. Coat. Technol.* 142-144 (2001) 337.
- [41] J. Vleck, A. D. Pajdarova, J. Musil, *Contrib. Plasma Phys.* 44 (2004) 426.
- [42] J. W. Bradley, T. Welzel, *Plasma Diagnostics*, in: D. Depla, S. Mahieu (eds.), *Reactive Sputter Deposition*, Springer Series in Materials Science 109, Springer-Verlag, Berlin, Heidelberg, 2008, ch. 6.
- [43] J. W. Bradley, T. Welzel, *Physics and Phenomena in Pulsed Magnetrons: An Overview*, *J. Phys. D: Appl. Phys.* 42 (2009) 093001.

-
- [44] H. M. Katsch, C. Manthey, J. A. Wagner, H. F. Döbele, Surf. Coat. Technol. 200 (2005) 831.
- [45] V. Stranak, J. Blazek, S. Wrehde, P. Adamek, Z. Hubicka, M. Tichy, P. Spatenka, R. Hippler, Contrib. Plasma Phys. 48 (5-7) (2008) 503.
- [46] I. Langmuir, H. Mott-Smith, General Electric Review 26, 11 (1923) 731.
- [47] E. O. Johnson, L. Malter, Phys. Rev. 80, 1 (1950) 58.
- [48] R. Pintaske, T. Welzel, N. Kahl, M. Schaller, J. Hahn, F. Richter, Surf. Coat. Technol. 90, 3 (1997) 275.
- [49] F. Richter, R. Pintaske, H. Hahn, T. Welzel, *Deposition of Cubic Boron Nitride by Magnetron Sputtering: Process Diagnostics and Film Characterization*, in A. Kumar, Y.-W. Chang, R.W.J. Chia (eds.): *Hard Coatings Based on Borides, Carbides and Nitrides: Synthesis, Characterization and Applications*, The Minerals, Metals and Materials Society, Warrendale, PA, USA, 1998, 153.
- [50] J. Hahn, F. Richter, R. Pintaske, M. Röder, E. Schneider, T. Welzel, Surf. Coat. Technol. 92 (1997) 129.
- [51] T. Welzel, T. Pfeifer, T. Dunger, F. Richter, Surf. Coat. Technol. 166, 1 (2003) 51.
- [52] T. Pfeifer, F. Richter, T. Welzel, H. Kupfer, P. Willich, J. Appl. Phys. 93, 4 (2003) 2009.
- [53] T. Welzel, F. Richter, Surf. Coat. Technol. 174-175 (2003) 658, 179 (2004) 118.
- [54] T. Welzel, I. Dani, F. Richter, Plasma Sources Sci. Technol. 11 (2002) 351.
- [55] L. Bardos, H. Barankova, T. Welzel, I. Dani, S. Peter, F. Richter, J. Appl. Phys. 90, 4 (2001) 1703.
- [56] K. Yamamoto, T. Okuda, J. Phys. Soc. Jap. 11, 1 (1956) 57.
- [57] S. Klagge, M. Tichy, Czech. J. Phys. B35, 5 (1985) 988.

-
- [58] A. A. Sonin, AIAA Journal 4, 9 (1966) 1588, A. A. Sonin, *The Behaviour of Free Molecule Cylindrical Langmuir Probes in Supersonic Flows and Their Application to the Study of the Blunt Body Stagnation Layer*, UTIAS Report 109, Institute for Aerospace Studies, University of Toronto, 1965.
- [59] T. Dunger, T. Welzel, B. Berger, F. Richter, *Temporal and spatial development of the charge carrier distribution on pulsed magnetron discharges: influence of substrate position*, SVC – 50th Annual Technical Conference Proceedings, The Society of Vacuum Coaters, 2007, 431.
- [60] F. Richter, T. Welzel, T. Dunger, H. Kupfer, Surface Engineering 20, 3 (2004), 163; Surface Engineering 20, 5 (2004) 400.
- [61] I. Swindells, P.J. Kelly, J. W. Bradley, New J. Phys. 8 (2006) 47.
- [62] A. Belkind, A. Freilich, J. Lopez, Z. Zhao, W. Zhu, K. Becker, New J. Phys. 7 (2005) 90.
- [63] P. Bryant, S. A. Voronin, J. W. Bradley, A. Vetushka, J. Appl. Phys. 102 (2007) 043302.
- [64] T. Welzel, T. Dunger, F. Richter, Plasma Processes and Polymers 4, S1 (2007) S931.
- [65] R. Pintaske, T. Welzel, M. Schaller, N. Kahl, J. Hahn, F. Richter, Surf. Coat. Technol. 99, 3 (1998) 266.
- [66] S. Welzel, *Untersuchungen einer gepulsten Magnetronentladung bei der Abscheidung von Oxidschichten mittels optischer Emissionsspektroskopie und elektrischer Sonden (Investigation of a pulsed magnetron discharge for the deposition of oxide films by means of optical emission spectroscopy and electrical probes)*, Diploma thesis, Chemnitz University of Technology, Institute of Physics, 2004.
- [67] J. B. Boffard, C. C. Lin, C. A. DeJoseph Jr., J. Phys. D: Appl. Phys. 37 (2004) R143.
- [68] T. Dunger, T. Welzel, S. Welzel, F. Richter, Surf. Coat. Technol. 200, 5-6 (2005) 1676.

-
- [69] T. Dunger, T. Welzel, I. Swindells, G.C.B. Clarke, J. W. Bradley, P. J. Kelly, *Time-Resolved Investigation of the Electron Energies in a Pulsed Magnetron Discharge by Means of Optical Emission Spectroscopy (OES) of He and Ar Atoms, Project Report to a DAAD Personal Exchange Project, Liverpool/Chemnitz, 2005.*
- [70] T. Dunger, *Plasmadiagnostische Charakterisierung gepulster Magnetronentladungen (Plasma diagnostic characterisation of pulsed magnetron discharges)*, PhD thesis, Chemnitz University of Technology, Institute of Physics, 2009, in preparation.
- [71] T. Welzel, T. Dunger, S. Welzel, H. Kupfer, F. Richter, *Surf. Coat. Technol.* 200, 1-4 (2005) 630.
- [72] J. E. Chilton, J. B. Boffard, R. S. Schappe, C. C. Lin, *Phys. Rev. A* 57, 1 (1998) 267.
- [73] G. A. Piech, J. B. Boffard, M. F. Gehrke, L. W. Anderson, C. C. Lin, *Phys. Rev. Lett.* 81, 2 (1998) 309.
- [74] J. Lopez, W. Zhu, A. Freilich, A. Belkind, K. Becker, *New J. Phys.* 38 (2005) 1769.
- [75] T. Weber, J. B. Boffard, C. C. Lin, *Phys. Rev. A* 68 (2003) 032719.
- [76] R. O. Jung, J. B. Boffard, L. W. Anderson, C. C. Lin, *Phys. Rev. A* 75 (2007) 052707.
- [77] R. F. Kemp, J. M. Sellen, *Rev. Sci. Instrum.* 37 (1966) 455.
- [78] N. Hershkowitz, B. Nelson, J. Pew, D. Gates, *Rev. Sci. Instrum.* 54 (1983) 29.
- [79] T. Welzel, T. Dunger, F. Richter, *Determination of Spatio-temporal Plasma Potential Variations in Asymmetric Bipolar Pulsed DC Magnetron Discharges by Emissive Probes*, in: J. Schmidt, M. Simek, S. Pekarek, V. Prukner (eds), *Proceedings of the 28th International Conference on Phenomena in Ionised Gases*, Prague, Czech Republic, July 15-20, 2007, 1585-1588, #4P06 17 (ISBN 078-80-87026-01-4).
- [80] M. A. Makowski, G. A. Emmert, *Rev. Sci. Instrum.* 54 (1983) 830.
- [81] M. Y. Ye, S. Takamura, *Phys. Plasmas* 7 (2000) 3457.

-
- [82] R. Schrittwieser, C. Ionita, P. Balan, R. Gstrein, O. Grulke, T. Windisch, C. Brandt, T. Klinger, R. Madani, G. Amarandei, A. K. Sarma, *Rev. of Sci. Instrum.* 79, 8 (2008) 083508.
- [83] J. W. Bradley, S. K. Karkari, A. Vetushka, *Plasma Sources Sci. Technol.* 13 (2004) 189.
- [84] S. K. Karkari, A. Vetushka, J. W. Bradley, *J. Vac. Sci. Technol.* A21 (2003) L28.
- [85] A. Vetushka, S. K. Karkari, J. W. Bradley, *J. Vac. Sci. Technol.* A22 (2004) 2459.
- [86] J. W. Bradley, S. K. Karkari, A. Vetushka, *Surf. Eng.* 20 (2004) 186.
- [87] S. A. Voronin, G. C. B. Clarke, M. Cada, P. J. Kelly, J. W. Bradley, *Meas. Sci. Technol.* 18 (2007) 1872.
- [88] G. J. Peter (Inficon), private communication.
- [89] S. M. Rosnagel, *J. Vac. Sci. Technol.* A6 (1988) 19.
- [90] I. Kolev, A. Bogaerts, *J. Appl. Phys.* 104 (2008) 093301.
- [91] S. Mahieu, D. Depla, *Appl. Phys. Lett.* 90 (2007) 121117.
- [92] K. Ellmer, *J. Phys. D.: Appl. Phys.* 33 (2000) R17.
- [93] M. Zeuner, H. Neumann, J. Zalman, H. Biedermann, *J. Appl. Phys.* 83 (1998) 5083.
- [94] S. Mraz, J. M. Schneider, *Appl. Phys. Lett.* 89 (2006) 051502.
- [95] S. Mraz, J. M. Schneider, *J. Appl. Phys.* 100 (2006) 023503.
- [96] T. M. Miller, *Electron Affinities*, in: D. R. Lide, H. P. R. Frederikse (eds.), *CRC Handbook of Chemistry and Physics*, CRC Press, Inc., Boca Raton, Ann Harbor, London, Tokyo, 1994, ch. 10.
- [97] T. Welzel, B. Liebig, T. Dunger, unpublished work.
- [98] M. A. Lieberman, A. J. Lichtenberg, *Principles of Plasma Discharges and Materials Processing*, John Wiley & Sons, Inc., New York, Chichester, Brisbane, Toronto, Singapore, 1994, ch. 8.

-
- [99] J. T. Gudmundsson, I. G. Kouznetsov, K. K. Patel, M. A. Lieberman, *J. Phys. D: Appl. Phys.* 34 (2001) 1100.
- [100] J. T. Gudmundsson, E. G. Thorsteinsson, *Plasma Sources Sci. Technol.* 16 (2007) 399.
- [101] F. Richter, T. Welzel, R. Kleinhempel, T. Dunger, *Investigation of the ion energies at the substrate in d.c. and pulsed d.c. magnetron sputtering*, in: R. de Gryse, D. Depla, D. Poelman, S. Mahieu, W. P. Leroy, H. Poelman (eds.), *Proceedings of the 14th Int. Conf. on Thin Films (ICTF14) & Reactive Sputter Deposition 2008 (RSD 2008)*, Gent, Belgium, November 17 – 20, 2008, pp. 87-90 (ISBN 978 90 334 7347 0).
- [102] T. Welzel, T. Dunger, R. Kleinhempel, K. Khedhri, W. Hoyer, T. Gopakumar, T. Schulze, M. Hietschold, F. Richter, Final Report to the project '*Neue PVD-Technologien zur hochproduktiven Abscheidung von Funktionsschichten für die Photovoltaik*' (*New PVD technologies for high-productive deposition of functional thin films for photovoltaics*), project number 11689/1864, 23/04/2008.
- [103] C. Muratore, J. J. Moore, J. A. Rees, *Surf. Coat. Technol.* 163 (2003) 12.
- [104] M. Misina, J. W. Bradley, H. Bäcker, Y. Aranda-Gonzalvo, S. K. Karkari, D. Forder, *Vacuum* 68 (2003) 171.
- [105] J. W. Bradley, H. Bäcker, Y. Aranda-Gonzalvo, P. J. Kelly, R. D. Arnell, *Plasma Sources Sci. Technol.* 11 (2002) 174.
- [106] S. K. Karkari, H. Bäcker, D. Forder, J. W. Bradley, *Meas. Sci. Technol.* 13 (2002) 1431.
- [107] F. Richter, T. Welzel, R. Kleinhempel, T. Dunger, T. Knoth, M. Dimer, F. Milde, *Ion energy distributions in AZO magnetron sputtering from planar and rotatable magnetrons*, *Surf. Coat. Technol.* (2009), accepted, DOI: 10.1016/j.surfcoat.2009.09.034.
- [108] J. W. Bradley, T. Welzel, *Physics and Phenomena in Pulsed Magnetrons: An Overview*, *J. Phys. D: Appl. Phys.* 42 (2009) 093001.
- [109] D. Depla, G. Buyle, J. Haemers, R. De Gryse, *Surf. Coat. Technol.* 200 (2006) 4329.

-
- [110] R. A. Scholl, *Power Supplies for Pulsed Plasma Technologies: State-of-the-Art and Outlook*, Whitepaper Advanced Energy, (2001) SL-WHITE9-270-01 1M.
- [111] S. Berg, T. Nyberg, *Thin Solid Films* 476 (2005) 215.
- [112] S. Schiller, U. Heisig, C. Korndörfer, G. Beister, J. Reschke, K. Steinfeld, J. Strümpfel, *Surf. Coat. Technol.* 33 (1987) 405.
- [113] I. Safi, *Surf. Coat. Technol.* 127 (2000) 203.
- [114] V. Kirchhoff, U. Heisig, *Surf. Coat. Technol.* 59 (1993) 101.
- [115] H. Kupfer, R. Kleinhempel, M. Herrmann, T. Welzel, F. Richter, U. Krause, T. Kopte, C. Peters, P. Frach, Y. Cheng, *A Controlled Pulsed Reactive Magnetron Sputtering Process for Oxide Film Deposition*, in: Ed. M.A. Aegeter, V. Kirchhoff (Eds.), *Proceedings of the 6th International Conference on Coatings on Glass and Plastics*, Dresden, Germany, June 18 – 22, 2006, p. 85, Published by the organizing committee.
- [116] private communication H. Bäcker (Pilkington Germany)
- [117] A.P. Ehasarian, R. New, P. Eh. Hovespian, J. Böhlmark, J. Alami, U. Helmersson, *47th Annual Technical Conference Proceedings of the Society of Vacuum Coaters*, Dallas, TX, USA, April 24–29, 2004, p. 437.
- [118] J. Musil, J. Lestina, J. Vlcek, T. Tölg, *J. Vac. Sci. Technol.* A19 (2) (2001) 420.
- [119] S. Mahieu, K. Van Aeken, D. Depla, *Transport of Sputtered Particles Through the Gas Phase*, in: D. Depla, S. Mahieu (eds.), *Reactive Sputter Deposition*, Springer Series in Materials Science 109, Springer-Verlag, Berlin, Heidelberg, 2008, ch. 6.
- [120] K. Meyer, I. K. Schuller, C. M. Falco, *J. Appl. Phys.* 52(9) (1981) 5803.
- [121] A. Gras-Marti, J. A. Valles-Abarca, *J. Appl. Phys.* 54(2) (1983) 1071.
- [122] K. Ellmer, D. Lichtenberger, *Surf. Coat. Technol.* 74-75 (1995) 586.
- [123] A. Belkind, F. Jansen, *Surf. Coat. Technol.* 99 (1998) 52.
- [124] G. Buyle, W. De Bosscher, D. Depla, K. Eufinger, J. Haemers, R. De Gryse, *Vacuum* 70 (2003) 29.

References available as reprints

- [A1] T. Welzel, T. Dunger, H. Kupfer, F. Richter, *J. Appl. Phys.* 96 (2004) 6994.
- [A2] T. Welzel, T. Dunger, F. Richter, *Surf. Coat. Technol.* 201, 7 (2006) 3959.
- [A3] T. Welzel, T. Dunger, B. Liebig, F. Richter, *New J. Phys.* 10 (2008) 123008.
- [A4] T. Welzel, R. Kleinhempel, T. Dunger, F. Richter, *Ion Energy Distributions in Magnetron Sputtering of Zinc Aluminium Oxide*, *Plasma Processes and Polymers*, in press, DOI: 10.1002/ppap.200930805.

List of frequently used symbols

| | |
|------------------------------|---|
| A | (surface) area |
| B | magnetic field (induction) |
| C | capacitance |
| d | separation, distance (S – between substrate and target) |
| D | bond strength |
| e | elementary charge: $1.602 \cdot 10^{-19}$ As |
| E | energy (0 – initial, aff - affinity, e – electron, i – ion, iz – ionisation, th – sputter threshold) |
| E | electric field (br – breakdown) |
| f | frequency (iz – ionisation, pl,e – electron plasma, pl,i – ion plasma) |
| g | factor of unbalance |
| H _s | heat of sublimation |
| I | current (d – double probe, D – discharge, dc – delivered by dc supply, i – ion, off – during 'off' time, 'on' – during 'on' time, plas – delivered to the plasma) |
| j | current density |
| J | (emission) intensity |
| k | rate coefficient |
| k _B | Boltzmann constant: $1.381 \cdot 10^{-23}$ J/K |
| m _e | electron mass |
| M | mass (i – ion, g – gas atom) |
| n | density (0 – initial, e – electrons, g – ground state, n – (neutral) gas, k – excited state) |
| N | particle number (therm – thermalised) |
| p | pressure |
| P | discharge power (dc – delivered by dc supply, off – during 'off' time, 'on' – during 'on' time, plas – delivered to the plasma) |
| q | particle charge |
| Q | charge |
| r | radius (c – gyration, g – gas atom, p – probe, s – sputtered atom) |
| R | projected range |
| s | sheath thickness (CL – Child-Langmuir, M – matrix) |
| s _n ^{TF} | rdcued stopping power |
| S _n | nuclear stopping power |
| t | time |
| T | temperature (e – electrons, i – ions, n – neutrals) |
| T | pulse period |

| | |
|---------------------|---|
| U | potential difference, voltage (b – breakdown, CL – Child-Langmuir, d – double probe, dc – delivered by dc supply, off – during ‘off’ time, ‘on’ – during ‘on’ time, plas – delivered to the plasma, T – target) |
| U_s | surface binding energy |
| v | velocity (B – Bohm (ion acoustic), th – thermal) |
| V | potential (fl – floating, pl – plasma, S – substrate, T – target) |
| $w_{1/2}$ | half width |
| W | fit values for sputtering yield |
| x | cartesian coordinate, distance |
| y | cartesian coordinate |
| Y | (sputter) yield |
| z | cartesian coordinate, distance |
| Z | atomic number |
| α | first Townsend coefficient |
| χ | electronegativity |
| ε | relative static permittivity, dielectric constant |
| $\hat{\varepsilon}$ | reduced energy |
| ε_0 | vacuum permittivity: $8.854 \cdot 10^{-12}$ As/Vm |
| Φ | energy distribution function |
| γ_{iSEE} | ion-induced secondary electron emission (second Townsend) coefficient |
| Γ | energy transfer factor |
| η | duty cycle |
| φ | (ejection) angle |
| κ, κ^* | mass ratio function |
| λ | length (D – Debye, mfp – mean free path) |
| μ | mass ratio |
| ρ | fit value for sputtering yield |
| σ | cross section (br – breakdown) |
| σ | surface charge density |
| τ | duration (off – ‘off’ time, on – ‘on’ time) |
| τ_{dec} | decay constant |
| ω | plasma (angular) frequency (e – electrons, i – ions) |
| Ω | solid angle |

List of Publications

Book chapters:

J. W. Bradley, T. Welzel, *Process Diagnostics*, in: D. Depla, S. Mahieu, *Reactive Sputtering Deposition* (Springer Series in Materials Science 109), Springer-Verlag, Berlin, Heidelberg, 2008, Chapter 7, p. 255-300 (ISBN: 3540766626).

Refereed papers and conference proceedings:

T. Welzel, T. Dunger, H. Kupfer, F. Richter, *Time-resolved Double LANGMUIR Probe Measurements in a Mid-frequency Pulsed Magnetron Discharge*, in: J. Meichsner, D. Loffhagen, H.-E. Wagner (eds.), *Proceedings of the 26th International Conference on Phenomena in Ionized Gases (ICPIG-26)*, Greifswald, Germany, July 15-20, 2003, vol. 1, p. 151 (ISBN 3-00-011689-3).

F. Richter, T. Welzel, T. Dunger, H. Kupfer, *Time-resolved Langmuir probe characterisation of reactive pulse magnetron sputtering of MgO thin films*, *Surface Engineering* 20 (2004) 3, 163-166, *Surface Engineering* 20 (2004) 5, 400-400.

F. Richter, T. Welzel, T. Dunger, H. Kupfer, *Time-resolved Characterisation of Pulsed Magnetron Discharges Using Langmuir Probes*, *Surf. Coat. Technol.* 188-189 (2004) 384-391.

T. Welzel, T. Dunger, H. Kupfer, F. Richter, *A Time-Resolved Langmuir Double Probe Method for the Investigation of Pulsed Magnetron Discharges*, *J. Appl. Phys.* 96, 12 (2004) 6994-7001.

T. Welzel, T. Dunger, S. Welzel, H. Kupfer, F. Richter, *Studies of the temporal behaviour of a pulsed magnetron deposition discharge*, *Surf. Coat. Technol.* 200, 1-4 (2005) 630-633.

T. Welzel, S. Welzel, F. Richter, *Time-resolved investigation of the optical emission in a pulsed magnetron deposition discharge*, in: E. M. van Veldhuizen (ed.), *Proceedings of the 27th International Conference on Phenomena in Ionised Gases*, Eindhoven, the Netherlands, July 17-22, 2005, #8-082 (ISBN 90-386-2231-7).

T. Dunger, T. Welzel, S. Welzel, F. Richter, *Time-resolved investigation of an asymmetric bipolar pulsed magnetron deposition discharge: Influence of pressure*, *Surf. Coat. Technol.* 200, 5-6 (2005) 1676-1682.

T. Welzel, T. Dunger, F. Richter, *Reactive Gas Effects in Pulsed Magnetron Sputtering: Time-Resolved Investigation*, *Surf. Coat. Technol.* 201 (2006) 3959-3963.

H. Kupfer, R. Kleinhempel, B. Graffel, T. Welzel, T. Dunger, F. Richter, W.-M. Gnehr, T. Kopte, *AC Powered Reactive Magnetron Deposition of Indium Tin Oxide (ITO) Films from a Metallic Target*, *Surf. Coat. Technol.* 201 (2006) 3964-3969.

T. Welzel, T. Dunger, F. Richter, *Two-Dimensional Double Probe Study of the Temporal Evolution of the Charge Carrier Density in a Pulsed Magnetron*, *Plasma Processes and Polymers* 4, S1 (2007) S931-936.

T. Dunger, H. Kupfer, B. Graffel, R. Kleinhempel, J. Lukas, T. Welzel, F. Richter, *Influence of different pulse modes on the plasma properties in a dual magnetron discharge used for the deposition of Indium Tin Oxide films from a Metallic Target*, *Plasma Processes and Polymers* 4, S1 (2007) S325-329.

R. Kleinhempel, B. Graffel, J. Lukas, H. Kupfer, T. Dunger, T. Welzel, F. Richter, *The influence of thermal load on the Properties of Indium Tin Oxide (ITO) Thin Films and their Correlation to the Process Parameters in Pulsed Dual Magnetron Discharges*, *Plasma Processes and Polymers* 4, S1 (2007) S282-286.

T. Dunger, T. Welzel, B. Berger, F. Richter, *Temporal and spatial development of the charge carrier distribution on pulsed magnetron discharges: influence of substrate position*, *SVC – 50th Annual Technical Conference Proceedings*, The Society of Vacuum Coaters, 2007, 431-435 (ISBN 0737-5921).

T. Welzel, T. Dunger, F. Richter, *Determination of Spatio-temporal Plasma Potential Variations in Asymmetric Bipolar Pulsed DC Magnetron Discharges by Emissive Probes*, in: J. Schmidt, M. Simek, S. Pekarek, V. Prukner (eds), *Proceedings of the 28th International Conference on Phenomena in Ionised Gases*, Prague, Czech Republic, July 15-20, 2007, 1585-1588, #4P06-17 (ISBN 078-80-87026-01-4).

T. Welzel, T. Dunger, B. Liebig, F. Richter, *Spatial and temporal development of the plasma potential in differently configured pulsed magnetron discharges*, *New J. Phys* 10 (2008) 123008.

J. W. Bradley, T. Welzel, *Physics and Phenomena in Pulsed Magnetrons: An overview*, *J. Phys. D: Appl. Phys.* 42 (2009) 093001.

T. Welzel, R. Kleinhempel, T. Dunger, F. Richter, *Ion Energy Distributions in Magnetron Sputtering of Zinc Aluminium Oxide*, *Plasma Processes and Polymers*, in press, DOI: 10.1002/ppap200930805.

F. Richter, T. Welzel, R. Kleinhempel, T. Dunger, T. Knoth, M. Dimer, F. Milde, *Ion energy distributions in ZAO magnetron sputtering from planar and rotatable magnetrons*, *Surf. Coat. Technol.* (2009), DOI:10.1016/j.surfcoat.2009.09.034.

Not or not yet refereed papers or conference proceedings:

H. Kupfer, R. Kleinhempel, M. Herrmann, T. Welzel, F. Richter, U. Krause, T. Kopte, C. Peters, P. Frach, Y. Cheng, *A Controlled Pulsed Reactive Magnetron Sputtering Process for Oxide Film Deposition*, in: Ed. M.A. Aegeter, V. Kirchhoff (Eds.), *Proceedings of the 6th International Conference on Coatings on Glass and Plastics*, Dresden, Germany, June 18 – 22, 2006, page 85, Published by the organizing committee.

Conference Posters:

T. Welzel, T. Dunger, H. Kupfer, F. Richter, *Time-resolved Double LANGMUIR Probe Measurements in a Mid-frequency Pulsed Magnetron Discharge*, 26th Int. Conference on Phenomena in Ionized Gases (ICPIG-26), Greifswald, Germany, July 15 – 20, 2003.

R. Kleinhempel, H. Kupfer, F. Richter, T. Welzel, T. Dunger, *MgO films for PDP applications – the measurement of the ion induced secondary electron emission and optical properties in dependence on the deposition parameters*, 68. DPG-Frühjahrstagung, Regensburg, 8. – 12. 3. 2004.

H. Kupfer, R. Kleinhempel, T. Welzel, T. Dunger, F. Richter, *Reaktive Abscheidung von MgO mittels gepulstem Dualmagnetron*, 12. Bundesdeutsche Fachtagung Plasmatechnologie, Braunschweig, 21.-23.3. 2005.

T. Dunger, T. Welzel, S. Welzel, F. Richter, *Time-resolved investigation of an asymmetric bipolar pulsed reactive magnetron discharge: Influence of pressure*, 32th International Conference on Metallurgical Coatings and Thin Films (ICMCTF '05), San Diego, California, USA, May 2 - 5, 2004.

T. Welzel, S. Welzel, T. Dunger F. Richter, *Time-resolved investigation of the optical emission in a pulsed magnetron deposition discharge*, 27th International Conference on Phenomena in Ionized Gases (ICPIG-27), Eindhoven, the Netherlands, July 17 - 22, 2005.

H. Kupfer, R. Kleinhempel, M. Herrmann, T. Welzel, F. Richter, U. Krause, T. Kopte, C. Peters, P. Frach, Y. Cheng, *A Controlled Pulsed Reactive Magnetron Sputtering Process for Oxide Film Deposition*, 6th International Conference on Coatings on Glass and Plastics, Dresden, June 18 – 22, 2006.

R. Kleinhempel, H. Kupfer, T. Dunger, T. Welzel, B. Graffel, F. Richter, *The Influence of Cross-Magnetron Effect on the Functional Film Properties of ITO Thin Films*, 72. DPG-Frühjahrstagung, Regensburg, 26. – 30. 3. 2007.

T. Welzel, T. Dunger, F. Richter, *Determination of Spatio-temporal Plasma Potential Variations in Asymmetric Bipolar Pulsed DC Magnetron Discharges by Emissive Probes*, 28th International Conference on Phenomena in Ionised Gases, Prague, Czech Republic, July 15 - 20, 2007.

Declarations / Erklärungen

Erklärung gemäß §5, Absatz 1, Satz 5 der Habilitationsordnung der Fakultät für Naturwissenschaften der Technischen Universität Chemnitz

Ich versichere, die vorliegende Arbeit selbständig und ohne andere als die darin angegebenen Hilfsmittel angefertigt zu haben. Stellen in der Arbeit, die wörtlich oder sinngemäß aus anderen Arbeiten entnommen wurden, sind in der Arbeit entsprechend gekennzeichnet.

Erklärung gemäß §5, Absatz 1, Satz 6 der Habilitationsordnung der Fakultät für Naturwissenschaften der Technischen Universität Chemnitz

Ich versichere, die vorliegende Habilitationsschrift an keiner anderen Fakultät zur Begutachtung vorgelegt zu haben. Die Arbeit ist noch nicht anderweitig veröffentlicht worden. Von der derzeit gültigen Habilitationsordnung der Fakultät für Naturwissenschaften der TU Chemnitz habe ich Kenntnis genommen.

Chemnitz, 16. Oktober 2009

Thomas Welzel

Appendix

Reprints

of selected published original works

A time-resolved Langmuir double-probe method for the investigation of pulsed magnetron discharges

Th. Welzel,^{a)} Th. Dunger, H. Kupfer, and F. Richter
Institut für Physik, Technische Universität Chemnitz, D-09107 Chemnitz, Germany

(Received 2 September 2003; accepted 31 August 2004)

Langmuir probes are important means for the characterization of plasma discharges. For measurements in plasmas used for the deposition of thin films, the Langmuir double probe is especially suited. With the increasing popularity of pulsed deposition discharges, there is also an increasing need for time-resolved characterization methods. For Langmuir probes, several single-probe approaches to time-resolved measurements are reported but very few for the double probe. We present a time-resolved Langmuir double-probe technique, which is applied to a pulsed magnetron discharge at several 100 kHz used for MgO deposition. The investigations show that a proper treatment of the current measurement is necessary to obtain reliable results. In doing so, a characteristic time dependence of the charge-carrier density during the “pulse on” time containing maximum values of almost $2 \cdot 10^{11} \text{ cm}^{-3}$ was found. This characteristic time dependence varies with the pulse frequency and the duty cycle. A similar time dependence of the electron temperature is only observed when the probe is placed near the magnesium target. © 2004 American Institute of Physics. [DOI: 10.1063/1.1808481]

I. INTRODUCTION

Since their development of Langmuir in 1923,¹ electrostatic probes have become one of the most important means for the investigation of electric glow discharges. They allow access to the plasma parameters charge-carrier density, electron temperature, and potentials. In contrast to many optical techniques and to integral measurements like electrode voltage or current, a local determination of the plasma parameters is possible, which is important because of the inhomogeneity of most discharges.

A pulsed operation of magnetron sputtering sources has been successfully applied to thin-film deposition processes in recent years.²⁻⁵ Especially in reactive environment, this has been proven to yield enhanced stability of the discharge due to reduced poisoning of the target and improved film quality.⁶ However, most differences in the process characteristics between dc or rf magnetron deposition on the one hand and pulsed deposition in the midfrequency range on the other are still subject to current investigations. Mass spectrometric measurements show that pulsed magnetrons exhibit high ion energies,⁷ and enhanced charge-carrier densities are also expected.⁸ A detailed study of the discharge behavior necessitates the time-resolved measurement of the electron component (density and temperature) and the potential of the plasma. It is therefore necessary to expand the Langmuir probe measurements in terms of time resolution. Up to now, only a few papers deal with time-resolved Langmuir probe measurements in pulsed magnetrons. Bradley and co-workers⁹⁻¹¹ used a Langmuir probe in an asymmetric-bipolar pulsed magnetron and found a remarkable variation of electron density and temperature within the discharge pulse, especially near the switching points. In a similar sys-

tem, Mahoney *et al.*¹² found an increase in an apparent electron temperature with the frequency but no significant changes of the electron density. In their paper, however, they report on the difficulties to measure above 100 kHz due to “noise” on the probe current. Macak *et al.*¹³ and Gudmundsson *et al.*^{14,15} investigated a high-power pulsed magnetron with a flat probe. Similar measurements were done by Böhlmark *et al.*,¹⁶ who combined the probe measurements with time-resolved optical spectroscopy.

All of these papers deal with Langmuir single probes. However, especially in deposition discharges, the Langmuir double probes provide some significant advantages like the symmetry of the probe characteristics and the possibility to measure in high-density plasmas. To our knowledge, only Smith and Overzet^{17,18} applied a time-resolved double probe in their investigation of a pulsed inductively coupled plasma discharge. We have developed a similar double-probe system. The theoretical background and experimental realization are described in Secs. II and III, respectively. The results obtained in pulsed magnetron discharge for MgO deposition are given and discussed in Sec. IV.

II. LANGMUIR DOUBLE PROBE

A single Langmuir probe is always connected to an electrode at fixed potential (e.g., ground). In cases where such an electrode does not exist or the plasma potential is varying significantly, this method is not applicable. This drawback was overcome by the development of the floating double probe by Johnson and Malter.¹⁹ As the whole probe system is floating, a falsification of the probe characteristics due to varying potential is eliminated. This enables probe operation also in discharges with strongly varying potential such as pulsed plasmas. An important advantage of the double probe in the deposition plasmas is its symmetric characteristic when both tips are of equal geometry. Generally, all surfaces

^{a)}Author to whom correspondence should be addressed; FAX: +49(0)371-531-3042; electronic mail: t.welzel@physik.tu-chemnitz.de

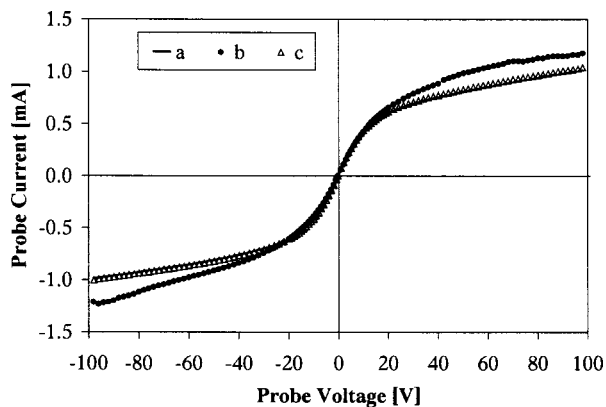


FIG. 1. Probe characteristics of a clean (a) and a contaminated (b) probe. After cleaning by ion bombardment, the symmetric characteristic is obtained again (c). ($\langle P \rangle = 200 \text{ W}$, $f = 200 \text{ kHz}$, and $\tau_{\text{rev}} = 2.0 \mu\text{s}$).

adjacent to the plasma become contaminated with deposits, so also does any probe. In the case of double probes, this can be easily recognized by a deviation from the symmetry of the characteristics, in contrast to the single probe, which has always asymmetric characteristics. Figure 1 gives an example for this situation. While curve (a) is obtained with a clean probe, curve (b) deviates from the symmetric shape due to a conducting deposit on the insulation. This causes an increased effective collection area and hence increased probe current. Just as such contamination is observed, the probe has to be cleaned *in situ*. This can be done by using a third electrode to draw a high electron current with both tips and remove the deposit by heating¹⁴ or—as in our case—by ion sputter cleaning due to alternatively applying a high negative potential (about -300 V) on either of the tips.²⁰ After the cleaning procedure, a symmetric characteristic is reproduced [Fig. 1(c)].

Because most of the characteristic is dominated by the ion saturation current, a determination of the electron energy distribution function (EEDF) is impossible. Thus, one has to assume that the EEDF has at least an approximately Maxwellian shape. The calculation of the electron temperature may then be done by the equivalent resistance method proposed by Johnson and Malter.¹⁹ This method has been extended by Yamamoto and Okuda²¹ to the more realistic case of a varying probe current in the saturation region. The electron temperature is then obtained by²²

$$\frac{kT_e}{e} = \frac{I_{d,fl}}{2 \left(\frac{dI_d}{dU_d} \right)_{fl} - \left(\frac{dI_d}{dU_d} \right)_{sat}}, \quad (1)$$

where $(dI_d/dU_d)_{fl}$ and $(dI_d/dU_d)_{sat}$ are the slopes of the characteristic at the floating potential ($U_d = 0 \text{ V}$) and in the saturation region, respectively. $I_{d,fl}$ is the ion current to the probe at floating potential, which, according to Ref. 21, should be taken from $(dI_d/dU_d)_{sat}$ at a voltage of about 0.15 of the value, that separates the regions mentioned earlier. For simplicity, we used the intersection of $(dI_d/dU_d)_{sat}$ with the ordinate axis instead. Compared to all other sources of uncertainty, in our case, this may lead to an acceptable underestimation of T_e by much less than 5%, provided that

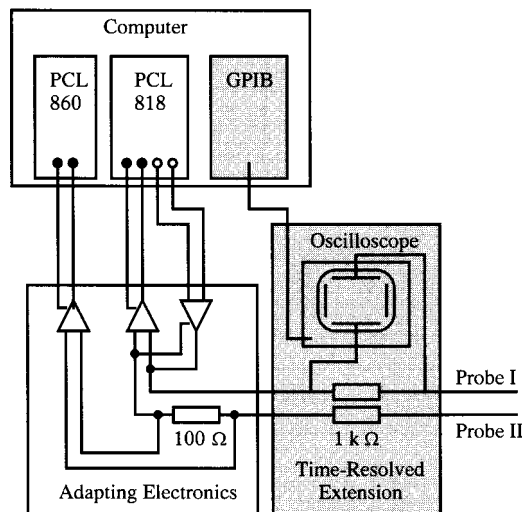


FIG. 2. Schematic of the probe setup. The white part is the original setup for integrated double-probe measurements. The grey-marked part is the extension for time-resolved measurements.

the electrons have a Maxwellian distribution. Subsequent to the calculation of T_e , the charge-carrier density was determined from the probe current at a fixed probe voltage of $10 kT_e/e$ following a method proposed by Sonin,²³ which he had proven to be reliable for different experimental conditions. The charge-carrier density is easily calculated from the Debye length, determined from the graph given in Ref. 23, under the assumption of predominance of singly ionized positive ions. In our case of a gas mixture, for the average mass of the ions, the average mass of the gas species was taken.

The time-resolved measurement was done by fixing the probe voltage and recording the corresponding probe current as a function of time, $I_U(t)$, for 500 equally distributed times. The recording was repeated for 120 different voltages yielding 120 $I_U(t)$ curves. It has to be noted that, as in the static case, voltage step widths were reduced near the floating potential to $\Delta U = 1 \text{ V}$, while being $\Delta U = 2 \text{ V}$ in the saturation regions for optimized resolution and short acquisition time. Following the procedure given in Ref. 17, the matrix of the $I_U(t)$ curves was finally transposed with a computer to yield the usual $I_t(U)$ characteristic for each of the 500 time steps. The calculation of the plasma parameters could then be carried out using the static procedure described earlier for selected $I_t(U)$ curves.

III. EXPERIMENTAL IMPLEMENTATION

A. Probe setup

The probe setup (Fig. 2) is based on a static Langmuir probe system, which was designed for double-probe measurements in stationary discharges.^{20,24,25} The operation of this system is as follows: A user-defined voltage ramp is generated by a digital-to-analog/analog-to-digital (DA/AD) card (PCL-818) of a computer and transformed into the probe voltage of $-100 \dots +100 \text{ V}$ by a self-made adapting electronics. This basically consists of three isolation amplifiers (AD2010AN), one of which providing the voltage trans-

formation. The actual voltage at the output of the adapting electronics is remeasured by means of the second isolation amplifier with the same DA/AD card. The probe current is measured across a 100- Ω resistor inside the adapting electronics by a high-resolution AD card (PCL-860), using the third isolation amplifier. The system additionally provides the opportunity to apply a separate voltage of up to 600 V to the probe to sputter clean it *in situ*, if contamination is observed.

Due to the response time of 200 ms of the PCL-860, one measurement includes many pulse periods yielding an averaged characteristic and is further referred to as “integrated measurement.” Time-resolved measurements in the kilohertz range were therefore not possible. In order to perform the time-resolved measurements described in Sec. II, the setup had to be extended (cf. Fig. 2). A 1-k Ω resistor was inserted in each of the two probe lines just outside the adapting electronics to enable the determination of the probe current from the voltage drop. The value of 1 k Ω —which is 10 times higher than for the static system—was chosen in order to have an increased voltage signal during the time-resolved measurements.

On the other hand, the voltage drop across the resistor should still be small in order to avoid a falsification of the probe voltage. The voltage drop across one of these resistors was recorded by means of a fast-digitizing oscilloscope (Tektronix, TDS 620B) with an impedance of 1 M Ω . The output of the oscilloscope was read out by a general purpose interface bus. To ensure a potential-free measurement, the whole system of adapting electronics, computer, and oscilloscope was powered by an insulating transformer. The current signal was connected to one channel of the oscilloscope with the plasma-sided connection at the 1-k Ω resistor being the middle connector at the oscilloscope and the computer-sided being the oscilloscope ground.

The measurement was triggered by the pulsed target voltage (see next section) to have a defined time base. In the case of time-resolved measurement, the probe voltage was varied stepwise. The $I_U(t)$ characteristics measured for each voltage were averaged over typically 20 trigger pulses. This provided a good compromise between a fast measurement and a good signal-to-noise ratio.

B. Pulsed magnetron

The experiments were carried out in a modified Balzers vacuum assembly with two 4-in. cylindrical magnetron sources.²⁶ One of them was equipped with a magnesium target and was used for the investigations. The base pressure of the turbomolecular-pumped system was about $5 \cdot 10^{-5}$ Pa and the operating pressure was fixed to 0.4 Pa. A gas mixture of 10 (cubic centimeter per minute at STP) sccmO₂ and 50-sccm Ar was used, as it was typically done in MgO deposition experiments. The probe tips (tungsten, $\varnothing=500 \mu\text{m}$, $l=10$ mm) were positioned on the symmetry axis of the magnetron. The tungsten tips were adjusted parallel to the target surface. The distance between each tip and the target surface

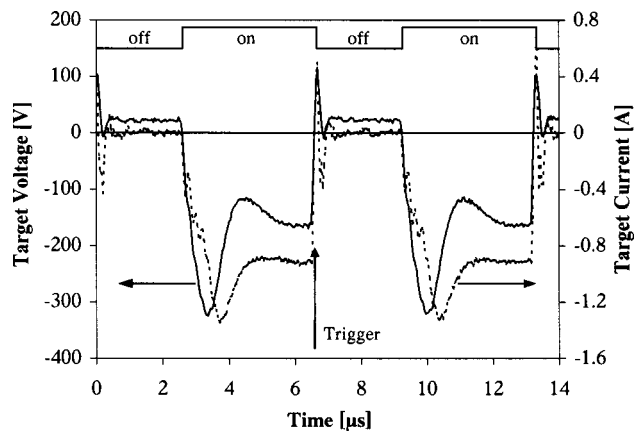


FIG. 3. Typical voltage and current wave forms at the target ($\langle P \rangle = 100$ W, $f = 150$ kHz, and $\tau_{\text{rev}} = 2.6 \mu\text{s}$). The voltage is used as trigger for the probe measurements and the position chosen is marked.

was in most cases 52 mm, thus operating in a region of weak magnetic field where no disturbance of the probe characteristic is to be expected.

The magnetron source was powered by a pulsed power supply (Advanced Energy Pinnacle Plus, max 5 kW, max 350 kHz) in an asymmetric-bipolar mode. An average power of 100 W was chosen for the experiments to avoid strong sputtering and contamination of the probe. The target voltage and target current were measured by a potential divider (Tektronix, P5200) and a current probe (Tektronix, A6306), respectively. A typical example for a frequency of 150 kHz is given in Fig. 3. In the “on” phase of the discharge, the absolute value of the target voltage is initially strongly increased, resulting in some overshoot before it adjusts to a stationary value. The target current slightly runs after the voltage. In the “off” phase—according to the asymmetric-bipolar mode—the target voltage is reversed, being slightly positive, after a short switching peak. The value of the voltage in this phase is 10% of the average target voltage during the on phase to discharge the surface of any dielectric film deposited onto the target surface by electrons. The average current through the target in the off phase is zero within the error of measurement. Following a frequently used convention, the duration of the off phase is referred to as “reverse time” throughout the paper. To get the double-probe measurements in phase with the discharge, a trigger has to be taken from the electrical parameters shown in Fig. 3. As the current probe has to be connected to ground and the double-probe measurement is necessarily ground-free, the trigger can only be obtained from the voltage measurement. It was taken as the switching from the on to the off phase. This slope is the steepest and most stable, whereas the transient at switching on is broader and depends on the pulse parameters. In the experiments, the pulse frequency was varied between 100 and 350 kHz with the reversed time adjusted so that the duty cycle was kept constant at about 60%. Additionally, the reverse time was varied while the frequency was kept constant at 150 kHz.

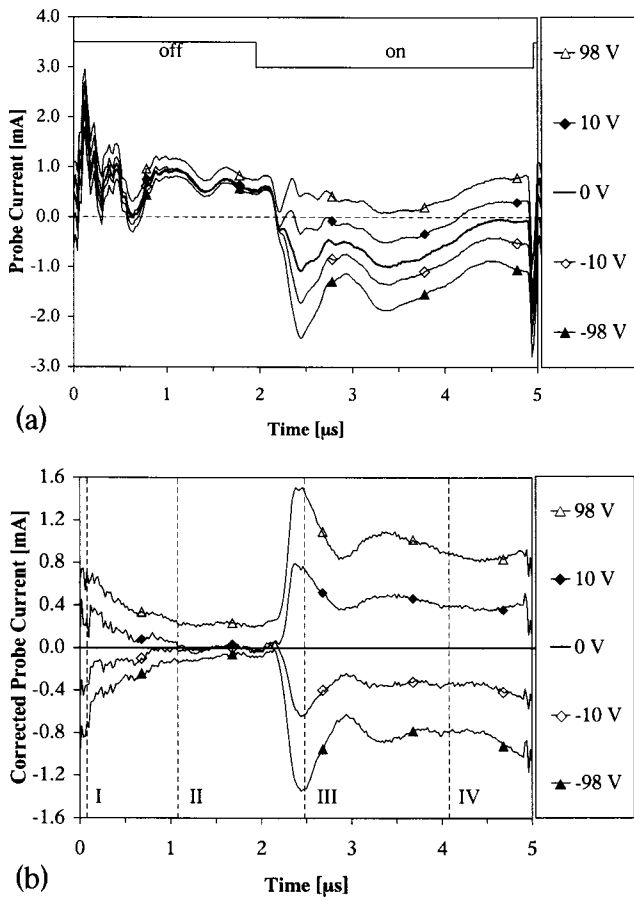


FIG. 4. Time-resolved current signal as directly measured (a) and corrected time-resolved probe current (b) for selected probe voltages ($f = 200$ kHz, $\tau_{rev} = 2.0$ μ s).

IV. RESULTS AND DISCUSSION

A. Probe current

A typical current signal delivered by the probe system for different probe voltages is given in Fig. 4(a). Here, the frequency was set to 200 kHz and the reverse time τ_{rev} was chosen to 2.0 μ s. The current signal can be clearly separated into two different regions: after the trigger impulse, the 2.0- μ s-long off phase of the discharge follows, where almost no dependence of the current on the probe voltage is observed. Subsequently, an approximately 3- μ s-long period with a significant variation of the current with the probe voltage is observed, which corresponds to the on phase of the discharge. The current is increasing with the probe voltage and seems to shift to more positive values as the voltage is increased. However, the current for positive and negative probe voltages is not symmetrical to the zero current, as should be expected for a double probe (cf. Fig. 1). Most significantly, for a zero probe voltage, the measured current is nonzero (partly above 1 mA) and varying periodically with the same period, as given by the power supply. Concerning the double-probe circuitry, this cannot be a real probe current from the plasma because for a probe voltage of 0 V—which is actually remeasured—both tips are on floating potential. A possible spatial variation of the floating potential is unlikely as the reason for the zero-voltage current, firstly, because of the small distance between both tips and, secondly, because

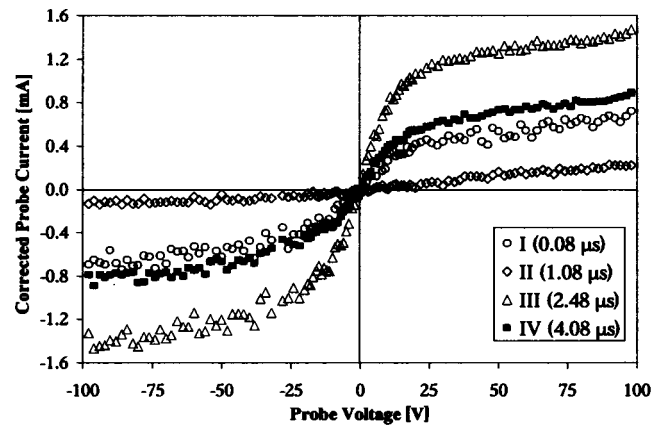


FIG. 5. Double-probe characteristics obtained from the wave forms of Fig. 4(b) for four selected times within one period.

of the relation to the currents at very high probe voltages. Those are sometimes, especially in the off phase, almost the same as the zero-voltage current.

It turned out that this zero-voltage current is superimposed as a background to the currents at each probe voltage and does not change with the probe voltage. It is most likely caused by interference on the lines and the electronic circuitry due to the fast-switching processes within the power supply. Any attempt to suppress it was not successful. Due to its constant nature, it is, however, possible to subtract it from each of the measured currents to obtain the actual probe current drawn from the plasma. The reference signal to subtract was obtained by measuring the current at zero voltage, where the “should be” current is essentially zero and the measured current is therefore the pure background signal. Subtracting this from each of the curves of Fig. 4(a) results in the actual probe current given in Fig. 4(b). Now, the currents still exhibit the typical time dependence correlated to the driving power supply but are additionally almost symmetrical to the zero line. As expected, this actual probe current is now higher in the on phase than in the off phase.

The matrix of the actual probe currents was then transposed according to Sec. II. The result is shown in Fig. 5 for the four selected time values indicated in Fig. 4(b) by the vertical lines. Within the on phase (III and IV), the characteristics obtained are typical double-probe characteristics with the three different slopes (cf. Fig. 1) and a symmetric shape. This also holds for the beginning of the off phase (I), where the charge-carrier density is still high. Only at the end of the off phase (II) it becomes impossible to seriously distinguish between the slopes within different parts of the characteristics. This is likely due to some asymmetry of the probe current [cf. fig. 4(b)] in this region, which is a consequence of the background subtraction. In this region, the apparent probe current is almost completely given by the background signal and the subtraction results in significant uncertainties in the low actual probe current. These effects are, however, negligible when the actual and the correction current are of the same order of magnitude.

B. Charge-carrier density

After the transposition of the matrix of the actual probe currents, one in five of the resulting $I-U$ characteristics was

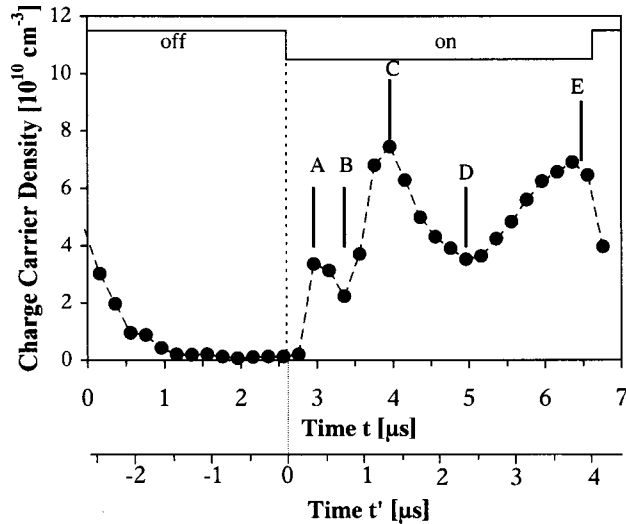


FIG. 6. Typical example of the charge-carrier density in dependence on the time within a period ($f=150$ kHz, $\tau_{\text{rev}}=2.6$ μs). The original axis t refers to the trigger position, the additional axis t' refers to the switching from the off to the on phase, and hence, to the time within the on phase.

evaluated. This resulted in 100 data points over the time interval of typically 1 or 2 periods displayed on the oscilloscope. In case a higher time resolution is needed, it is possible to evaluate more I - U characteristics in particular time intervals. The charge-carrier density obtained in dependence on the time within a period is given as an example in Fig. 6, for a frequency of $f=150$ kHz and a reverse $\tau_{\text{rev}}=2.6$ μs . By switching from the on to the off phase, the charge-carrier density starts to decrease rapidly from its initial value of about $5 \cdot 10^{10}$ cm^{-3} . The behavior can be well described by an exponential decay. For the example given in Fig. 6, the time constant for this decay was determined to be 490 ns. In total, this time constant was found to be independent of the pulse frequency, the duty cycle, and the reverse time, having a value of 450 ± 60 ns. This result is explained by the fact that the geometric conditions, which determine the electron loss, were unaltered. The absolute value of the decay time is essentially lower than that in Ref. 10, where 40 μs have been measured. However, in our system, we have a completely differing geometry with a massive substrate holder and wall parts close to the discharge (see Ref. 26), which may largely promote the drain of electrons.

The behavior of the charge-carrier density in the on phase is not as simple as in the off phase (cf. Fig. 6). Shortly after switching from the off to the on phase the charge-carrier density starts to increase, reaching a first maximum (labeled A) much sooner as either the target current or target voltage is peaking. After going through a minimum (B), a second maximum (C) is reached near the target current maximum until, finally, the charge-carrier density approaches the stationary state (E) after going through another minimum (D). This typical time dependence of the charge-carrier density, with its characteristic extrema Y , was observed for all pulse frequencies and reverse times investigated. Therefore, the extrema have been studied in terms of their height (the value of the charge-carrier density) and their temporal position in dependence on the reverse time at a constant pulse

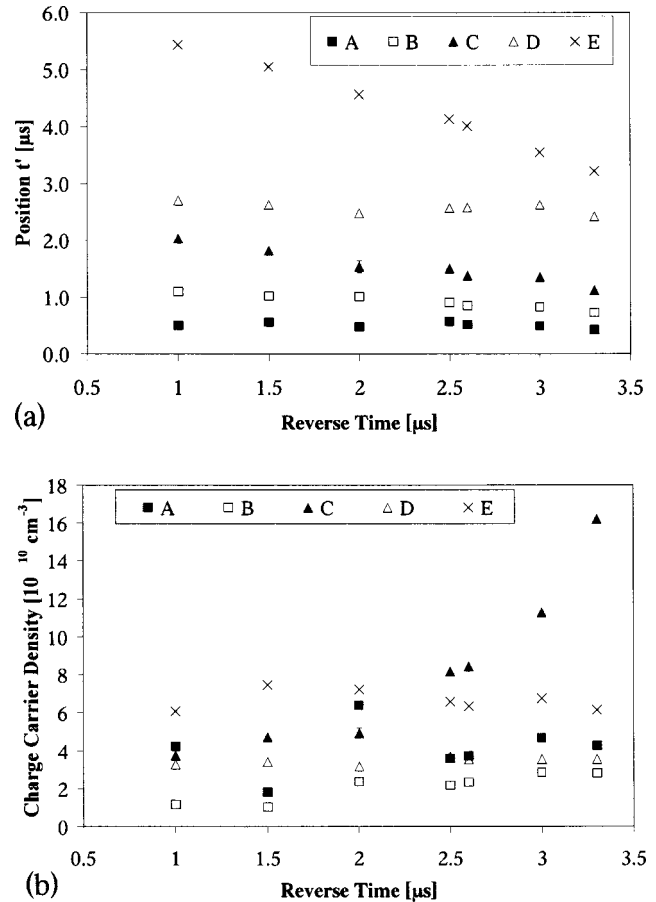


FIG. 7. Temporal positions (a) and heights (b) of the characteristic extrema of the charge-carrier density during the on phase in dependence on the reverse time ($f=150$ kHz).

frequency of $f=150$ kHz. As the discussion is focused on the on phase, a second time scale t' is introduced (cf. Fig. 6) so that the position $t'(Y)$ refers to the point of time where the discharge is switched from off to on.

Figure 7(a) shows the temporal position of the extrema in dependence on the reverse time. The most significant changes are observed for the position of E, which marks the switch-off point of the pulse, which due to the constant pulse frequency is decreasing as the reverse time is increased. The position of D, in contrast, is independent of the reverse time. The position of C is decreasing with the reverse time $t'=2.0$ μs for $\tau_{\text{rev}}=1$ μs to $t'=1.3$ μs for $\tau_{\text{rev}}=3.3$ μs . Contrary, the position of the first maximum A does not show any clear correlation to the reverse time but is constant at $t'=0.5$ μs . B appears slightly earlier with the increased reverse time in accordance with the movement of the position of C. A similar situation is observed with respect to the values of the extrema [Fig. 7(b)]. The value of E is slightly decreasing with the increased reverse time because the on time is decreasing and the position of E moves toward the fixed minimum D, “scanning” the curve in its development to a stationary state (cf. Fig. 6). The value of D is again constant, and also A does not show any clear dependence on the reverse time. Fluctuations occur at low reverse times, especially for A, which are probably due to a partly unstable discharge, where the target surface is not sufficiently dis-

charged during the off phase. The maximum C again shows the most striking dependence on the reverse time increasing from $3.8 \cdot 10^{10} \text{ cm}^{-3}$ for $\tau_{\text{rev}} = 1 \mu\text{s}$ to $1.6 \cdot 10^{11} \text{ cm}^{-3}$ for $\tau_{\text{rev}} = 3.3 \mu\text{s}$, thus becoming the dominant feature for high reverse times, whereas at low reverse time it is at level with A .

A clear dependence of the maximum C on the reverse time at constant frequency was observed both regarding its temporal position and even more its value. A similar effect was also detected when the frequency is varied and the duty cycle is kept constant.²⁷ Comparing the measurements, where several pulse parameters were changed, it turned out that the best parameter to correlate to, especially the maximum C , is actually the reverse time. These results are published in more detail elsewhere.²⁸ Up to now, there is no obvious explanation for the behavior or the occurrence of the two leading maxima in the charge-carrier density during the on phase. However, as they are dependent on the reverse time, i.e., due to the exponential decay during the off phase also on the charge-carrier density at the end of this phase, we propose the following simple conception of their formation: For this, we neglect the complex structure of the magnetic field, suppose an ideal rectangular shape of the voltage wave form and assume that the plasma at the end of the off phase is more or less uniformly distributed. When the negative voltage is applied to the target, the electrons are immediately pushed away from the target, leaving behind a matrix sheath of ions and an ionizing gas during their movement. This is suggested to cause peak A . The ions, which formed the matrix sheath, are subsequently accelerated toward the cathode. Taking a residual charge-carrier density $n = 10^9 \text{ cm}^{-3}$ and a peak voltage $V_0 = -300 \text{ V}$, the dimension of the sheath $d_{\text{Sh}} = (2e_0V_0/en)^{1/2}$ is about 5.7 mm, and an ion originating from the sheath edge, which is accelerated to the cathode, will take about 0.3 μs to cross it. The secondary electrons emitted when the ions hit the surface may again cause an ionization wave directed to the probe, which causes the maximum C . Considering the rise time of the voltage of 0.8 μs to this ion transit time, then the result is with 1.1 μs , quite close to the measured position of C . Following these two processes, which are essentially depending on the residual charge carriers, the discharge develops into the stationary state and a formation of a Child-Langmuir sheath in front of the target. With the help of this simple model, the existence and temporal position of A and C can be explained. For their dependence on the pulse parameters, further investigations are necessary, as for this, the assumptions have to be refined and the complex interplay with the pulse power supply has to be taken into account.

C. Electron temperature

The situation for the electron temperature is given in Fig. 8 for a pulse frequency of $f = 150 \text{ kHz}$ and a reverse time of $\tau_{\text{rev}} = 2.6 \mu\text{s}$, corresponding to Fig. 6. Contrary to the charge-carrier density, no significant changes are observed during the on time. The electron temperature stays almost constant at about 6 eV for all the parameter sets investigated. This still holds until 1 μs into the off phase. Later, considerable deviations are observed and electron temperatures between 2 and

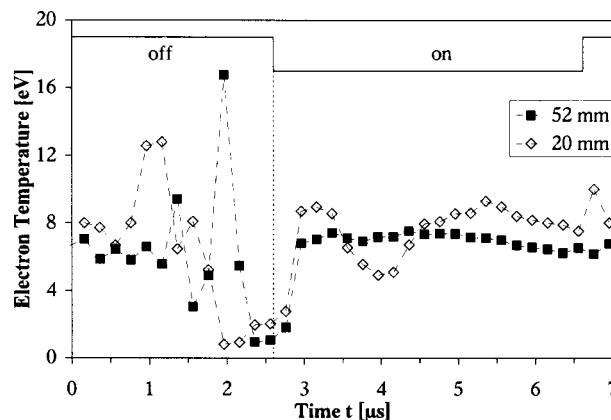


FIG. 8. Electron temperature in dependence on the time within a period for the typical probe distance of 52 mm from the target and for a distance of 20 mm.

16 eV are received. These values, however, are not trustworthy. They result from the poor quality of the probe characteristics in this period of time, as discussed above. It is impractical in this region to fit the three slopes, and thus, the calculation of T_e according to Eq. (1) results in unacceptable errors. The finding of a constant electron temperature within the on phase is contradictory to the work of Bradley *et al.*,¹⁰ who measured the peaks in the electron temperature at the beginning of the on phase of up to 13 eV and after switching off up to 30 eV with a single probe. They also worked with a Pinnacle Plus power supply but with a rectangular magnetron equipped with a titanium target. The most important difference, however, is that they observed the most intense peaks with the probe close to the target (10 mm), whereas we used a distance of 52 mm. To compare the results, we moved the probe closer to the target to a distance of 20 mm (cf. Fig. 8). Similar to Ref. 10, a maximum is then observed at 0.5 μs after switching on the discharge, which reaches up to 9 eV and a second, rather broad, maximum appears at about 3 μs . The minimum in between has a value of only 5 eV. The changes in the electron temperature are thus significantly weaker than in Ref. 10, which might be due to the magnetic-field configuration of the unbalanced magnetrons as their magnetic null is with 60 mm from the target, twice as far as in our case. It is also probable that the double probe is not sensitive enough to such “burst electrons,” as the double probe detects only a small region of the electron energy distribution function near the floating potential. Here, further investigations and a comparison of the different probe methods are necessary in the future.

D. Reliability of the results

The reliability of the time behavior of the charge-carrier density and electron temperature was examined by the comparison of two subsequent periods, which mostly were displayed simultaneously on the oscilloscope screen (similar to Fig. 3). This comparison is an indication of the error, which results from the zero-current subtraction. Maximum deviations of 4% were observed between one period and the other in their on phase. This value is also valid for the first microsecond of the off phase. Later in the off phase, a deviation of

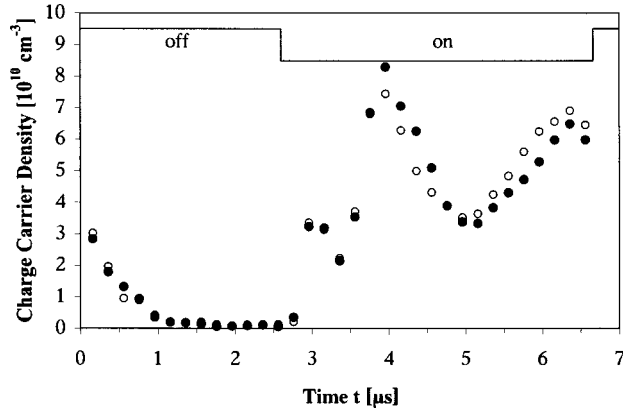


FIG. 9. Temporal behavior of the charge-carrier density over one period ($f=150$ kHz, $\tau_{\text{rev}}=2.6$ μs) obtained in two different measurements.

up to 50% is possible due to the low current. A more realistic error value is obtained when different measurements are compared. In this case, all errors that result from the state of the chamber or discharge, the probe positioning, and the measurement system are included. A typical result is displayed in Fig. 9. The resulting maximum relative deviation is now 10% in the on phase. In the off phase, the maximum deviation is still 50%. For the electron temperature, a somewhat higher deviation is observed: in the on phase, 5% for the comparison of two periods and 15% for the comparison of two different measurements. In the off phase, the maximum deviation may exceed 100%.

To check the time resolution of the system, a sine generator of 100 MHz was connected to the probe tips. The measurement was done firstly with the adapting electronics disconnected and the end of the probe lines short circuited, and secondly, with the complete acquisition electronics connected and powered. Both measurements produced the same smooth sine signal across the resistors with a frequency of 100 MHz and alike amplitude. The circuitry itself is obviously able to measure frequencies of about 100 MHz. The actual time resolution will be influenced by changes in the discharge, too. To obtain a stable current measurement, the sheath around the probe tips has to stabilize. The time for this process can be estimated by the ion frequency, ω_i , assuming that it will be limited by the slow ion movement. Taking an ion mass, m_i , of 40 amu for argon and the value of n_i at the end of the on phase, which is about $5 \cdot 10^{10}$ cm^{-3} (see Sec. IV C), this leads to a value for ω_i of 47 MHz or a period of 130 ns. The time resolution of the whole measurement system connected to the plasma is therefore limited by the changes in the sheath around the probe tips. The changes in the plasma can therefore be measured if they are slower than about 150 ns. This is obviously enough to rely on the observed peak structure because after all, the interval between two data points in Fig. 6 is 200 ns and each of the peaks consists of more than just one data point.

The time-resolved measurements have also been compared to integrated measurements. For this reason, the time-resolved values of the charge-carrier density and the electron temperature have been subsequently averaged mathematically over a period. Figure 10 shows the comparison for the

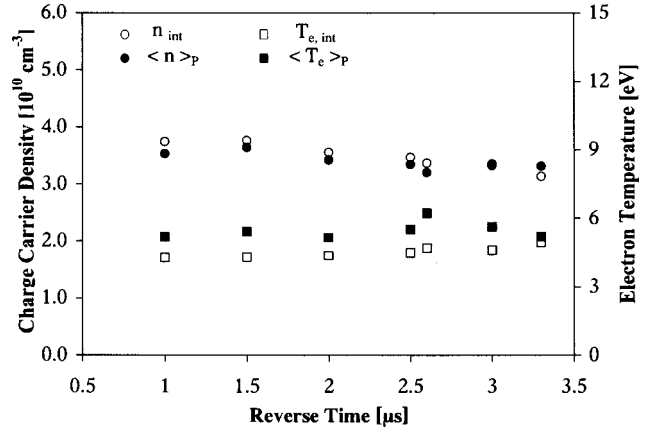


FIG. 10. Comparison of time-resolved and integrated measurements ($f=150$ kHz). The circles and squares represent the charge-carrier density and electron temperature, respectively. The filled and open symbols stand for values averaged over the period and integrated values, respectively.

variation of the reverse time at fixed frequency. The charge-carrier density from the integrated measurement, n_{int} , and the average over the full period calculated from the time-resolved measurement, $\langle n \rangle_p$, agree well. Moreover, these average values stay constant at $3.4 \cdot 10^{10}$ cm^{-3} over the whole range of the reverse time investigated. This is an important fact as the time-resolved measurements reveal significant changes in $n(t)$. The corresponding values for the electron temperature exhibit a weaker coincidence. $T_{e,\text{int}}$ and $\langle T_e \rangle_p$ stay constant at about 6 eV when the reverse time is varied. The scattering of the values is, however, somewhat larger than in the charge-carrier density, as the averaging procedure also includes the unreliable values at the end of the off phase.

V. CONCLUSIONS

A Langmuir double-probe system was developed on the basis of a static system to allow the time-resolved measurements in a midfrequency pulsed magnetron sputtering discharge. The probe current is measured versus time for different voltages, and the data matrix is subsequently transposed. The characteristics turned out to be superimposed by a time-dependent background signal, which was constant for all probe voltages. A subtraction of the zero-voltage current from the measured current, however, provided the actual probe current.

The probe system was applied to an asymmetric-bipolar pulsed magnetron used for MgO deposition. With the correction of the probe current, reliable results were obtained for the charge-carrier density and the electron temperature at most times of the period except for the last part of the off phase. A typical time dependence of the charge-carrier density was found in the on phase with two leading maxima ranging from 0 to $1.6 \cdot 10^{11}$ cm^{-3} and a plateau of about $5 \cdot 10^{10}$ cm^{-3} belonging to the stationary discharge state. It has been shown that the two leading maxima strongly depend on the pulse parameters, but there is no physical explanation for this behavior yet. The typical time dependence revealed, however, provides a basis for a more detailed clarification of pulsed magnetron discharges and the processes in them. Almost no variations in the electron temperature of

about 6 eV were observed in the substrate region but appeared as the probe was approached to the target.

ACKNOWLEDGMENTS

The authors would like to thank P. Schlott and S. Peter for many helpful discussions on the technical details, as well as Th. Förster for the technical assistance. This work was financially supported by the Bundesministerium für Bildung und Forschung (BMBF) under Grant No. 13N8053.

- ¹I. Langmuir and H. Mott-Smith, *Gen. Electr. Rev.* **26**, 731 (1923).
- ²S. Schiller, K. Goedicke, J. Reschke, V. Kirchhoff, S. Schneider, and F. Milde, *Surf. Coat. Technol.* **61**, 331 (1993).
- ³P. J. Kelly and R. D. Arnell, *Vacuum* **56**, 159 (2000).
- ⁴P. J. Kelly, P. S. Henderson, R. D. Arnell, G. A. Roche, and D. Carter, *J. Vac. Sci. Technol. A* **18**, 2890 (2000).
- ⁵A. P. Ehasarian, W.-D. Münz, L. Hultman, U. Helmersson, and I. Petrov, *Surf. Coat. Technol.* **163–164**, 267 (2003).
- ⁶J. O'Brien and P. J. Kelly, *Surf. Coat. Technol.* **142–144**, 621 (2001).
- ⁷M. Misina, J. W. Bradley, H. Bäcker, Y. Aranda-Gonzalo, S. K. Karkari, and D. Forder, *Vacuum* **68**, 171 (2002).
- ⁸H. Bartzsch, P. Frach, and K. Goedicke, *Surf. Coat. Technol.* **132**, 244 (2000).
- ⁹J. W. Bradley, H. Bäcker, P. J. Kelly, and R.D. Arnell, *Surf. Coat. Technol.* **135**, 221 (2001).
- ¹⁰J. W. Bradley, H. Bäcker, P. J. Kelly, and R. D. Arnell, *Surf. Coat. Technol.* **142–144**, 337 (2001).
- ¹¹H. Bäcker, P. S. Henderson, J. W. Bradley, and P. J. Kelly, *Surf. Coat. Technol.* **174–175**, 909 (2003).
- ¹²L. Mahoney, G. McDonough, D. Carter, G. Roche, and H. Walde, *Substrate and Plasma Heating within High Frequency Pulsed-DC Magnetron Sputtering Applications*, 46th AVS International Symposium, Seattle, Washington, USA, 25–29 October 1999.
- ¹³K. Macak, V. Kouznetsov, J. Schneider, U. Helmersson, and I. Petrov, *J. Vac. Sci. Technol. A* **18**, 1533 (2001).
- ¹⁴J. T. Gudmundsson, J. Alami, and U. Helmersson, *Appl. Phys. Lett.* **78**, 3427 (2001).
- ¹⁵J. T. Gudmundsson, J. Alami, and U. Helmersson, *Surf. Coat. Technol.* **161**, 249 (2002).
- ¹⁶J. Böhlmark, J. Alami, U. Helmersson, A. P. Ehasarian, and W.-D. Münz, presentation made at the 30th International Conference on Metallurgical Coatings and Thin Films, San Diego, California, 28 April–2 May 2003.
- ¹⁷B. A. Smith and L. J. Overzet, *Rev. Sci. Instrum.* **69**, 1372 (1998).
- ¹⁸B. A. Smith and L. J. Overzet, *Plasma Sources Sci. Technol.* **8**, 70 (1999).
- ¹⁹E. O. Johnson and L. Malter, *Phys. Rev.* **80**, 58 (1950).
- ²⁰R. Pintaske, Th. Welzel, N. Kahl, M. Schaller, J. Hahn, and F. Richter, *Surf. Coat. Technol.* **90**, 275 (1997).
- ²¹K. Yamamoto and T. Okuda, *J. Phys. Soc. Jpn.* **11**, 57 (1956).
- ²²S. Klage and M. Tichy, *Czech. J. Phys., Sect. B* **35**, 988 (1985).
- ²³A. A. Sonin, *AIAA J.* **4**, 1588 (1966).
- ²⁴Th. Welzel, I. Dani, and F. Richter, *Plasma Sources Sci. Technol.* **11**, 351 (2002).
- ²⁵Th. Welzel and F. Richter, *Surf. Coat. Technol.* **174–175**, 658 (2003); **179**, 118 (2004).
- ²⁶F. Richter, H. Kupfer, P. Schlott, T. Gessner, and C. Kaufmann, *Thin Solid Films* **389**, 278 (2001).
- ²⁷Th. Welzel, Th. Dunger, H. Kupfer, and F. Richter, Time-resolved Double Langmuir Probe Measurements in a Mid-frequency Pulsed Magnetron Discharge, Proceedings of the 26th International Conference on Phenomena in Ionized Gases, Greifswald, Germany, 15–20 July 2003.
- ²⁸F. Richter, Th. Welzel, Th. Dunger, and H. Kupfer, *Surf. Eng.* **20**, 3 (2004).



Reactive gas effects in pulsed magnetron sputtering: Time-resolved investigation[☆]

Th. Welzel^{*}, Th. Dunger, F. Richter

Chemnitz University of Technology, Institute of Physics, D-09107, Germany

Available online 11 September 2006

Abstract

A pulsed magnetron deposition discharge in argon with different admixtures of oxygen as reactive component has been studied. The target material used was magnesium and the pulsed discharge was operated in metallic and reactive mode. The discharge evolution during each pulse has been characterised by the time-resolved Langmuir double probe and time-resolved optical emission spectroscopy. Charge carrier density and optical emission exhibit two more or less strong peaks at the beginning of the “on” phase, the second of which being the most dominant. The temporal development of the discharge is clearly different for the two discharge modes: in the reactive mode, the structures in the “on” phase — except of the first maximum — significantly shift to shorter times compared to the metallic mode. This is suggested to be due to the much higher secondary electron emission coefficient (γ) of MgO in comparison to Mg leading to increased ionisation starting with the second maximum. The first maximum, however, is attributed to residual electrons from the precedent pulse and is thus independent of the γ coefficient. A significant feedback from the discharge to the power supply is observed by changes in the voltage waveform: the more efficient discharge development is accompanied by a sharper and lower peak in the voltage.

© 2006 Elsevier B.V. All rights reserved.

Keywords: Reactive sputtering; Magnetron; Pulsed; Magnesium ([D]); Oxides

1. Introduction

Magnetron sputtering is an established technique to deposit thin films of different materials. Whereas conducting materials can be sputtered using d.c., insulating films or targets are mostly sputtered with r.f. power. This process typically suffers from comparatively low deposition rates. Recently, pulsed d.c. processes in the mid-frequency range between several tens and hundreds of kHz have gained more and more attention. These processes allow the deposition of high quality, insulating, and especially highly transparent oxide films [1–3]. This is a consequence of the periodically interrupted or reversed target voltage which enables a neutralisation of charge accumulated on

the insulating target surface. Less arcing and, hence, better film quality are the result [4–6]. In most cases, pulsed sputtering is combined with a feedback control for the reactive gas flow based on time-averaged discharge characteristics [7]. This allows process operation in the so-called transition mode. Without this control the sputtering process is, in most cases, limited to either the metallic mode with insufficient reactive gas supply and high deposition rate or the reactive mode with excess reactive gas supply but low deposition rate [8]. The operation in the transition region allows the combination of both high deposition rate and high transparency of the films [9]. While this rate effect between metallic and reactive mode has been quite well understood, the differences in the characteristics of the plasma, which additionally may influence the film properties significantly, are less well known. Distinct hysteresis effects in the target voltage course, however, prove that such differences exist. To better understand the fundamental processes leading to these differences, plasma diagnostic measurements, especially also time-resolved within each pulse, have to be carried out (see e.g. the works of the groups of Bradley and Belkind, [10,11]). To perform such time-

[☆] Paper presented at the International Conference on Metallurgical Coatings and Thin Films (ICMCTF 2006), May 1–5, 2006, Town and Country Hotel, San Diego, CA, USA.

^{*} Corresponding author. Tel.: +49 371 531 3038; fax: +49 371 531 3042.

E-mail address: t.welzel@physik.tu-chemnitz.de (Th. Welzel).

resolved studies the operation in both stable modes without a feedback loop is often adequate to simplify the situation. In this paper we present time-resolved investigations of an asymmetric-bipolar pulsed circular magnetron in both metallic and reactive mode with Mg as target material. As diagnostic techniques, a time-resolved Langmuir double probe and time-resolved optical emission spectroscopy (OES) were applied.

2. Experimental

The experiments were performed in a high-vacuum chamber which contained two cylindrical magnetrons, one of which was equipped with a magnesium (\varnothing 100 mm) target and was used for the investigations presented here. The other one was floating. Opposite to these magnetron sources a massive rotatable substrate holder and a shielding in front of it were mounted. The shielding was situated 20 mm away from the substrates which corresponds to a distance of 60 mm from the target surface. The gas mixture was varied between 50 sccm argon (99.995%) and a mixture of 50 sccm Ar and 50 sccm oxygen (99.998%). The pumping speed of the turbomolecular pump was adjusted by means of a regulating valve to obtain a fixed total pressure of 0.4 Pa for each experiment. The discharge was operated in the metallic mode with pure argon and in the reactive mode for oxygen flows higher than 3 sccm. It was powered by a Pinnacle Plus (max. 5 kW, Advanced Energy) power supply in asymmetric-bipolar mode with a small positive target voltage (10% of the average negative value) in the “off” phase.

The power supply was operated in the power controlled mode and the average power was set to 100 W. This low value was mainly chosen to avoid strong sputtering in the metallic mode. The pulse frequency was fixed to 150 kHz and a “reverse” time (duration of the “off” phase) of 2.7 μ s was applied, resulting in a duty cycle of about 0.6.

The time dependence of the charge carrier density was measured with a time-resolved Langmuir double probe which has been developed in-house and described in detail in a previous paper [12]. The probe consisted of two tungsten wires (10 mm length, 500 μ m diameter) which were mounted 52 mm away from the target surface on the axis of symmetry of the discharge. The measurements allow a spatial resolution of several mm and a temporal resolution of about 200 ns depending on the charge carrier density. The time-resolved results were obtained by measuring the $I(t)$ curves for different probe voltages and a reference voltage and subsequently transforming the data matrix to $I(U)$ characteristics for different times. The detection limit of the method is about $5 \cdot 10^9$ cm $^{-3}$. Time-resolved optical emission spectroscopy was carried out with a Jobin Yvon spectrometer (HR 460S) equipped with an intensified CCD camera (ICCD, iStar DH 734, Andor Technology) which allows time-resolution better than 100 ns. Also in the case of the OES, a reference (dark) signal had to be subtracted from the measured values to account for noise. This was done prior to each measurement with the mechanical shutter of the monochromator closed.

3. Results

The temporal development of the charge carrier density during one pulse in the reactive mode (10 sccm O $_2$) is displayed in Fig. 1. In the “on” phase, when a negative voltage is applied at the target, two relatively sharp peaks are observed just at the beginning. Immediately when the target voltage is switched to negative values, a weak maximum — which we have labelled “A” in earlier publications [12,13] — is observed within significantly less than 1 μ s. This is followed by a dominating maximum (labelled “C” [12,13]) 1 to 2 μ s after the “on” phase has started. The driving target voltage itself shows only one maximum just between the two maxima in the charge carrier density. The target current is also peaking only once and lags behind the target voltage (cf. Fig. 1). After having reached its maximum value C, the charge carrier density drops down following the reduction of the target voltage before both quantities reach to a stationary value which would equal the d.c. case. Assuming that the emission of argon lines should be among others proportional to the density of the exciting electrons, it could also serve as a measure of the charge carrier density as long as the electron energy distribution does not change too much. As shown by an analysis of the excitation mechanisms [14,15], this is best fulfilled by the argon line at 750.4 nm. Its emission is also included in Fig. 1. Indeed, the argon emission exhibits a similar behaviour at the beginning of the “on” phase, the subsequent relaxation and transition into some stationary state. The temporal position, especially of the maximum C, is comparable to that measured with the Langmuir double probe. A distinct difference between charge carrier density and optical emission is the intensity of the two maxima compared to the intensity in the rest of the “on” phase. The maximum A is hardly visible in the emission at all. This is believed to be due to the different detection volume: the Langmuir probe measures the charge carrier density space-resolved on the axis of symmetry whereas the optical emission is detected along the line-of-sight parallel to the target surface

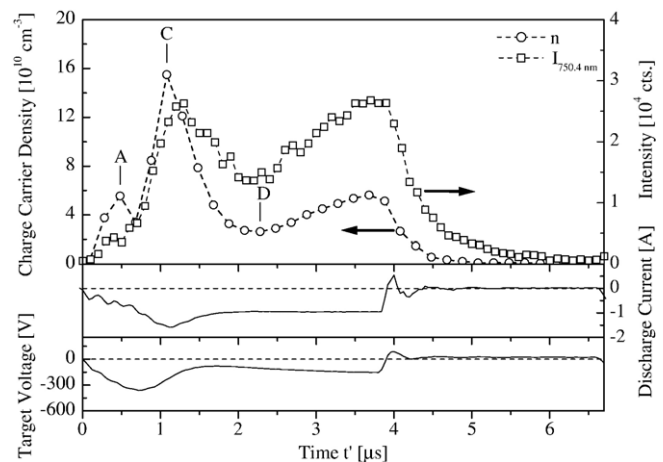


Fig. 1. Time dependence of charge carrier density (n) and optical emission intensity of the 750.4 nm argon line ($I_{750.4 \text{ nm}}$) in reactive mode (10 sccm O $_2$ + 50 sccm Ar).

and, hence, the measurement integrates over the cross section of the discharge. Both techniques reveal a fast decay in the “off” phase when the voltage is reversed to positive values. The time dependence of the charge carrier density can be well fitted with an exponential decay. This yields decay constants of 500 ns for the charge carrier density and 700 ns for the optical emission, respectively, which is essentially the same within the error of measurement.

In Fig. 2, the same time courses are displayed but this time for the metallic mode (0 sccm O₂). In principle, the time courses are similar to those in the reactive mode. There is a weak maximum A both in the charge carrier density and the optical emission. Similarly as before, it is at a temporal position significantly earlier than 1 μs. The second maximum C, however, is strongly delayed in comparison to the reactive mode as it is formed more than 2.5 μs after starting the pulse. This part of the discharge is obviously hindered in its development. This also leads to the situation that the rest of the development observed in the reactive mode, namely the minimum (labelled “D” [12,13]) and the transition to the stationary state, are almost not observed in the metallic mode. The “on” phase is finished before the plasma is able to start its development into the stationary state. This behaviour is again observed with both techniques equivalently. The behaviour in the “off” phase, is, however, comparable to the reactive mode: the decay constant is again about 500 ns.

The temporal positions of the weaker first and the dominant second maximum have both been analysed in more detail. The result is given in Fig. 3. For the second maximum, its position from the optical emission, $I_{\lambda}(C)$ is also displayed. Also, the maximum of the target voltage, U_{Max} is given. Two clear regions can be distinguished from these positions. In the reactive mode, all the maxima referred to as C and U_{Max} appear extremely early in the “on” phase as was observed for the example shown above. The target voltage peak is earliest at times of about 0.8 μs followed almost at the same time by the charge carrier density and the optical emission peak (between 1.1 and 1.5 μs). There is no difference in the appearance of

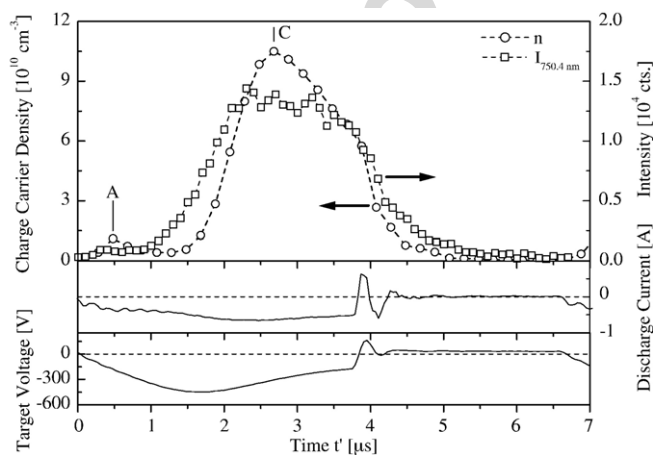


Fig. 2. Time dependence of charge carrier density (n) and optical emission intensity of the 750.4 nm argon line ($I_{750.4 \text{ nm}}$) in metallic mode (0 sccm O₂ + 50 sccm Ar).

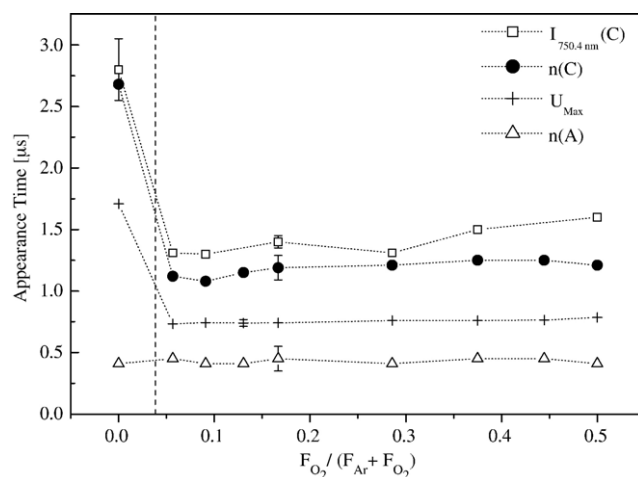


Fig. 3. Temporal position of maxima A and C in the charge carrier density ($n(A)$, $n(C)$) and of C in the optical emission ($I_{750.4 \text{ nm}}(C)$) in dependence on the gas mixture. U_{Max} refers to the peak value of the negative target voltage in the “on” phase. The vertical line indicates the transition from metallic to reactive mode.

either one for different gas mixtures in the reactive mode. As soon as the oxygen flow is reduced below values which are characteristic for the hysteresis (1 to 3 sccm), the appearance times change abruptly to higher values. The target voltage peaks at 1.7 μs and charge carrier density as well as optical emission show the second maximum at about 2.8 μs. The first weaker maximum A in those plasma characteristics, however, does not undergo any significant changes over the whole gas mixture range, including the transition from reactive to metallic mode.

The variation of the height of the maximum C with the gas mixture is given in Fig. 4. For clarity, the values $n(C)$ and $I_{\lambda}(C)$ were normalised to have a value of one at an oxygen flow of 3 sccm, i.e. $F(O_2)/(F(Ar)+F(O_2))=0.057$. There is a clear jump for small changes of the oxygen flow between 0 and 3 sccm characterising the transition from metallic to reactive mode, especially in U_{Max} and $n(C)$. Lesser changes are observed

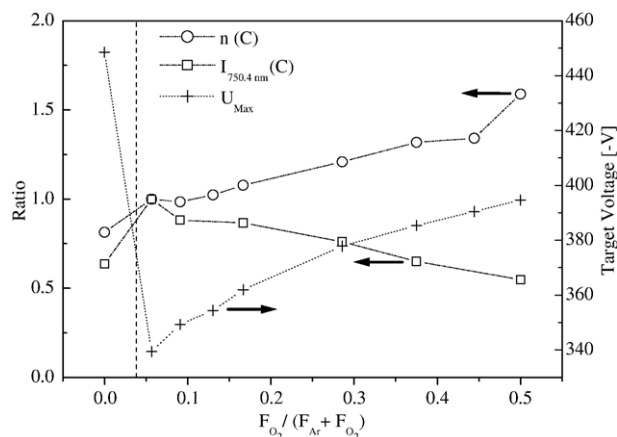


Fig. 4. Height of the maximum C in the charge carrier density (n) and the optical emission ($I_{750.4 \text{ nm}}$) in dependence on the gas mixture given relative to the values at 3 sccm O₂. U_{Max} represents the maximum of the target voltage taken during the Langmuir probe measurements. Its values do not notably differ from those during the OES measurements. The vertical line symbolises the transition from metallic to reactive mode.

when the oxygen flow is increased further in similar steps within the reactive mode. There, all dependences show a nearly linear behaviour. The target peak voltage is increasing for higher oxygen flow. As could be expected, the generation of charge carriers follows the higher accelerating voltage resulting in an increased charge carrier density at the maximum C. However, in this case the optical emission intensity of the argon line does not follow this behaviour. It rather decreases monotonically with increased oxygen content. A possible reason will be discussed in the next section.

4. Discussion

Commonly, to sustain a stable discharge, electrons created by ionising collisions in the volume and secondary electrons released from the cathode are necessary. We have proposed a model that in the initial state of the “on” phase these two processes determine the discharge development one after the other [16]. The model is based on the assumption that ions and electrons from the prior pulse are still present after the “off” phase and that those are almost homogeneously distributed. The electrons are accelerated away from the cathode when the negative voltage is applied. As soon as they have reached enough energy for a sufficient ionisation, i.e. about 100 eV, they cause the first density maximum A. In both the reactive and metallic mode, the equivalent voltage to obtain this energy is reached 0.15 to 0.3 μs after the start of the “on” phase (as indicated in Fig. 5). This is the time when the maximum A is observed in the charge carrier density and the optical emission (cf. Figs. 1 and 2). Although the slope of the voltage rise is different for the two modes, no significant difference in the appearance time is found. There is a very small shift to longer times in the metallic mode but this is considered to be rather below the error of measurement. Subsequent to maximum A the charge carrier density drops because no electrons are left for further ionisation.

The second burst of ionisation is then caused by secondary electrons which are released from the target surface by the bombardment with the residual ions. Due to their higher mass,

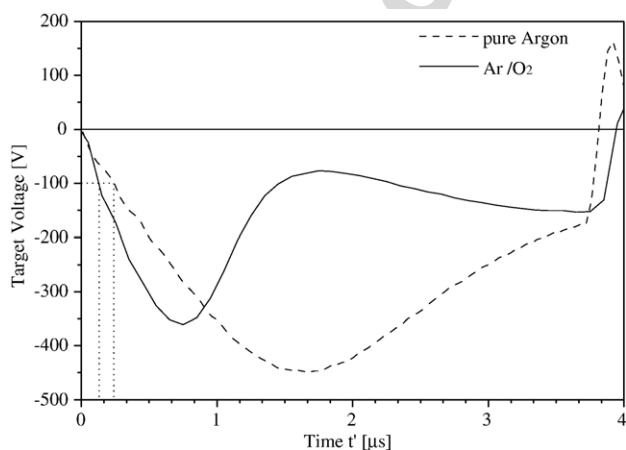


Fig. 5. Comparison of the target voltage time dependence during the “on” phase in metallic (50 sccm Ar) and reactive (10 sccm O_2 + 50 sccm Ar) mode.

they are accelerated much less than the electrons by the target potential and the delay of the second peak is a consequence of their transit time to the target. As soon as the ions reach the target, they — together with the emitted secondary electrons — cause the increase in the target current. The secondary electrons are accelerated by the full target voltage and the subsequent ionisation by collisions is observed almost at once as $n(\text{C})$ due to the low mass and thus high velocity of the electrons.

Comparing the voltage course for the metallic and reactive mode (cf. Fig. 5) it is clear that the voltage rises less in the metallic mode. Probably, there is a feedback from the plasma into the characteristics of the power supply, which is not exactly known. The consequence is that the ions are accelerated less strongly to the target surface and the majority of the secondary electrons is thus released later. This causes the temporal shift of both n and I_λ peaks in the metallic mode compared to the reactive mode. However, this argumentation alone cannot explain the fact that in the metallic mode the maximum of the target voltage, U_{Max} is higher than in the reactive mode but the peak density, $n(\text{C})$ and the emission intensity are lower. Here, the surface properties of the target have to be taken into account because maximum C is related to secondary electrons from it.

MgO has an extremely high ion-induced secondary electron emission coefficient (iSEEC) which is the reason why it is considered to be used as cathode material in flat panel plasma displays [17]. Choi et al. [18] report values of the iSEEC of up to 0.24 for argon ion bombardment of an MgO (111) surface with 500 eV. For most pure metal surfaces, Depla et al. [19] give values well below 0.15 for argon ions independent of the ion energy. Especially for Mg they cite an iSEEC of 0.137. Hence, in the fully reactive mode where the target surface is completely poisoned with MgO a better secondary electron emission is to be expected. This is in agreement with our observations that the average target voltage (displayed at the power supply) to reach the set power of 100 W is -175 V in the metallic and about -100 V in the reactive mode. This explains the behaviour of the charge carrier density maximum C: Although the peak voltage is less in the reactive mode than in the metallic mode, $n(\text{C})$ is higher because of the more efficient electron emission and subsequently ionisation. In other words, the lower peak voltage in the reactive mode is due to the fact that the current necessary to obtain the required power is obtained with less voltage accelerating the electrons. Finally, the extremely different iSEEC of Mg and MgO should be responsible for a further delay of $n(\text{C})$ and $I_\lambda(\text{C})$ against U_{Max} in the metallic mode (cf. Fig. 3): As in the metallic mode, the contribution of the secondary electrons is reduced and the discharge build-up has to be driven more by the volume ionisation. The net electron generation gets less efficient and the discharge development is delayed. Consequently, in the metallic mode $n(\text{C})$ and $I_\lambda(\text{C})$ lag about 1 μs behind U_{Max} whereas in reactive mode the difference is only about 0.6 μs .

Within the reactive mode itself, the changes in the temporal behaviour of the plasma characteristics are not so significant over a wide range of gas mixtures. It seems that differences in the volume ionisation between argon and oxygen play a minor role compared to the surface effect through the secondary

electrons. The appearance time of U_{Max} , $n(\text{C})$, and $I_{\lambda}(\text{C})$ is unchanged within the error of measurement (cf. Fig. 3). Only their height changes slightly (cf. Fig. 4). The peak voltage rises with increasing oxygen content. The charge carrier density $n(\text{C})$ follows this increase. The latter is consistent with the higher energy the secondary electrons gain by the increased target voltage if one assumes that the surface properties do not change significantly once the surface is poisoned in the reactive mode. The higher energy will be converted into a higher ionisation upon collisions. The optical emission shows an oppositional trend, i.e. is decreasing with higher oxygen content. This is in contrast to the expected behaviour: The emission line selected is mainly excited directly [14]. Therefore, one would expect the emission intensity to reproduce the dependence of the charge carrier density on the gas mixture, which is not the case. Here, it has to be noted that the probe measurements were made up for a comparison with the OES to identically match the discharge parameters a couple of months later than the OES measurements. It cannot be excluded that with increasing oxygen flow the excitation conditions worsen leading to a deviation between the charge carrier density and the optical emission. However, it is more likely that in the intervening period between the measurements long-term drift effects, mainly the erosion of the race track, caused this deviation. A first indication for this is that the absolute height of the first maximum A, which is very sensitive to changes of the discharge environment [20], has also changed between the two sets. The effect of the erosion state of the target will be investigated more detailed in the future.

5. Conclusions

We have studied the influence of different Ar/O₂ gas mixtures on the temporal development of a pulsed magnetron discharge with a time-resolved Langmuir double probe and optical emission spectroscopy. Both stable target modes, i.e. the metallic and reactive mode, have been investigated. Charge carrier density and optical emission show two peaks at the beginning of the “on” phase. These peaks are assigned to be i) due to volume ionisation by residual electrons from the previous pulse and ii) to secondary electrons released by ion irradiation from the target. The development, especially of the latter, is predominantly governed by the ion-induced secondary electron emission coefficient (iSEEC) of the target surface as well as by the behaviour of the power supply. The high iSEEC of MgO in the reactive mode leads to a fast development of the discharge compared to the metallic mode. Additionally, the peak charge carrier density is more pronounced in the reactive mode although the target voltage peak is lower than in the metallic mode. It can be concluded that the influence of the gas mixture on the plasma formation within one pulse is dominated indirectly through the surface properties rather than volume

processes in the gas. Differences in the peak height indicate a significant influence of long-term drift effects such as the erosion depth of the target which have to be studied further.

Acknowledgements

The authors like to thank the Institute of Low Temperature Plasma Physics in Greifswald, Germany for the temporary supply of the ICCD camera and St. Welzel for OES optimisation as well as Th. Förster and Th. Weber for technical assistance. The work was partially funded by the Saxon State Ministry for Economic Affairs and Labour and the European Union under grant no. 7679/1216.

References

- [1] P.J. Kelly, R.D. Arnell, *Vacuum* 56 (2000) 159.
- [2] P.J. Kelly, C.F. Beevers, P.S. Henderson, R.D. Arnell, J.W. Bradley, H. Bäcker, *Surf. Coat. Technol.* 174–175 (2003) 795.
- [3] G. Bräuer, M. Ruske, J. Szczyrbowski, G. Teschner, A. Zmelty, *Vacuum* 51 (1998) 655.
- [4] S. Schiller, K. Goedicke, J. Reschke, V. Kirchhoff, S. Schneider, F. Milde, *Surf. Coat. Technol.* 61 (1993) 331.
- [5] A. Belkind, A. Freilich, R. Scholl, *J. Vac. Sci. Technol., A* 17 (4) (1999) 1934.
- [6] P.J. Kelly, P.S. Henderson, R.D. Arnell, G.A. Roche, D. Roche, *J. Vac. Sci. Technol., A* 18 (6) (2000) 2890.
- [7] W.D. Sproul, *Vacuum* 51 (1998) 641.
- [8] S. Berg, T. Nyberg, *Thin Solid Films* 476 (2005) 215.
- [9] H. Kupfer, R. Kleinhempel, F. Richter, C. Peters, U. Krause, T. Kopte, Y. Cheng, *J. Vac. Sci. Technol., A* 24 (1) (2005) 106.
- [10] R.D. Arnell, P.J. Kelly, J.W. Bradley, *Surf. Coat. Technol.* 188–189 (2004) 158.
- [11] A. Belkind, A. Freilich, J. Lopez, Z. Zhao, W. Zhu, K. Becker, *New J. Phys.* 7 (2005) 90.
- [12] Th. Welzel, Th. Dunger, H. Kupfer, F. Richter, *J. Appl. Phys.* 96 (2004) 6994.
- [13] F. Richter, Th. Welzel, Th. Dunger, H. Kupfer, *Surf. Coat. Technol.* 188–189 (2004) 384.
- [14] Th., Welzel, St., Welzel, F. Richter, Time-resolved investigation of the optical emission in a pulsed magnetron deposition discharge, in: E. M. van Veldhuizen (ed.), *Proc. Int. Conf. Phenomena in Ionised Gases*, Eindhoven, the Netherlands, July 17–22, 2005, #8-082 (CD-ROM, ISBN 90-386-2231-7).
- [15] Th. Dunger, Th. Welzel, St. Welzel, F. Richter, *Surf. Coat. Technol.* 200 (2005) 1676.
- [16] F. Richter, Th. Welzel, Th. Dunger, H. Kupfer, *Surf. Eng.* 20 (2004), 163, 400.
- [17] H. Kajiyama, U.S. Patent No. 6,816,134 (issued Sept. 11, 2004).
- [18] E.H. Choi, H.-J. Oh, Y.-G. Kim, J.-J. Ko, J.-Y. Lim, J.-G. Kim, D.-I. Kim, G. Cho, S.-O. Kang, *Jpn. J. Appl. Phys.* 37 (1998) 7015.
- [19] D. Depla, G. Buyle, J. Haemers, R. de Gryse, *Surf. Coat. Technol.* 200 (14–15) (2006) 4329.
- [20] Th. Welzel, Th. Dunger, St. Welzel, H. Kupfer, F. Richter, *Surf. Coat. Technol.* 200 (2005) 630.

New Journal of Physics

The open-access journal for physics

Spatial and temporal development of the plasma potential in differently configured pulsed magnetron discharges

Th Welzel¹, Th Dunger, B Liebig and F Richter

Institute of Physics, Chemnitz University of Technology,
D-09107 Chemnitz, Germany

E-mail: t.welzel@physik.tu-chemnitz.de

New Journal of Physics **10** (2008) 123008 (16pp)

Received 30 July 2008

Published 9 December 2008

Online at <http://www.njp.org/>

doi:10.1088/1367-2630/10/12/123008

Abstract. Time-resolved emissive probe measurements have been performed to study the spatio-temporal development of the plasma potential in an asymmetric bipolar pulsed magnetron discharge. The influence of the substrate potential as well as of the substrate position has been investigated while the further conditions were the same. To access the entire potential range which was between -100 V and $+400$ V and to obtain sufficient time-resolution of the emissive probe, different heating currents had to be used. The plasma potential has been found to be typically close to zero in the 'on' phase, about $+40$ V in the stable 'off' phase and up to $+400$ V at the beginning of the 'off' phase, which is in agreement with the results of other authors. However, the positive values in the 'off' phase are generally lower than those reported and stay mostly below the target potential. This is explained by macroscopic considerations of the quasineutrality of the plasma taking into account a magnetic and geometrical shielding of the target, acting as an anode in the 'off' phase, and the potential and position of the substrate holder and environment.

¹ Author to whom any correspondence should be addressed.

Contents

| | |
|---|-----------|
| 1. Introduction | 2 |
| 2. Experimental | 3 |
| 3. Results | 6 |
| 3.1. Experimental procedure | 6 |
| 3.2. ‘On’ phase | 7 |
| 3.3. Stable ‘off’ phase | 9 |
| 3.4. Beginning of the ‘off’ phase | 11 |
| 4. Discussion | 11 |
| 5. Conclusions | 15 |
| Acknowledgments | 16 |
| References | 16 |

1. Introduction

Magnetron sputtering is an established tool for high rate and large area deposition of high-quality thin films [1]. The structure and properties of these coatings can be controlled by the parameters of the discharge such as the density and energy of the particles, i.e. ions, electrons and neutrals, which interact with the substrate. In many cases it is desired to systematically reduce the energy which is transferred from the plasma to the film, especially when thermally sensitive substrates such as polymers are used. Practical process optimization, however, turns out to be complicated due to many involved species. Recently, pulsed magnetron sputtering discharges have frequently been used, especially when dielectric coatings are to be deposited [2]–[5]. The pulsed operation of the discharge prevents significant charging of insulating films deposited also on the target surface. Consequently, the formation of arcs is suppressed and the discharge is much more stable whereby the quality of the coatings, e.g. their transparency, conductivity and structure, is enhanced [6]. The periodic interruption or reversal of the discharge voltage leads on the other hand to strong temporal changes of the plasma parameters (see e.g. [7]–[14]) which make a physical description even more difficult, and a tailoring of the deposition process for pulsed magnetron sputtering is to date practically impossible.

One of the important plasma parameters is the plasma potential, V_{PI} , in the discharge volume. It determines the electric field which accelerates the electrons to sustain the discharge, and its spatial distribution is therefore crucial for the discharge formation and distribution. On the other hand, the value of the plasma potential in front of each electrode or wall at fixed potential determines the energy with which the ions hit the surface and controls the charge flux to the electrodes. Its knowledge is thus important directly for the film deposition as long as the substrate is not at floating potential which adjusts itself according to the plasma potential and the electron energy.

The plasma potential can be determined using Langmuir single probes (see e.g. [15]). This often applied method is based on the fact that when the probe potential equals the plasma potential the electron current to the probe changes its voltage dependence. At probe potentials below the plasma potential electrons are repelled according to their energy distribution whereas at probe potentials above the plasma potential electrons are drawn from the plasma according

to their random thermal current and the sheath width. Extrapolating these two regions yields the plasma potential at the junction of both lines. This procedure in many cases gives rather imprecise results due to too ideal assumptions for both potential ranges. Other methods use the first or second derivative of the characteristics to obtain V_{pl} , which is difficult with often noisy characteristics. Furthermore, in pulsed discharges where the plasma potential is varying with time, it cannot be accessed with all these methods because the characteristics obtained will be an average over differently shifted I - V curves. In such discharges, the plasma potential has to be measured time-resolved by taking probe characteristics at each time within the pulse as done by Bradley and others [11, 16]. Another possibility to determine the plasma potential is the use of an energy-dispersive ion mass spectrometer. Positive ions which are detected against ground have to pass through the potential difference between plasma and ground so that their energy distribution reproduces the plasma potential. Due to the time-of-flight within the spectrometer, the measurement is not time-resolved unless a gating technique is used [17, 18]. Therefore, the assignment of structures in the ion energy distribution function (IEDF) to changes in the plasma potential is not straightforward. However, as demonstrated in [16], temporal changes in the plasma potential can be obtained from the interpretation of the IEDF together with the knowledge of the target voltage trace.

A rather simple alternative is the use of an emissive probe [19]–[21]. The principle is based on an ordinary Langmuir single probe. Through an appropriate heating of the probe tip it emits electrons, which act as an apparent additional positive ion current drawn by the probe from the plasma. The floating potential measured by such a probe thus approaches the plasma potential and serves as a good measure for it—in an ideal case with an error in the order of kT_p/e , where T_p is the probe temperature—as soon as the probe temperature is high enough. The advantage of the method is that it is not necessary to acquire the complete characteristics to obtain the plasma potential, rather it can be accessed from a single measurement of the floating potential which is easily obtained through a high impedance measurement against ground. With this measurement being performed with an oscilloscope, a time-resolved determination of varying plasma potentials is possible. The method has been applied to an asymmetric-bipolar pulsed magnetron with a carbon target for a fixed parameter set of 583 W, 0.7 Pa and a duty cycle of 50% by the group of Bradley [22]–[25]. They found a plasma potential close to ground during the whole ‘on’ phase where the target potential is strongly negative. In the ‘off’ phase with the target potential, V_T , being positive, positive plasma potentials just above V_T were observed throughout the discharge volume with the plasma potential following a strong positive spike just at the beginning of the ‘off’ phase. The authors conclude that this behaviour is likely to be representative for other discharge parameters. In an earlier work [26], we have found a similar behaviour but could not generally confirm a positive plasma potential with respect to the target potential in the ‘off’ phase.

In this paper, we present time- and space-resolved plasma potential measurements with an emissive probe in a similar setup but with different geometries. Particularly, the substrate holder has been placed at two different positions opposite to the target. To further investigate the influence of the substrate electrode potential it could be either grounded or insulated.

2. Experimental

The experiments were performed in a purpose-build vacuum chamber with a diameter of 300 mm pumped by a system of a turbomolecular and a rotary pump down to a base pressure

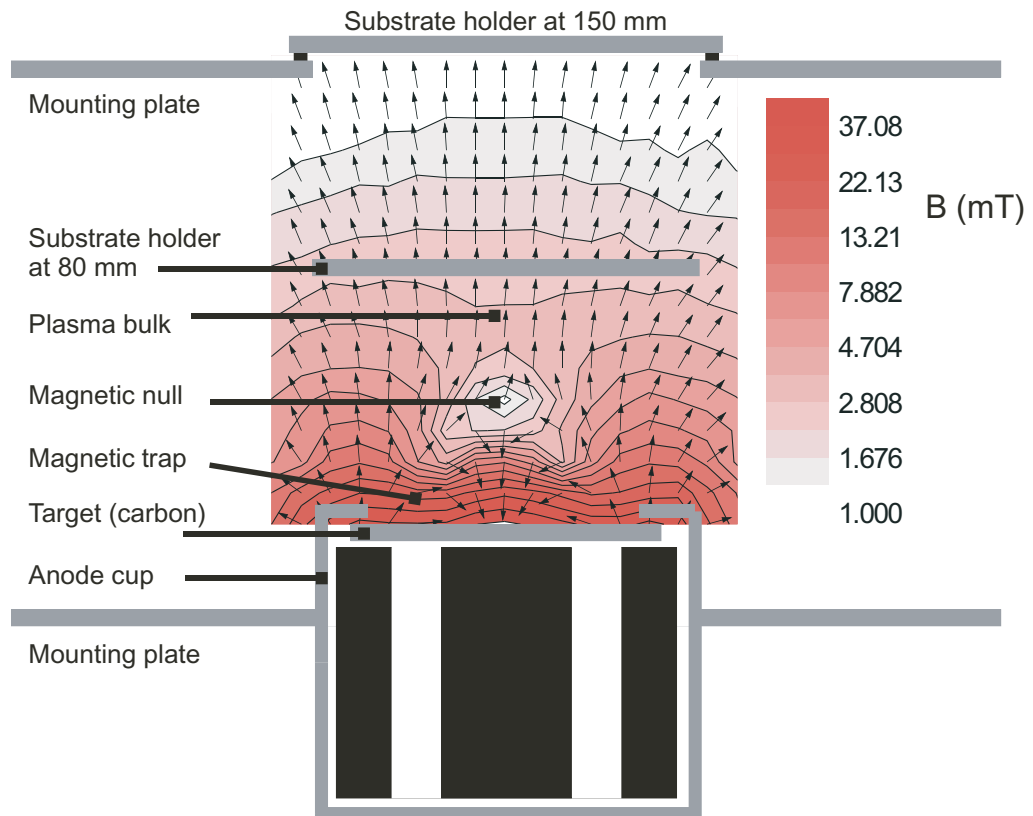


Figure 1. Schematic (drawn to scale) of the discharge setup. The measured magnetic field (flux density B) is given as normalized arrows indicating the direction and on a (logarithmic) colour scale its absolute value in mT.

of 3×10^{-4} Pa. The working gas used was argon (purity 99.999%) at a pressure of 0.45 Pa. The geometrical setup together with the measured magnetic flux is shown in figure 1. The magnetron equipped with a carbon target of 100 mm in diameter and a grounded anode cup was fixed in a mounting plate at ground potential 31 mm below the anode surface. The anode itself was located at a distance between 3 and 7 mm above the target surface and had an inner diameter of 90 mm. Opposite the target the substrate holder (diameter 125 mm) was situated at a target-to-substrate distance of either 80 or 150 mm. It was mounted on another grounded plate at a distance of 140 mm from the target which surrounded it (cf figure 1). The substrate holder was electrically isolated from the grounded mounting plate. An external connection allowed to ground or float the substrate holder at both distances. The magnetron was powered by a Pinnacle Plus (Advanced Energy)-pulsed power supply which was operated in constant power mode. Throughout the experiments, a constant power of 400 W was used with a pulse frequency of 100 kHz, and the duty cycle, i.e. the ratio between pulse 'on' to total pulse duration, was 0.6. In one particular case, a frequency of 50 kHz and a duty cycle of 0.8 were utilized. The anode of the power supply was connected to the grounded anode cup. Thus the discharge was operated in asymmetric-bipolar mode with the positive target potential in the 'off' phase being above ground potential with a value of about 10% of the average negative potential in the 'on' phase.

The emissive probe was constructed of a thoriated tungsten wire of $50 \mu\text{m}$ diameter and a length of about 10 mm, which was formed into a closed loop. At its ends, it was clamped

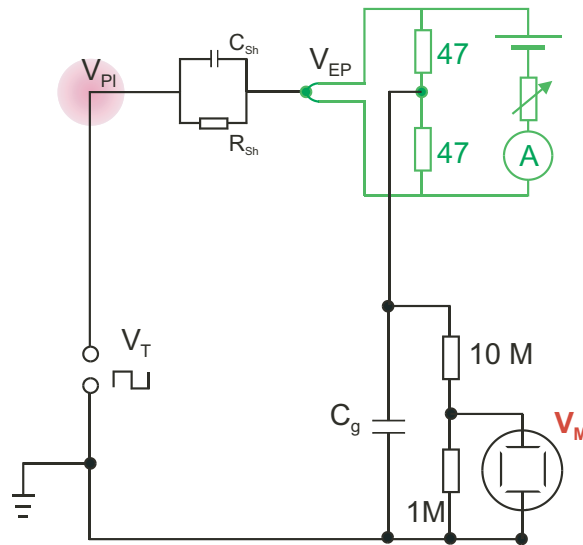


Figure 2. Circuitry of the emissive probe measurement.

within tungsten connecting wires of $500\ \mu\text{m}$ diameter, which were housed in quartz tubes to be isolated from the plasma and allowed contact of only the thin probe with the plasma. The whole system was fixed on a holder which was mounted on a linear-rotary feed-through to achieve radial and axial movement within the discharge volume. The loop was oriented parallel to the target surface resulting in an axial resolution of 2 mm and a radial resolution of about 6 mm. The scan of the discharge cross section was performed in axial steps of $\Delta z = 8\ \text{mm}$ from $z = 12\ \text{mm}$ to $z = 68\ \text{mm}$ or $z = 12\ \text{mm}$ to $z = 132\ \text{mm}$ distance from the target for a substrate distance of 80 or 150 mm, respectively. For each axial distance the discharge was radially scanned between $x = -49\ \text{mm}$ and $x = +49\ \text{mm}$ in steps of $\Delta x = 7\ \text{mm}$. Additional experiments were done with a slightly modified probe holder to allow a closer approach to the target. In this case, the quartz tubes were slightly bent towards the target so that they could be moved over the anode cup, while the probe tip itself was below the anode surface. With this setup, a distance of the probe from the target down to 4 mm was obtained. However, due to the bending the loop was not aligned parallel with the target surface in this case, resulting in a poorer axial resolution of about 4 mm.

The electrical setup of the emissive probe is shown in figure 2. The probe was heated with an insulated dc heating circuit which consisted of a battery (max 15 V and 1.5 A) in series with a variable resistor of max $47\ \Omega$ to adjust the probe heating current. The typical voltage at the probe connectors was 3.5 V which gave a current of 0.7 A. Two $47\ \Omega$ resistors were connected parallel with the probe and the probe potential was taken between them to minimize the falsification by the longitudinal potential drop along the probe tip. Therefore, the accuracy of the absolute value of the time-resolved plasma potential is about 3 V. The relative error during the scans, i.e. the reproducibility, has been 1 V in the stable phases and about 5 V during transient phases of the discharge. The time-dependent voltage signal of the emissive probe was recorded via a 1:10 voltage divider (Iwatsu SS-0130P, 100 MHz) with a digitizing oscilloscope (Tektronix, TDS 620B). The battery as the heating source was selected to minimize the capacitance of the system to ground (C_g) given in figure 2, which strongly influences the time resolution. In the final setup, a capacitance to ground of about 130 pF has been achieved.

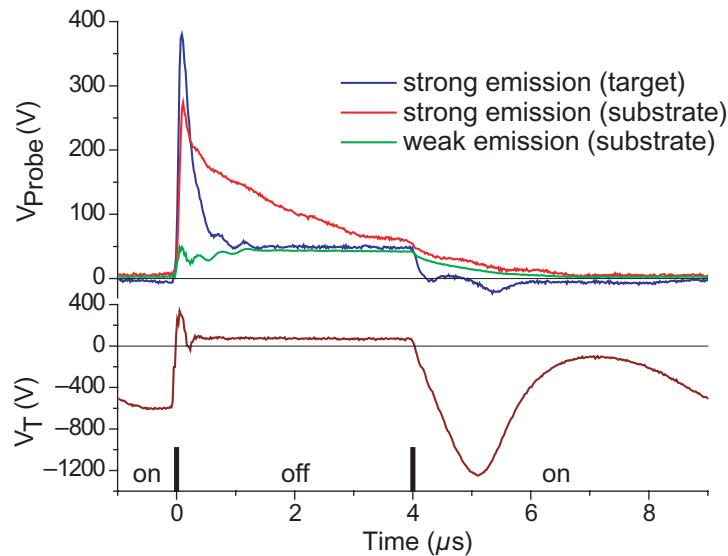


Figure 3. Potential traces measured with the emissive probe (top) for three different conditions: (blue) strongly heated at $(x, z) = (21 \text{ mm}, 12 \text{ mm})$, (red) strongly heated at $(x, z) = (28 \text{ mm}, 68 \text{ mm})$, (green) moderately heated at $(x, z) = (28 \text{ mm}, 68 \text{ mm})$. The temporal development of the target potential with the indication of the ‘on’ and ‘off’ phases is given in the bottom diagram.

3. Results

3.1. Experimental procedure

Three examples of the time dependence of the potential measured by the emissive probe are shown in figure 3. They were obtained at different positions in the discharge and with differently strongly heated probe tips. The potential of the probes that were strongly heated shows a significant spike of up to +400 V at the beginning of the ‘off’ phase which temporally coincides with a high positive potential at the target which is obtained just as the target voltage is reversed to positive values (see figure 3). Subsequently to the peak, both probe and target potential decrease to lower positive values. As soon as the target potential is switched to negative values in the ‘on’ phase, the probe potential also decreases and approaches values close to zero. Close to the target, slightly negative values are measured. Generally, at phases with decreasing target potential the probe potential reacts rather slowly away from the target and when the probe is strongly heated.

The response time of the probe circuit is given by $\tau = R_{\text{sh}} Z_{\text{sh}} / (R_{\text{sh}} + Z_{\text{sh}}) \cdot C_{\text{g}}$ [24], where R_{sh} and Z_{sh} are sheath resistance and the capacitive sheath impedance, respectively, and C_{g} is the capacitance of the circuit to ground which we have measured as 130 pF. The sheath resistance may be expressed as the voltage drop across the sheath over the current through the sheath. The capacitive sheath impedance is $1/(\omega C_{\text{sh}})$ with $C_{\text{sh}} = \epsilon_0 A/d$, d being the sheath width and A the probe area. Taking a potential drop of the order of kT_e/e , a current of the order of the random thermal electron current, and a sheath width of the order of the Debye length $(\epsilon_0 \cdot kT_e / (e^2 n))^{1/2}$, we can roughly estimate the response time. The frequency ω of the fast changes in the potential is about 50 MHz. Then a response time in front of the target in the

magnetic trap of ~ 10 ns (taking $n = 5 \times 10^{11} \text{ cm}^{-3}$ [27], $T_e = 5$ eV) and in front of the substrate of ~ 500 ns (taking $n = 5 \times 10^9 \text{ cm}^{-3}$ [28], $T_e = 2$ eV) is obtained, which is of the order of magnitude that we observed (cf figure 3). Importantly, it should be noted that the estimation shows that the response time is strongly dependent on the charge carrier density n of the local plasma.

At phases where the plasma potential is falling rapidly, electrons delivered from a strongly emitting probe may be repelled from the plasma, which becomes more negative than the emitting probe. Karkari *et al* [22] suggest that the electrons then form a negative space charge around the probe, which impairs the current through the sheath. Such increased sheath resistance reduces the response time further. Strong emission hence can falsify the values in the stable phases. This can be seen in figure 3 where a strongly and a weakly emitting probe have been used under otherwise same conditions. On the other hand, the spike at the beginning of the ‘off’ phase which coincides with that in the target potential can only be measured with a strongly emitting probe, which is in agreement with the findings of other authors [24]. Intermediate heating is sufficient for the other times during the pulse.

This is shown in more detail in figure 4. Here, the potential obtained from the emissive probe is displayed as a function of the heating current which is a measure of the hardly accessible probe temperature. Three different times during the pulse have been selected: the end of the ‘on’ and of the ‘off’ phase where the changes in the target potential are small and the beginning of the ‘off’ phase where the spike was observed. When the probe starts to emit a sufficient number of electrons, the apparent floating potential measured by the probe increases and approaches the plasma potential. As soon as the plasma potential at a given time is reached, the apparent floating potential saturates and a further increase of the heating current only leads to a very small increase of the order of kT_e/e [29] which is due to space charge effects. The plasma potential has been obtained from this saturation value without correction of the space charge effects. For the stable periods of time in the ‘on’ and ‘off’ phases, a heating current of 0.55 A was sufficient. However, to saturate the probe potential during the potential spike, much higher heating currents of more than 0.8 A were required (cf figure 4).

Due to the worse time resolution and the short lifetime of the strongly emitting probe, the scans of the cross section were divided into two series. Very hot probes were only used for the determination of the spike at the beginning of the ‘off’ phase and were renewed for each radial scan. The other times were measured with moderately heated probes which allowed the complete scan with one probe. Four particular times during the pulse were investigated: the minimum in the ‘on’ phase, the stable ‘on’ phase, the stable ‘off’ phase, and—with the very hot probe—the beginning of the ‘off’ phase.

3.2. ‘On’ phase

In figure 5, the distribution of the plasma potential during the ‘on’ phase is shown with the substrate holder at the 80 mm distance position. The distribution at the end of the ‘on’ phase (bottom of figure 5) resembles what could be expected for a dc magnetron. With the substrate holder at ground potential, the plasma potential in the bulk plasma, i.e. above the magnetic null of the unbalanced magnetron, is slightly positive. With the substrate at floating potential, the plasma potential in the bulk plasma is significantly lowered and a stronger radial inhomogeneity is observed which images the magnetic field distribution.

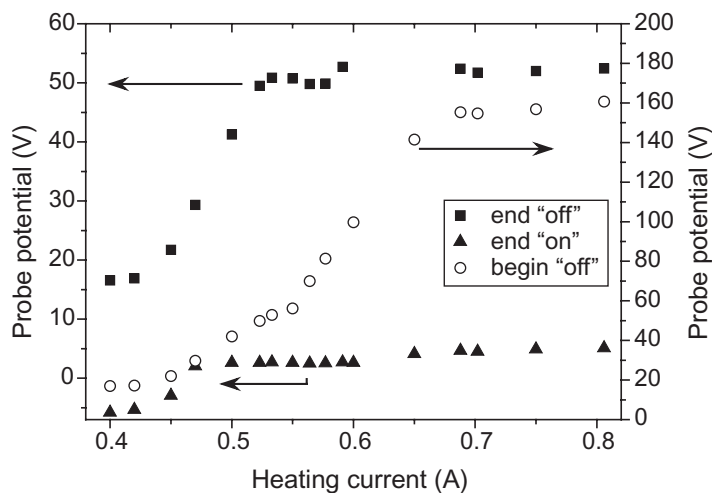


Figure 4. Apparent floating potential as a function of the heating current through the probe wire which was considered to be representative of the probe temperature, for different selected moments during the pulse. At each moment, the plasma potential is obtained when the apparent floating potential saturates. (For these measurements a different pulse frequency of 50 kHz and duty cycle of 0.8 were utilized.)

In the early moments of the ‘on’ phase, the target voltage passes through a strong voltage minimum (cf figure 3) which reached -1250 V. This has a significant influence on the momentary plasma potential throughout the whole discharge volume as shown in the upper part of figure 5. Except on the edges of the discharge, where the plasma potential is almost unaltered, the values of the plasma potential are decreased also, resulting in a stronger inhomogeneity. Even when the substrate is grounded, slightly negative plasma potentials of -1 V are observed close to the substrate. In the magnetic trap, the plasma potential temporarily drops to -45 V compared with -25 V for the stable ‘on’ phase for both substrate potentials investigated.

Figure 6 shows the plasma potential distribution at the end of the ‘on’ phase for two distances of the substrate holder. Also included are measurements performed close to the target at 4 mm distance. At these distances the plasma potential is strongly negative as the probe position is deeper in the pre-sheath. The minimum values agree quite well with -40 V and -36 V for the 80 mm and 150 mm distances. Like the potential of the substrate (cf figure 5) this demonstrates again that the geometrical and electrical conditions away from the target do not much influence the potential structure close to the target. However, there are apparent differences in the potential of the bulk plasma extending to the substrate which in both cases is held at floating potential. When it is located 80 mm from the target, the plasma potential stays below zero along the centre line with about -8 V close to the substrate. With a distance of 150 mm (see figure 6(b)) the potential distribution is flattened 40 mm above the target and the absolute values are closer to zero. This potential distribution looks more like that for a grounded substrate (cf figure 5(d)) than a floating one. In fact, the potential distribution measured at the same geometry as in figure 6(b) but with the substrate holder grounded (not shown here) is almost the same as in figure 6(b).

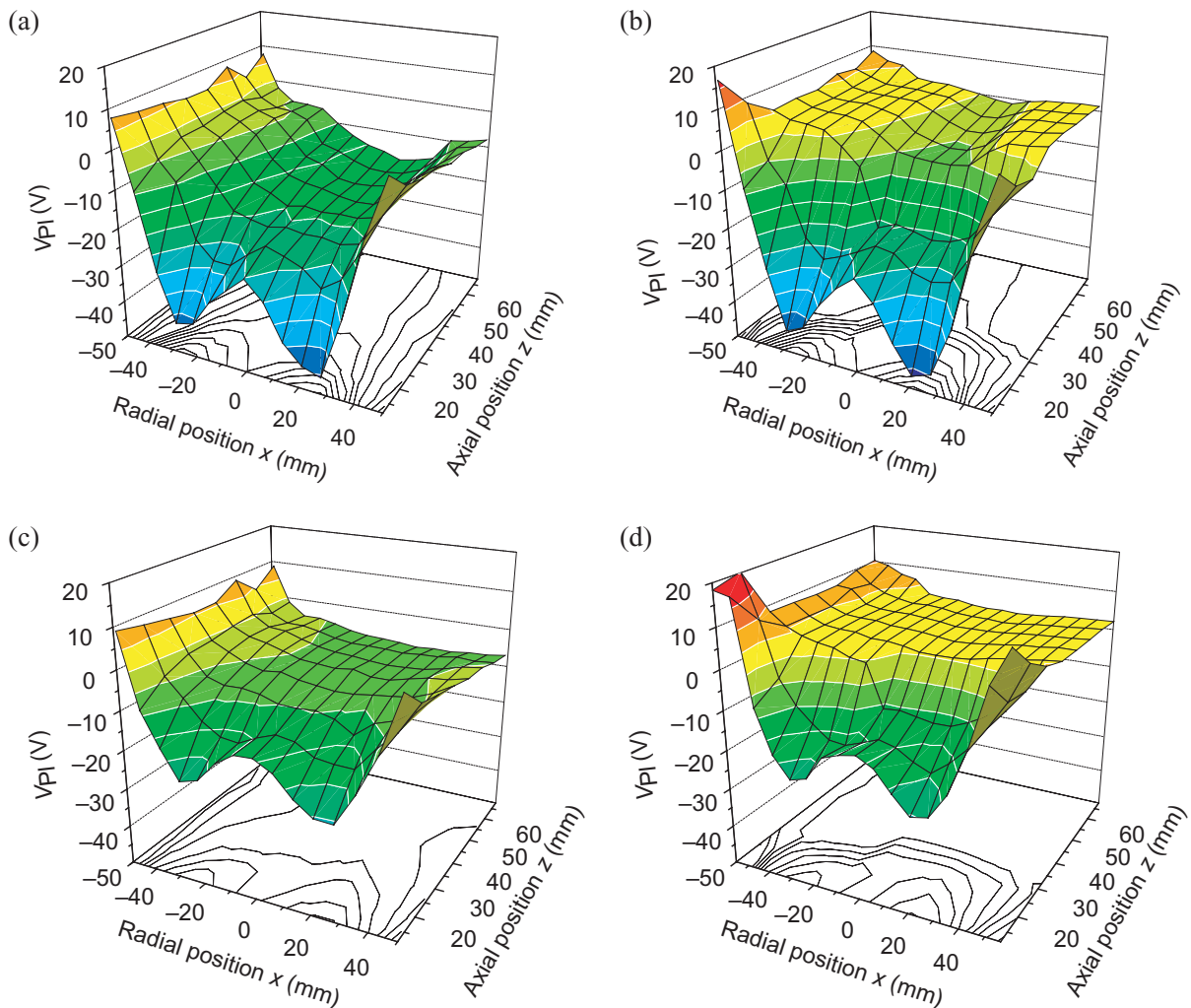


Figure 5. Plasma potential distribution during the ‘on’ phase of the pulsed discharge with a substrate distance of 80 mm from the target: (a) and (b) during the target voltage overshoot ($V_T = -1240, \dots, -1250$ V, cf figure 3), (c) and (d) at the end of the ‘on’ phase ($V_T = -600, \dots, -605$ V). For the left figures ((a) and (c)) the substrate is at floating, for the right figures ((b) and (d)) at ground potential.

3.3. Stable ‘off’ phase

The plasma potential distribution at the end of the ‘off’ phase is shown in figure 7 for the target-to-substrate distance of 150 mm. Generally, V_{PI} at this time is positive slightly above +40 V, a fact that has also been found by other authors [22]–[25]. The plasma potential in discharges typically adjusts close to the potential of the most positive electrode. In the ‘off’ phase of the asymmetric-bipolar pulsed discharge this electrode is the target, which had a momentary potential of +68 ··· +69 V in the present case while anode cup and walls act as cathode where most of the potential drop occurs. Most interestingly, we always observe plasma potentials which are, although positive, below the target potential at the end of the ‘off’ phase. There

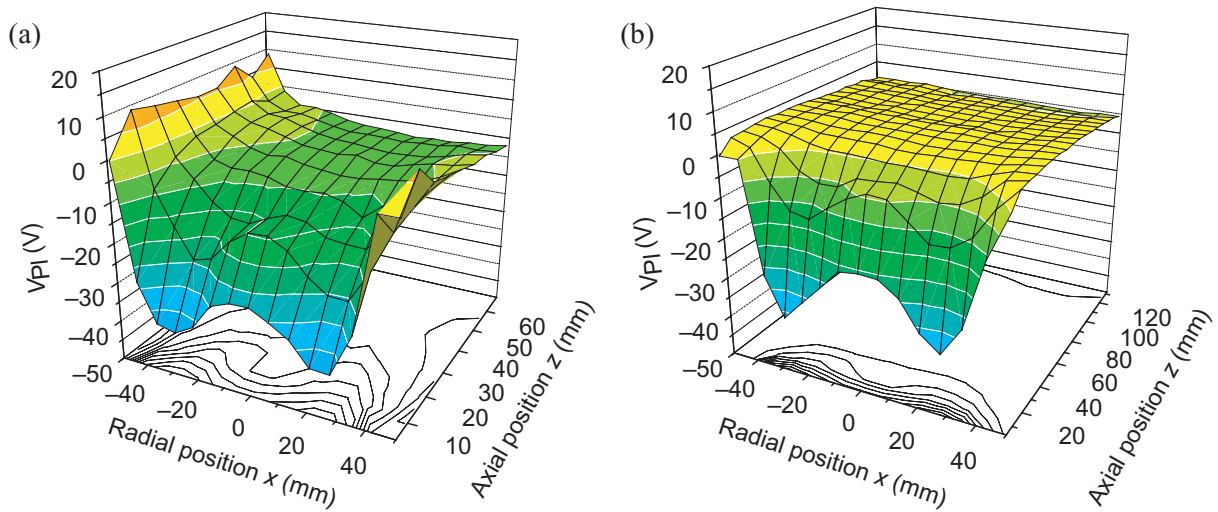


Figure 6. Plasma potential distribution at the end of the ‘on’ phase of the pulsed discharge with a floating substrate: (a) represents the situation with the substrate at a distance of 80 mm from the target ($V_T = -600$ V), (b) represents a distance of 150 mm ($V_T = -560$ V). Note that the data at $x = \pm 49$ mm and $z = 4$ mm could not be measured because of geometrical restrictions and are displayed at zero potential.

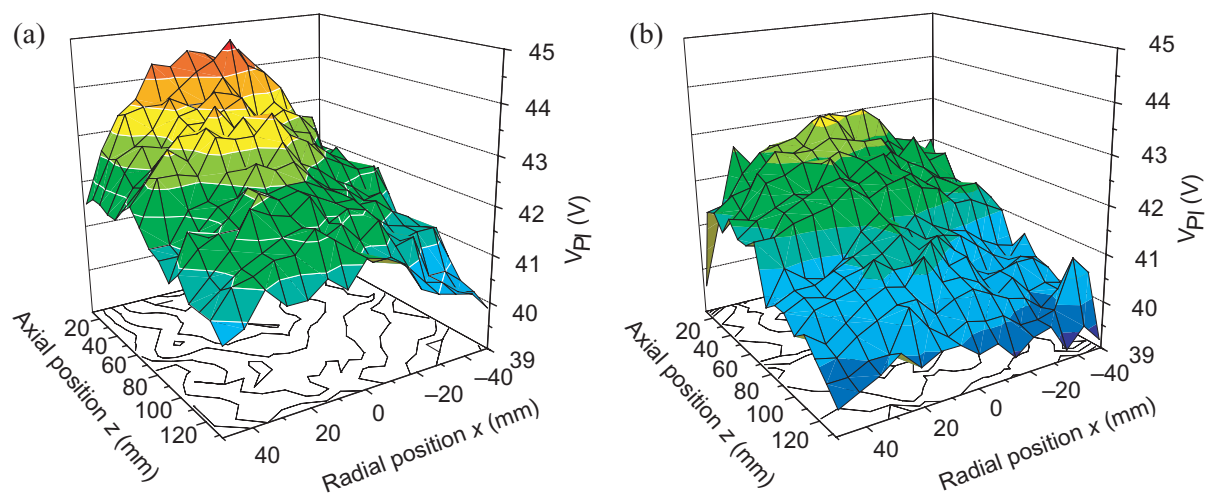


Figure 7. Plasma potential distribution during the stable ‘off’ phase of the pulsed discharge with a substrate distance of 150 mm from the target: (a) substrate floating ($V_T = +68$ V) and (b) substrate grounded ($V_T = +69$ V).

is a slight drop in the plasma potential from the target to the substrate at 150 mm of about 3 V for both substrate potentials, resulting in a very weak electric field of 25 V m^{-1} pointing towards the substrate. The small potential changes result in a humpy distribution corresponding to the relative uncertainty of the measurements of about 1 V. Comparing the potential distribution for the floating (figure 7(a)) with that of the grounded (figure 7(b)) substrate, a shift of 1–2 V in the absolute values is clearly seen.

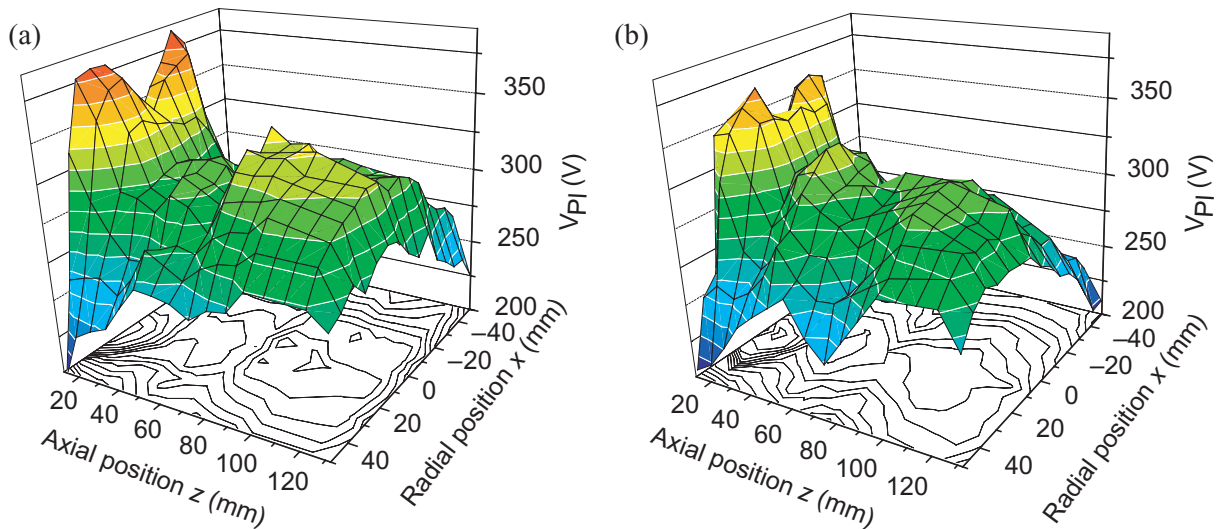


Figure 8. Plasma potential distribution during the positive peak in the target voltage (about +340 V) at the beginning of the ‘off’ phase with a substrate distance of 150 mm from the target: (a) substrate floating and (b) substrate grounded.

The same behaviour has been observed for a substrate distance from the target of 80 mm (not shown here). The plasma potential dropped from the target region to 68 mm by about 2 V and was on average 1 V lower in the grounded case. Again, the plasma potential was below the target potential.

3.4. Beginning of the ‘off’ phase

Figure 8 shows the plasma potential distribution at the beginning of the ‘off’ phase for a target-to-substrate distance of 150 mm. Generally, the plasma potential exhibits strongly positive values throughout the discharge volume. The highest values are measured close to the positive target with the magnetic trap being clearly reflected in the potential distribution by a particularly high plasma potential. Both figures show that the plasma potential immediately follows the strong rise of the target potential so that it stays close to the potential value of the target. This fact confirms the observation of others [22]–[25]; however, because of the different discharge geometries it is not possible to establish a general rule yet. The potential distributions have also been measured for a substrate distance of 80 mm and confirm those in figure 8. They particularly proved that V_{PI} is always slightly lower (10 V) in the bulk for the grounded substrate compared with the floating one.

The structures which seem to be present in figure 8 within the bulk of the plasma resulting in some local minima along the axis of symmetry, especially the apparent minimum around $z = 50$ mm, are an artefact of the target potential fluctuations in the spike during the time-consuming measurements with the very hot probe.

4. Discussion

The plasma potential distribution can be determined from the Poisson relation

$$\varepsilon_0 \cdot \Delta V_{PI}(\vec{r}) = e [n_e(\vec{r}) - n_i(\vec{r})], \quad (1)$$

(ε_0 , dielectric constant; e , elementary charge; n_e , electron density; n_i , (positive) ion density). To calculate the distribution in the pulsed magnetron, the spatial density distributions of the electrons and ions have to be known for each moment during the pulse in combination with boundary conditions for the electric field and the potential. Considering the extremely inhomogeneous discharge, this is almost impossible to solve analytically. Instead, a macroscopic approach which is based on the quasineutrality of the plasma shall be used to understand the temporal and spatial behaviour of the plasma potential in the pulsed magnetron discharge. For any given homogeneous discharge in the stationary state, the flux of ions to the cathode has to be compensated by an equal electron flux to the anode. In a pulsed magnetron the situation is more complicated because of rapid temporal changes and the strong inhomogeneity of the discharge but the general requirement holds that no net charge should be extracted.

During the 'on' phase of the discharge ions are extracted from the plasma with the Bohm flux [30]

$$J_i = 0.61 \cdot e \cdot n_i \cdot \sqrt{\frac{kT_e}{m_i}}, \quad (2)$$

(k , Boltzmann constant; m_i , ion mass (Ar); T_e , electron temperature, taken to be $kT_e/e = 5$ V) to the target but due to the strongly negative potential no electrons flow to the target. Taking a local argon ion density n_i in front of the target of the order of $5 \times 10^{11} \text{ cm}^{-3}$ and assuming that due to the very inhomogeneous discharge only half of the target effectively collects ions, one obtains an ion current of about 0.7 A which is a typical value for our magnetron. In a first approximation, secondary electron emission is neglected as it is typically only 10% of the ion current. Then, the same current of electrons has to flow to the grounded parts of the setup. The closest of those is the anode cup, which would require significant cross-field drift to the magnetic field to be reached. Thus, the grounded substrate acts as the main drain for electrons which, without potential barrier, would be subject to the random thermal electron current

$$J_e = \frac{1}{4} \cdot e \cdot n_e \cdot \sqrt{\frac{8kT_e}{\pi m_e}}, \quad (3)$$

(m_e , electron mass). Taking n_e of the order of $5 \times 10^9 \text{ cm}^{-3}$ and $T_e = 2$ eV, an electron current of 2.3 A can be calculated. This is much more than the ion current to the target. To keep quasineutrality, the electron current must be reduced by a potential barrier ($V_{PI} - V_S$) to equalize the ion current leading to

$$V_{PI} - V_S = \frac{kT_e^{(A)}}{e} \ln \left[\frac{n_e^{(A)} A^{(A)}}{0.61 \cdot n_i^{(C)} A_{\text{eff}}^{(C)}} \left(\frac{m_i T_e^{(A)}}{2\pi m_e T_e^{(C)}} \right)^{1/2} \right], \quad (4)$$

where A and A_{eff} are the collecting areas and the superscripts (C) and (A) refer to the cathode and the anode, respectively. Taking the above example, a potential barrier of about 2.5 V is necessary. This is in good agreement with the measurement shown in figure 5(d). Close to the target, secondary electrons which are released from the target are confined in the magnetic trap, mostly above the race track. This locally trapped excess negative charge that is prevented from reaching the anode lowers the potential V_{PI} in this region which becomes strongly negative (cf figure 5).

When the substrate is instead at floating potential and does not drain any net current, the electrons have to move to the grounded mounting plate around the substrate to close the

circuit. However, most of the magnetic field lines of the unbalanced magnetron terminate on the substrate holder when it is at 80 mm distance so that an effective electron drain to the mounting plate is prevented. This results in much lower values for the plasma potential than for the grounded substrate at 80 mm (cf figure 5(c)).

The situation is different when the substrate holder is at 150 mm distance, in the plane of the mounting plate (cf figures 6(a) and (b)). The magnetic field is diverging for distances above 70 mm from the target (cf figure 1). Without the floating substrate holder in the way, more electrons can thus reach the grounded plate and cause a net electron drain. Consequently, the plasma potential is raised and is comparable with the situation with the grounded substrate at 80 mm (see figure 5(c)). An additional grounding of the substrate holder at 150 mm only leads to a small further increase of the plasma potential (+1.6 V) as it has already been attached to the grounded plate.

About 1 μ s after the start of the ‘on’ phase, the target voltage has a strong overshoot about twice as much as at the end of the ‘on’ phase (–1250 V versus –600 V). At this moment, more secondary electrons are released from the target surface into the discharge volume and lower the plasma potential as an excess negative charge (see figures 5(a) and (b)). The effect is recognized within the whole discharge volume with a delay of only 250 ns (see figure 3). This delay is caused by the ions which have to cross the sheath before they can release more electrons due to their higher energy. The temporal plasma potential decrease is strongest close to the target because most of the additional secondary electrons are trapped above the race track. The weaker decrease in the bulk is caused by electrons that either start at field lines extending to the substrate region or are scattered onto them. There is no detectable difference in the delay between the two regions because an electron which is accelerated by 1250 V will travel 20 cm within only 10 ns.

During the ‘off’ phase with a positive target voltage, the potential relations are reversed. The target then acts as the anode of the discharge and any grounded surface adjacent to the plasma acts as cathode. For simplicity, at first we consider the unrealistic case that only the target shall act as an electrode and the walls are imagined as being too distant and draw only a negligible current. The target would then have to be subjected to an equal electron and positive ion flux to keep up quasineutrality and the plasma potential would adjust positive to V_T to obtain this. Such a behaviour was reported by the group of Bradley [22]–[25], who also concluded that the plasma potential should always be above the target potential. We have, however, observed the plasma potential being consistently lower than V_T in the stable ‘off’ phase. To explain this, we have to consider the substrate/walls and the magnetic field configuration at the target. If a grounded substrate is present, it will be subject to a net ion current according to equation (2) that has to be compensated by a net electron drain to the target. Compared with the hypothetical situation above, the plasma potential is then lowered to allow this increased electron current. Because the random thermal current density of the electrons is typically much larger than the ion current density, V_{PI} is still close to the potential of the most positive electrode (here the target) but its absolute value is dependent on the geometrical conditions [31]. A small cathode (grounded surface) or a large anode (target surface) leads to a high plasma potential, whereas a large grounded surface or a small target results in a lower plasma potential. Moreover, the effective electron collecting target area will be dependent on the magnetic field. Electrons from the plasma bulk which provides the majority of the discharge volume are prevented from entering the region of the magnetic trap. Because of our unbalanced magnetron, they will be deflected to the outer edge of the magnetron. Given the configuration of our anode cup which intersects the majority of those field lines, the electrons will mostly be reflected. This results

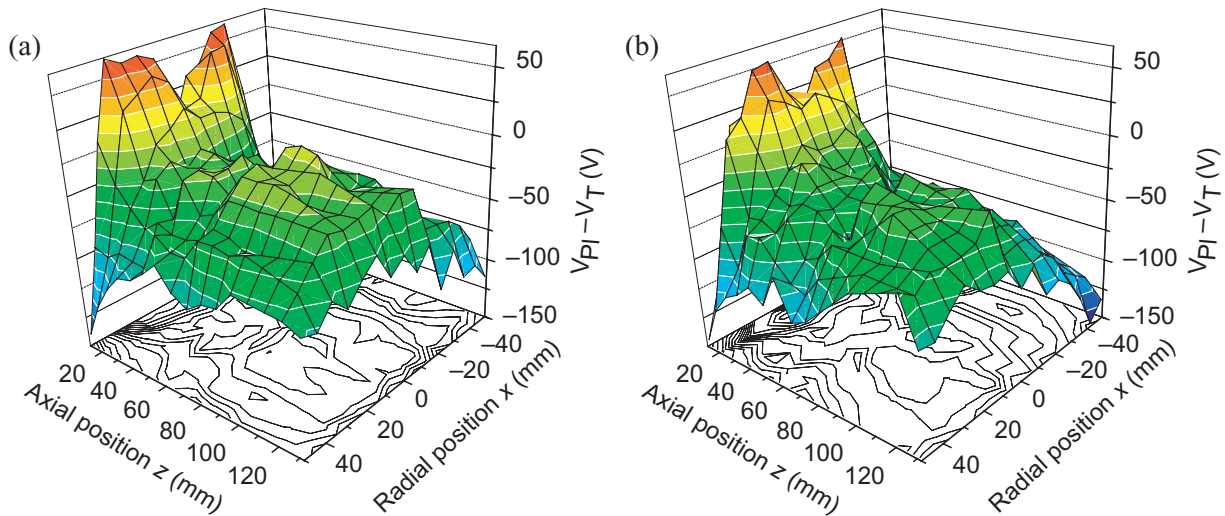


Figure 9. Distribution of the plasma potential from figure 8 reduced by the actual target potential value taken at each point: (a) substrate floating and (b) substrate grounded.

in a small effective area of the target in our case which leads to a low plasma potential: while others [22]–[25] report about a plasma potential of 2 V [23, 25] or 4–5 V [24] above V_T at the end of the ‘off’ phase, we thus found a plasma potential 28 V below V_T . This is reasonable because in the references no or only a small substrate holder is described and the target with a diameter of 150 mm has more than twice our area and no intersecting anode cup.

Because the electron current limitation to the magnetically shielded target determines the plasma potential in the stable ‘off’ phase, the substrate holder potential is only of little influence (cf figure 7). The plasma potential is 1 V lower with a grounded substrate compared with a floating one because the net ion collection area is increased. This necessitates an increased electron current to the target and thus a decreased plasma potential.

Because the plasma potential has been found to always adjust close to the most positive electrode, it is very sensitive to changes of the positive target potential in the ‘off’ phase. To exclude the influence of any drift of the target voltage, the actual value of V_T which was measured simultaneously has been subtracted from the measured V_{PI} . The result is given in figure 9, where the deep valley from figure 8(a) and the dips from figure 8(b) have almost completely vanished, proving that these structures were indeed an artefact of random V_T changes. However, especially the high positive values close to the target remain. These result from a depletion of electrons as soon as the target voltage is reversed to positive values and electrons are immediately accelerated to the target. This process is most effective in the magnetic trap as all magnetic field lines from this region terminate on the target surface. It creates a high electron current of several amps on the target and leaves an excess positive charge. The plasma potential in the rest of the discharge is also temporarily raised. This is particularly the case close to the axis of symmetry where the unbalanced magnetic field still has some field lines that terminate on the target so that a drift along them leads to a drain of electrons. Again, we observe that the plasma potential in the bulk does not or not significantly rise above the target potential, which we again attribute to the strongly magnetically shielded target in our case. As for the stable ‘off’ phase the plasma potential with the grounded substrate is slightly lower

than with the floating one due to additional ion extraction to the substrate holder. Although the duration of the spike is very short (about 100 ns) and potential changes will mainly affect the electron movement to the target, the first ions arrive at the opposite surface allowing an increased electron current to the target by a slightly reduced plasma potential which is more effective with the grounded substrate. Plasma potentials much lower than the target potential are measured at the radial edges. At these positions no drift of the electrons to the target along magnetic field lines is possible and no rapid drain in the early moments of the 'off' phase occurs.

5. Conclusions

An asymmetric-bipolar pulsed magnetron discharge has been investigated with two different target-to-substrate distances and with the substrate at floating and ground potential for both geometries. The plasma potential distribution has been measured time-resolved with an emissive probe. The plasma potential in the 'on' phase attains values close to ground throughout almost the whole discharge volume. In the 'off' phase, it is permanently positive while it follows the target voltage, adjusting itself close to it. It therefore amounts to several 10 V in the stable 'off' phase and up to several 100 V at the beginning of the 'off' phase. In general, these results confirm those found previously by others for a single set of parameters in a slightly different pulsed magnetron. The most significant difference in our case is that the plasma potential in the 'off' phase stays below the target potential, which is explained by the geometry and the concept of quasineutrality for the stationary state.

In the stable 'on' phase with the substrate holder close to the target the plasma potential stays below zero on-axis when the substrate is insulated but slightly above ground when it is grounded. In the latter case, the electron current to the substrate has to be limited by a potential barrier to keep on the same value as the ion current to the target. When the substrate distance is increased, the grounded mounting plate determines the electron current and the potential distribution. During the very negative overshoot in the target voltage, the plasma potential in the magnetic trap and the centre of the plasma bulk is always lowered by a few volts due to temporary excess electrons.

At the end of the 'off' phase, the plasma potential is positive but stays below the target potential. The reason is that the substrate holder and/or mounting plate is draining ions from the plasma but the electron current to the positive target is hindered by the anode cup of the magnetron which intersects magnetic field lines together with our comparably small magnetron area. Therefore, a smaller potential barrier is required and the plasma potential is rather low.

At the beginning of the 'off' phase, when the target potential is temporarily (for only about 100 ns) at about +400 V, electrons are immediately extracted from the region of the magnetic trap with its magnetic field lines terminating at the target. As a consequence, the plasma potential in the region even rises above the high target potential. In the rest of the discharge, especially along the centre line, it is also elevated by the quick electron extraction, but again keeps below the target potential.

The temporal response of the emissive probe is strongly improving with increasing charge carrier density. It was significantly worsened at strong heating because of reflection of the emitted electrons at the plasma boundary at decreasing plasma potential. However, strong heating is necessary to detect the peak at the beginning of the 'off' phase.

Acknowledgments

We thank the German Research Council (DFG) for financial support as well as Th Förster for valuable technical support with the probe technique.

References

- [1] Nadel S J, Greene P, Rietzel J and Strümpfel J 2003 *Thin Solid Films* **442** 11–4
- [2] Schiller S, Goedicke K, Reschke J, Kirchhoff V, Schneider S and Milde F 1993 *Surf. Coat. Technol.* **61** 331–7
- [3] Belkind A, Freilich A and Scholl R 1999 *J. Vac. Sci. Technol. A* **17** 1934–40
- [4] Kelly P J and Arnell R D 2000 *Vacuum* **56** 159–72
- [5] Sproul W D 1998 *Vacuum* **51** 641–6
- [6] Kelly P J, Henderson P S, Arnell R D, Roche G A and Carter D 2000 *J. Vac. Sci. Technol. A* **6** 2890–6
- [7] Bradley J W and Welzel T 2008 *Reactive Sputtering Deposition (Springer Series in Materials Science 109)* ed D Depla and S Mahieu (Berlin: Springer) chapter 7 pp 255–300
- [8] Welzel T, Dunger T, Kupfer H and Richter F 2004 *J. Appl. Phys.* **96** 6994–7001
- [9] Welzel T, Dunger T, Welzel S and Richter F 2005 *Surf. Coat. Technol.* **200** 1676–82
- [10] Welzel T, Dunger T and Richter F 2006 *Surf. Coat. Technol.* **201** 3959–63
- [11] Bradley J W, Bäcker H, Kelly P J and Arnell R D 2001 *Surf. Coat. Technol.* **142–144** 337–41
- [12] Swindells I, Kelly P J and Bradley J W 2006 *New J. Phys.* **8** 47
- [13] Belkind A, Freilich A, Lopez J, Zhao Z, Zhu W and Becker K 2005 *New J. Phys.* **7** 90
- [14] Vlcek J, Pajdarova A D and Musil J 2004 *Contrib. Plasma Phys.* **44** 426–36
- [15] Chen F F 1965 *Plasma Diagnostic Techniques* ed R H Huddleston and S L Leonard (New York: Academic) chapter 4
- [16] Bradley J W, Bäcker H, Aranda-Gonzalvo Y, Kelly P J and Arnell R D 2002 *Plasma Sources Sci. Technol.* **11** 165–74
- [17] Misina M, Bradley J W, Bäcker H, Aranda-Gonzalvo Y, Karkari S K and Forder D 2002 *Vacuum* **68** 171–81
- [18] Voronin S A, Clarke G C B, Cada M, Kelly P J and Bradley J W 2007 *Meas. Sci. Technol.* **18** 1872–6
- [19] Hershkowitz N, Nelson B, Pew J and Gates D 1963 *Rev. Sci. Instrum.* **54** 29–34
- [20] Makowski M A and Emmert G A 1983 *Rev. Sci. Instrum.* **54** 830–6
- [21] Kemp R F and Sellen J M 1965 *Rev. Sci. Instrum.* **37** 455–61
- [22] Karkari S K, Vetushka A and Bradley J W 2003 *J. Vac. Sci. Technol. A* **21** L28–32
- [23] Vetushka A, Karkari S K and Bradley J W 2004 *J. Vac. Sci. Technol. A* **22** 2459–68
- [24] Bradley J W, Karkari S K and Vetushka A 2004 *Plasma Sources Sci. Technol.* **13** 189–97
- [25] Bradley J W, Karkari S K and Vetushka A 2004 *Surf. Eng.* **20** 186–8
- [26] Welzel T, Dunger T and Richter F 2007 Determination of spatio-temporal plasma potential variations in asymmetric bipolar pulsed DC magnetron discharges by emissive probes *Proc. 28th Int. Conf. on Phenomena in Ionised Gases (Prague, Czech Republic, July 15–20, 2007)* ed J Schmidt, M Simek, S Pekarek and V Prukner pp 1585–8
- [27] Welzel T, Dunger T and Richter F 2007 *Plasma Processes Polym.* **4** S931–6
- [28] Richter F, Welzel T, Dunger T and Kupfer H 2003 *Surf. Eng.* **20** 163–6
Richter F, Welzel T, Dunger T and Kupfer H 2003 *Surf. Eng.* **20** 400 (Erratum)
- [29] Ye M Y and Takamura S 2000 *Phys. Plasmas* **7** 3457
- [30] Bohm D 1949 *The Characteristics of Electrical Discharges in Magnetic Fields* ed A Guthrie and R K Wakerling (New York: McGraw-Hill) chapter 3
- [31] Belkind A and Jansen J 1998 *Surf. Coat. Technol.* **99** 152–9

Ion Energy Distributions in Magnetron Sputtering of Zinc Aluminium Oxide

Thomas Welzel^{a,*}, Ronny Kleinhempel^{a,b}, Thoralf Dunger^a, and Frank Richter^a

^a Chemnitz University of Technology, Institute of Physics, D-09107 Chemnitz, Germany

^b present address: Southwall Europe GmbH, Southwallstraße 1, D-01900 Großröhrsdorf, Germany

* corresponding author: Phone: +49 (0) 371-531-21710, Fax: +49 (0) 371-531-21719, E-mail: t.welzel@physik.tu-chemnitz.de

Keywords: ion-energy distribution function (IEDF), magnetron, plasma potential, pulsed discharges, mass spectrometry, sputtering

Summary

Ion energy distributions have been measured with an energy-dispersive mass spectrometer during magnetron sputtering of Al doped ZnO. A d.c. and a pulsed d.c. discharge have been investigated. Different positive ions from the target material have been observed with low energies in d.c. and a second energy peak of about 30 eV in pulsed d.c. with only weak additional energy due to the sputter process. Negative ions are mainly O⁻ with energies corresponding to the target voltage of several 100 eV. They originate from the target and barely from the (O₂) gas and hit the substrate opposite the race track. In pulsed d.c., due to the varying target voltage, energies of up to 500 eV have been observed. With increasing pressure, negative ions at the substrate are reduced exponentially in their density but not in their energy.

1. Introduction

Transparent conductive oxide (TCO) thin films offer the possibility to contact components with transparent electrodes. They are increasingly applied e.g. in flat panel display technology or photovoltaics. The thin film material best studied and widely used is tin doped indium oxide (ITO). However, due to the limited resources of indium, ITO will not be suited for cheap mass production, especially of solar cells.^[1] One alternative for TCO films is aluminium doped zinc oxide (AZO) which provides similar properties.^[2-4] Magnetron sputtering either in d.c., pulsed, or r.f. mode from ceramic or metal targets is a convenient method for high rate large area deposition of AZO thin films.^[5-7] The contradictory demands of a high electrical conductivity and a simultaneously high optical transparency provide only a small process window and require a precise adjustment of the process parameters.^[5,8] This is up to date a difficult task because the physical understanding of the different species, their density and energy and how they contribute to the film growth and properties is still limited. This is all the more the case when the discharge is pulsed and the relevant parameters are subject to a significant temporal variation (see Refs. 9-11 and references therein). Ion bombardment of the growing film is often an advantage of magnetron sputtering to improve the film quality. However, it is reported that energies of bombarding species have to be restricted to values below 50 eV to prevent crystal damage during AZO deposition.^[5] Furthermore, it is supposed that in reactive sputtering using electronegative gases – such as O₂ in the case of AZO – negative ions can be present which acquire high energies and may bombard the film with energies exceeding 100 eV.^[13] A direct detection of these negative ions is often impossible because their current is superimposed by the electron current which typically is orders of magnitude higher. A possibility to detect negative as well as positive ions and their energy distribution function (IEDF) at the substrate is the use of an energy-dispersive ion mass spectrometer (so-called plasma monitor) with which ions can be separated according to their mass and energy and which is placed at the substrate position.^[14]

In this paper we present plasma monitor measurements of a magnetron sputtering discharge from an AZO target in pure Ar and O₂ atmosphere. Positive and negative ions were investigated in d.c. but also in pulsed d.c. mode.

2. Experimental Details

The experiments were carried out in a high vacuum chamber which was pumped down to a base pressure of $3 \cdot 10^{-4}$ Pa. Ar (99.998%) or O₂ (99.998%) was used as working gas with a flow rate of 100 sccm. The working pressure was adjusted between 0.3 Pa and 2.0 Pa by means of a throttling valve. The chamber contained a planar magnetron source which was equipped with a circular target of ZnO with 2 wt% Al₂O₃ (purity 99.95%) having a diameter of 100 mm. Further details of the magnetron source and its magnetic field are given elsewhere.^[15] The magnetron was operated with d.c. or pulsed d.c. For d.c., an MDX 1.5K power supply (Advanced Energy) was used in the power controlled mode with a discharge power of 100 W. Asymmetric-bipolar operation with a positive target voltage in the “off” phase of 10% of the average negative value during the “on” phase was achieved by a Pinnacle Plus unit (Advanced Energy). The pulsed discharge was also power controlled with an average power of 100 W. The pulse frequency was fixed at 100 kHz.

Ion energy distributions were measured with a plasma monitor PPM 422 (Inficon). With the PPM, ion energies of up to 500 eV against ground potential can be measured in the mass-to-charge number (m/z) range from 1 to 512. By changing the polarity of the whole detection system the device offers the possibility to measure either positive or negative ions. To prevent an influence of the magnetic field of the magnetron on the ion trajectories within the PPM and thus on the signal, its barrel was surrounded by a magnetic shield. Furthermore, in contrast to most similar systems, the detector was placed on-axis which allowed a linear construction and therefore an increased flexibility for the position of the extraction hood within the chamber of up to 600 mm from the chamber wall. The barrel was positioned such that the extraction orifice (100 μ m in diameter) was at a typical substrate position 100 mm in front of the target with the extraction hood of the barrel facing the target. It was desired to perform measurements on different positions relative to the symmetry axis of the magnetron, in particular on the symmetry axis and opposite the race track. Because the acceptance angle of the PPM is small with only a few degrees, this should give information about the origin of the species that are detected. Therefore, the magnetron was moved such that the entrance orifice of the fixed PPM was either opposite the target centre or a point in the race track. The PPM offers the possibility to adjust the potential of the barrel and the extraction orifice to minimise disturbance of the plasma to be measured. In the present case, the plasma monitor was electrically insulated keeping the barrel front and extraction hood at floating potential (V_{fl}). This is on one hand closest to the situation for a substrate at V_{fl} . On the other hand it provides the

best entrance potential in the pulsed discharge where the plasma potential (V_{PI}) is strongly varying in time. Because V_{PI} varies simultaneously, similar ion extraction conditions are obtained during the complete pulse whereas a fixed entrance potential could alter these conditions and even block ion extraction at particular moments of the pulse.

3. Results

In the d.c. discharge positive ions of the working gas as well as of the target material were found. Their IEDF shows a single peak at low energy. In Ar ambient, Ar^+ and Ar^{2+} were observed at $m/z = 40$ and $m/z = 20$, respectively. In oxygen, O^+ or O_2^{++} ($m/z = 16$) and O_2^+ ($m/z = 32$) were detected. Further strong positive ion signals appeared at $m/z = 27$ and $m/z = 64$ which were assigned to the target material ions Al^+ and Zn^+ . Their energy distribution is shown in Figure 1. The figure also shows that at $m/z = 43$ and $m/z = 80$ additional ions could be detected which were attributed to molecular ions of the target material, AlO^+ and ZnO^+ . Figure 1 represents the case of pure Ar as working gas. Nevertheless, a significant ion count rate is obtained for O^+ which originated from the target. As mentioned above, the positive ion IEDFs exhibit one strong peak at low energy of about 2 eV which is almost the same for all ions and represents V_{PI} in front of the floating barrel of +2 V. This peak is also observed very sharp for Ar^+ which is not included in Figure 1. Many of the IEDFs show a high energy tail which is a remnant of the sputter energy distribution of the atoms which are post-ionised in the discharge but cooled down to a certain extent by collisions with the gas. The high energy tail on the IEDF significantly differs for the different species or masses. While it dominates over the sharp peak at 2 eV for O^+ , it is only seen as a high-energetic shoulder for Al^+ and Zn^+ and vanishes for AlO^+ and ZnO^+ . However, it is in all cases much less intense than expected for the original sputter distribution.

Negative ions were measured almost only at $m/z = 16$ (O^-) and $m/z = 32$ (O_2^-). Only at $m/z = 43$ a weak signal was additionally observed which can be attributed to AlO^- . The count rate of O_2^- was always much weaker than that for O^- . This was the case for both Ar and O_2 . The count rate ratio O^-/O_2^- was typically 5-10 and the O_2^- signal was rather noisy. For this reason, in the following only O^- was particularly investigated. The IEDF of the observed negative ions in the d.c. discharge is generally similar to those shown in Figure 2 for the O^- ion measured opposite the race track. It has a dominant peak at high energies of up to several 100 eV depending on the target voltage. A more detailed analysis shows that the maximum in all cases is only a few eV above the equivalent to the target voltage (eV_T). The peak exhibits a

high energy tail extending over 50 to 100 eV but a sharp edge at its low energy side. At low energies, the energy spectrum has a sharp cut-off at some 10 eV representing V_{fl} . Between these two characteristic energies corresponding to V_T and V_{fl} , only low count rates are observed which in the case of O^- (cf. Figure 2) form weak maxima. Such maxima are observed for the conditions presented in Figure 2 at energies of about 70 eV, 100 eV, and 200 eV. The IEDF of O^- shown in Figure 2 for Ar as working gas has also been measured in pure O_2 ambient. Interestingly, it does not change either its structure or the absolute count rate significantly. Also in O_2 , a dominant maximum at about 400 eV, a weak maximum at 200 eV, and the cut-off at 20 eV are observed. Only the very weak maxima at 70 and 100 eV are missing. The absolute count rates are, however, extremely altered when the position of the plasma monitor relative to the magnetron is changed. This is shown in Figure 2 for the high-energy part of the spectrum. The distribution measured opposite the race track exhibits maximum count rates of well above 10^5 counts per second (cps) whereas the maximum opposite the magnetron centre is below 10^4 cps. As a consequence, the low energy part could not be measured in the discharge centre because it was too noisy.

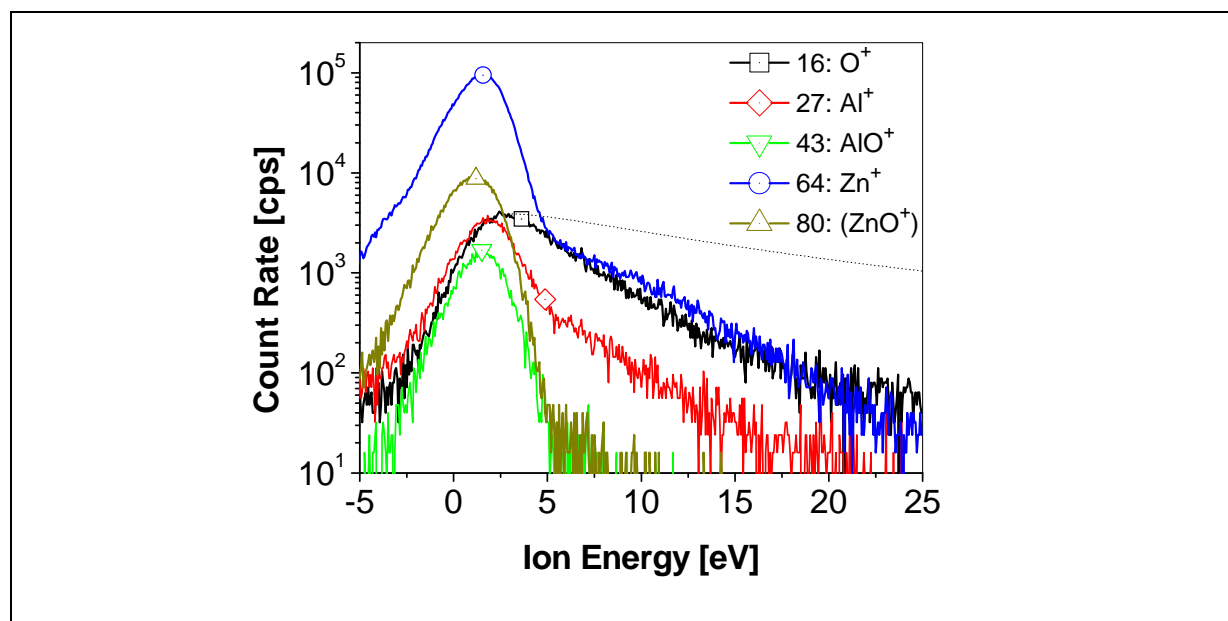


Figure 1: IEDFs of different positive ions of species sputtered from the target (d.c. discharge, 0.3 Pa Ar, centre position). The dotted line represents the expected sputter energy distribution.

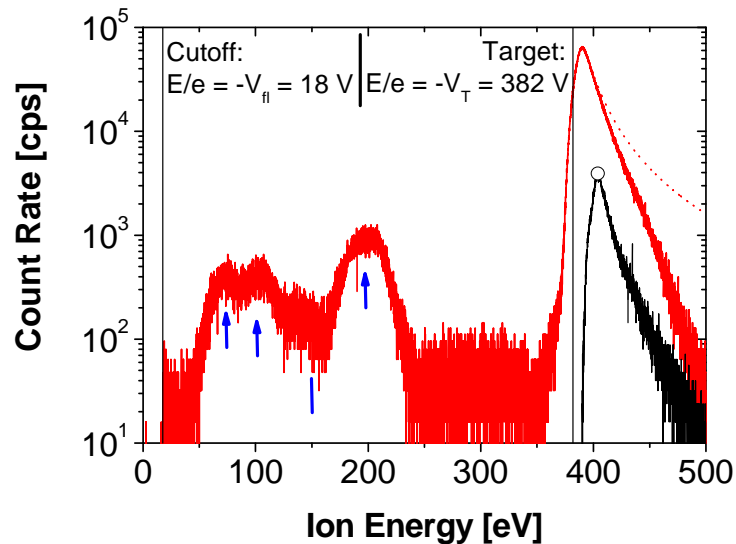


Figure 2: IEDF of the O^- negative ion (d.c. discharge, 0.5 Pa Ar, race track position). The arrows mark the position of fragment ions, the bar marks the position of the missing fragment from AlO^- . The IEDF marked with a circle was obtained at the same parameters but in the magnetron centre position.

The correlation between the target voltage and the energetic position of the maximum in the negative IEDF suggests that the ions originate from the target surface and their signal should be very sensitive to the pressure as they have to pass the discharge volume before they are detected. This is shown in Figure 3 for the high-energy part of the O^- IEDF for a pressure varied between 0.3 Pa and 2.0 Pa. Increasing pressure leads to strongly reduced flux of negative ions at the substrate: in the present case by a factor of more than 50. At the same time, the maximum of the distribution is not shifted in energy and even the form of the high energy tail remains unchanged.

When asymmetric-bipolar pulsed d.c. is applied instead of d.c., the energy distributions become much more complex. This is shown in Figure 4a for Ar^+ exemplarily for all positive ions. For positive ions originating from sputtered target material only the high energy tail shown in Figure 1 is added to the peak structures. Figure 4a still shows a low energy peak as in the d.c. case at +7 V which does not change its energy when the duty cycle (ratio between “on” time and pulse duration) is changed by an “off” time variation. However, there are additional peaks at higher energies between 20 and 50 eV which were also observed by other authors.^[14,16-18] Some very weak signals are observed up to 110 eV. These peaks are clearly dependent on the pulse parameters. The longer the “off” time is chosen the higher the peaks

above 20 eV become. At the same time, they consistently move towards lower energy and the low-energy peak is reduced in its count rate. The IEDF of O^- (cf. Figure 4b) does not change as much from d.c. to pulsed d.c. Still, a dominant peak is observed above 200 eV with a steep low-energy edge and a shallower high-energy tail. In contrast to d.c. where the tail converges to zero at high energy, the signal starts to increase again at very high energies up to the limit of the detector at 500 eV giving rise to the assumption that in pulsed d.c. higher energetic negative ions hit the substrate than in d.c.

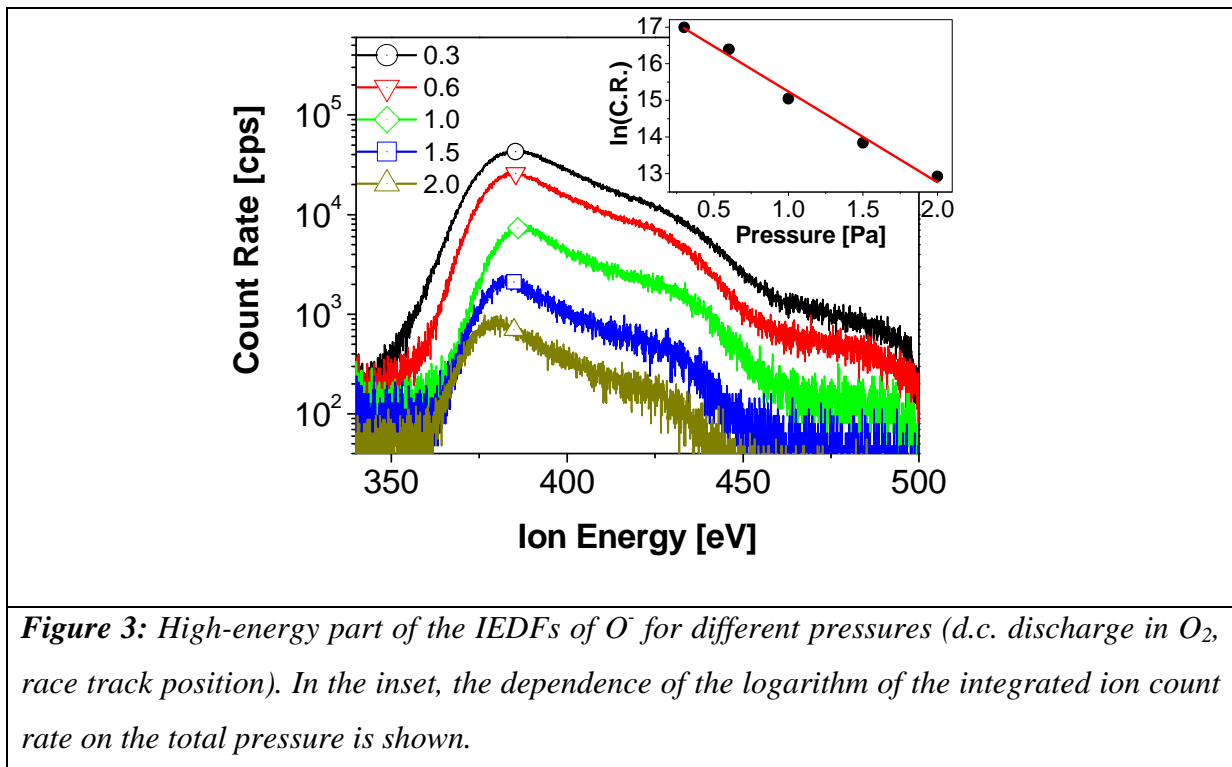


Figure 3: High-energy part of the IEDFs of O^- for different pressures (d.c. discharge in O_2 , race track position). In the inset, the dependence of the logarithm of the integrated ion count rate on the total pressure is shown.

4. Discussion

Positive ions which are created in the plasma enter the plasma monitor at the floating entrance orifice with an energy $e(V_{PI}-V_{fl})$. After energy selection they are then detected with eV_{PI} against ground. Thus all thermalised neutral species, such as Ar, which are ionised in the discharge will exhibit a sharp peak in their distribution at eV_{PI} . When the species have an additional velocity toward the substrate as it is the case with sputtered atoms because of their sputter energy distribution, this will increase their energy in the respective part of the IEDF. On the other hand, if the ions are formed in the sheath close to the entrance orifice by charge transfer collisions, they will have lower energy. This is the reason why also negative energies are present in Figure 1. The influence of the additional sputter energy is particularly well seen in Figure 1 for Zn^+ : completely thermalised Zn atoms cause a sharp peak at eV_{PI} with 2 eV

but a high energy tail extending above 5 eV is present. The high energy part is differently pronounced for different species: while for O^+ it is significant, it is completely lacking for AlO^+ . This effect is dependent on the mass of the sputtered species. The energy exchange during elastic collisions with the gas on the way from the target to the substrate is proportional to $m_t m_g / (m_t + m_g)$ with m_t and m_g being the mass of the sputtered target species and m_g the mass of the gas particles, respectively. When Ar ($m_g = 40$ amu) is used as working gas as in Figure 1, the most efficient energy transfer is expected for AlO ($m_t = 43$ amu) resulting in a completely thermalised distribution. The more the mass ratio differs the more of the original energy distribution is still observed, best seen for O^+ . The original energy distribution of species sputtered from the target should follow the form $E/(U_0+E)^3$ where E is the energy of the sputtered particle and U_0 is the surface binding energy approximated by the sublimation energy.^[19] Taking $U_0 = 7.6$ eV,^[5] the dotted curve is obtained for the high-energy part of the IEDF of O^+ . Clearly, it does not match the measured one showing that even the least thermalised species have lost most of their energy by collisions even at a pressure of 0.3 Pa at 10 cm distance. The IEDF of $m/z = 80$ which was attributed to ZnO^+ in Figure 1 does not fit into this scheme. Although this species has twice the mass of Ar, no high-energy tail is observed. Further, using O_2 as working gas its signal decreases much more than those for the Al^+ , Zn^+ , and AlO^+ which should not be the case if it were ZnO^+ . Investigations with a titanium target in Ar showed a similar peak at $m/z = 80$ although there was no match to any target species. Thus, the explanation of the unexpected behaviour in our case is that the signal is mostly Ar_2^+ and barely ZnO^+ .

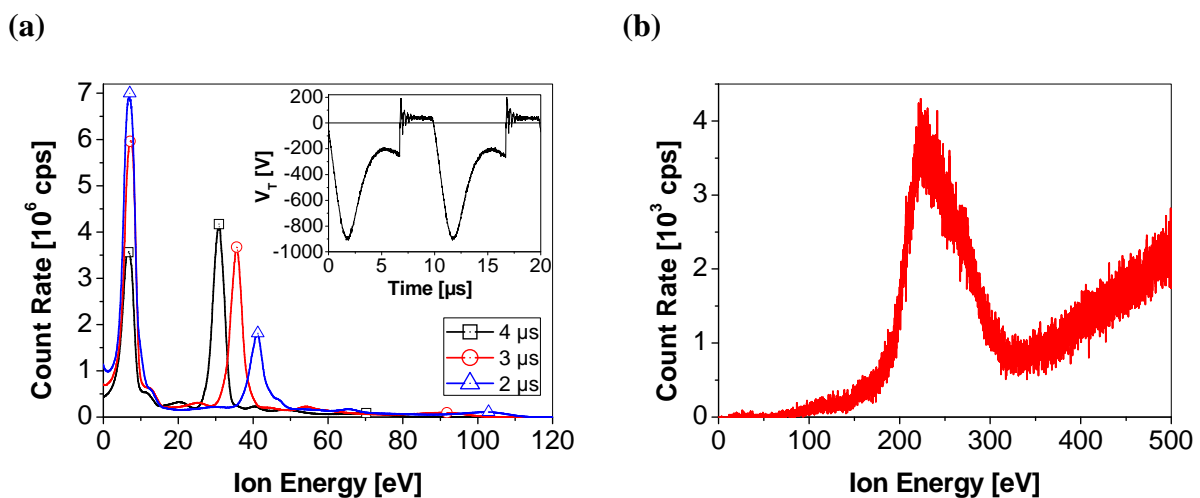


Figure 4: IEDFs of (a) Ar^+ for different pulse “off” times and (b) O^- for an “off” time of 4.0 μs (pulsed discharge in Ar, 0.5 Pa, race track position)

The majority of the negative ions arriving at the substrate have energies which correspond to the target potential V_T (cf. Figure 2 and 3) which means that they are formed directly at the target surface. By crossing the target sheath they gain the full energy $e(V_{PI}-V_T)$ which is reduced on entrance into the PPM by V_{PI} . According to the sputter energy distribution, higher energies than eV_T are obtained because the particles leave the target with an additional energy. As shown in Figure 2 by the dotted line which represents the expected sputter distribution for $U_0 = 7.6$ eV and in contrast to the positive target material ions, the high energy tail of the peak reproduces the original distribution quite well. This is reasonable because high energetic O^- colliding with gas atoms will either be neutralised and will not be measured as O^- at all or will be completely removed from the range of the shifted sputter energy distribution (at 400 to 450 eV) to much lower energies. Positive ions that collide, are, however, scattered into the low energy part of their sputter energy distribution (several eV). Negative ions that are completely thermalised are physically impossible to detect. Their energy is much less than the potential barrier between the plasma (V_{PI}) and the extraction orifice (V_{fl}). That is the reason why the IEDF of the negative ions has a cut-off to low energy from which V_{fl} can be obtained (-18 V in the case of Figure 2). All O^- that undergo any collision will be removed from the original "beam". The count rate of the ions which still reach the substrate directly, should then follow an exponential decay with the pressure. The inset in Figure 3 shows exactly this behaviour. However, it can not be ruled out from the measurements, that the substrate is still subject to high energetic bombardment through scattered O^- (or O created from O^- through collision) because the PPM does not detect inclined incidence. The advantage of the small detection angle, however, is a high lateral resolution. Owing to that, negative ions with high energy are particularly detected opposite to the race track. These ions are accelerated through the thin sheath in front of the target perpendicular to its surface and will therefore primarily hit the substrate directly opposite. The substrate will thus be subject to an inhomogeneous bombardment of negative ions with energies that are far above the limit of 50 eV given by Ellmer.^[5]

The similarity of the O^- IEDF in Ar and O_2 even in its absolute height shows that almost all negative ions are not only formed on the target surface but are produced of target material. If reflected oxygen played a significant role, the O^- IEDF would be enhanced in O_2 ambient which, however, was not observed. The weak maxima below the main peak have energies which would be exactly expected for O^- as a fragment of larger molecules that have been accelerated by the full sheath voltage: 200 eV corresponds to O^- from O_2^- , 100 eV to O^- from AlO_2^- , and 70 eV to O^- from ZnO^- (arrows in Figure 2), resp.. Surprisingly, just AlO^- which

has been directly observed is missing in this assignment (line in Figure 1). Further research is necessary to understand the mechanism for this “fragmentation”. However, it should be noted that we found a similar scheme for Ti sputtering in O_2 .^[20] Moreover, Mraz et al. found fragment energies in O^- IEDFs attributed to AlO^- and AlO_2^- for Al sputtering in Ar/ O_2 and to O_2^- for different other target materials.^[21,22]

When the discharge is pulsed asymmetric-bipolar, V_T is modulated. In the “on” phase it is negative with a deep valley of about -900 V about 2 μs after switching before it settles at a value of about -200 V. In the “off” phase it attains high positive values of up to +260 V immediately after switching before, after some oscillations, it settles at about +40 V. V_{PI} has been found to follow these changes in the “off” phase but keeps close to zero in the “on” phase.^[9,15,23] Because the energy of the positive ions which are formed in the plasma bulk is determined by V_{PI} , the IEDFs reproduce the changes in V_{PI} . The peak at 7 eV (cf. Figure 4a) is thus due to positive ions from the “on” phase and is not much changed in its energy when the “off” time is varied. The peaks at higher energy belong to ions from the “off” phase. The dominant ones of them corresponds to the stable “off” phase, higher energies are obtained from the ringing before the stabilisation and the target voltage overshoot.^[14] However, an energy of up to 260 eV corresponding to the peak potential was not observed probably due to its shortness. When the “off” time is shortened, the ion energies increase because the target potential in the “off” phase increases and the ion intensity decreases because the time for their creation is shortened. At the same time, the low energy peak increases its intensity because the “on” time is increased (fixed pulse frequency). For the negative ions created at the target surface only the “on” time with negative V_T is decisive. As in the d.c. case, they are produced with the full sheath voltage. This causes a peak (cf. Figure 4b) for this comparably long stable “on” phase. However, for a short time, V_T is much lower so that negative ions with even more energy are produced. This leads to the significant ion count rates for energies above 300 eV. They probably extend to the full target potential equivalent (i.e. 900 eV) but could only be measured up to 500 eV with the PPM. Asymmetric-bipolar pulsed d.c. thus causes significantly higher energy of negative ions at the substrate than a comparable d.c. discharge.

5. Conclusions

Ion energy distributions (IEDFs) in d.c. and asymmetric-bipolar pulsed d.c. magnetron sputtering of aluminium doped zinc oxide were studied in pure Ar or O₂ with a plasma monitor facing the AZO target. Positive target material ions of Zn⁺, Al⁺, O⁺ and AlO⁺ were identified. The IEDFs of positive ions exhibit a single low-energy peak corresponding to V_{pl}. Only a weak remnant of the sputter distribution is observed even at low pressure of 0.3 Pa which depends on the ion mass. O⁻ and O₂⁻ ions were observed with O⁻ being dominant. They are all formed at the target surface thus showing mainly a high-energy peak of several 100 eV in the IEDF which corresponds to the target voltage. They move perpendicularly to the target surface and produce a lateral inhomogeneity at the substrate which reflects their inhomogeneous production at the target. With pulsed d.c., the variation of the target voltage leads to more complex IEDF of positive ions with an additional peak structure at about 30 eV due to positive target and plasma potentials. If the substrates are grounded they will be subject to these high energies. The negative IEDFs look similar to those for d.c., but additionally show a significant amount of ions with energies far beyond the typical peak due to momentary strong negative target potentials. These can affect film growth on grounded as well as floating potential.

Acknowledgements

The authors thank G. Peter (Inficon) for many helpful discussions as well as Th. Förster and Th. Weber for technical assistance. The work was financially supported by the European Union and the Saxon State Ministry of Labour and Economic Affairs under grant no. 11689/1864 and by the German Research Society under grant no. WE 1478/1-1.

References

- [1] A. Chipman, *Nature* **2007**, 449, 113.
- [2] B. Szyszka, *Thin Solid Films* **1999**, 351, 164.
- [3] B. Thestrup, J. Schou, *Appl. Phys. A* **1999**, 69, S807.
- [4] T. Minami, *Semiconductor Sci. Technol.* **2005**, 20, S35.
- [5] K. Ellmer, *J. Phys. D: Appl. Phys.* **2000**, 33, R17.
- [6] Y. Zhou, P. J. Kelly, A. Postill, O. Abu-Zeid, A.A. Alnajjar, *Thin Solid Films* **2004**, 447-448, 33.
- [7] R. Kleinhempel, B. Graffel, J. Lukas, H. Kupfer, Th. Dunger, Th. Welzel, F. Richter, *Plasma Processes and Polymers* **2007**, 4 S1, S325.
- [8] C. Guillen, J. Herrero, *Thin Solid Films* **2006**, 515, 640.
- [9] J.W. Bradley, Th. Welzel, "Process Diagnostics", in: *Reactive Sputtering Deposition (Springer Series in Materials Science 109)*, D. Depla, S. Mahieu, Eds., Springer-Verlag, Berlin, Heidelberg, 2008, Chapter 7, p. 255 (ISBN: 3540766626).
- [10] Th. Welzel, Th. Dunger, F. Richter, *Surf. Coat. Technol.* **2006**, 201, 3959.
- [11] I. Swindells, P.J. Kelly, J.W. Bradley, *New J. Phys.* **2006**, 8, 47.
- [12] A. Belkind, A. Freilich, J. Lopez, Z. Zhao, W. Zhu, K. Becker, *New J. Phys.* **2005**, 7, 90.
- [13] K. Tominaga, K. Kuroda, O. Tada, *Jpn. J. Appl. Phys.* **1988**, 27, 1176.
- [14] J. W. Bradley, H. Bäcker, Y. Aranda-Gonzalvo, P. J. Kelly, R. D. Arnell, *Plasma Sources Sci. Technol.* **2002**, 11, 165.
- [15] Th. Welzel, Th. Dunger, B. Liebig, F. Richter, *New J. Phys.* **2008**, 10, 123008.
- [16] S. A. Voronin, G. C. B. Clarke, M. Cada, P. J. Kelly, J. W. Bradley, *Meas. Sci. Technol.* **2007**, 18, 1872.
- [17] M. Misina, J. W. Bradley, H. Bäcker, Y. Aranda-Gonzalvo, S. K. Karkari, D. Forder, *Vacuum* **2003**, 68, 171.
- [18] S. K. Karkari, H. Bäcker, D. Forder, J. W. Bradley, *Meas. Sci. Technol.* **2002**, 13, 1431.
- [19] J. A. Thornton, J. E. Green, "Sputter Deposition Processes", in: *Handbook of Deposition Technologies for Films and Applications*, R. F. Bunshah, Ed., Noyes Publications, Park Ridge, 1994, ch. 5, p. 249.
- [20] Th. Welzel, unpublished work.
- [21] S. Mraz, J. M. Schneider, *Appl. Physics Letters* **2006**, 89, 051502.
- [22] S. Mraz, J. M. Schneider, *J. Appl. Phys.* **2006**, 100, 023503.
- [21] A. Vetushka, S. K. Karkari, J. W. Bradley, *J. Vac. Sci. Technol.* **2004**, A22(6), 2459.